NASA
Technical
Paper
2043

August 1982

Effect of Nozzle and Vertical-Tail Variables on the Performance of a Three-Surface F-15 Model at Transonic Mach Numbers

Odis C. Pendergraft, Jr.,
and E. Ann Bare

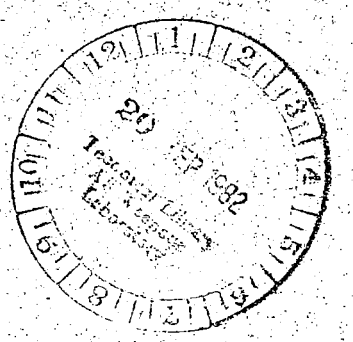

NASA

NASA
Technical
Paper
2043

1982

Effect of Nozzle and Vertical-Tail Variables on the Performance of a Three-Surface F-15 Model at Transonic Mach Numbers

Odis C. Pendergraft, Jr.,
and E. Ann Bare
Langley Research Center
Hampton, Virginia

NASA
National Aeronautics
and Space Administration

**Scientific and Technical
Information Branch**

SUMMARY

An investigation was conducted in the Langley 16-Foot Transonic Tunnel to determine the longitudinal aerodynamic characteristics of twin two-dimensional (2-D) nozzles and twin baseline axisymmetric nozzles installed on a fully metric 0.047-scale model of the F-15 three-surface configuration (canards, wing, horizontal tails). The effects of 2-D nozzle in-flight thrust reversing, locations and orientation of the vertical tails, and deflections of the horizontal tails were also determined. Test data were obtained at static conditions and at Mach numbers from 0.60 to 1.20 over an angle of attack range from -2° to 15°. Nozzle pressure ratio was varied from jet off to about 6.5.

Results of the investigation indicate that thrust reversing had essentially no effect on longitudinal stability and only small effects on horizontal-tail control effectiveness. Nacelle-mounted vertical tails produced slightly lower drag than the baseline, boom-mounted vertical tails at subsonic Mach numbers. The axisymmetric nozzles with baseline or nacelle-mounted vertical tails had lower drag than the two-dimensional convergent-divergent nozzles.

INTRODUCTION

Recent studies of twin-engine fighter aircraft (refs. 1 to 5) have identified a number of potential advantages of nonaxisymmetric nozzles as compared to conventional round or axisymmetric nozzles. One important benefit of nonaxisymmetric nozzles is the adaptability of the design to include thrust vectoring and reversing with less weight penalty than conventional axisymmetric nozzles. (See refs. 5 and 6.) The addition of thrust reversing capabilities to most current and future fighter aircraft would greatly enhance short field take-off and landing (STOL) performance. Also, the use of in-flight thrust reversing has the potential to improve airplane agility during air-to-air combat.

The performance of nonaxisymmetric nozzle thrust reversers at static and subsonic flight conditions has been determined in several experimental investigations (refs. 7 to 13). These results indicate that highly efficient nonaxisymmetric nozzles with thrust reversers can be designed. However, use of the in-flight thrust reverser could cause significant changes in airplane tail loads, particularly for twin-vertical-tail configurations (ref. 14) and could also degrade the control effectiveness of horizontal-tail (ref. 11) and rudder surfaces (ref. 12). The effect of in-flight thrust reversing on stability and control at angle of attack is also of great importance.

This paper presents the longitudinal aerodynamic characteristics of a three-surface F-15 model with baseline axisymmetric nozzles installed and with two-dimensional convergent-divergent (2-D C-D) nozzles installed. Each nozzle type was tested in the positive thrust mode, and the 2-D C-D nozzles were also tested in partial and full reverse thrust modes.

This investigation was conducted in the Langley 16-Foot Transonic Tunnel at static conditions and at Mach numbers from 0.60 to 1.20. Angle of attack was varied from -2° to 15°, and nozzle pressure ratio was varied from jet off (1.0) to about 6.5

depending on Mach number. Two twin-vertical-tail locations, three twin-vertical-tail toe angles (leading edge out), and three horizontal-tail deflection angles were tested.

SYMBOLS

A_e nozzle-exit area, cm^2

A_t nozzle-throat area, cm^2

C_D thrust-removed drag coefficient, $\frac{D}{q_\infty S}$

$C_{(D-F)}$ drag-minus-thrust coefficient, $\frac{D - F}{q_\infty S}$

C_L total lift coefficient, $\frac{\text{Total lift}}{q_\infty S}$

$C_{L,a}$ lift coefficient with static thrust component removed, $\frac{\text{Lift}}{q_\infty S}$

C_m total pitching-moment coefficient, $\frac{\text{Total pitching moment}}{q_\infty S\bar{c}}$

$C_{m_{\delta H}}$ horizontal-tail pitch-control effectiveness, $\frac{C_m(\delta_H=5^\circ) - C_m(\delta_H=0^\circ)}{5}$

$\bar{c}$ wing mean geometric chord, 22.83 cm

D drag, N

F thrust, N

F_g gross thrust, N

F_i ideal isentropic gross thrust, $\dot{m}\sqrt{\frac{2\gamma}{\gamma - 1} RT_{t,j}\left[1 - \left(\frac{p_\infty}{p_{t,j}}\right)^{\frac{\gamma-1}{\gamma}}\right]}$, N

M free-stream Mach number

$\dot{m}$ measured mass-flow rate, kg/sec

$\dot{m}_i$ ideal mass-flow rate, kg/sec

$p_{t,j}$ average jet total pressure, Pa

p_∞ free-stream static pressure, Pa

q_∞ free-stream dynamic pressure, Pa

R	gas constant (for $\gamma = 1.3997$), 287.3 J/kg-K
S	wing reference area, 1244.9 cm^2
$T_{t,j}$	jet total temperature, K
α	angle of attack, deg
γ	ratio of specific heats, 1.3997 for air
δ_H	horizontal-tail deflection angle, positive leading edge up, deg
δ_{REV}	nozzle thrust-reverser flap angle, deg (fig. 11)

Abbreviations:

A/B	afterburning
ASME	American Society of Mechanical Engineers
B.L.	butt line, cm
C-D	convergent-divergent
DSW	divergent sidewalls
F.S.	fuselage station, cm
L.E.	leading edge
L.H.	left hand
NPR	nozzle pressure ratio
PTJ	nozzle jet-total-pressure orifices
R.H.	right hand
SSW	fixed, straight sidewalls
VSW	variable sidewalls
W.L.	waterline
2-D	two-dimensional (nonaxisymmetric)

APPARATUS AND PROCEDURE

Wind Tunnel

This investigation was conducted in the Langley 16-Foot Transonic Tunnel, a single-return, continuous-flow, atmospheric wind tunnel with a slotted, octagonal test section measuring 4.8 m diametrically to midflat center line. With the aid of a compressor system, which draws air out through slots in the test section for

M > 1.05, the test-section airspeed is continuously variable between Mach numbers of 0.20 and 1.30. Further details on dimensions and the operating characteristics of the Langley 16-Foot Transonic Tunnel can be found in reference 15.

Support System

The model was supported in the tunnel by a sting-strut system as shown in figure 1. High-pressure air lines and all instrumentation were routed through the support system. The complete model was mounted on an internal, six-component strain-gage balance through an adapter to the sting strut.

Propulsion Simulation System

The facility high-pressure air system provided a continuous flow of clean, dry, heated air to the model. This high-pressure air is transferred from a common high-pressure plenum in the front of the model to the nozzles by means of dual flow-transfer assemblies. A sketch of the assembly is shown in figure 2. The two sets of flexible metal bellows (longitudinal) in conjunction with the two side-mounted metal bellows (lateral) serve to minimize pressurization tares while still maintaining sufficient flexibility for proper force balance operation in all six components.

Transition (from round to rectangular cross section) and instrumentation sections were downstream of 30-percent-open choke plates which were located in each exhaust flow tailpipe at fuselage station 83.35. The transition section terminated at fuselage station 91.592, which was the common connect point for all two-dimensional nozzles. The axisymmetric nozzles used an externally tapered ring to fair between F.S. 91.592 and F.S. 93.259 - the axisymmetric nozzle common connect point.

Model

The model used for this investigation was a 0.047-scale model of a F-15 three-surface configuration (canards, wing, horizontal tails) with axisymmetric nozzles. This model is a fully metric jet-effects model with faired-over inlets to allow propulsion simulation. A sketch of the model is shown in figure 3. Figure 4 shows a photograph of the model installed in the Langley 16-Foot Transonic Tunnel. Model geometric characteristics are given in table I. The baseline configuration is characterized by boom-mounted twin vertical tails (toe angle, L.E. out, of 2°), aft-located boom-mounted horizontal tails, closely spaced axisymmetric twin engines, and forward inlet-mounted canards. For this investigation, the canards were set at a nominal angle of -6° (leading edge down) - the minimum drag angle for subsonic cruise flight as determined from unpublished wind-tunnel data. In order to adapt the model afterbody for smooth integration of the rectangular nozzle shape, hardware interfairings were used.

Baseline axisymmetric nozzles.- Sketches of the two baseline axisymmetric nozzles showing their geometry are given in figure 5. The nozzles with the smaller throat area (fig. 5(a)) represent the maximum dry-power setting for all Mach numbers less than 1.10, while the nozzles with the larger throat area (fig. 5(b)) represent the maximum-afterburning-power setting (A/B) for Mach numbers less than 1.10. A sketch and the coordinates of the fixed fairing around the nacelle ahead of the movable nozzle boattails are given in figure 6.

Baseline (boom-mounted) vertical tails were mounted at 2° (L.E. out) toe angle and also at 0° and 4° (L.E. out). An alternate tail configuration with the vertical tails mounted forward on the engine nacelles at 2° toe angle and 15° cant angle was also tested. In conjunction with this position of the vertical tails, a different set of booms were used to mount the horizontal tails. Photographs of this vertical-tail configuration are shown in figure 7(a), and a sketch giving the important dimensions of the model (with 2-D nozzles installed) is shown in figure 7(b).

Two-dimensional convergent-divergent nozzles.- A photograph of the two-dimensional convergent-divergent (2-D C-D) nozzles installed on the F-15 model is shown in figure 8. Sketches of the dry and A/B power positive-thrust 2-D C-D nozzles are shown in figure 9. The dry and A/B power nozzle flaps for use with straight sidewalls are shown in figure 9(a), and the dry-power nozzle flaps for use with the divergent sidewalls are shown in figure 9(b). The three sidewall configurations are shown in figure 9(c). The fixed, straight sidewalls represent sidewalls that do not change shape as the nozzles are closed down to dry power from the A/B power setting, creating channels over the movable flap surfaces. (See photograph in fig. 8.) The fixed divergent sidewalls are shown in the center of figure 9(c) and present an attempt to reduce nozzle sidewall boattailing. These were used only with the divergent sidewall flaps shown in figure 9(b). For these sidewalls, throat and exit heights were reduced slightly to retain the same throat area as the straight sidewall dry-power positive-thrust nozzles. The variable sidewalls shown at the bottom of figure 9(c) represent the nozzles in the dry-power condition but without any exposed sideplates.

Figure 10 is a photograph of the fully deployed thrust reversers installed on the F-15 model. Sketches of the two reverser deployments tested are shown in figure 11. The partially deployed (90°) reverser was designed to spoil all forward thrust, while the fully deployed (130°) reverser was designed to produce approximately 50 percent reverse thrust.

This 2-D C-D nozzle design simulates a variable-area internal expansion nozzle. The throat area and the exit area of the full-scale hardware would be independently controlled by the separate actuation of the convergent and divergent nozzle flaps. Thrust reversal would be accomplished by actuation of the convergent flaps, closing the throat area while simultaneously opening the reverse flow ports upstream. For a complete description of this nozzle mechanism, see reference 8.

Instrumentation

Model forces and moments were measured by an internal six-component strain-gage balance. Internal cavity pressures were measured at two forward and two aft locations.

Mass-flow rate in each nozzle was determined from total pressure and temperature measurements in the flow transfer assemblies (fig. 12) using flow constants determined from the calibrations with ASME standard nozzles. The total mass-flow rate (both nozzles) was measured by a turbine flow meter (external to the tunnel). These data were used as a back-up to the calculated values. The flow conditions in each nozzle were determined by two total-pressure probes - one from the top and one from the side of each tailpipe - and one total-temperature probe in each nozzle. All nozzle instrumentation was located aft of the choke plate and transition section (see section "Model and Support System"). All pressures were measured with individual pressure transducers.

Tests

Test data were taken at Mach numbers of 0, 0.60, and 0.90 for all configurations and at 1.20 for selected configurations. Angle of attack was varied from -2° to 15° depending upon Mach number; nozzle pressure ratio varied from approximately 1.0 (jet off) to about 6.5 depending upon Mach number. Basic data were obtained by holding nozzle pressure ratio constant and varying angle of attack. Nozzle-pressure-ratio sweeps were conducted at 0° angle of attack for selected configurations. Undeflected horizontal tails were tested with all configurations, and selected configurations were tested with horizontal tails deflected at -15° and 5° and with tails off.

Boundary-layer transition was fixed on the model by means of 0.25-cm-wide strips of No. 120 carborundum grit. These strips were located 1.91 cm aft (streamwise) of the nose and the inlet fairings. Transition strips on all lifting surfaces were located at 5 percent local chord. The methods described in references 16 and 17 were used to determine the locations of these strips and the grit size.

Data Reduction

All data for both the model and the wind tunnel were recorded simultaneously on magnetic tape. For each data point approximately 50 frames of data, taken at a rate of 10 frames per second, were used to obtain average recorded data. The recorded data were used to compute standard force and moment coefficients using wing area, mean geometric chord, and span for reference area and lengths. Corrections were made to the force data to account for bellows/balance interaction tares (refs. 7 and 11). In addition, balance corrections were also made to account for internal cavity pressure/area tares.

Model angle of attack α was computed from the strut pitch angle. This angle was corrected by applying sting deflection terms caused by bending under aerodynamic load. A flow angularity adjustment of 0.1°, which is the average angle measured in the Langley 16-Foot Transonic Tunnel, was applied to the angle of attack.

Total-pressure profiles were determined for the ASME calibration nozzles and the 2-D C-D nozzles with straight sidewalls by use of movable Kiel probes (total pressure). Each internal total-pressure probe was corrected to the integrated value of jet total pressure at the nozzle throat.

Thrust-removed coefficients were obtained by determining the components of thrust in the axial, normal, and pitch directions and subtracting these values from the measured forces. These thrust components at forward speeds were determined from measured static data and are a function of the free-stream static and dynamic pressure.

Data from this investigation may be used to correct aerodynamic forces and moments obtained on an unpowered model having the correct inlet geometry and inlet flow. A 0.047-scale sting-mounted aerodynamic model of the F-15 three-surface configuration with the correct inlet shape and mass flow has previously been tested and the results are reported in reference 18. Aerodynamic force and moment data for a 0.047-scale F-15 model without canards, using the axisymmetric nozzles of this investigation to simulate the actual nozzles at operating nozzle pressure ratios, as well as these nozzles plus choke nozzles to match flow-through nozzle pressure ratios, can be found in reference 19. These data should further aid in sorting out the propulsion effects for the three-surface configuration.

PRESENTATION OF RESULTS

The results of this investigation are presented in plotted coefficient form except for the static-performance data, which are presented in ratio form. Unless otherwise noted on the figures, data are for the baseline configuration with boom-mounted twin vertical tails (toe angle, L.E. out, of 2°) and boom-mounted horizontal tails at 0° deflection.

The static-performance data are presented in the following figures:

The basic drag-minus-thrust performance data for all configurations are presented in the following figures:

The thrust-removed longitudinal aerodynamic characteristics are presented in the following figures:

Comparison and summary data plots are presented in the following figures:

DISCUSSION

Basic Data

Static (M = 0) performance.- Static performance of the axisymmetric and 2-D C-D nozzles in the forward thrust mode is shown in figures 13 to 15, and static reverse thrust performance of the 2-D C-D SSW dry-power nozzles is shown in figure 16. For-

ward thrust performance F_g/F_i exhibits the normal single point peak expected for nozzle types with all internal exhaust flow expansion. (See, for example, fig. 15.) The peaks, though not well defined because of the low values of A_e/A_t involved, appear to occur near the nozzle pressure ratios required for fully expanded exhaust flow (NPR = 3.2 for dry-power nozzles and NPR = 4.5 for the A/B power nozzles). Nozzle pressure ratios above about 3.70 could not be achieved for the A/B power nozzles at static conditions because of bellows pressure limitations produced at the higher mass flows required. This problem only occurs at static conditions and is relieved with increasing Mach number as static pressure is reduced. This limitation prevented static test data being taken near the A/B nozzle operating NPR's, so it was necessary to extrapolate the data up to about NPR = 5 to match the highest NPR data points taken at M = 0.90.

Reverse thrust performance for the two reverser positions, along with the forward thrust performance for comparison, is shown in figure 16. The 90° reverser flap is positioned to spoil the nozzle thrust but statically does produce up to 17 percent reverse thrust with increasing nozzle pressure ratio. The resultant reverse flow is probably due to the uncontained flow upstream of the four nozzle ports caused by the very short nozzle length upstream, compared to the longer flap downstream. The fully deployed reverser, with consideration for internal losses, is designed to produce approximately 50 percent reverse thrust but statically attains only about 45 percent. It will be shown in later figures that these reverse thrust values increase at forward speeds.

Drag-minus-thrust performance at forward speeds.- For all the configurations investigated, basic data concerning effects on the longitudinal aerodynamic characteristics of the three-surface F-15 model at forward speeds are presented in aerodynamic coefficient form, including thrust contributions, in figures 17 to 36. The data for the complete configurations (all tail surface in place) exhibit the normal characteristics for advanced fighter aircraft. The configuration is slightly unstable at M = 0.60 and M = 0.90 and stable at M = 1.20. For the axisymmetric nozzle configurations, NPR has little or no effect on pitching-moment coefficient or lift coefficient and, of course, large effects on drag-minus-thrust coefficient. (See, for example, fig. 17.) With their larger throat areas and much larger mass flow, the afterburning-power nozzles produce approximately twice the change in $C_{(D-F)}$ as the dry-power nozzles for the same NPR. (See fig. 18.)

For the 2-D C-D nozzle configurations, the data exhibit trends similar to the axisymmetric nozzle configurations except that NPR has a much larger effect on pitching-moment coefficient, especially for the divergent sidewall nozzles. (See fig. 20.) This is probably due to slight differences between the upper and lower nozzle flaps and/or slight differences in alignment of the nozzle flaps with the model center line at assembly. In many cases where basic model configurations were tested, data were taken at jet off and at up to four additional NPR's to help determine in more detail the effects of NPR on the data. (See, for example, fig. 17.) Much of these data are replotted versus NPR in later figures to show the effects. Many of the remaining configurations were tested only at jet off and operating NPR values to reduce the length of the wind-tunnel test program. (See, for example, fig. 18.) Figures 17 to 27 contain data for configurations without thrust reversers deployed, figure 28 is for partially deployed reversers (δ_{REV} = 90°), and figures 29 to 36 are for fully deployed reversers (δ_{REV} = 130°). Again, small differences in nozzle geometry may be causing the large effects on pitching-moment coefficient, especially since small differences in the throat area (top to bottom) would have even larger effects on moment than for the forward thrust nozzles. As expected, removal of the horizontal tails made the configuration more unstable. (For example,

compare fig. 32 with fig. 29.) Operation of the reversers has little or no effect on the pitching-moment slopes except for $M = 1.20$, indicating minimal effects on longitudinal stability at subsonic speeds. (See fig. 29.) This result is also reported in references 10 and 12 for the F-15 configuration with boom-mounted vertical and horizontal tails. The aft location of the vertical tails serves to shield the reverser flow, minimizing effects on the horizontal tails. Removing the vertical tails produces a large adverse change in pitching moment with reverser operation, indicating significant reductions in the shielding effect. (Compare fig. 34(b) with fig. 29(b).) Mounting the vertical tails farther forward on the nacelles produces similar but less reverser effects on the horizontal tails. (Compare fig. 35 with fig. 29.) Further results of the reverser effects on horizontal-tail effectiveness are discussed later in a summary figure. Differential reversing ($\delta_{REV} = 0°$ for left nozzle and $\delta_{REV} = 130°$ for right nozzle) has only small effects on longitudinal data and reduces reverse thrust by more than half. (Compare fig. 36 with fig. 29.)

Thrust-removed performance at forward speeds.- Basic longitudinal data with the thrust removed (determined from static-thrust-calibration runs made before each tunnel run) are presented in figures 37 to 56 in the form of $C_{L,a}$ plotted versus α and C_D. Note that both the α and C_D scales have been expanded from the previous figures. For the forward thrust configurations (figs. 37 to 47), operation of the jets generally produces slight decreases in drag coefficient and has little or no effect on lift coefficient except for maximum afterburner power. (See fig. 38.) For the reverse thrust configurations (figs. 48 to 56), operation of the jets significantly increases the drag coefficient and slightly reduces or has little effect on the lift coefficient. The lift reduction with reverser operation is the more important phenomenon, since this reduction could adversely affect maneuverability during reverser use. Summary data plots (with $p_{t,j}/p_\infty$ and NPR) are presented later to further show the effects of jet operation.

Comparison and Summary Data

The effects of the following configuration changes on the drag-minus-thrust performance are to be discussed:

Nozzle type.- The lift and drag-minus-thrust performance of the configurations with 2-D C-D SSW dry-power nozzles is compared with the configurations with axisymmetric dry-power nozzles in figures 57 to 59 for several angles of attack from 0° up to 15° depending on Mach number. The same comparison is made for the afterburning-power-nozzle configurations, but only at $\alpha = 0°$. (See fig. 60.) In general, the axisymmetric nozzle configurations had slightly better drag-minus-thrust performance than the 2-D C-D nozzle configurations for all Mach numbers and angles of attack and for all but the highest values of $p_{t,j}/p_\infty$. The thick nozzle sidewalls (about 13.46 cm full scale) and the necessary nozzle sidewall closure, along with steep nozzle boattailing, contribute to the poorer performance of the 2-D C-D nozzle. It is felt, however, that elimination of the internozzle closure would substantially improve this performance, probably to or above the level of the axisymmetric nozzle configurations. Nozzle shape does not affect the lift characteristics enough to indicate any significant trends.

Twin-vertical-tail position.- The drag-minus-thrust performance of the dry-power axisymmetric nozzle configuration with boom-mounted vertical tails (baseline) is compared in figure 61 for the same nozzle configuration with nacelle-mounted vertical tails (2° L.E. out, toe angle) canted out 15° and having streamlined booms. The same

comparison is also made in figure 62 for the configuration with dry-power 2-D C-D SSW nozzles. For most conditions and both nozzle types, the configuration with nacelle-mounted vertical tails had slightly better performance. This result was expected, since mounting the vertical tails on the nacelles also moves them forward - substantially reducing afterbody closure rate near the nozzles and moving them partially out of the most critical interference region. Further information on tail-location effects for a single-engine generic model may be found in reference 20.

Nozzle sidewall shape.- The drag-minus-thrust performance of the dry-power 2-D C-D nozzle configurations with the three different nozzle sidewall shapes is presented in figure 63 for $M = 0.60$ and $M = 0.90$. The variable sidewall (VSW) and the fixed, straight sidewall (SSW) configurations had about the same performance for both Mach numbers. Both nozzle configurations had significantly better performance than the divergent sidewall (DSW) nozzle configuration. The VSW and SSW nozzles had the same internal geometry so that the slight differences in performance between them are due to the external flow differences caused by the channel effects of the fixed, straight sidewall exposed surfaces above the nozzle flaps at the dry-power setting. By comparing the jet-off data to the jet-on data, it is evident that the loss in performance for the DSW nozzle configuration is due to internal losses in the nozzles. The divergent sidewalls upstream of the nozzle throats further aggravate the already difficult flow transition from round to rectangular in the nozzle ducts - producing additional total-pressure loss and hence thrust loss.

Vertical tails on/off.- Removal of the twin vertical tails decreases drag-minus-thrust coefficient at all conditions (figs. 64 to 66) as would be expected. At Mach numbers greater than 0.6, there is a small increase in lift. This lift increment may be attributed to the smoother flow field of the afterbody without vertical tails. There is no effect of jet operation on the lift and drag increments.

Twin-vertical-tail toe angle.- The effect on drag-minus-thrust coefficient of varying the twin-vertical-tail toe angle from the baseline 2° L.E. out is shown in figure 67. The best overall drag-minus-thrust performance was exhibited by the 4° toe-out configuration. There is a channeling effect of the twin vertical tails, as noted in reference 14. At subsonic Mach numbers, the local velocity between the tails is higher than the velocity outside the tails. The turning of the twin-vertical-tail toe angle (L.E. out) reduces this channeling effect and, therefore, the drag, as seen at $M = 0.90$ with the jet off (fig. 67(b)). With increase in angle of attack, the drag reduction increment decreases as expected. With the jet on, the pumping action of the flow further reduces drag-minus-thrust performance.

Amount of thrust reversal.- Use of the 2-D nozzle in-flight thrust reversers shows that besides the obvious effect of increased drag with reverser deployment, there is also an effect on lift and pitching moment, as shown in figure 68. The drag-minus-thrust increment due to thrust-reverser deployment decreases with increasing Mach number; however, both the 130° (fully deployed) and the 90° (partially deployed) remain effective at Mach 1.20.

The change in lift due to reverser deployment is an incremental reduction in lift that is not dependent on the degree of reverser deployment. This is probably attributable to testing only at the 90° and 130° positions. Testing at other lower reverser angles should show that the lift reduction is a function of reverser position, but mostly occurring at lower angles than 90°.

As previously discussed, this F-15 three-surface configuration is subsonically unstable. The trend of pitching moment is basically unaffected by deployment of

thrust reverser. In the basic data it was shown that for subsonic Mach numbers (figs. 42, 48, and 49) reverser installation (jet-off data) caused an increment change in basic pitching moment and that reverser operation decreases this increment. (Compare fig. 17 with fig. 29.) The deployment of thrust reversers does not alter the basic longitudinal stability of this F-15 three-surface configuration.

Twin-vertical-tail position.- The effect of nacelle-mounted vertical tails (2° L.E. out, toe angle) with reversers fully deployed is shown in figure 69. As previously discussed, there is a reduction in drag with the jet off and with the nacelle-mounted tails. Jet-on data at $M = 0.60$ reverse the trend observed with the jet off. The baseline tails, being farther aft, are more influenced by the reverse flow plume, which may cause blockage of the free-stream flow. As previously discussed, this reduction in local velocities between the vertical tails can reduce drag. The nacelle tails, being canted outward 15° plus being farther forward of the reverse flow, do not show the same effect. At $M = 0.90$, this jet effect is no longer seen. Drag-minus-thrust coefficient is lower with both the jet off and the jet on for the nacelle-mounted tails.

Horizontal-tail pitch-control effectiveness.- A major concern of using thrust reversers in flight is the effect of reverse flow on control surfaces, particularly the horizontal tails (ref. 11). Figure 70 shows the horizontal-tail pitch-control effectiveness with thrust reversers fully deployed. The increment jet off to jet on shows the thrust-reverser jet plumes produced only small changes in the level of horizontal-tail pitch effectiveness. This small effect is due to the arrangement of the horizontal and vertical tails on the F-15 (fig. 7(b)). The vertical tails shelter the horizontal tails from the reverser flow. Possible concerns with this configuration are increases in twin-vertical-tail loads (ref. 14) and the possibility of affecting rudder control power.

CONCLUSIONS

An investigation was conducted in the Langley 16-Foot Transonic Tunnel to determine the longitudinal aerodynamic characteristics of twin two-dimensional (2-D) nozzles and twin baseline axisymmetric nozzles installed on a fully metric 0.047-scale model of the F-15 three-surface configuration (canards, wing, horizontal tails). The effects of 2-D nozzle in-flight thrust reversing, locations and orientation of vertical tails, and horizontal-tail deflections of -15°, 0°, and 5° were also determined. Test data were obtained at static conditions and at Mach numbers from 0.60 to 1.20 over an angle of attack range from -2° to 15°. Nozzle pressure ratio was varied from jet off to about 6.5. Results from this investigation indicate the following conclusions:

1. The two thrust-reverser positions tested (90° and 130°) produced up to 17 percent and 45 percent reverse thrust at static conditions, but at the two subsonic Mach numbers investigated, they produced substantially higher values of reverse thrust.

2. The axisymmetric nozzle configurations had better drag-minus-thrust performance than the 2-D C-D (two-dimensional convergent-divergent) nozzle configurations.

3. For both the 2-D C-D SSW (two-dimensional convergent-divergent straight-sidewall) nozzle configurations and the axisymmetric nozzle configurations,

using streamlined booms and mounting the vertical tails forward on the engine nacelles produced better drag-minus-thrust performance for most test conditions.

4. The divergent-sidewall nozzles produced lower performance than the straight-sidewall nozzles due to internal losses in the round to rectangular flow transition duct.

5. The leading-edge-out toe angle of the twin vertical tails reduced measured drag-minus-thrust at subsonic Mach numbers.

6. The use of in-flight thrust reversers did not alter the basic longitudinal stability of this F-15 three-surface configuration.

7. The thrust-reverser jet plumes produced only small changes in horizontal-tail pitch effectiveness.

Langley Research Center
National Aeronautics and Space Administration
Hampton, VA 23665
June 14, 1982

REFERENCES

1. Martens, Richard E.: F-15 Nozzle/Afterbody Integration. J. Aircr., vol. 13, no. 5, May 1976, pp. 327-333.

2. Hiley, P. E.; Wallace, H. W.; and Booz, D. E.: Nonaxisymmetric Nozzles Installed in Advanced Fighter Aircraft. J. Aircr., vol. 13, no. 12, Dec. 1976, pp. 1000-1006.

3. Berrier, Bobby L.; Palcza, J. Lawrence; and Richey, G. Keith: Nonaxisymmetric Nozzle Technology Program - An Overview. AIAA Paper 77-1225, Aug. 1977.

4. Capone, Francis J.: The Nonaxisymmetric Nozzle - It Is for Real. AIAA Paper 79-1810, Aug. 1979.

5. Miller, Eugene H.; and Protopapas, John: Nozzle Design and Integration in an Advanced Supersonic Fighter. AIAA Paper 79-1813, Aug. 1979.

6. Stevens, H. L.: F-15/Nonaxisymmetric Nozzle System Integration Study Support Program. NASA CR-135252, 1978.

7. Capone, Francis J.; and Maiden, Donald L.: Performance of Twin Two-Dimensional Wedge Nozzles Including Thrust Vectoring and Reversing Effects at Speeds Up to Mach 2.20. NASA TN D-8449, 1977.

8. Capone, Francis J.: Static Performance of Five Twin-Engine Nonaxisymmetric Nozzles With Vectoring and Reversing Capability. NASA TP-1224, 1978.

9. Hiley, P. E.; Kitzmiller, D. E.; and Willard, C. M.: Installed Performance of Vectoring/Reversing Nonaxisymmetric Nozzles. J. Aircr., vol. 16, no. 8, Aug. 1979, pp. 532-538.

10. Pendergraft, O. C.: Comparison of Axisymmetric and Nonaxisymmetric Nozzles Installed on the F-15 Configuration. AIAA Paper 77-842, July 1977.

11. Capone, Francis J.; and Berrier, Bobby L.: Investigation of Axisymmetric and Nonaxisymmetric Nozzles Installed on a 0.10-Scale F-18 Prototype Airplane Model. NASA TP-1638, 1980.

12. Capone, Francis J.; Re, Richard J.; and Bare, E. Ann: Thrust Reversing Effects on Twin-Engine Aircraft Having Nonaxisymmetric Nozzles. AIAA-81-2639, Dec. 1981.

13. Re, Richard J.; and Berrier, Bobby L.: Static Internal Performance of Single Expansion-Ramp Nozzles With Thrust Vectoring and Reversing. NASA TP-1962, 1982.

14. Bare, E. Ann; Berrier, Bobby L.; and Capone, Francis J.: Effect of Simulated In-Flight Thrust Reversing on Vertical-Tail Loads of F-18 and F-15 Airplane Models. NASA TP-1890, 1981.

15. Corson, Blake W., Jr.; Runckel, Jack F.; and Igoe, William B.: Calibration of the Langley 16-Foot Transonic Tunnel With Test Section Air Removal. NASA TR R-423, 1974.

16. Braslow, Albert L.; Hicks, Raymond M.; and Harris, Roy V., Jr.: Use of Grit-Type Boundary-Layer-Transition Trips on Wind-Tunnel Models. Conference on Aircraft Aerodynamics, NASA SP-124, 1966, pp. 19-36. (Also available as NASA TN D-3579.)

17. Braslow, Albert L.; and Knox, Eugene C.: Simplified Method for Determination of Critical Height of Distributed Roughness Particles for Boundary-Layer Transition at Mach Numbers From 0 to 5. NACA TN 4363, 1958.

18. Henderson, William P.; and Leavitt, Laurence D.: Stability and Control Characteristics of a Three-Surface Advanced Fighter Configuration at Angles of Attack up to 45°. NASA TM-83171, 1981.

19. Berrier, Bobby L.; and Maiden, Donald L.: Effect of Nozzle-Exhaust Flow on the Longitudinal Aerodynamic Characteristics of a Fixed-Wing, Twin-Jet Fighter Airplane Model. NASA TM X-2389, 1971.

20. Berrier, Bobby L.: Effect of Nonlifting Empennage Surfaces on Single-Engine Afterbody/Nozzle Drag at Mach Numbers From 0.5 to 2.2. NASA TN D-8326, 1977.

TABLE I.- MODEL GEOMETRIC CHARACTERISTICS

Overall model length, m	0.93
Wing:	
Span, m	0.612
Area, m^2	0.124
Root chord (theoretical), m	0.33
Tip chord (theoretical), m	0.082
Mean geometric chord, m	0.228
Aspect ratio	3.0
Taper ratio	0.25
Sweepback of leading edge, deg	45
Airfoil section	NACA 64A-series with modified conical camber L.E.
Horizontal tail (exposed each side):	
Span, m	0.113
Area, m^2	0.012
Root chord (theoretical), m	0.165
Tip chord (theoretical), m	0.055
Sweepback of leading edge, deg	50
Airfoil section	NACA 64-series
Vertical tail (exposed each panel):	
Span, m	0.146
Area, m^2	0.013
Root chord, m	0.137
Tip chord, m	0.037
Sweepback of leading edge, deg	36.57
Toe-out angle (baseline only), deg	2
Airfoil section	NACA 64-series
Canard (exposed each panel):	
Span, m	0.088
Area, m^2	0.006
Root chord, m	0.113
Tip chord, m	0.028
Sweepback of leading edge, deg	50
Airfoil section	NACA 64-series
Dihedral angle, deg	20

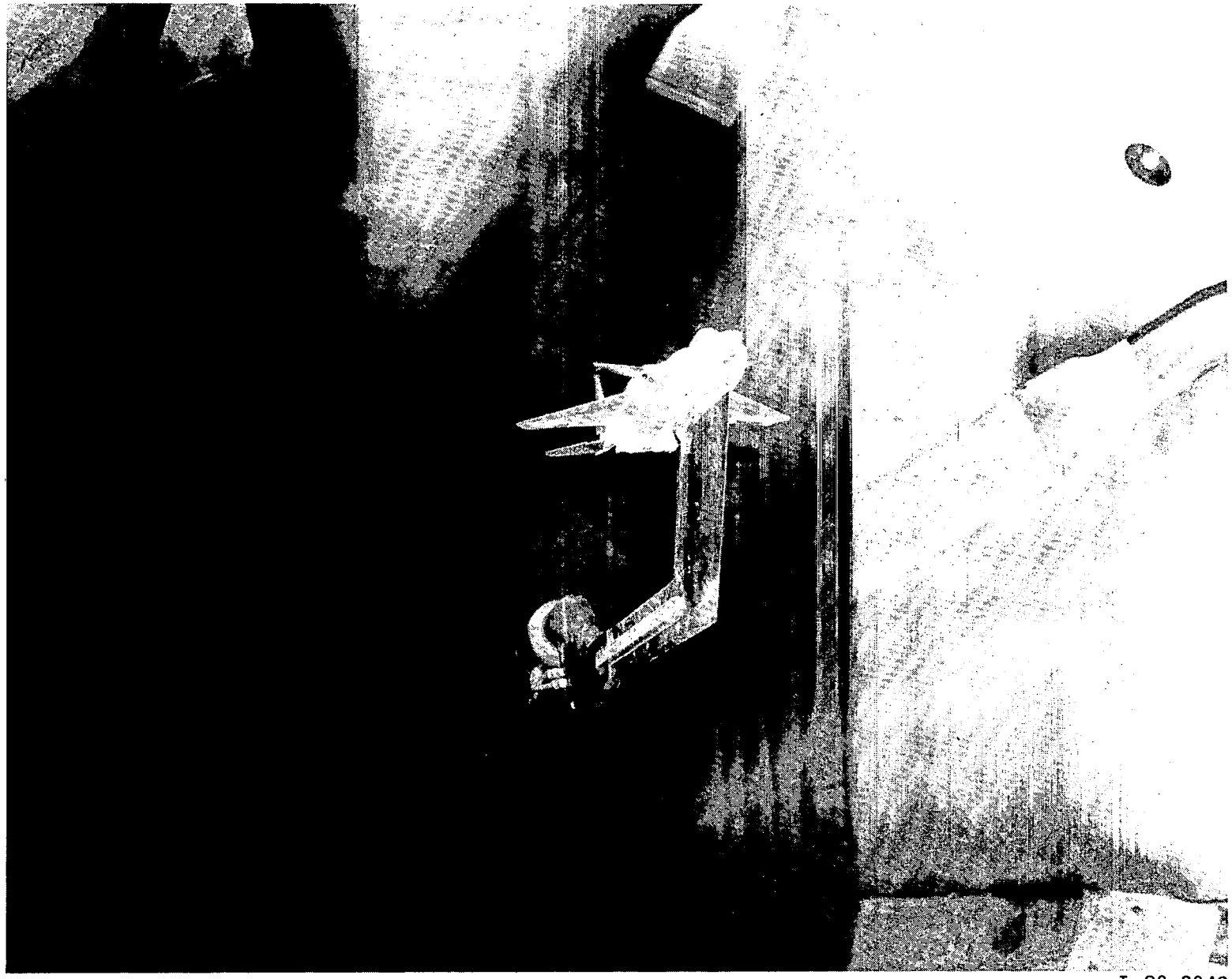

L-80-2042

Figure 1.- Photograph showing sting-strut arrangement of 0.047-scale F-15 propulsion model installed in Langley 16-Foot Transonic Tunnel.

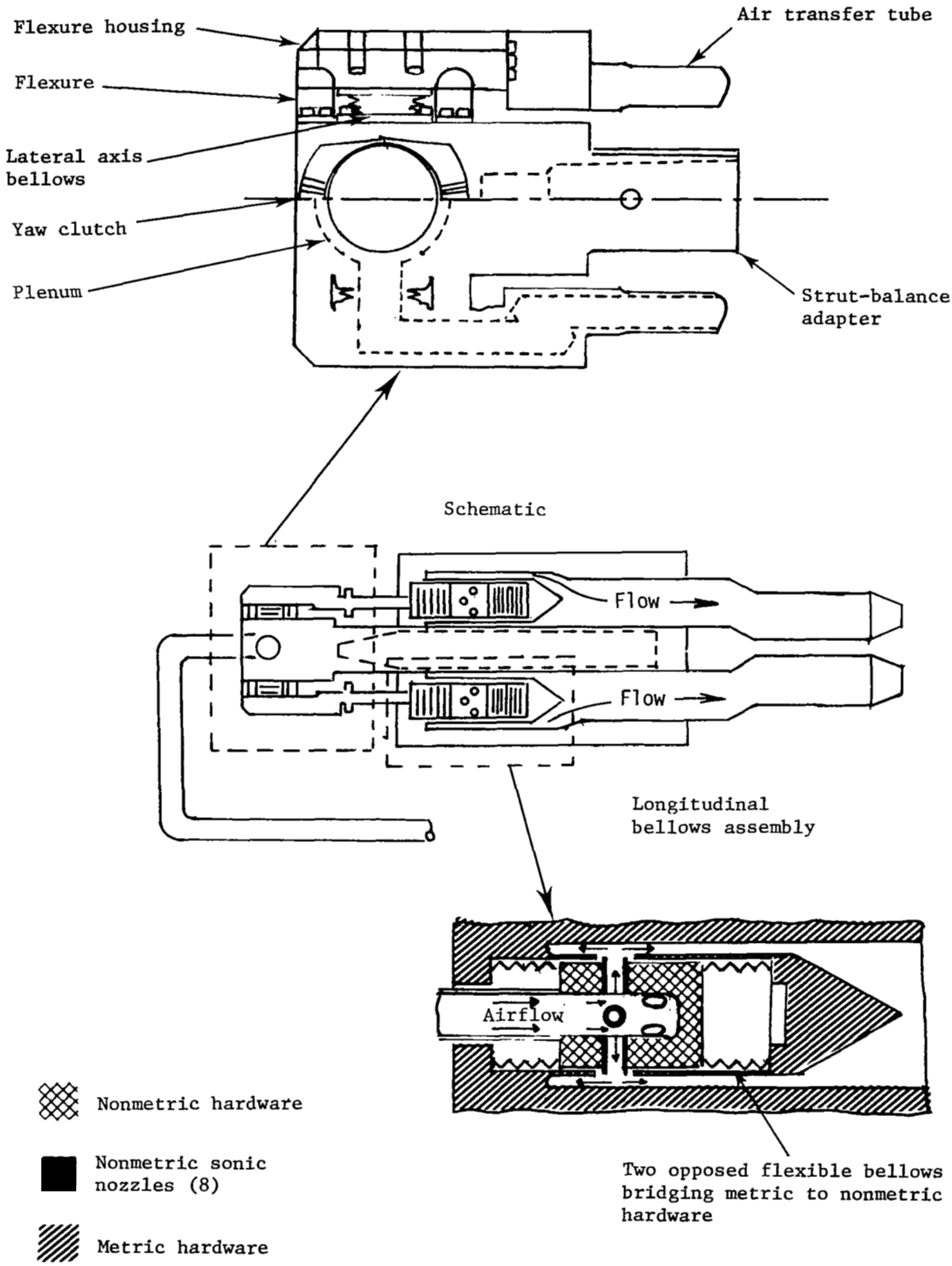

Figure 2.- Sketch showing high-pressure air transfer methods of propulsion system.

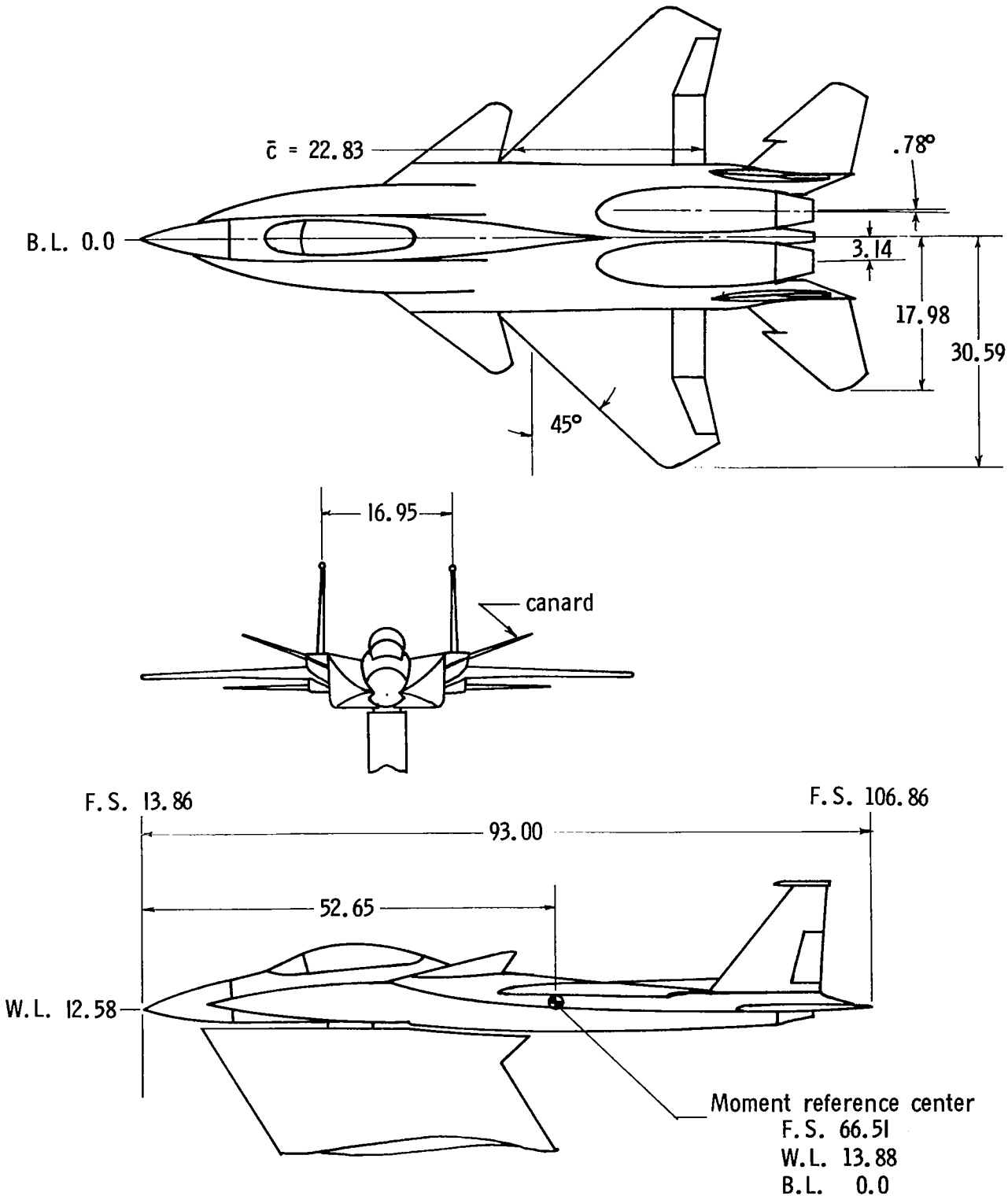

Figure 3.- Sketch of 0.047-scale three-surface F-15 model. All dimensions are in centimeters unless otherwise noted.

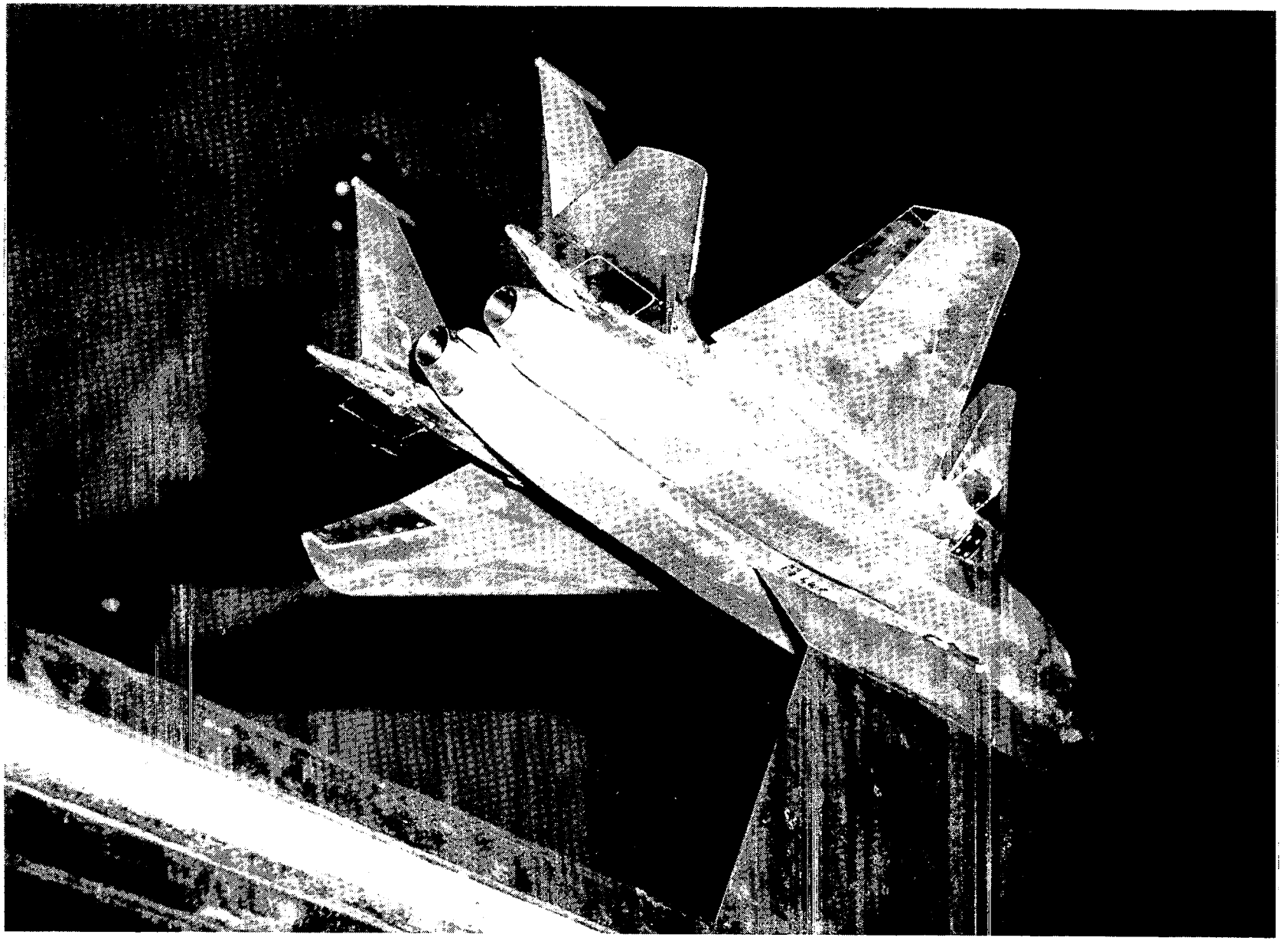

L-80-2019

Figure 4.- Photograph of baseline three-surface F-15 model with axisymmetric dry-power nozzles.

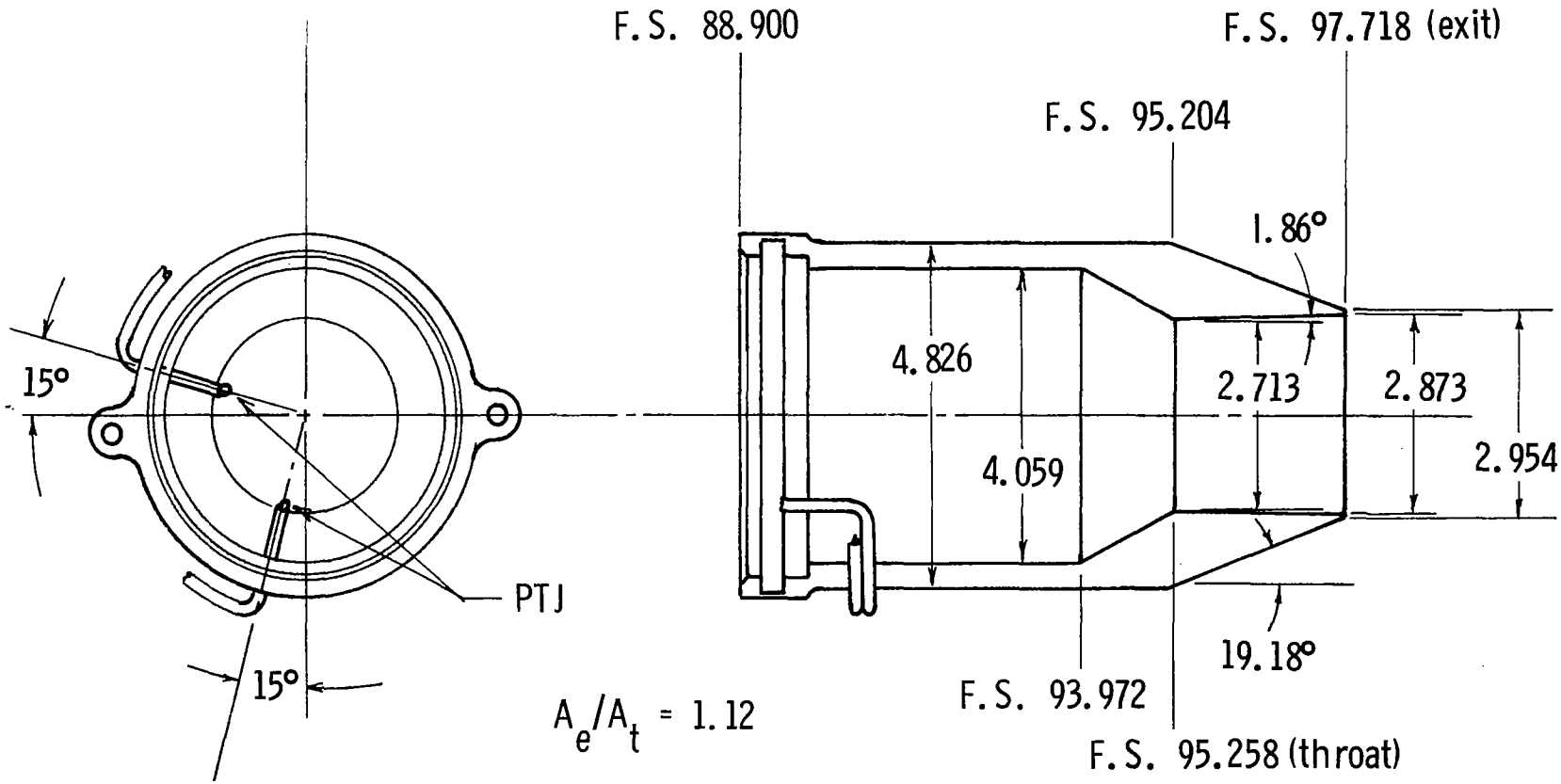

(a) Dry-power nozzles.

Figure 5.- Sketches of axisymmetric nozzles. All dimensions are in centimeters unless otherwise noted.

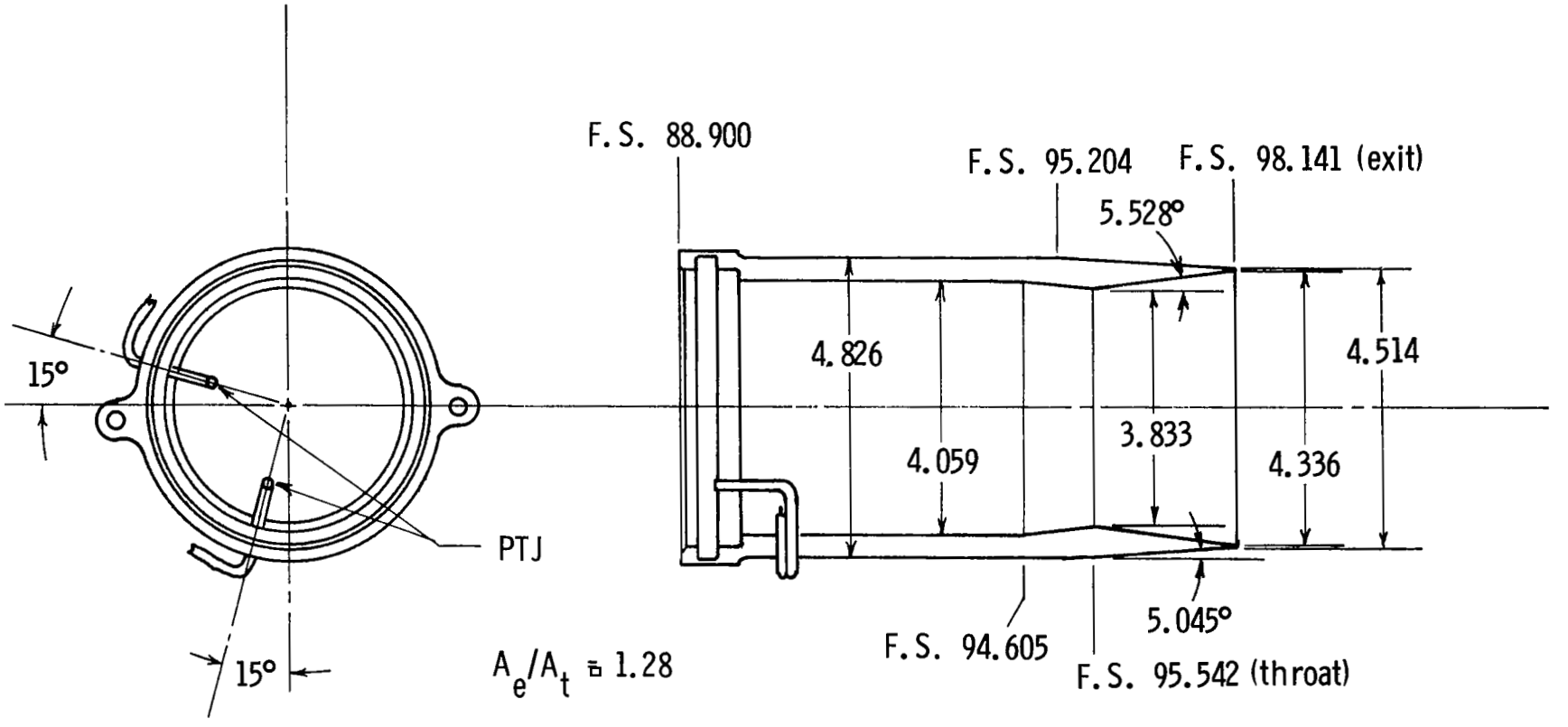

(b) Maximum-afterburning-power nozzles.

Figure 5.- Concluded.

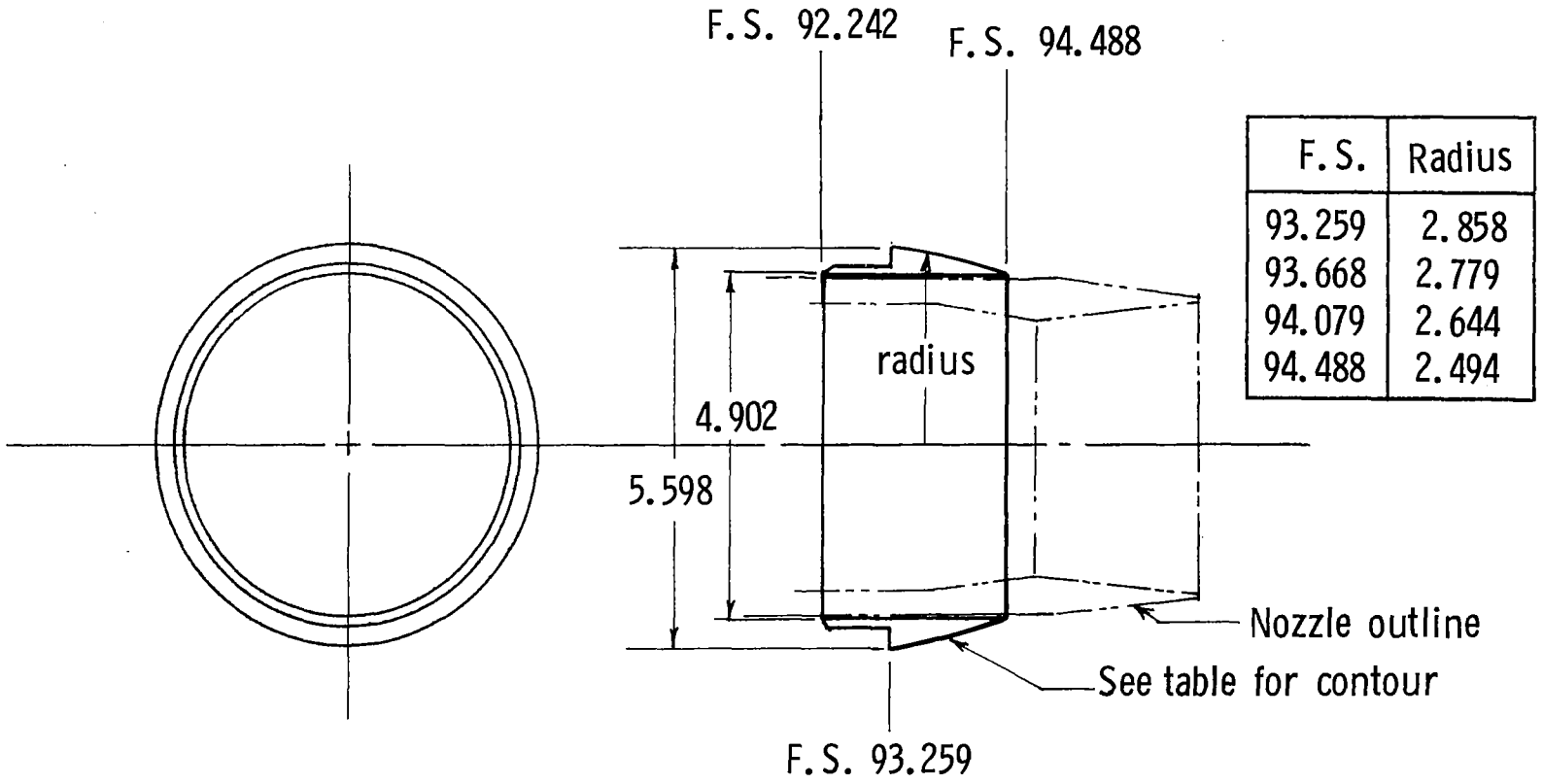

F.S.	Radius
93.259	2.858
93.668	2.779
94.079	2.644
94.488	2.494

Figure 6.- Sketch of axisymmetric external nozzle shrouds. All dimensions are in centimeters.

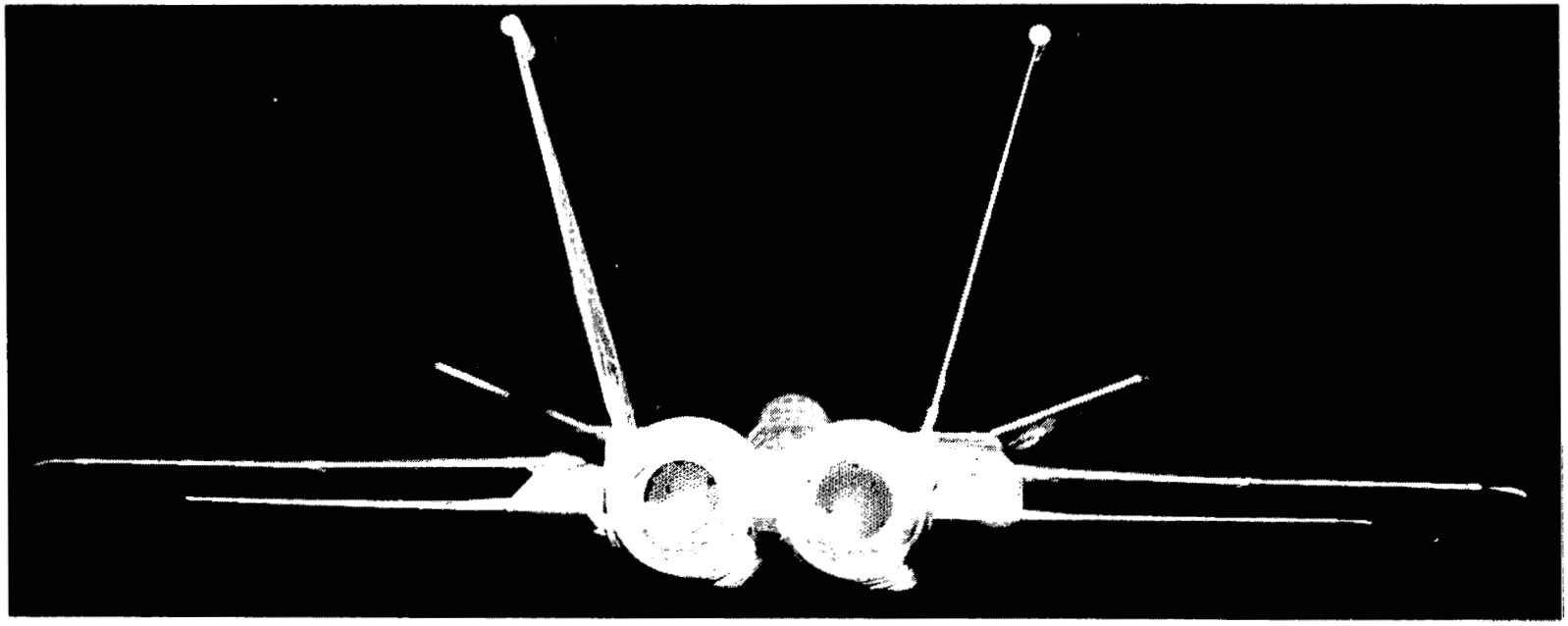

L-80-2016

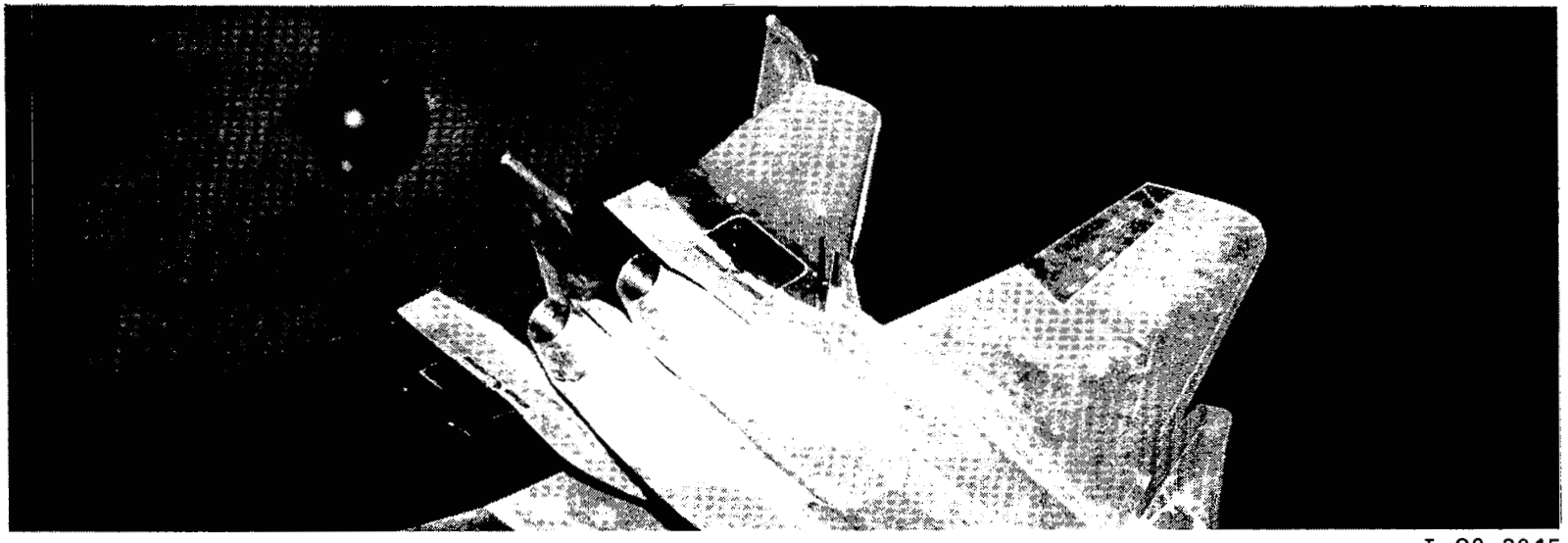

L-80-2015

(a) Photographs of model with axisymmetric dry-power nozzles installed.

Figure 7.- Three-surface F-15 model with nacelle-mounted vertical tails and modified tail booms.

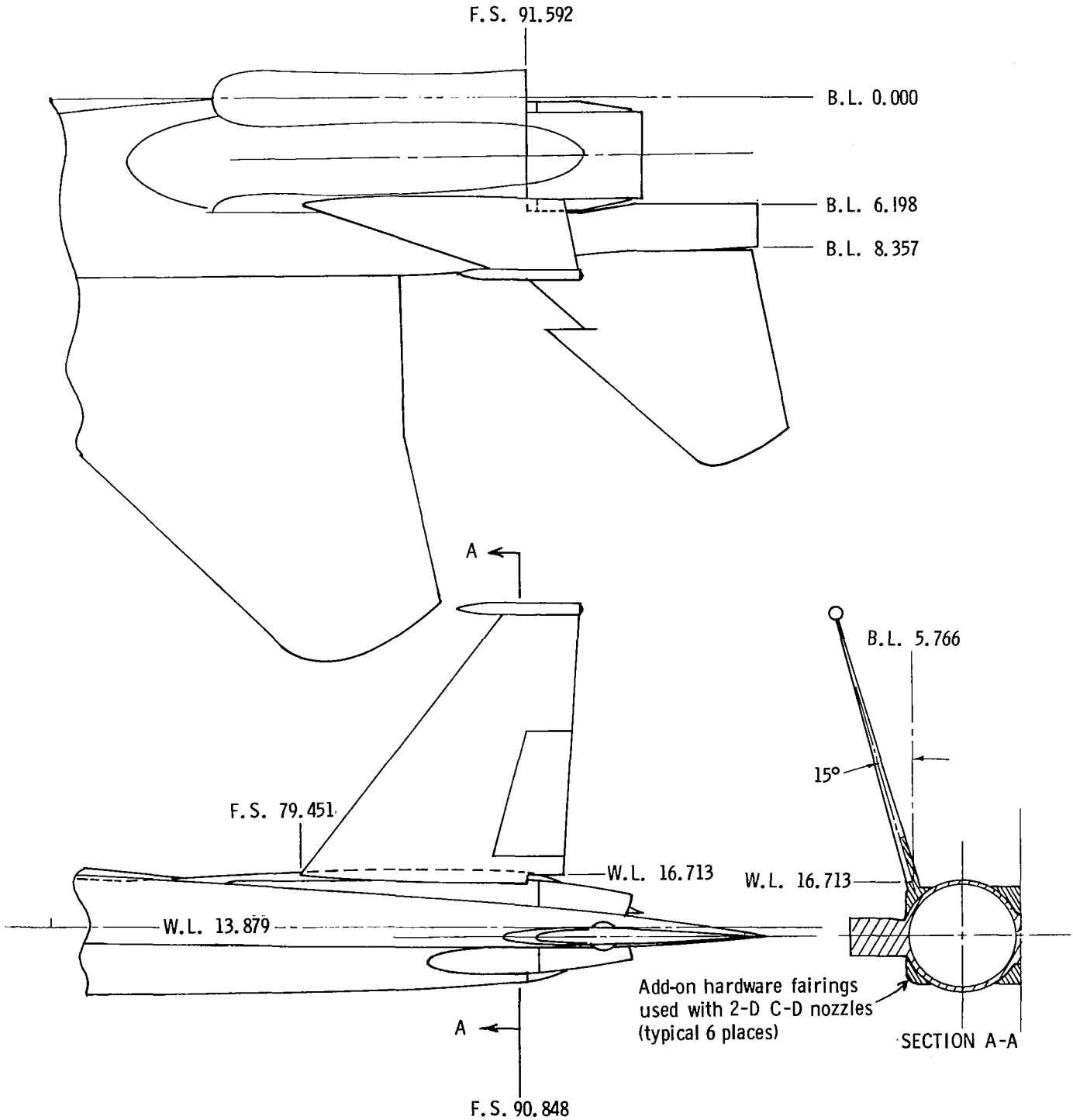

(b) Sketch of model afterbody and tail surfaces with 2-D C-D dry-power nozzles installed. All dimensions are in centimeters unless otherwise noted.

Figure 7.- Concluded.

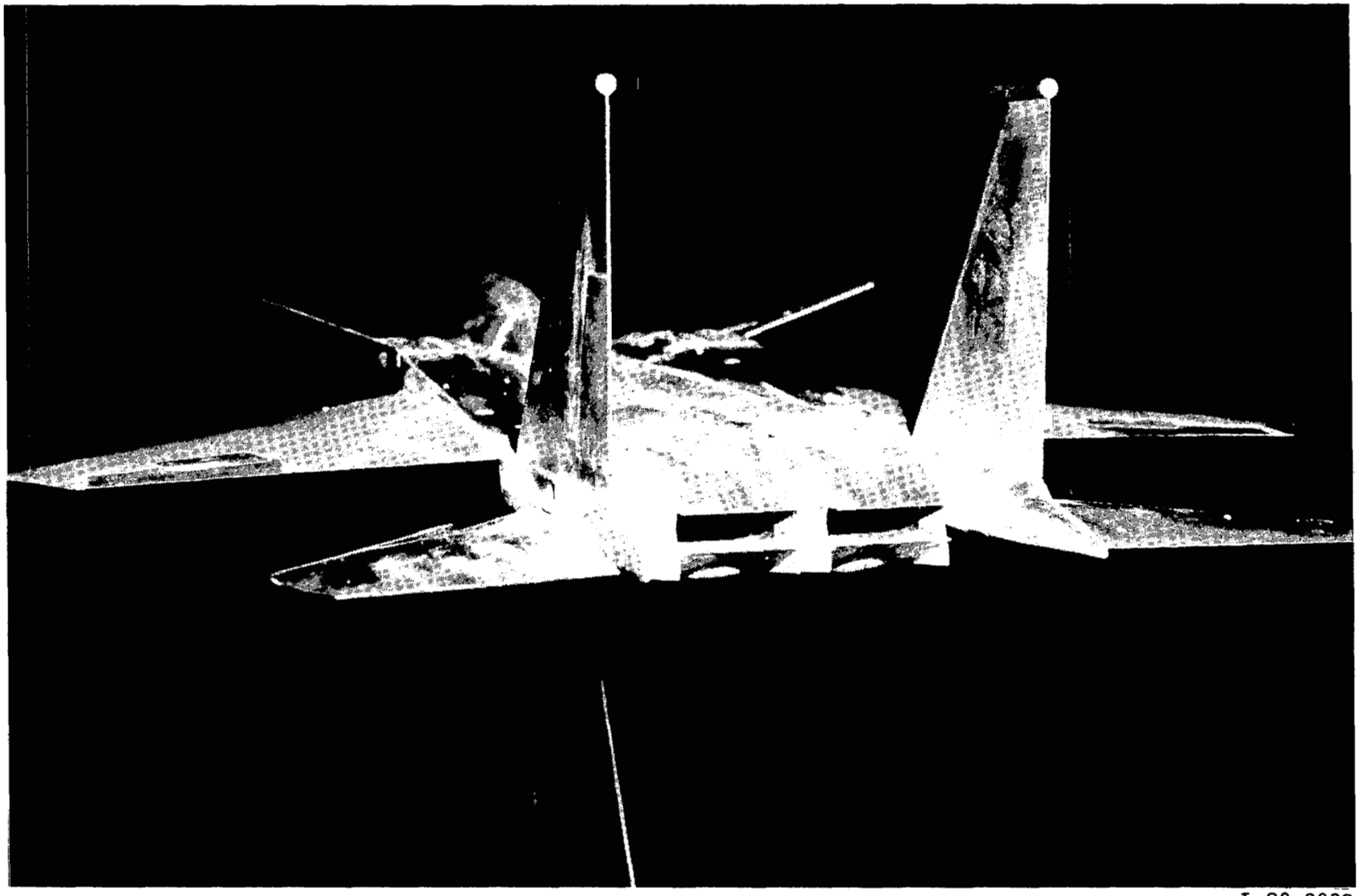

L-80-2038

Figure 8.- Photograph of model with 2-D C-D SSW dry-power nozzles installed.

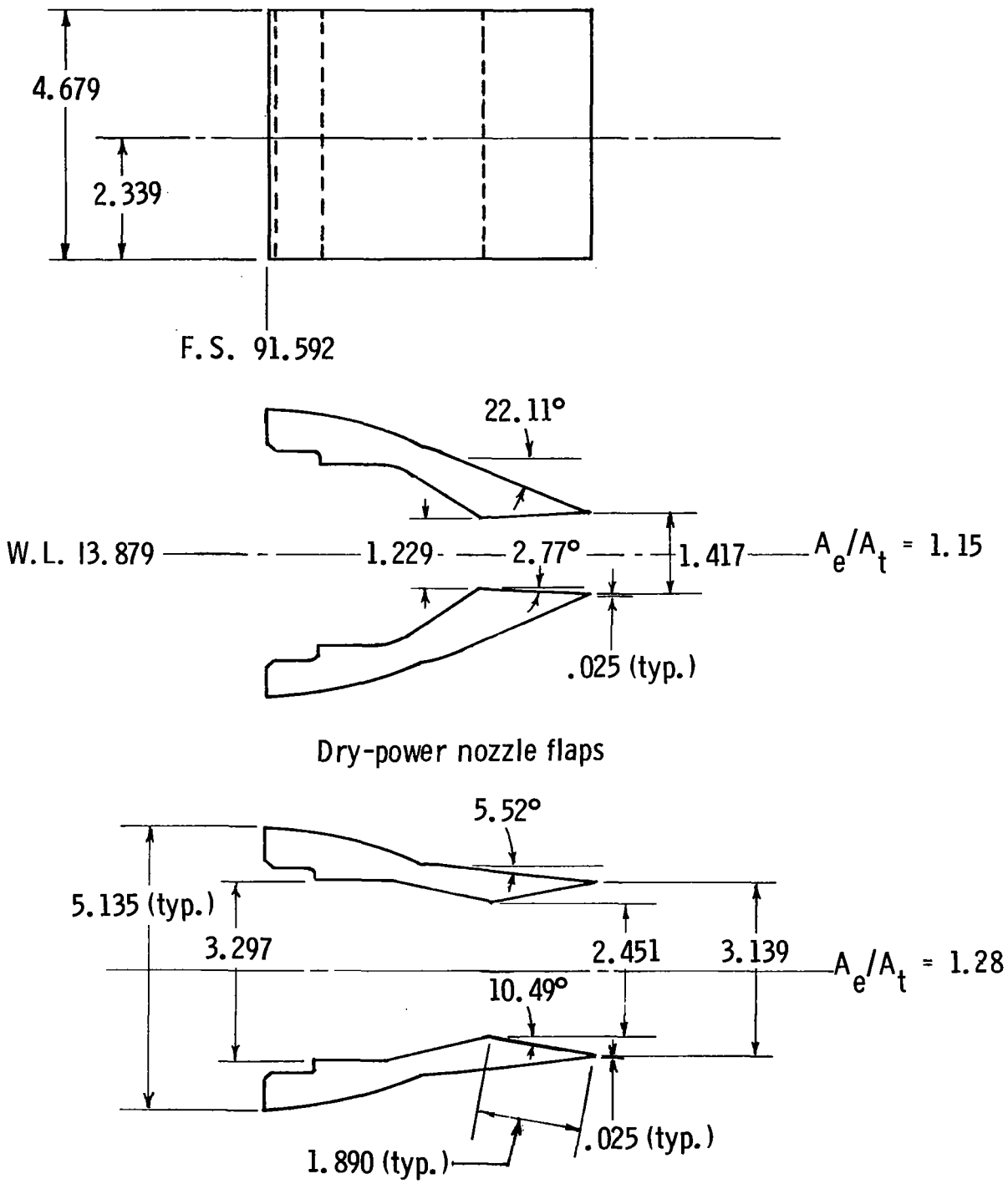

(a) Dry-power and maximum-afterburning-power nozzle flaps for straight sidewalls.

Figure 9.- Sketches of various 2-D C-D nozzle flap and sidewall configurations. All dimensions are in centimeters unless otherwise noted.

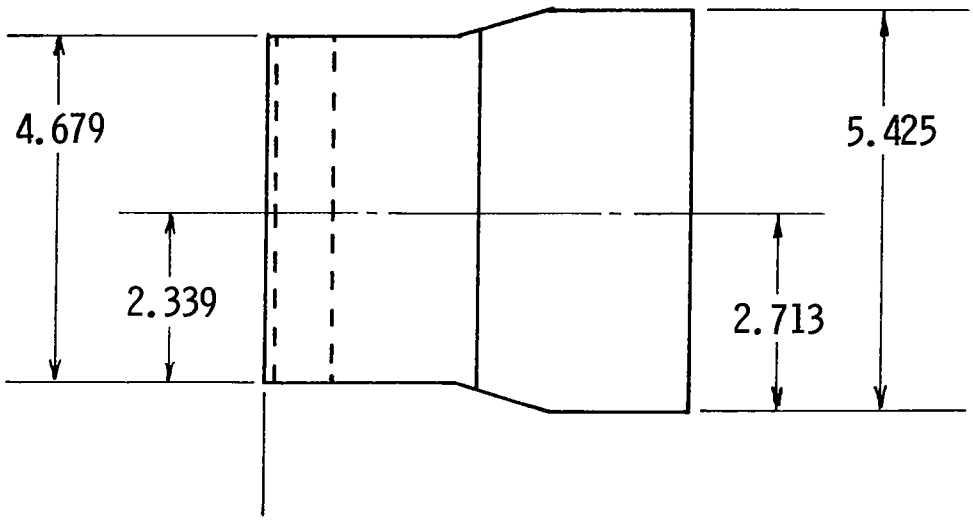

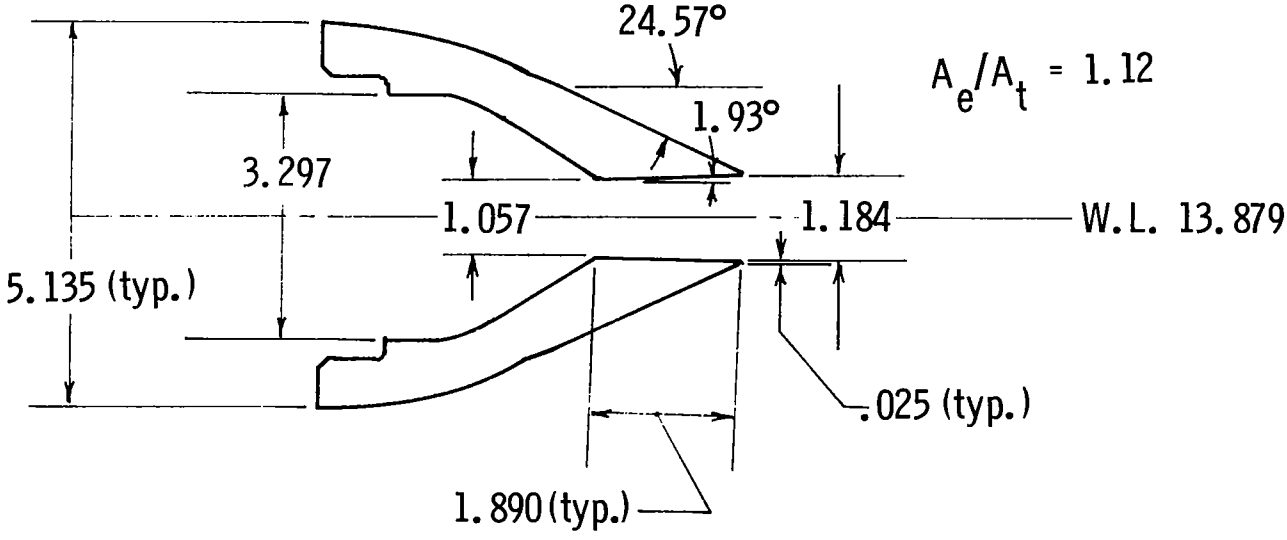

(b) Dry-power nozzle flaps for divergent sidewalls.

Figure 9.- Continued.

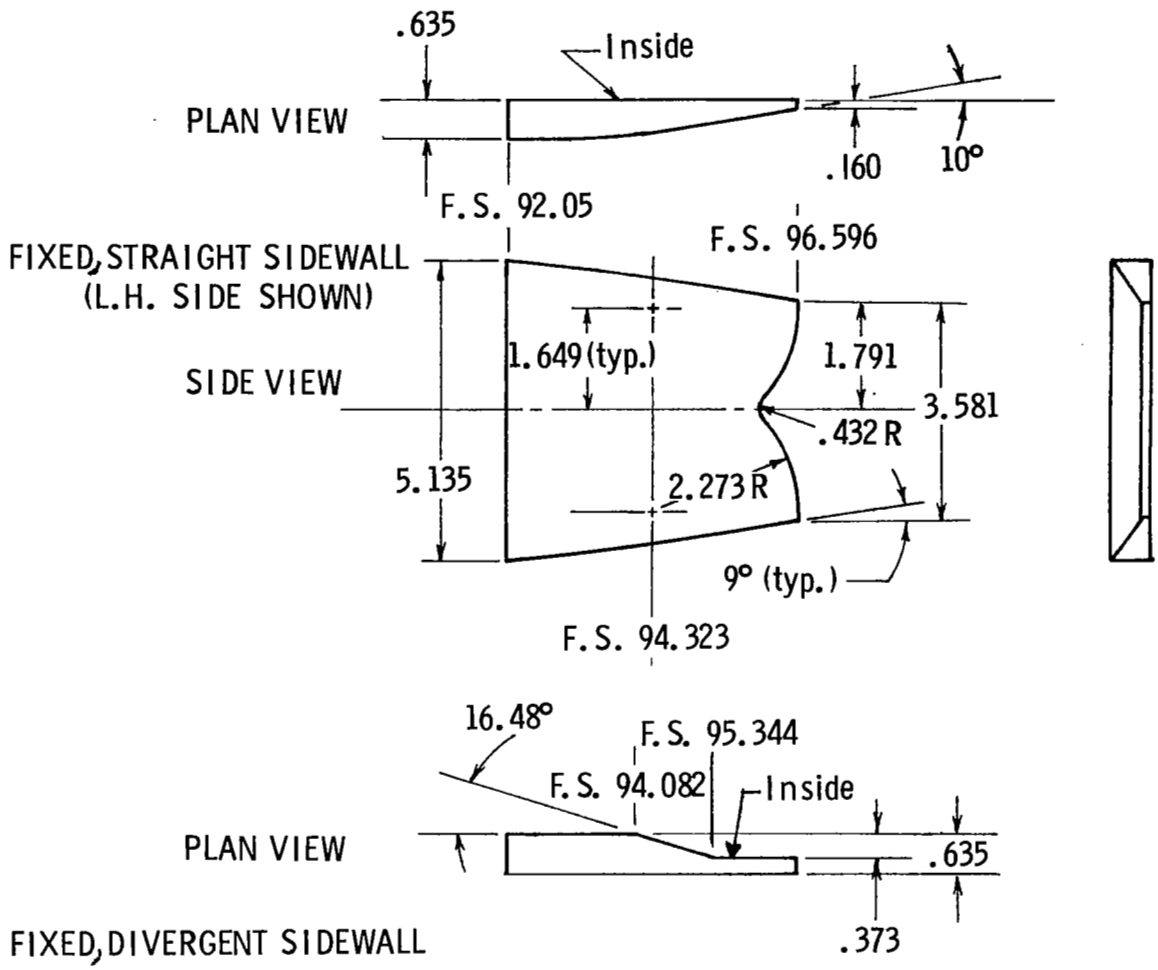

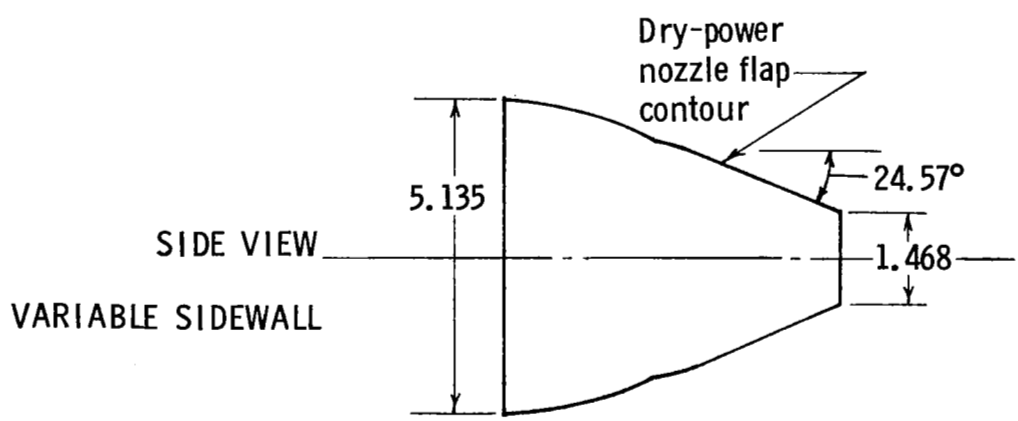

(c) Various sidewalls.

Figure 9.- Concluded.

L-80-2671

Figure 10.- Photograph of model with simulated, fully deployed thrust reversers.

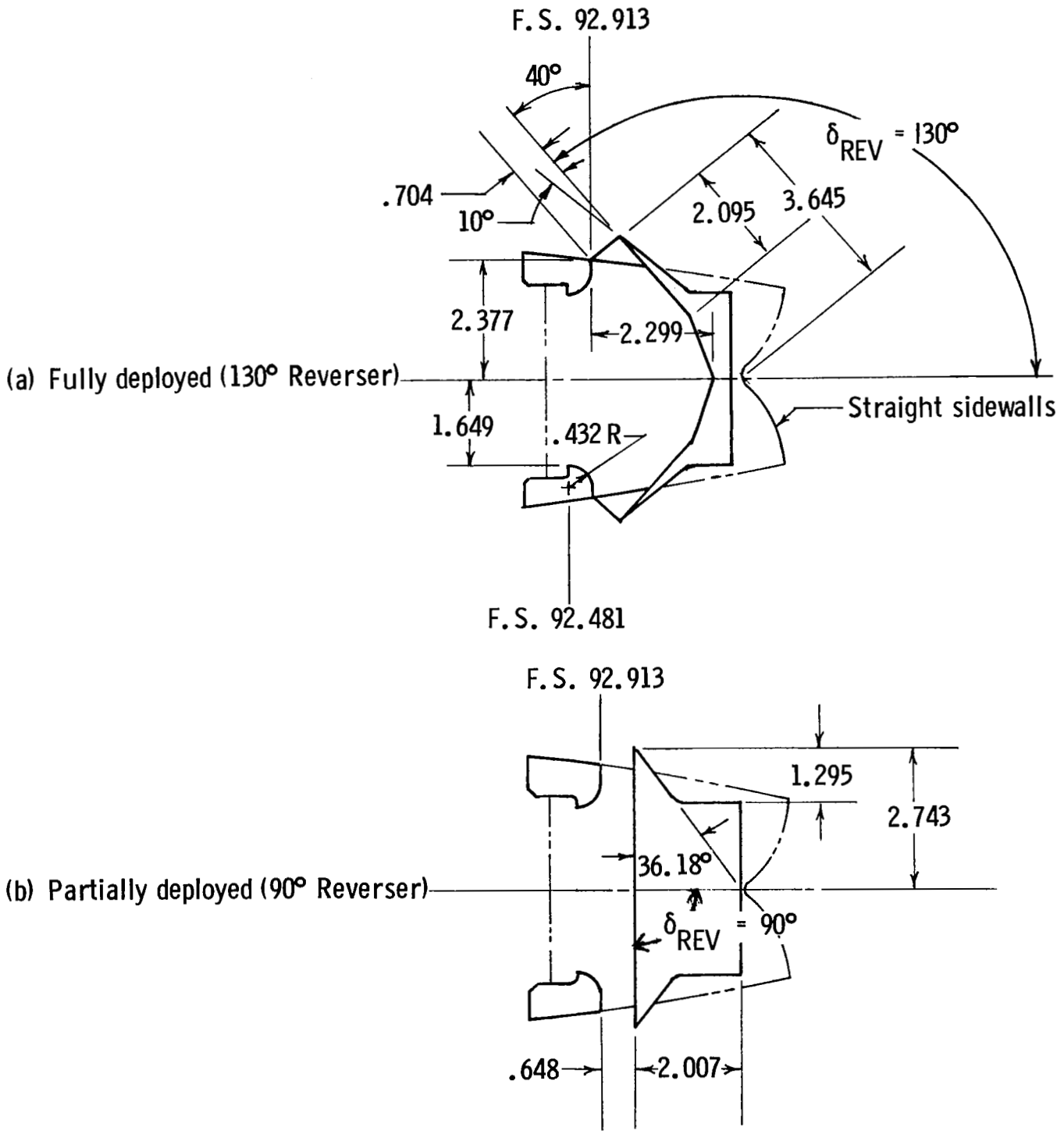

Figure 11.- Side-view sketches of 2-D C-D nozzle thrust-reverser flaps. All dimensions are in centimeters unless otherwise noted.

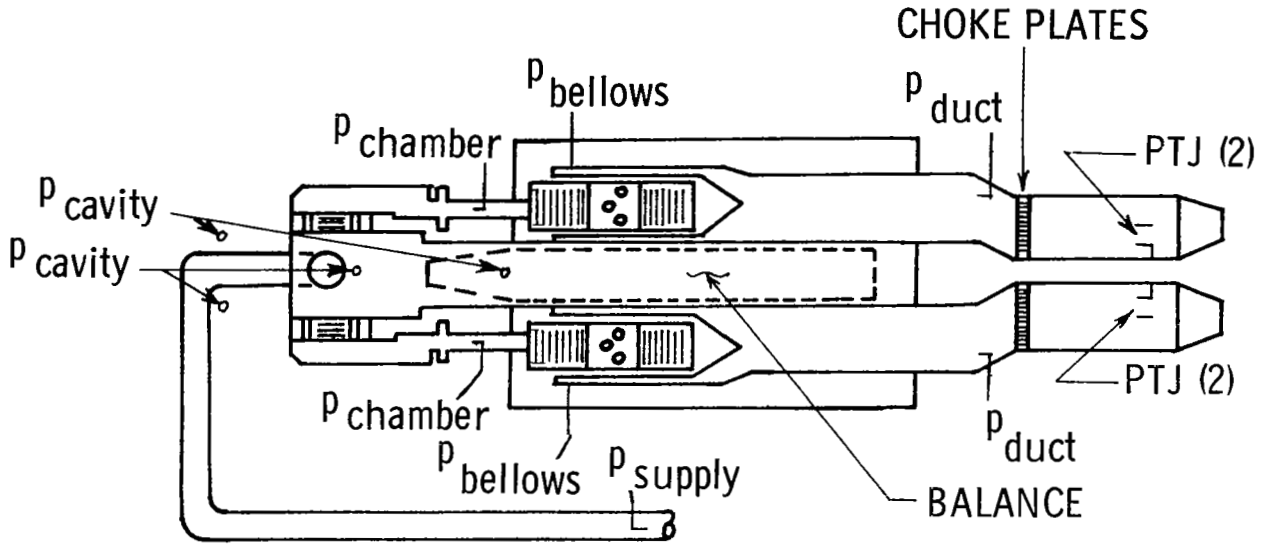

PRESSURE INSTRUMENTATION

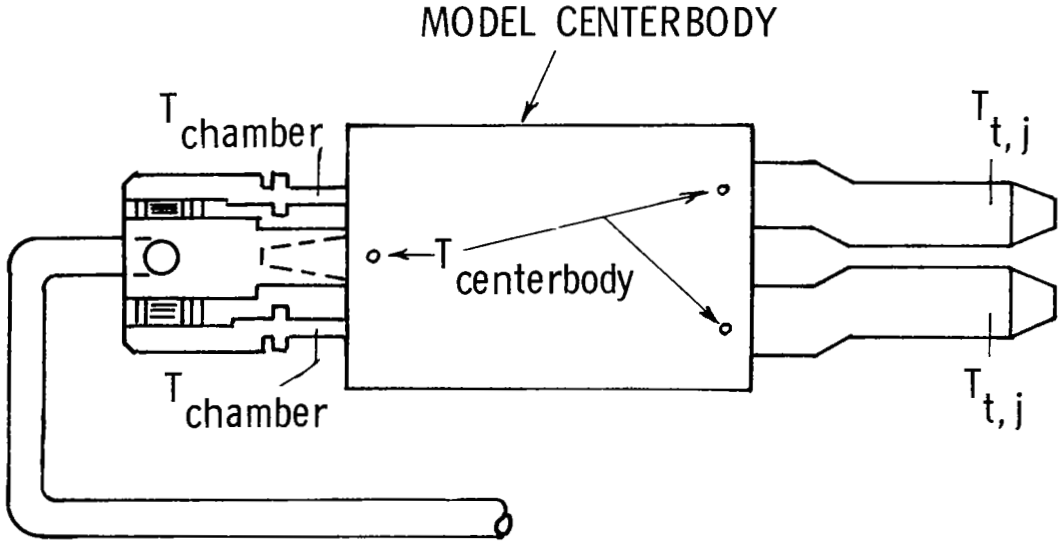

TEMPERATURE INSTRUMENTATION

Figure 12.- Sketch of model showing locations of pressure p and temperature T probes for airflow system.

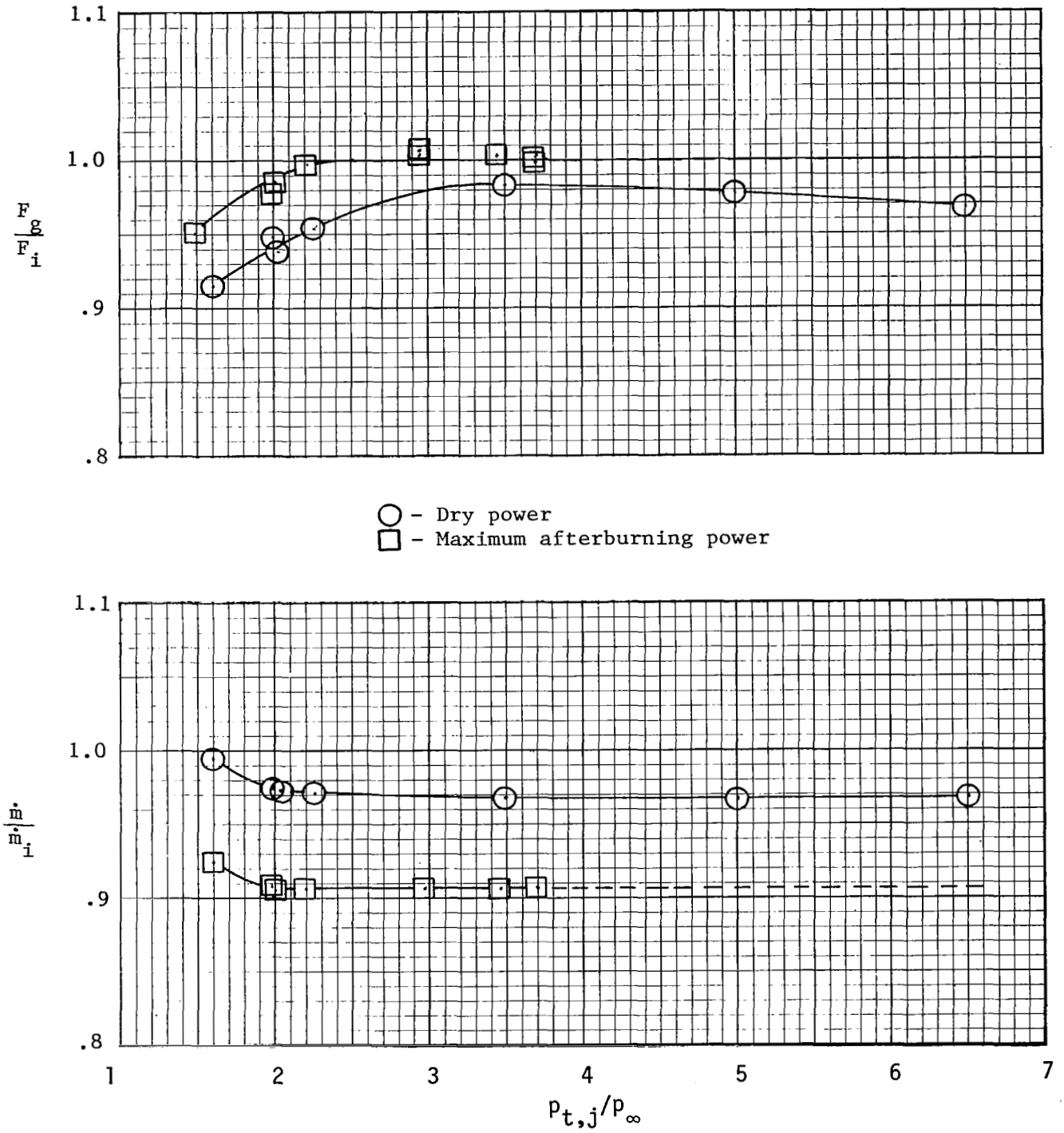

Figure 13.- Static performance of configuration with axisymmetric nozzles installed on baseline 0.047-scale three-surface F-15 model.

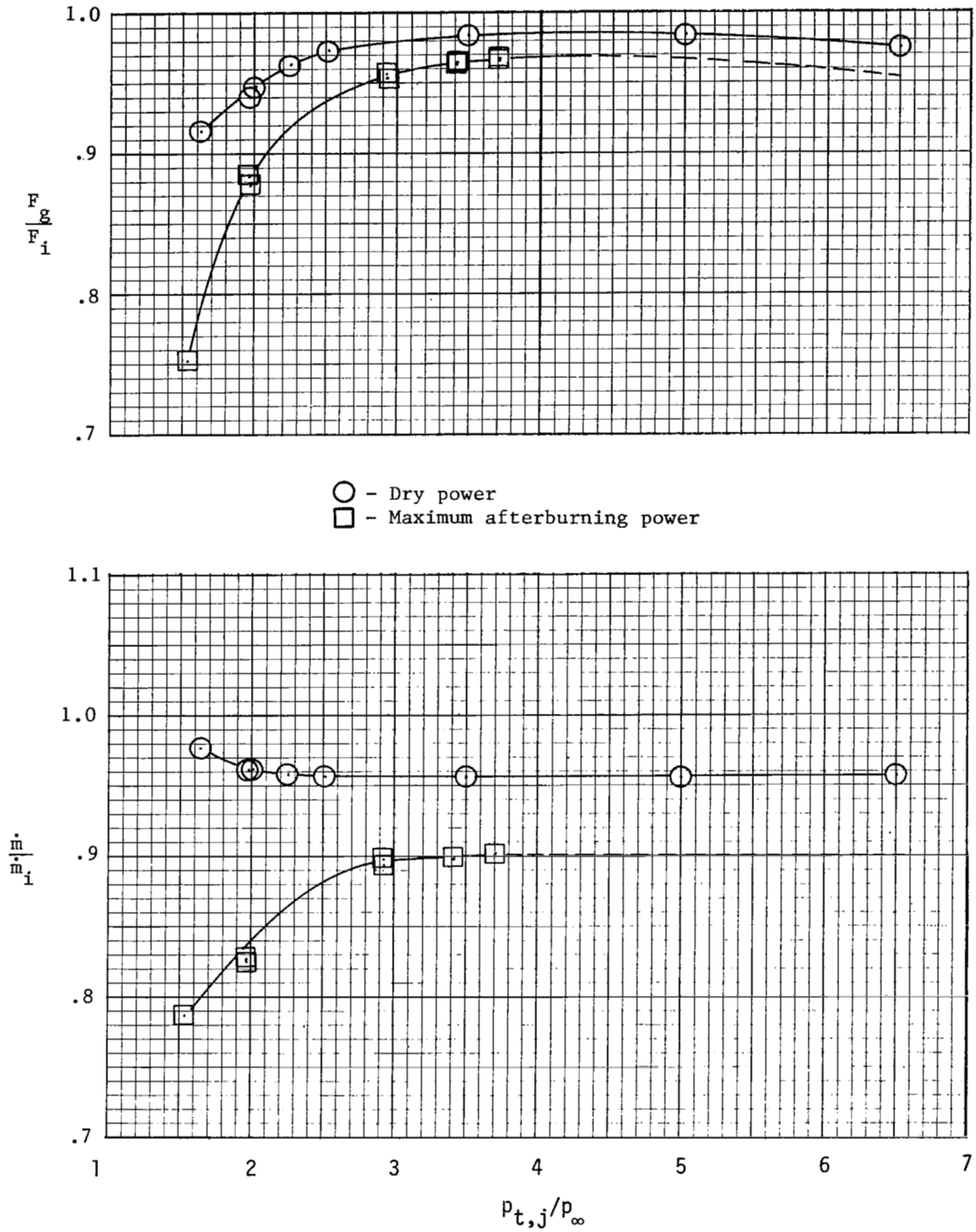

Figure 14.- Static performance of configuration with 2-D C-D nozzles and fixed, straight sidewalls (SSW).

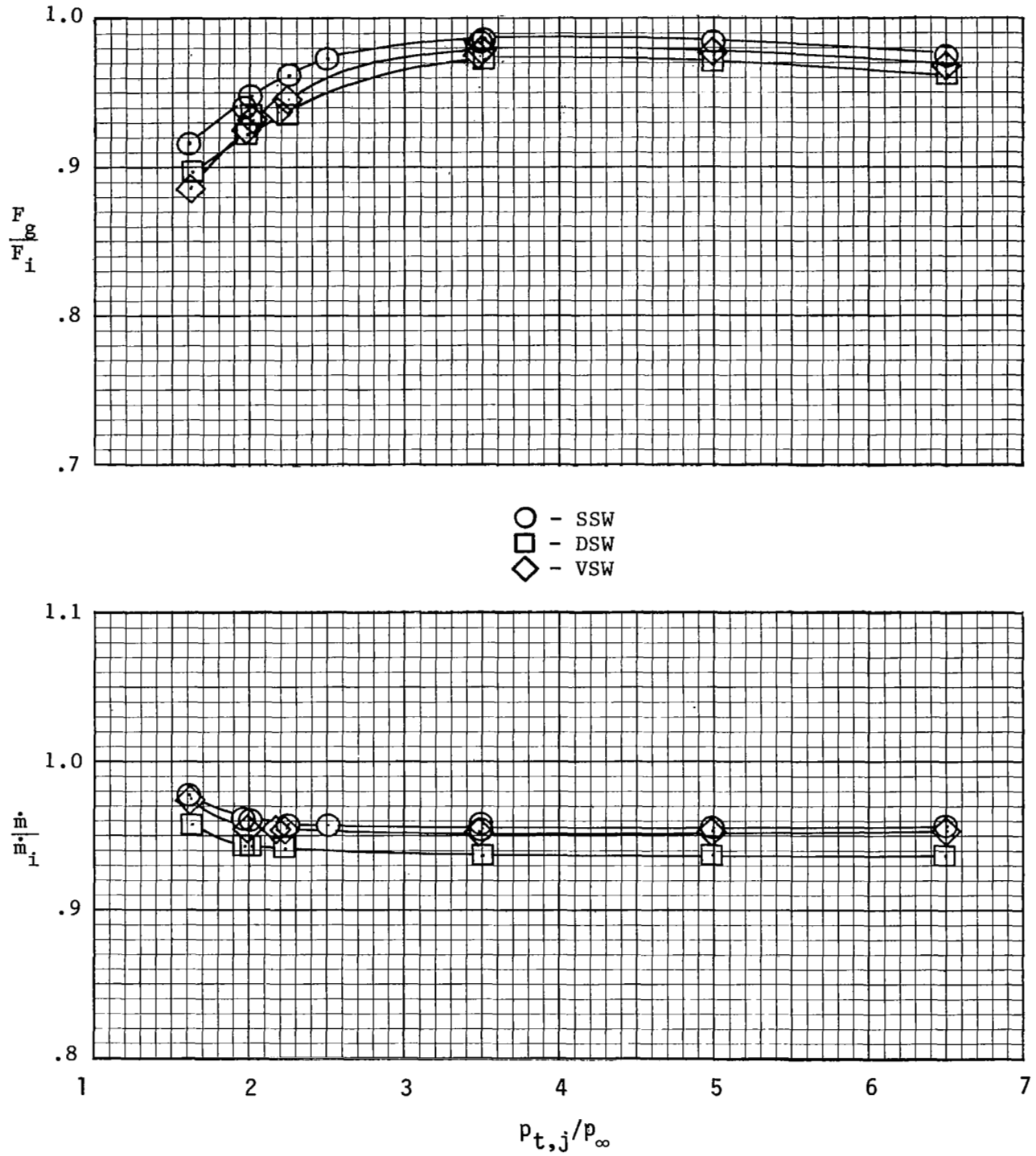

Figure 15.- Static performance of configuration with 2-D C-D SSW nozzles and with two different nozzle sidewalls.

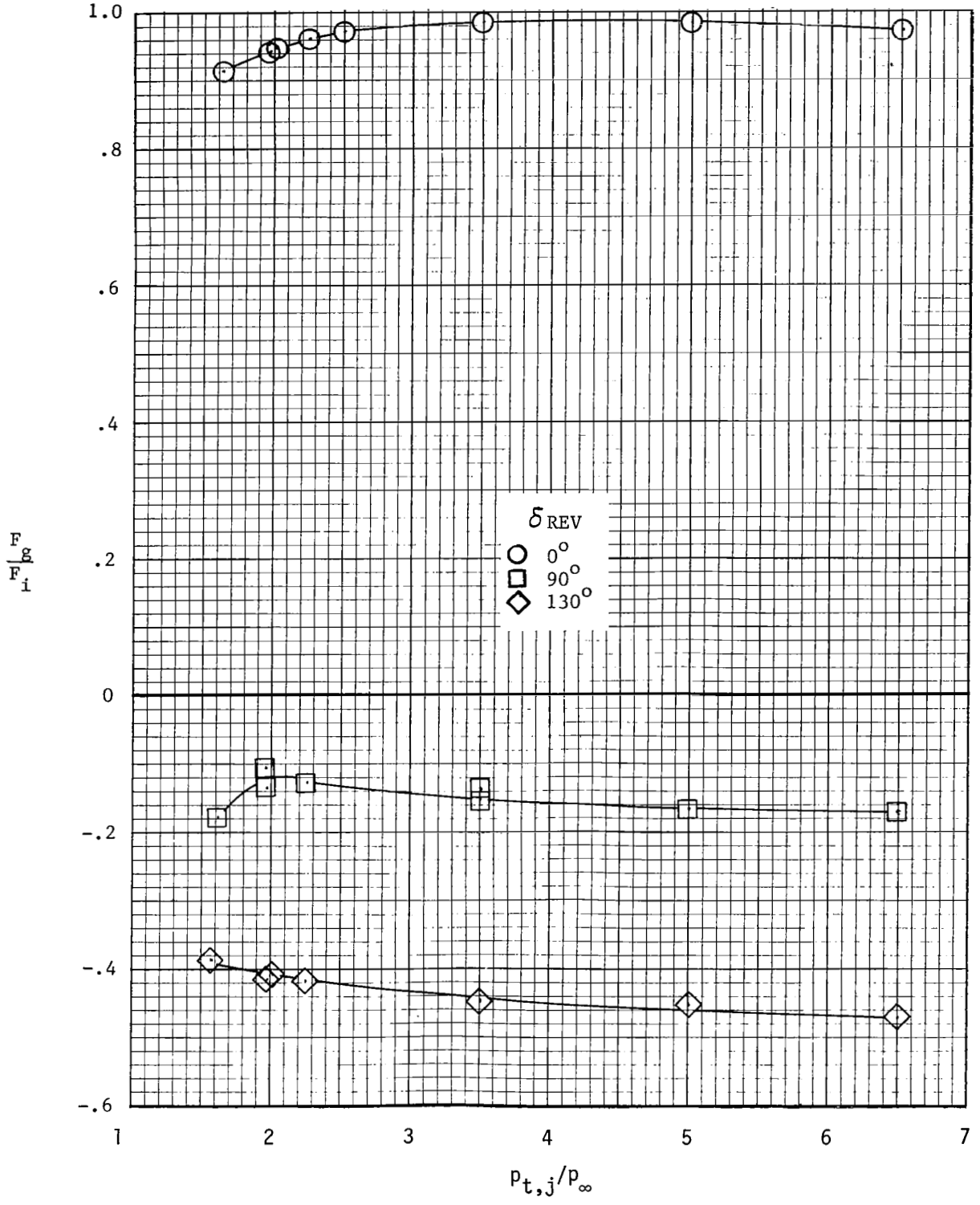

Figure 16.- Static reverse thrust performance of configuration with 2-D C-D SSW nozzles.

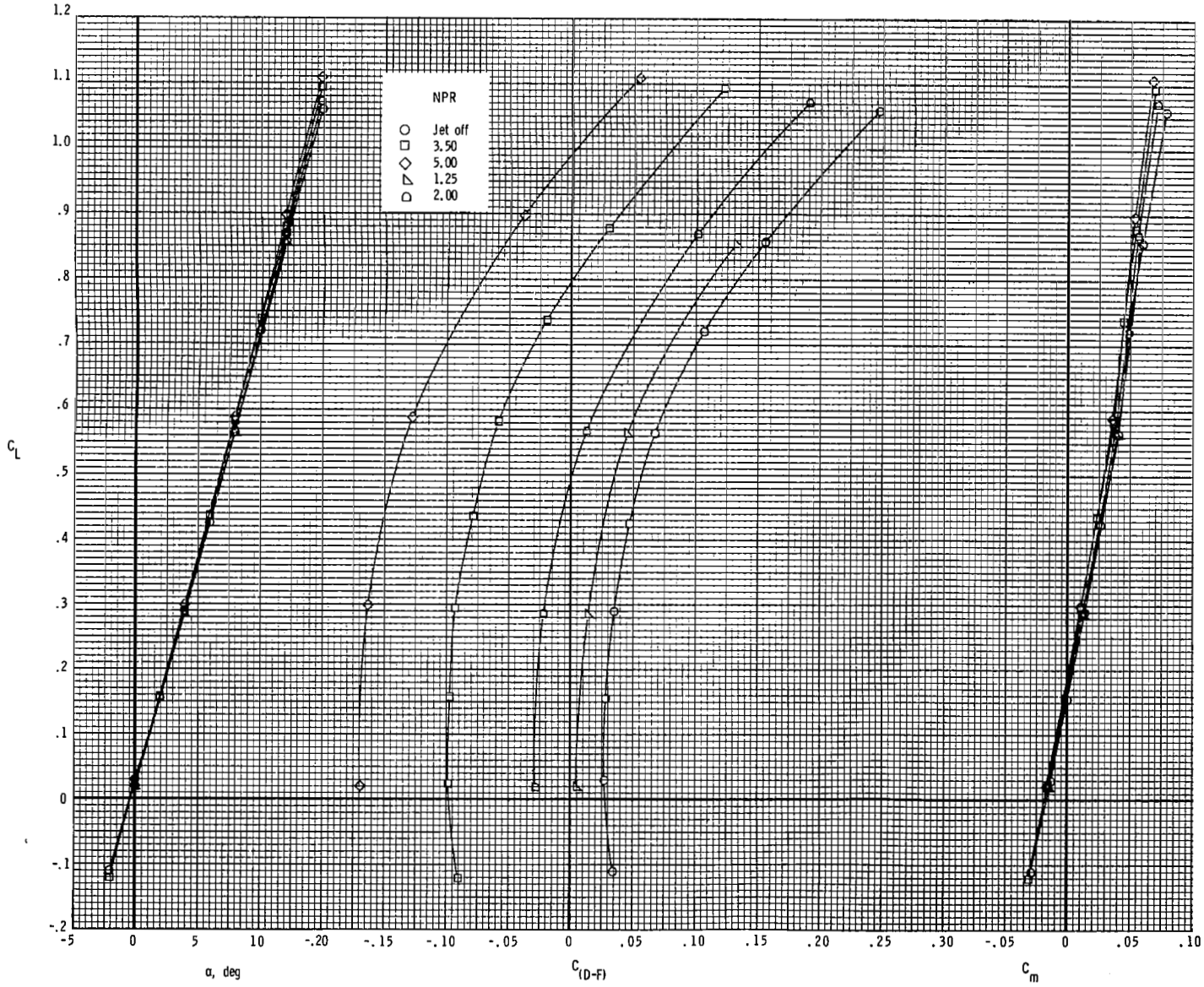

(a) M = 0.60.

Figure 17.- Drag-minus-thrust performance of configuration with dry-power axisymmetric nozzles installed on baseline 0.047-scale three-surface F-15 model.

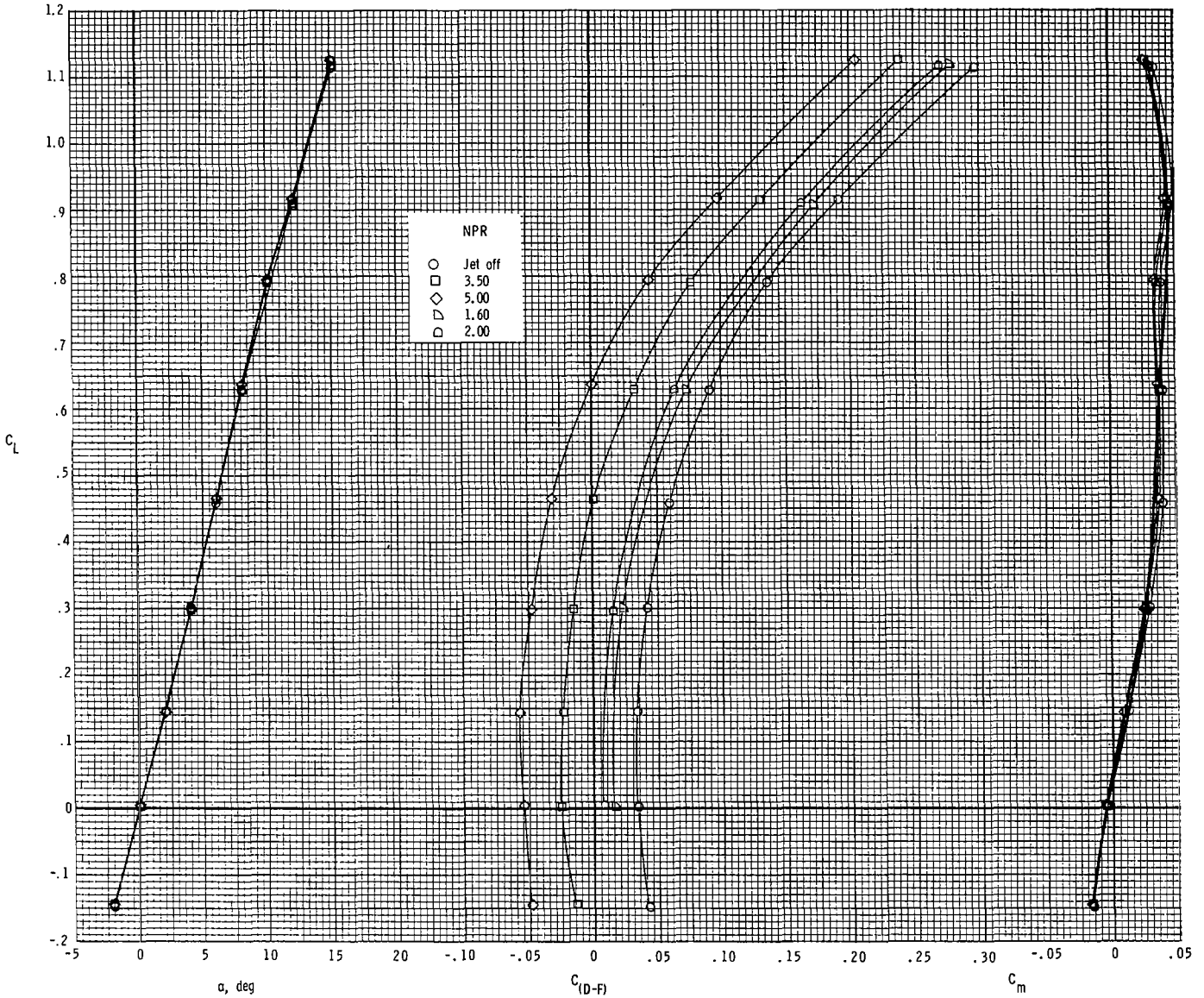

(b) M = 0.90.

Figure 17.- Continued.

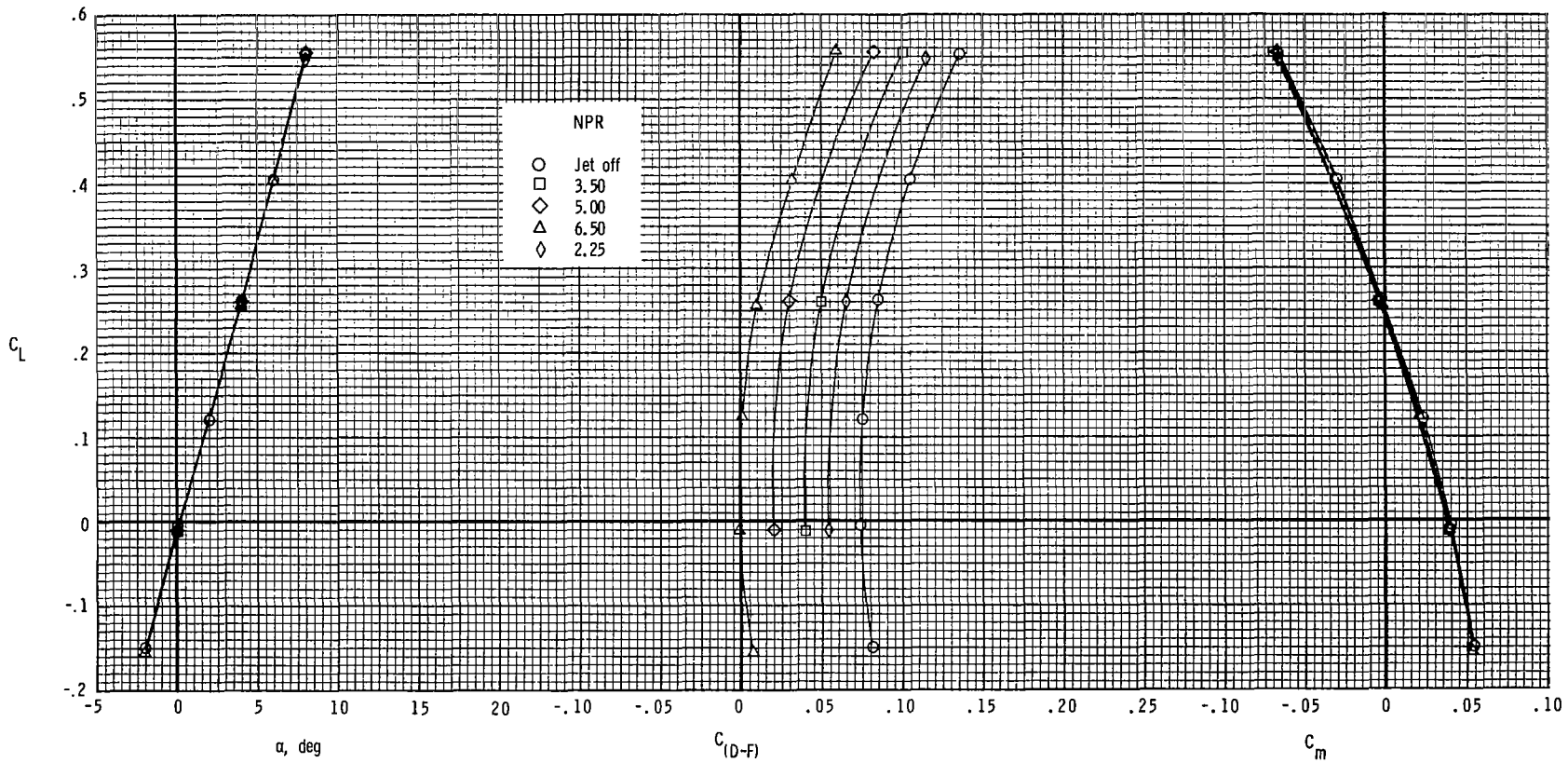

(c) M = 1.20.

Figure 17.- Concluded.

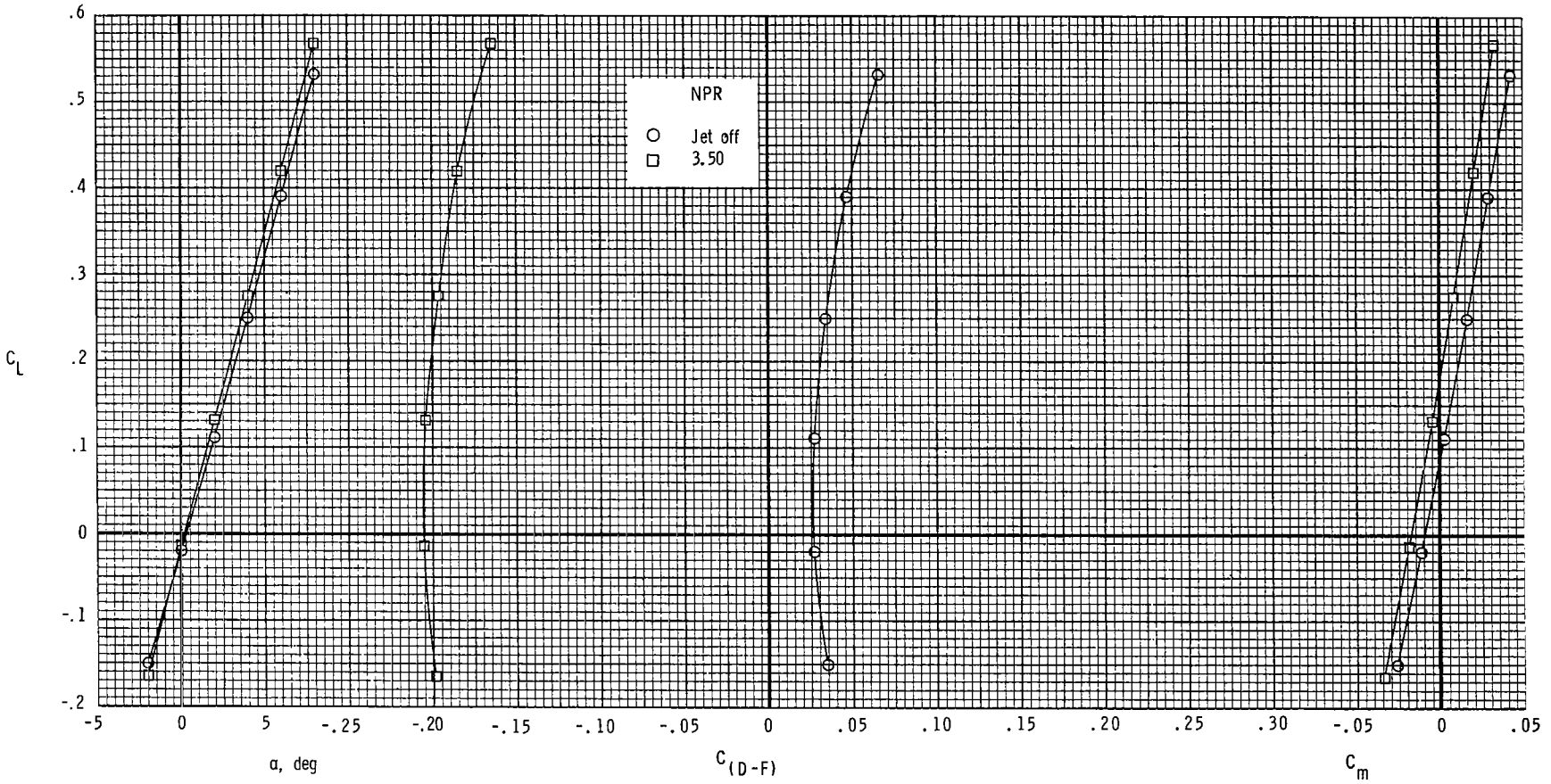

(a) M = 0.60.

Figure 18.- Drag-minus-thrust performance of baseline configuration with maximum-afterburning-power axisymmetric nozzles.

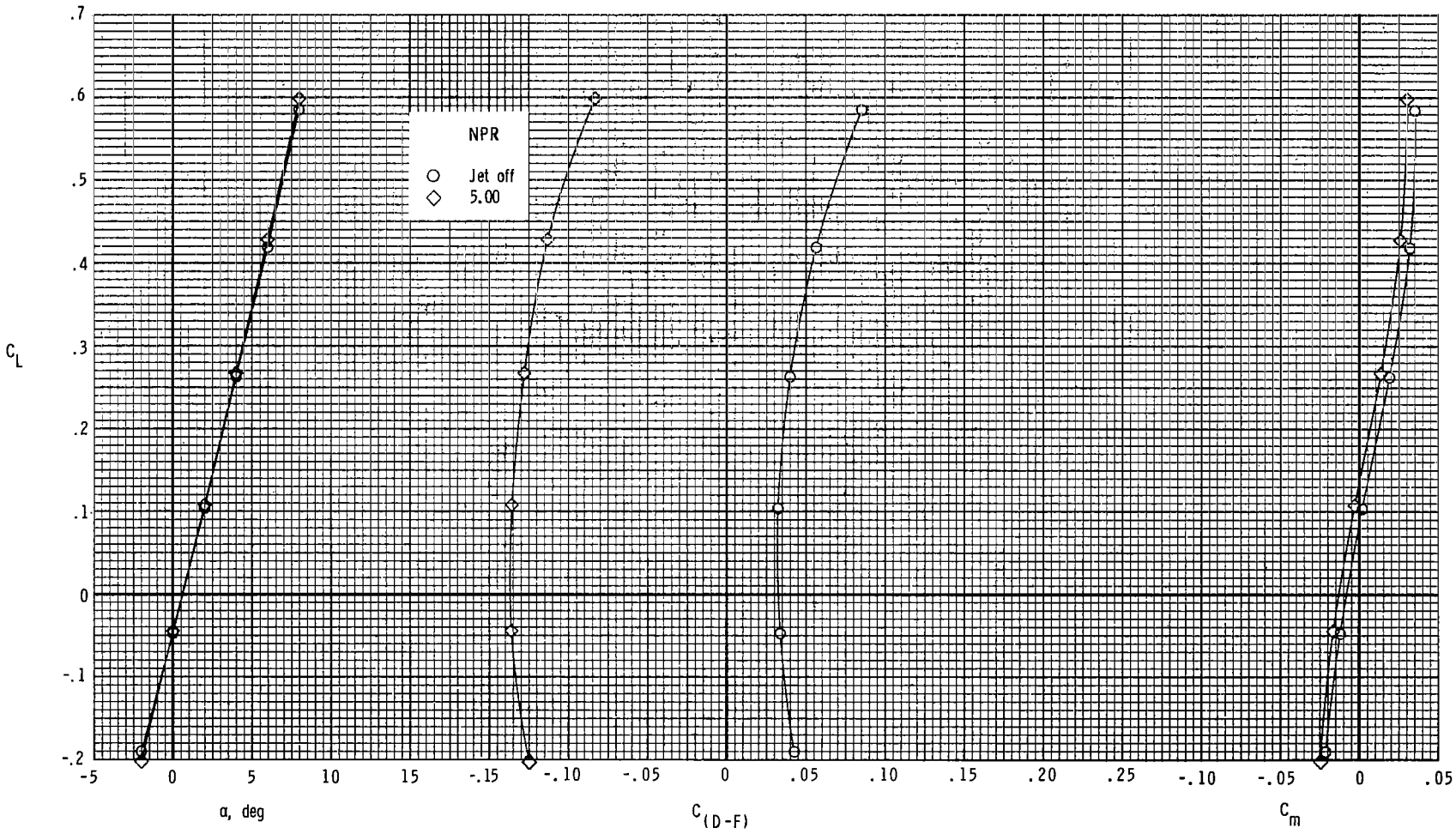

(b) M = 0.90.

Figure 18.- Concluded.

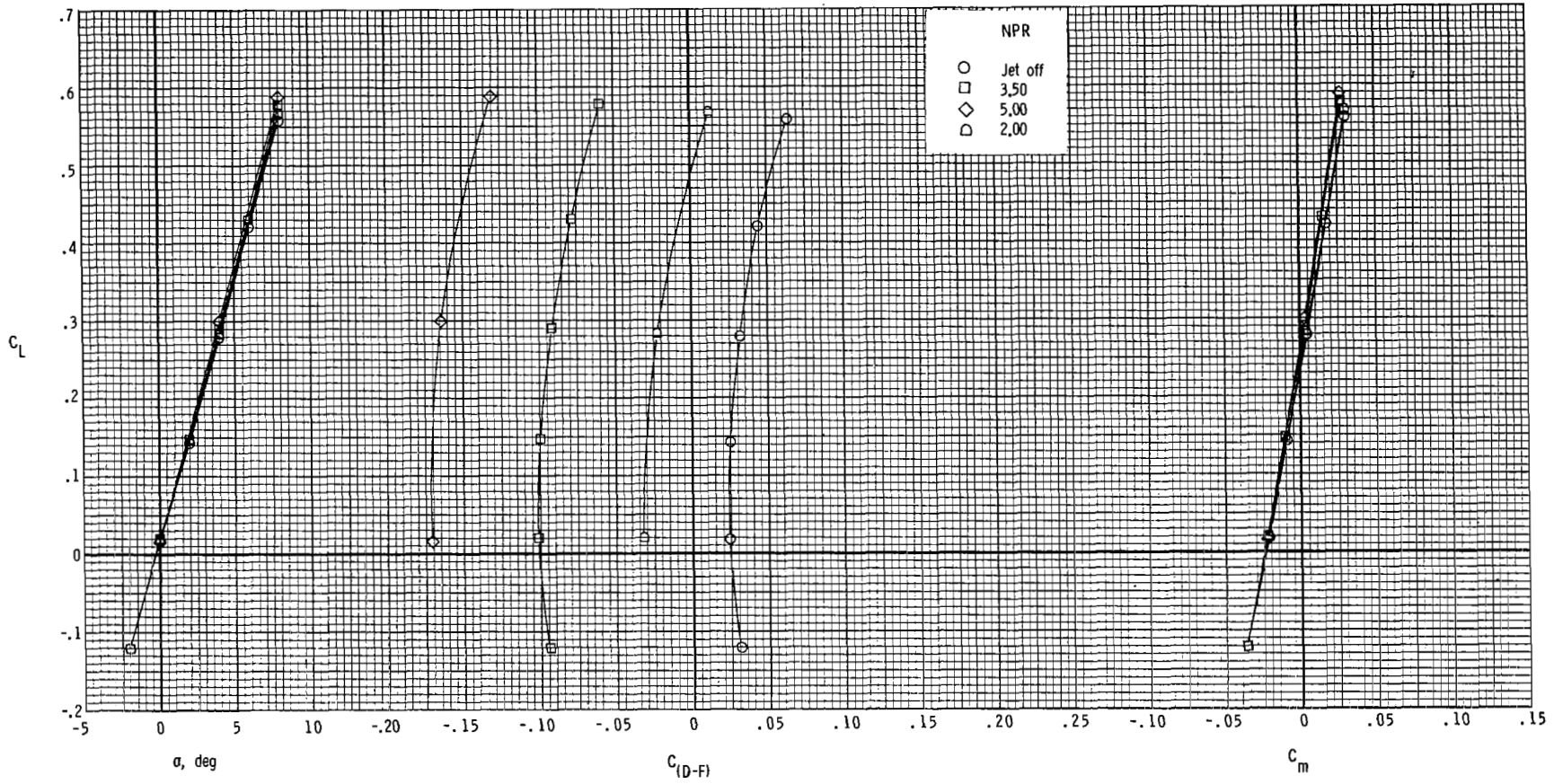

(a) M = 0.60.

Figure 19.- Drag-minus-thrust performance of configuration with nacelle-mounted twin vertical tails, toe angle (L.E. out) of 2°, modified tail booms, and dry-power axisymmetric nozzles.

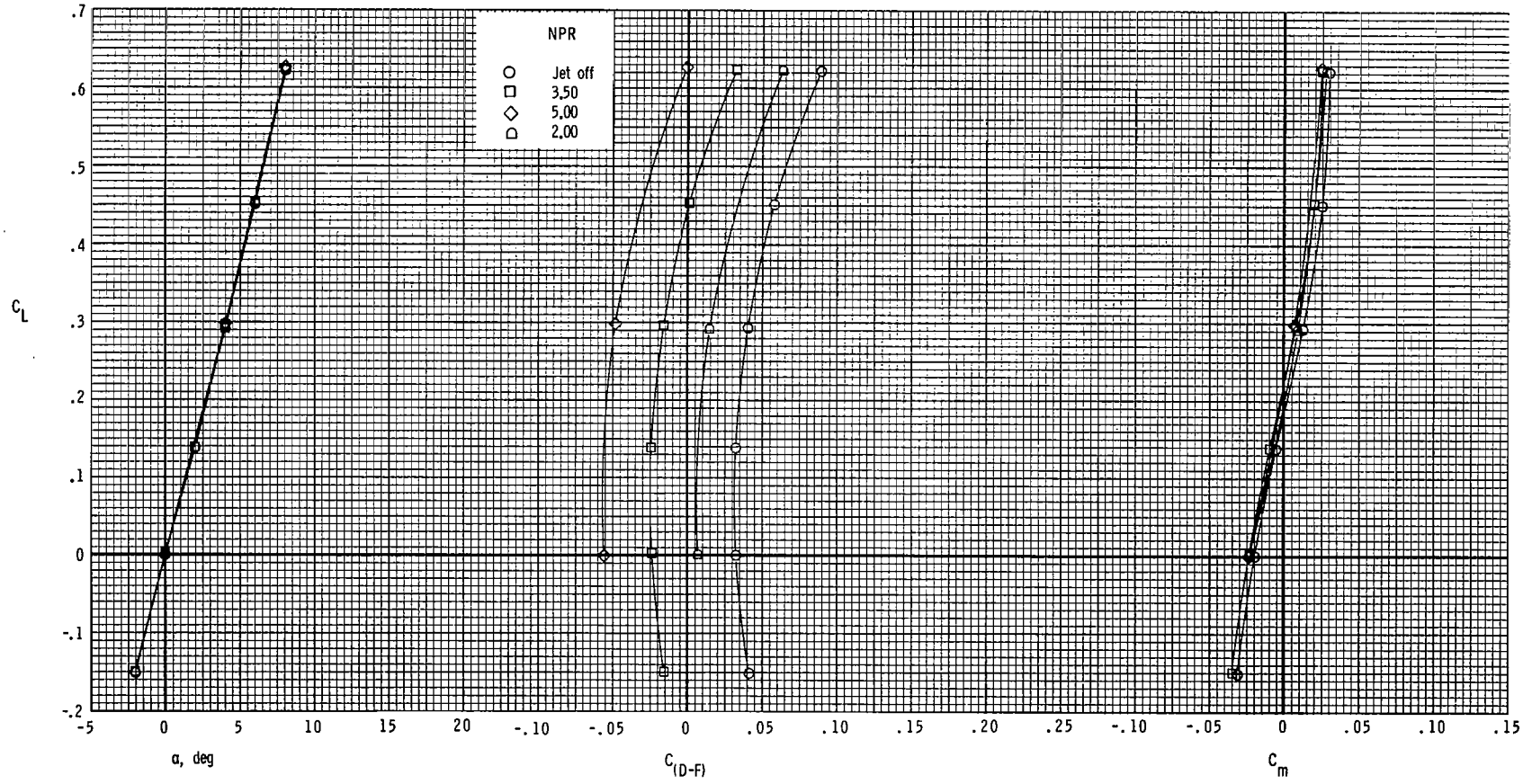

(b) M = 0.90.

Figure 19.- Concluded.

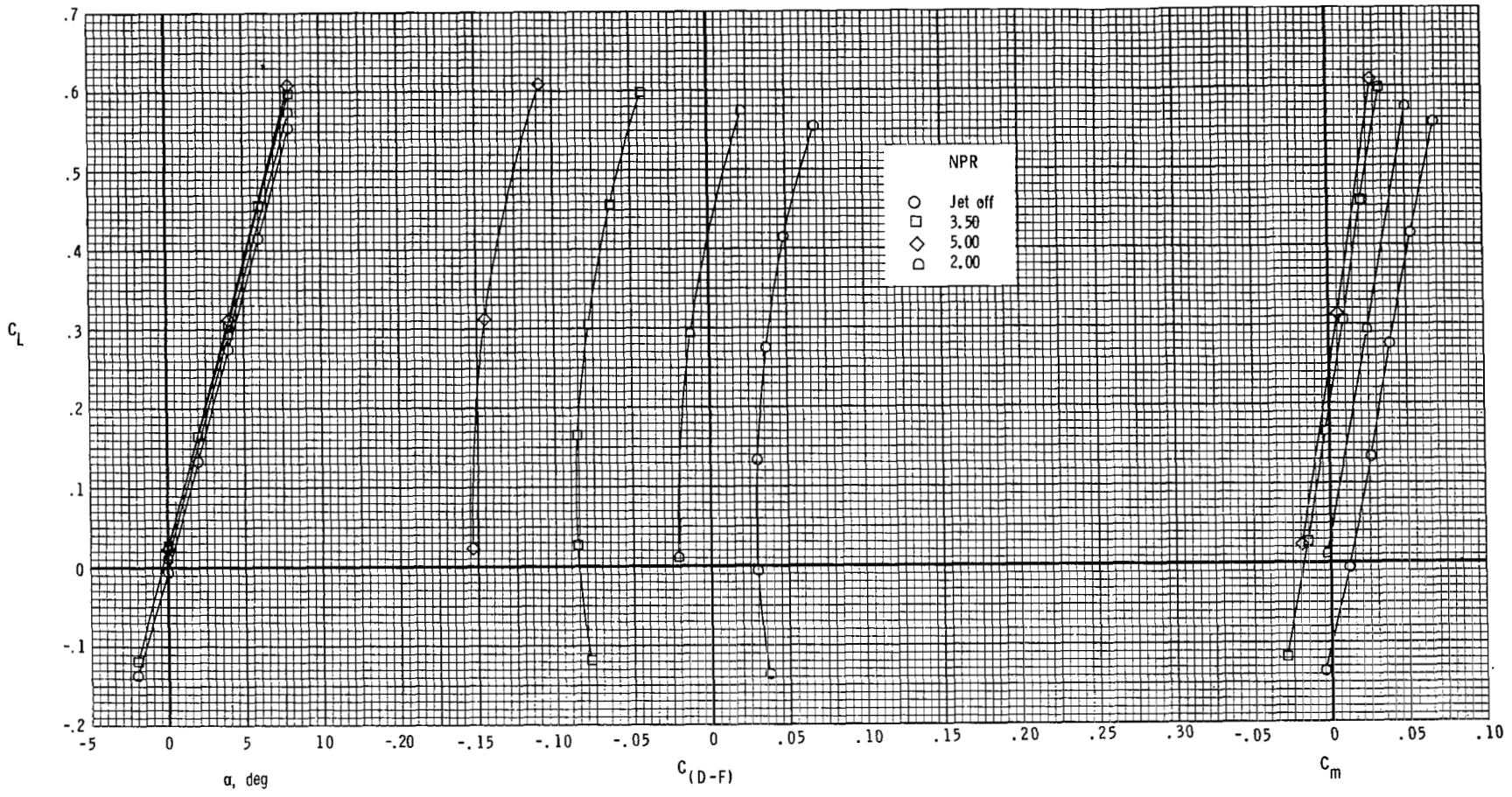

(a) M = 0.60.

Figure 20.- Drag-minus-thrust performance of configuration with 2-D C-D dry-power nozzles and divergent sidewalls (DSW).

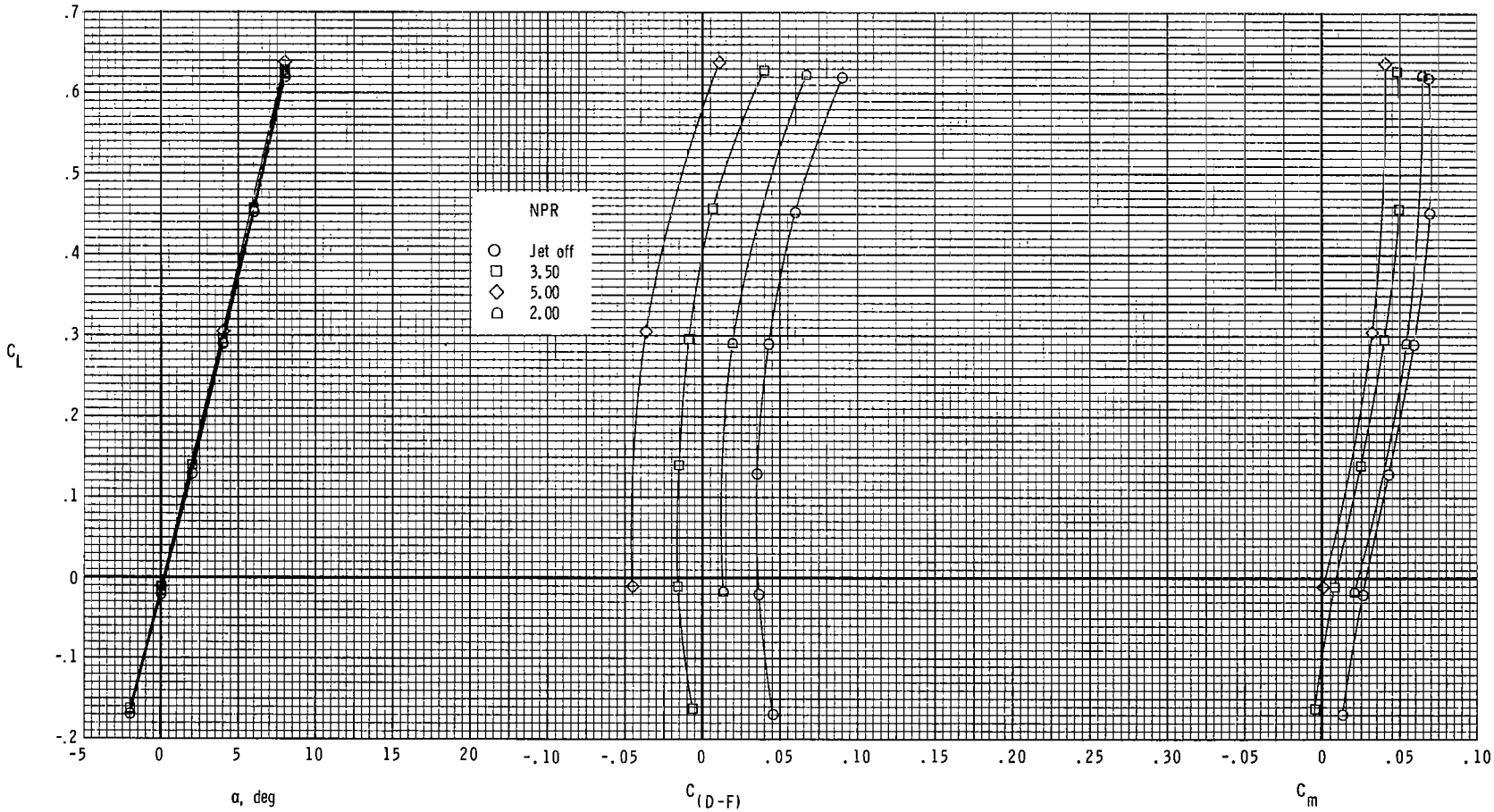

(b) M = 0.90.

Figure 20.- Concluded.

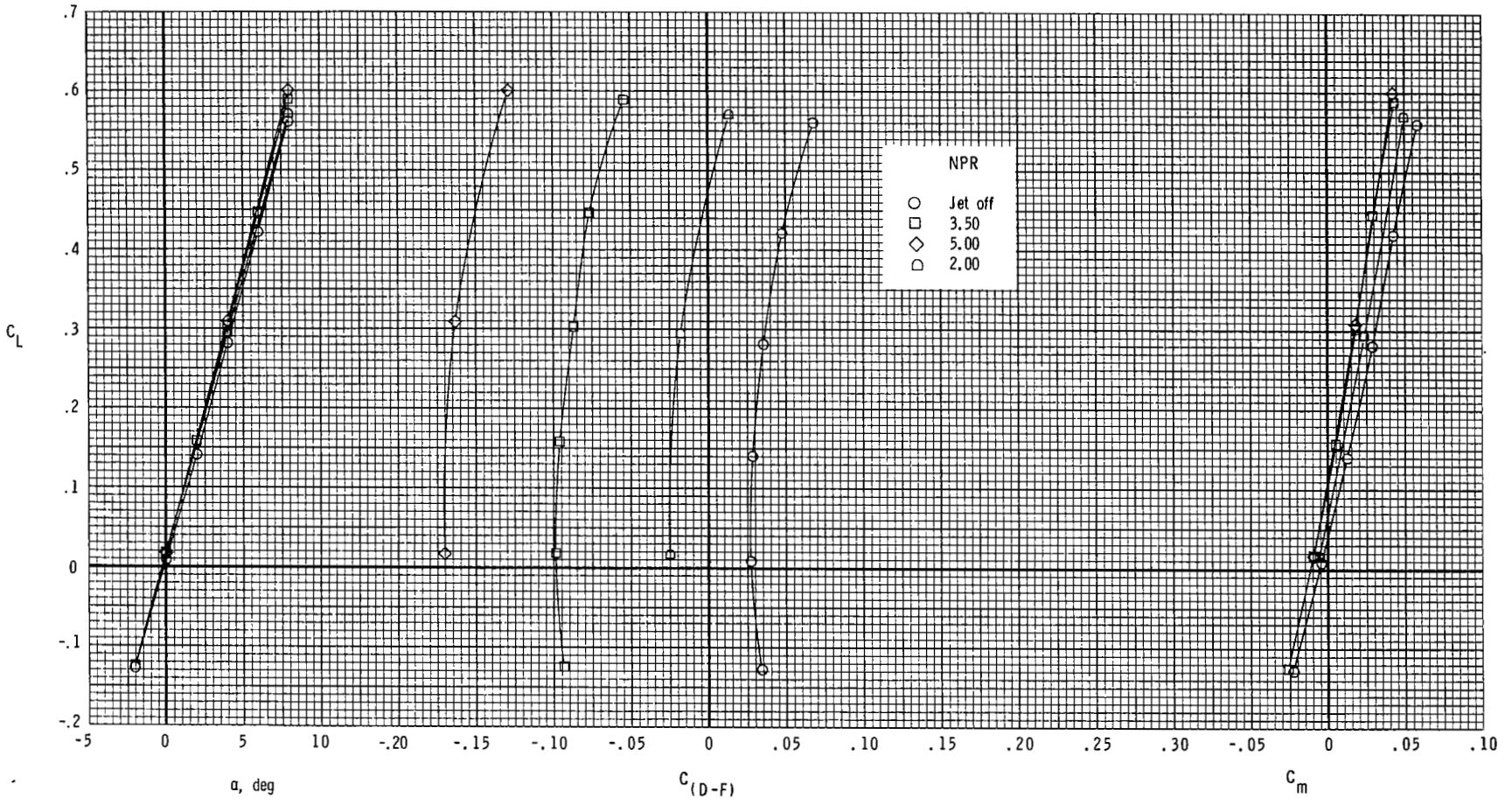

(a) M = 0.60.

Figure 21.- Drag-minus-thrust performance of configuration with 2-D C-D dry-power nozzles and variable sidewalls (VSW).

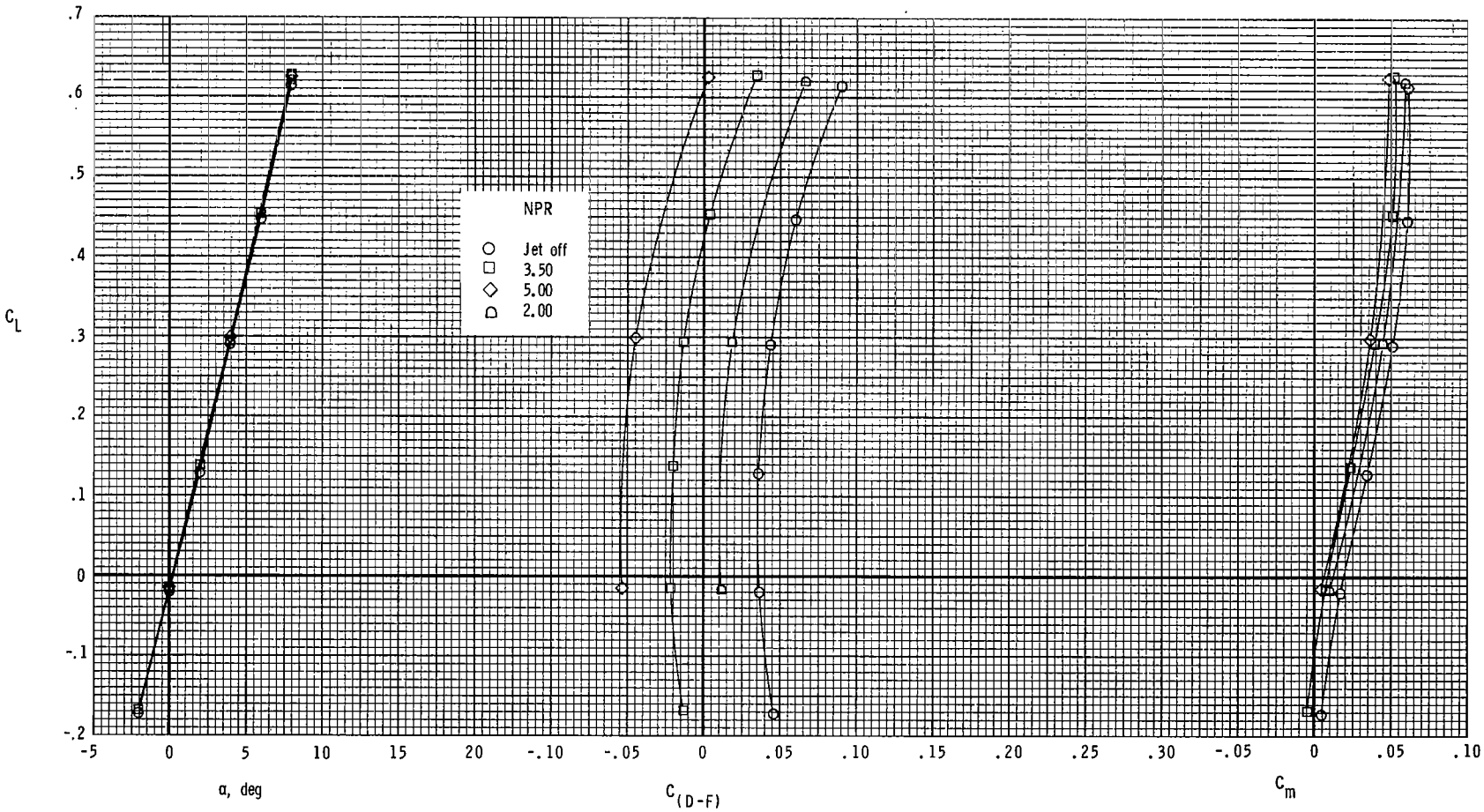

(b) M = 0.90.

Figure 21.- Concluded.

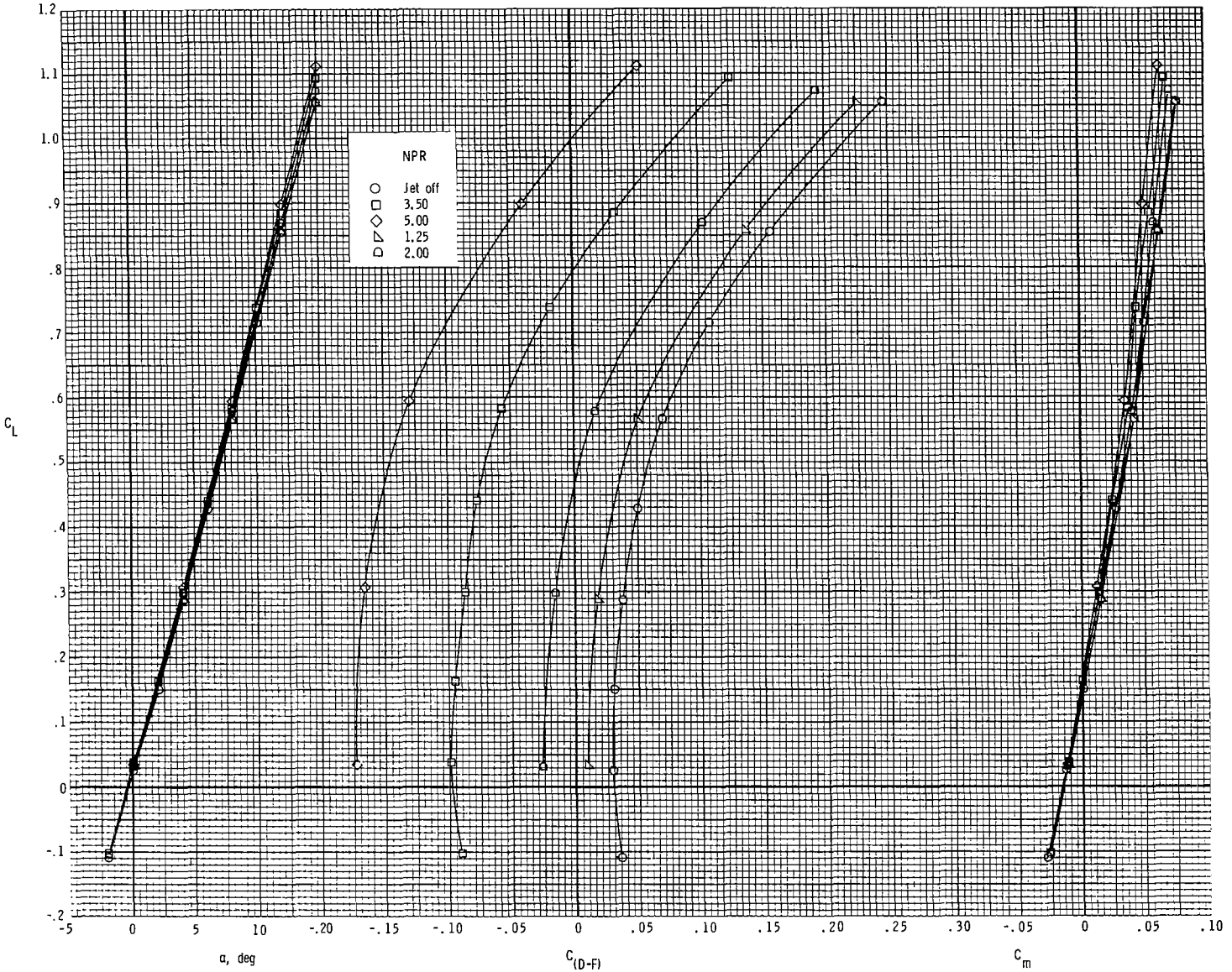

(a) M = 0.60.

Figure 22.- Drag-minus-thrust performance of configuration with 2-D C-D dry-power nozzles and fixed, straight sidewalls (SSW).

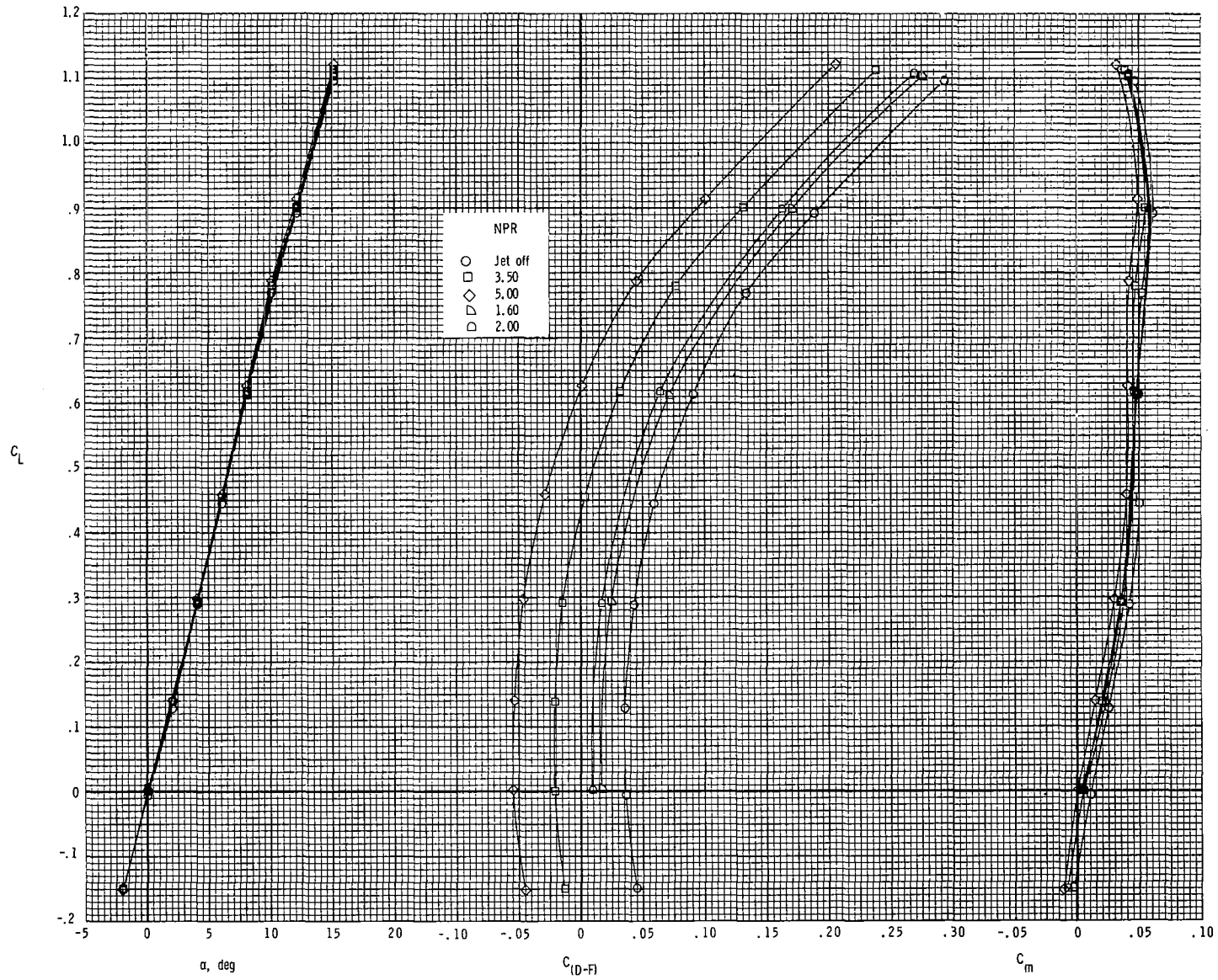

(b) M = 0.90.

Figure 22.- Continued.

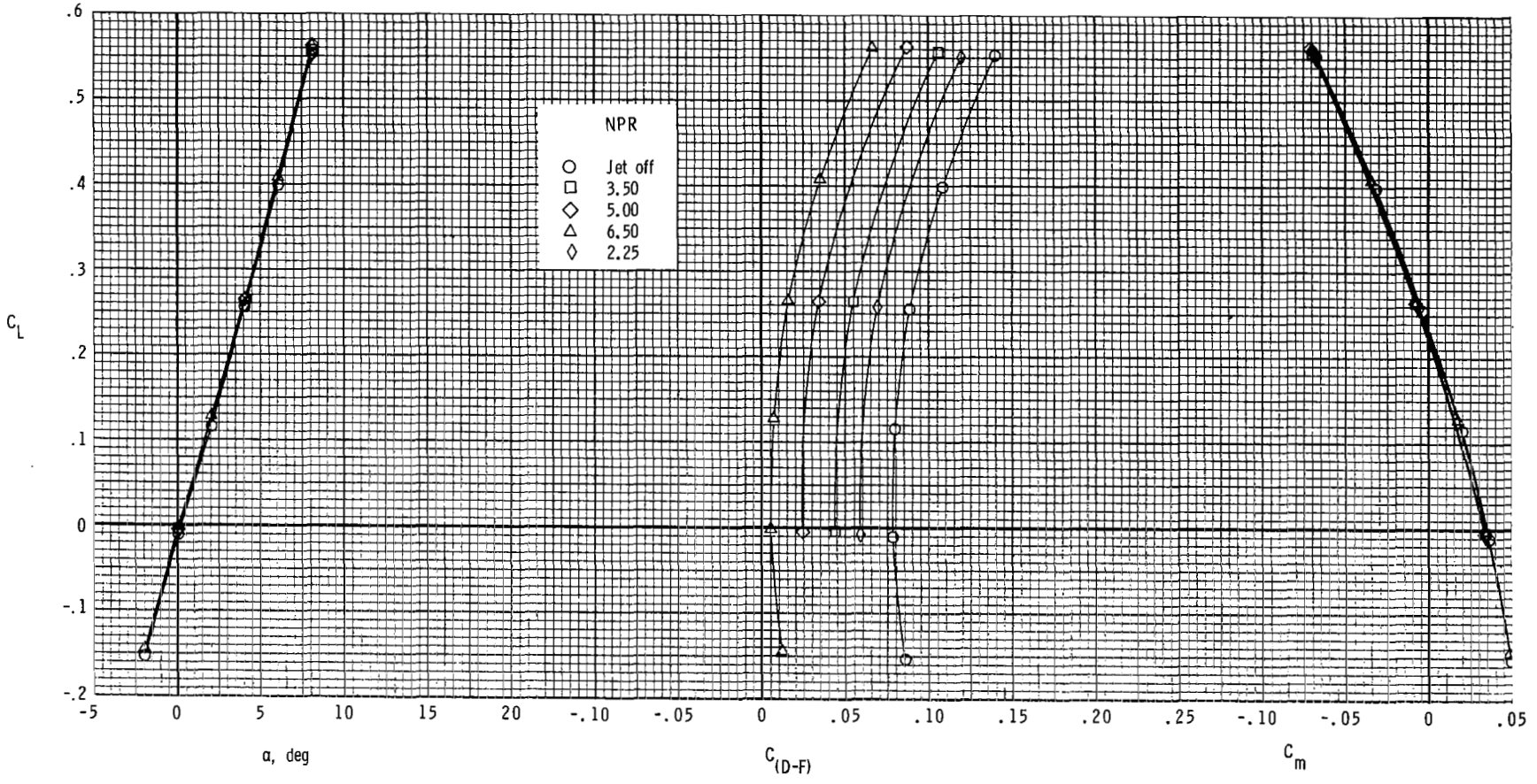

(c) M = 1.20.

Figure 22.- Concluded.

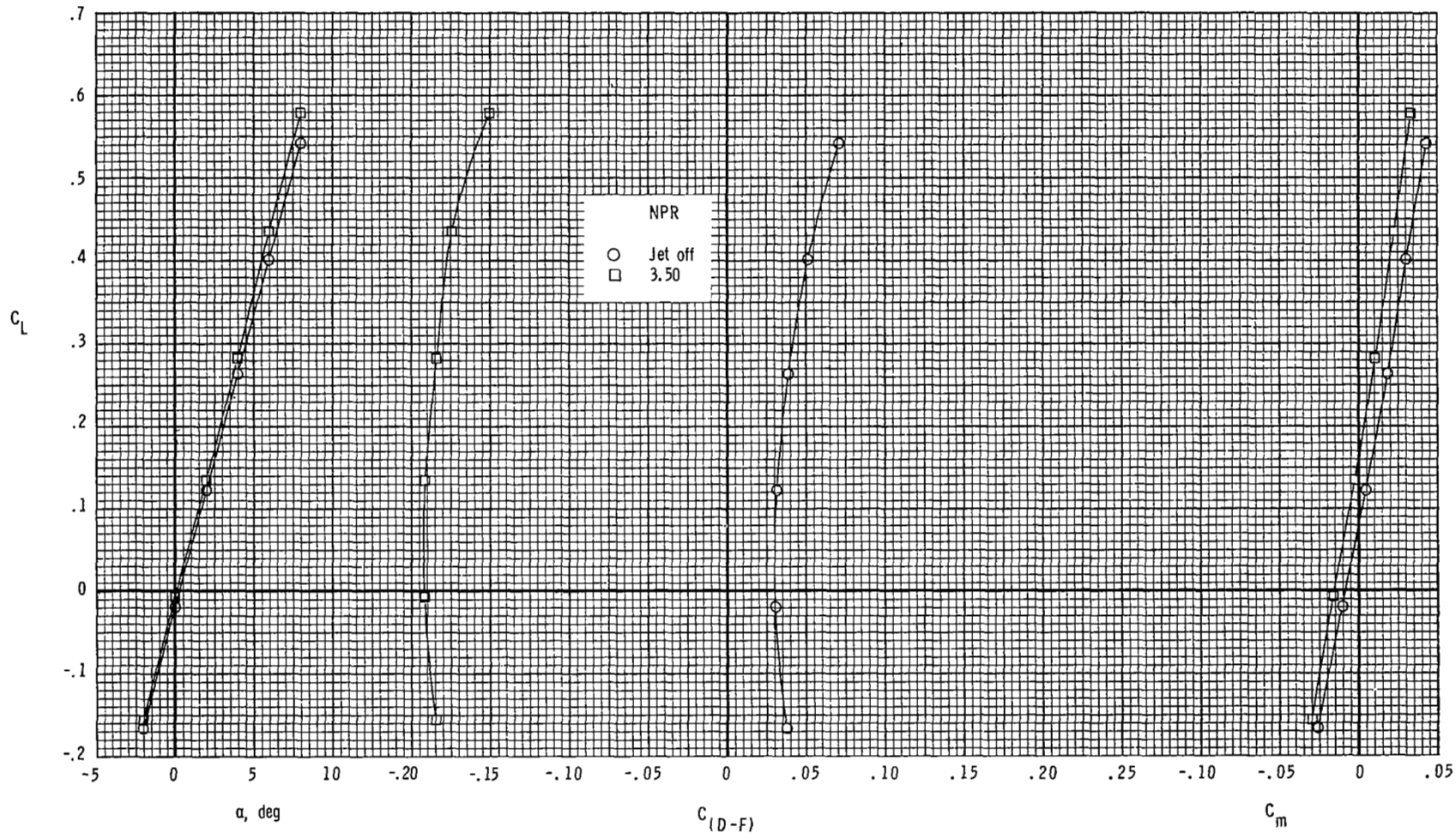

(a) M = 0.60.

Figure 23.- Drag-minus-thrust performance of configuration with 2-D C-D maximum-afterburning-power SSW nozzles.

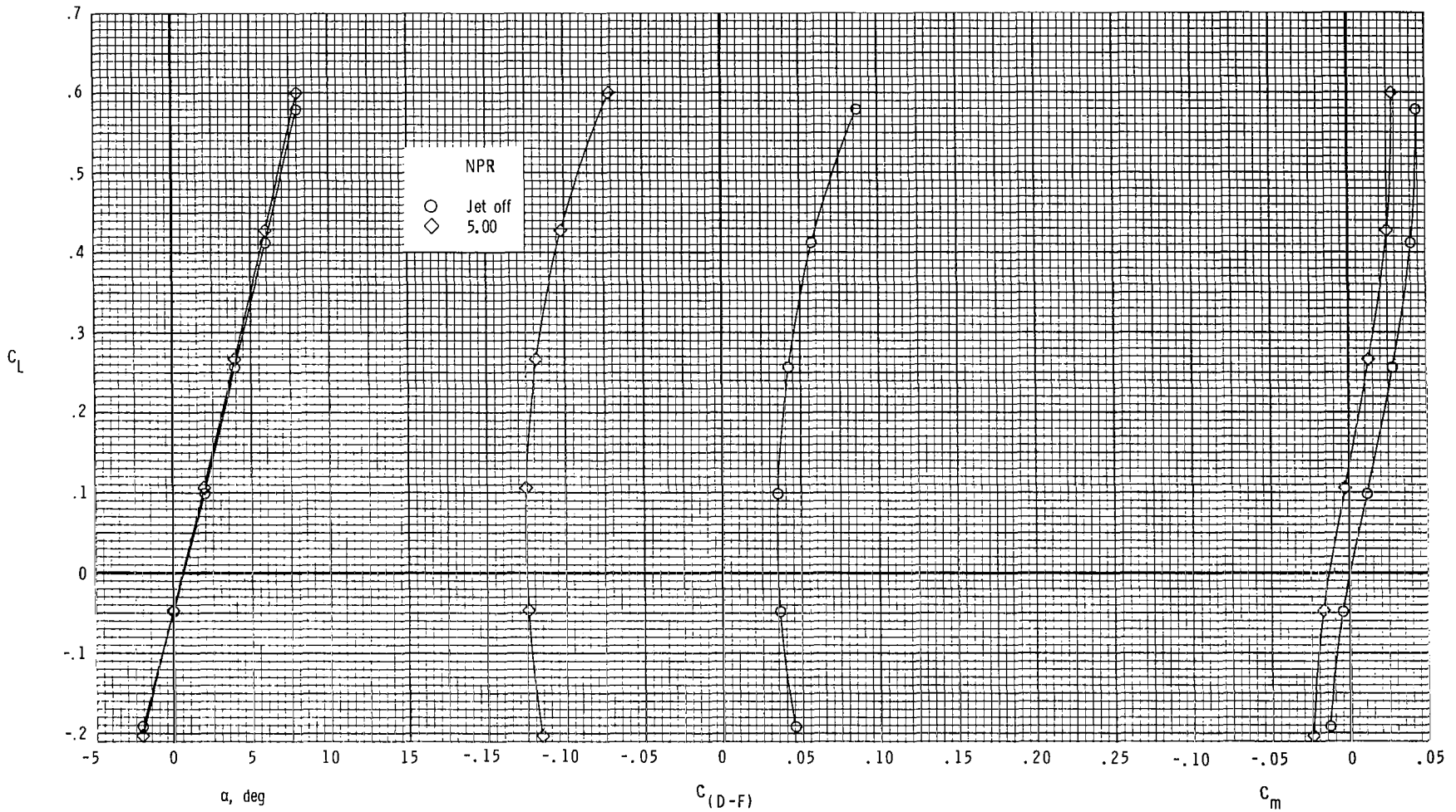

(b) M = 0.90.

Figure 23.- Concluded.

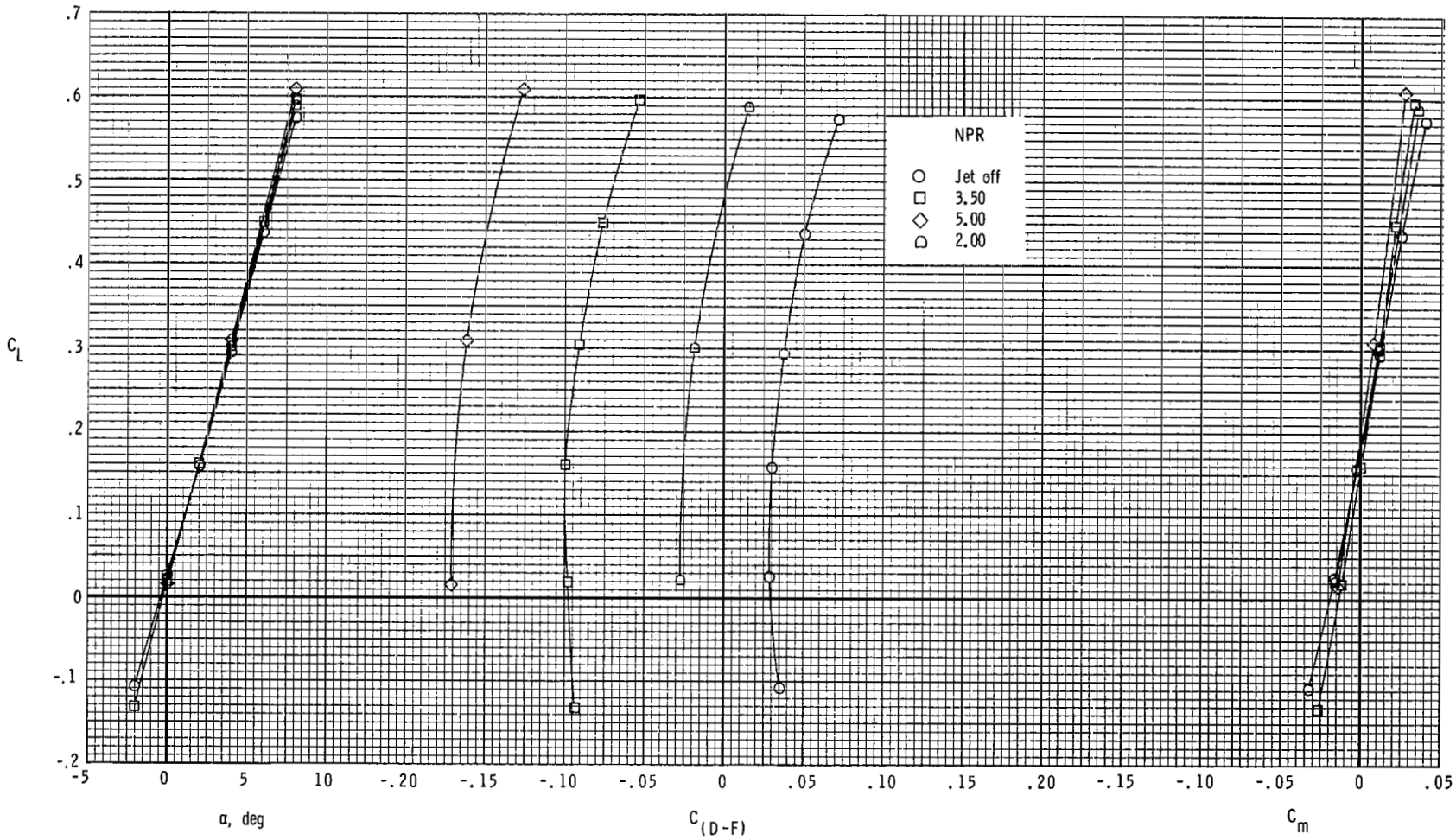

(a) M = 0.60.

Figure 24.- Drag-minus-thrust performance of configuration with nacelle-mounted twin vertical tails, toe angle (L.E. out) of 2°, modified tail booms, and dry-power 2-D C-D SSW nozzles.

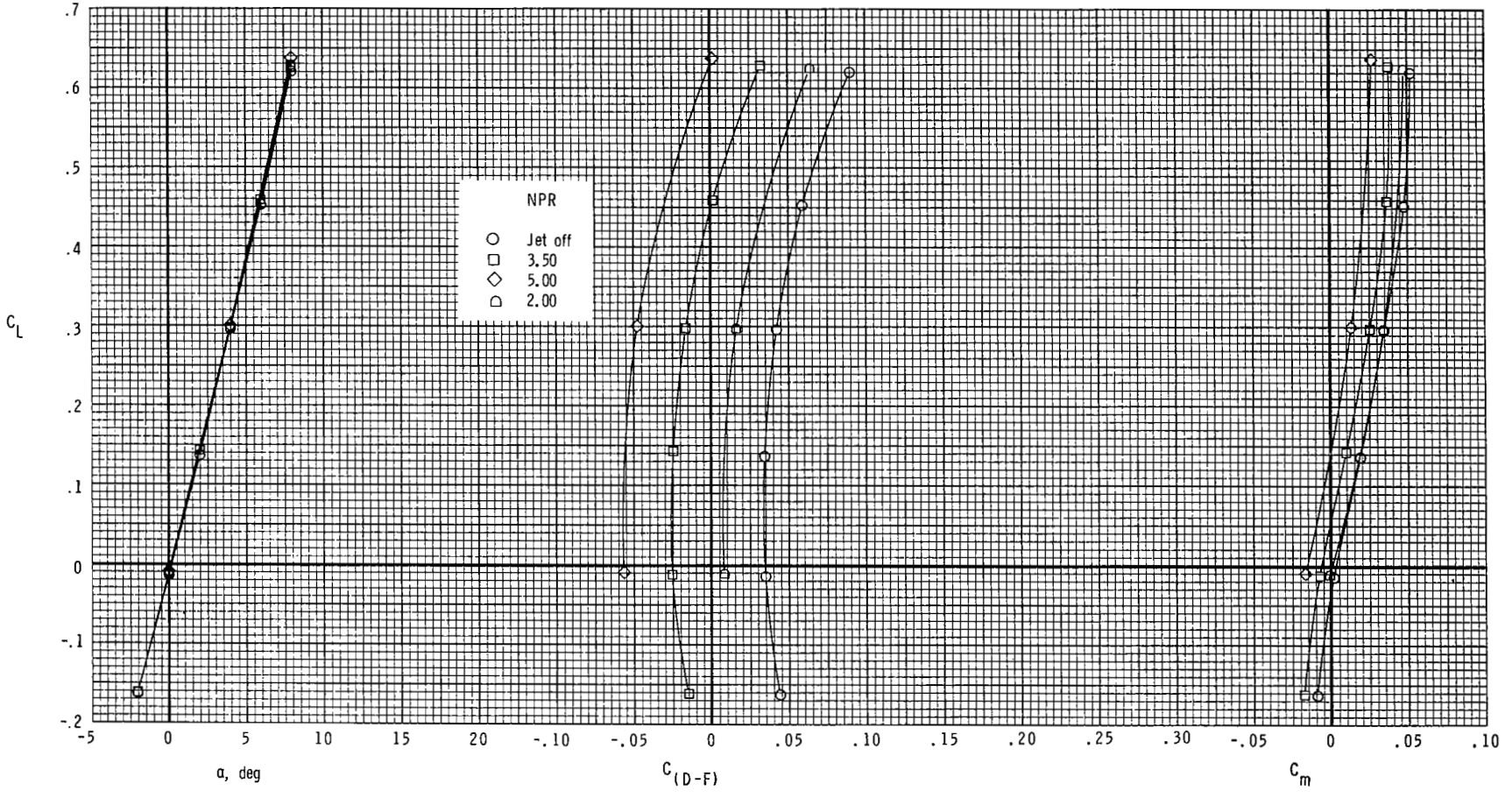

(b) M = 0.90.

Figure 24.- Concluded.

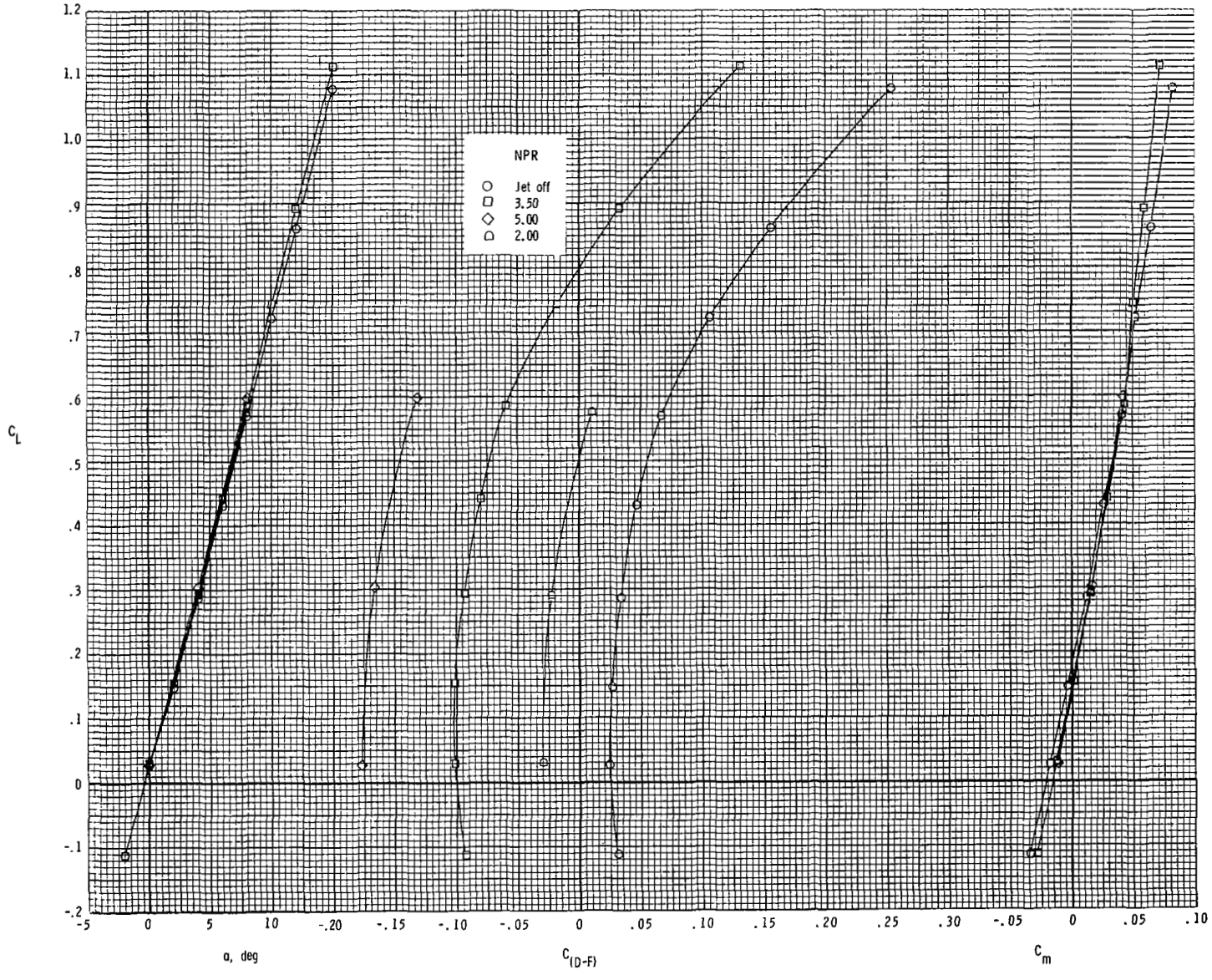

(a) M = 0.60.

Figure 25.- Drag-minus-thrust performance of configuration with dry-power 2-D C-D SSW nozzles and twin vertical tails off.

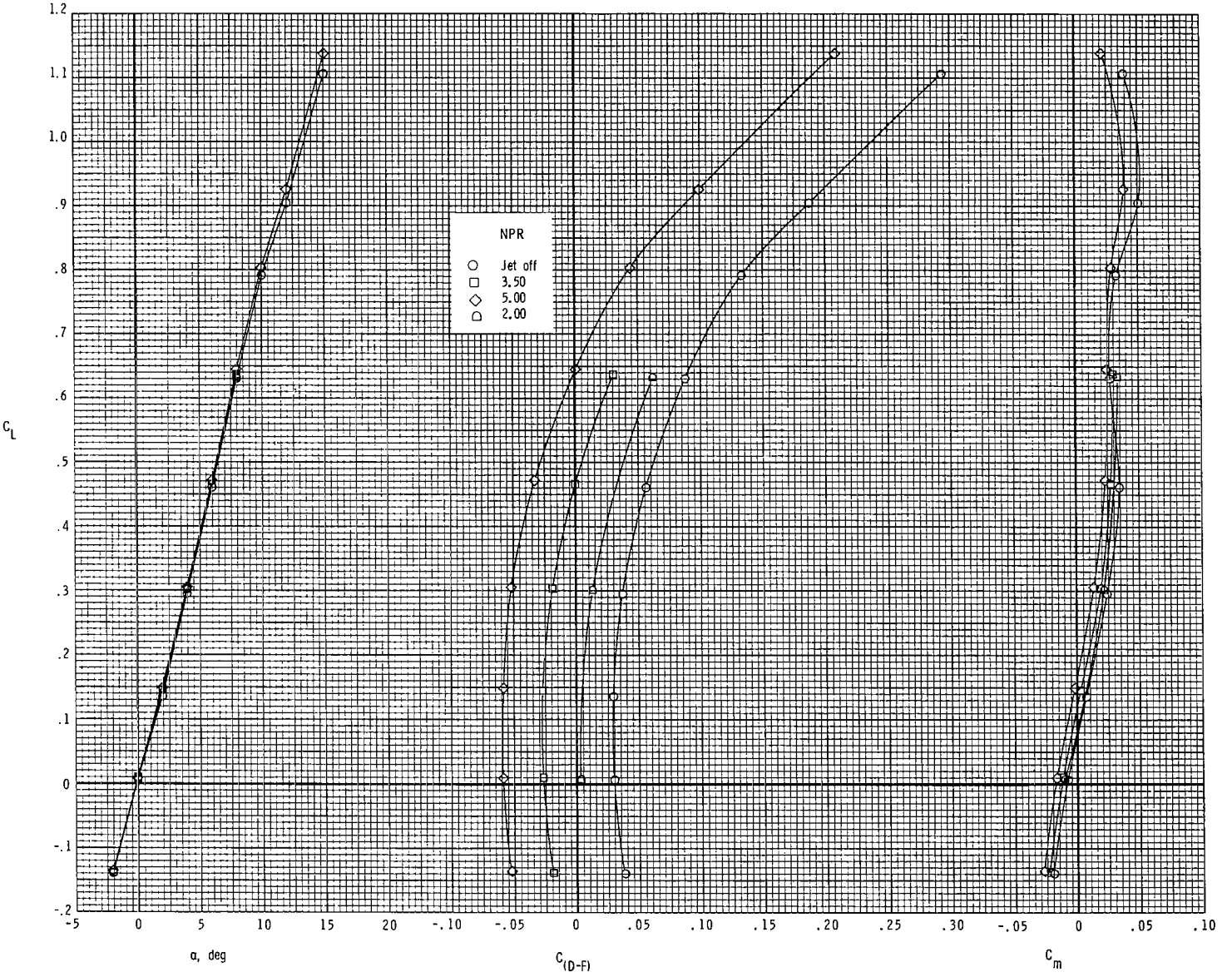

(b) M = 0.90.

Figure 25.- Continued.

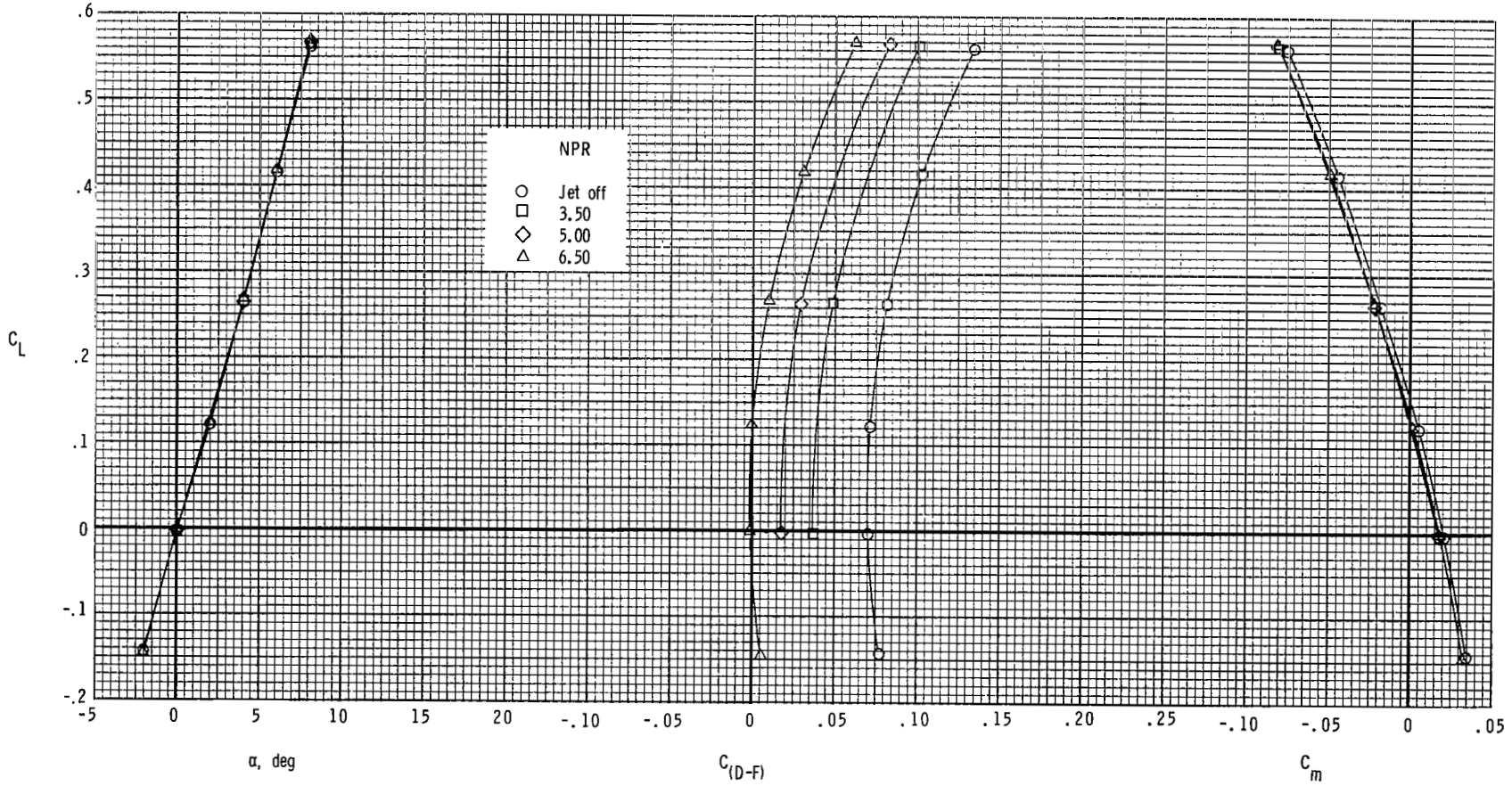

(c) M = 1.20.

Figure 25.- Concluded.

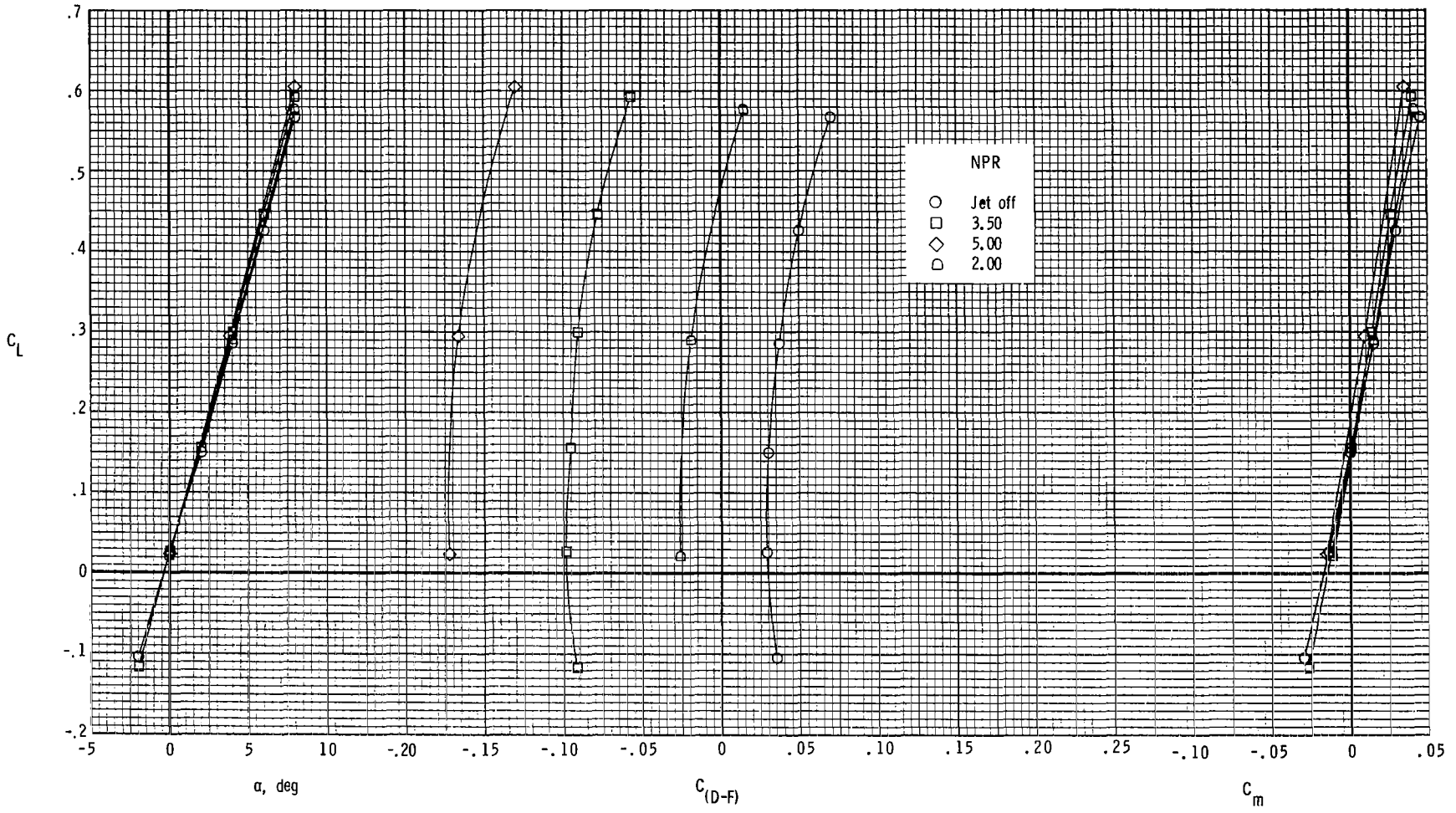

(a) M = 0.60.

Figure 26.- Drag-minus-thrust performance of configuration with dry-power 2-D C-D SSW nozzles, boom-mounted twin vertical tails, and toe angle of 0°.

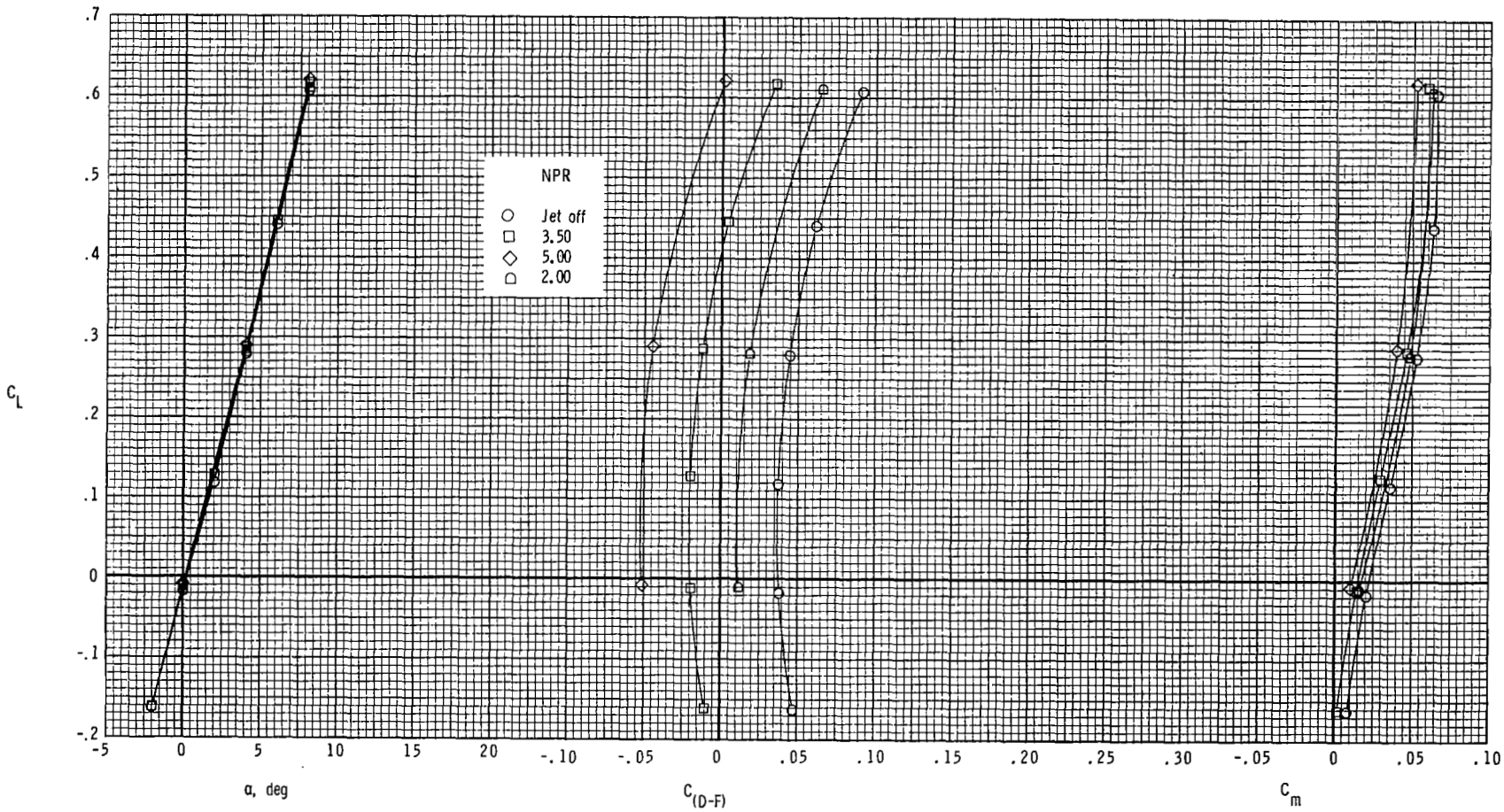

(b) M = 0.90.

Figure 26.- Concluded.

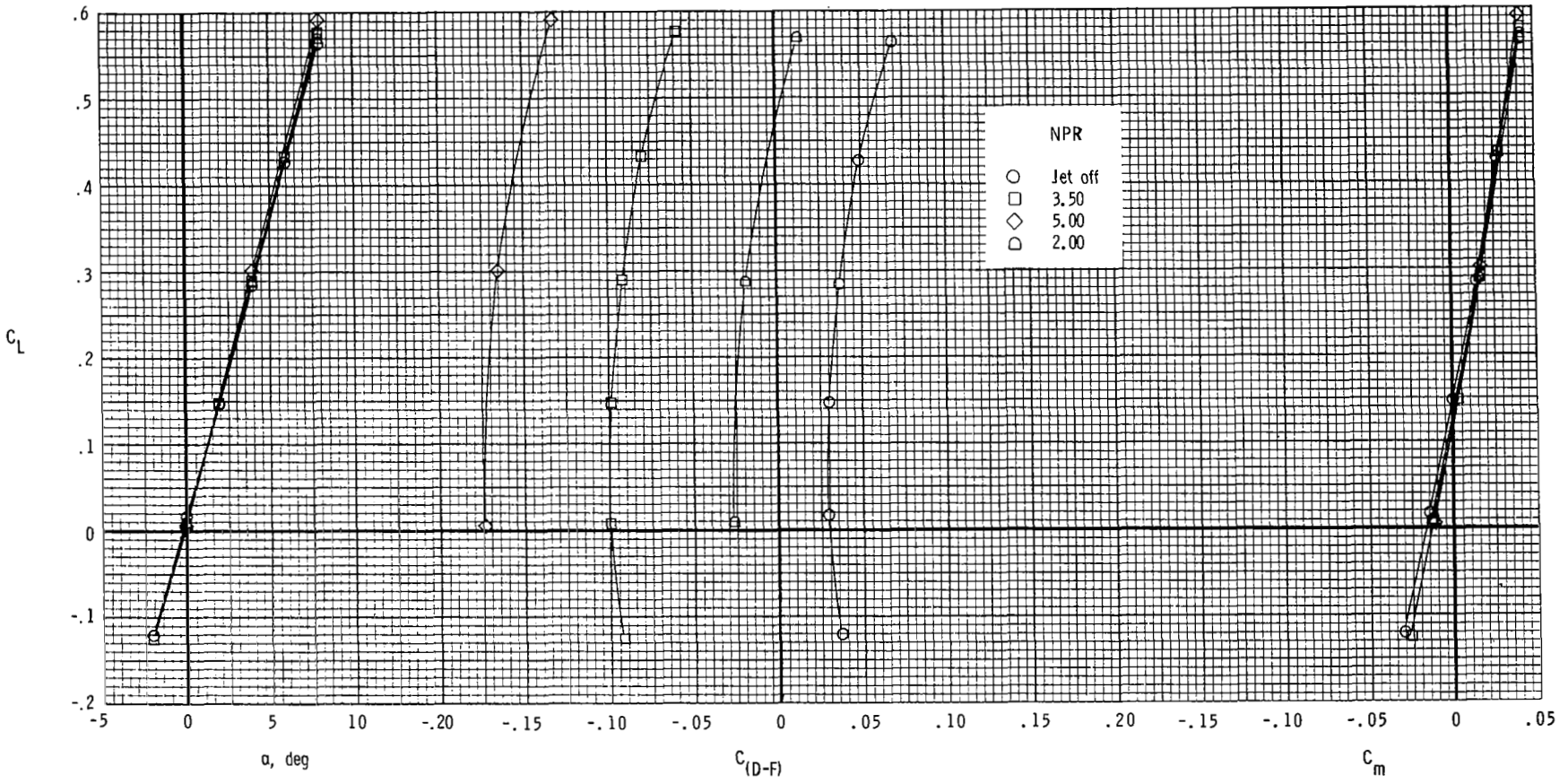

(a) M = 0.60.

Figure 27.- Drag-minus-thrust performance of configuration with dry-power 2-D C-D SSW nozzles, boom-mounted twin vertical tails, and toe angle (L.E. out) of 4°.

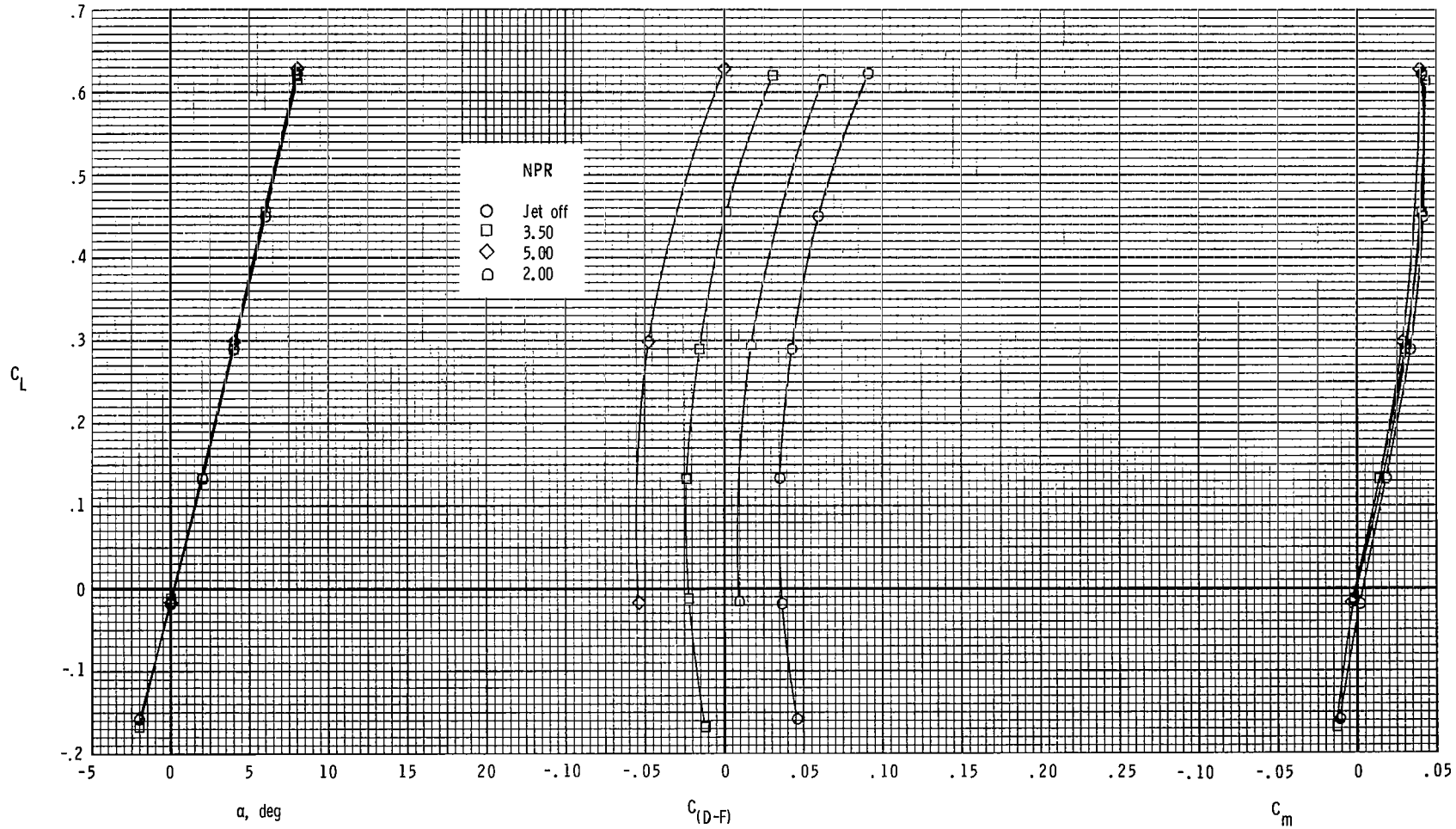

(b) M = 0.90.

Figure 27.- Concluded.

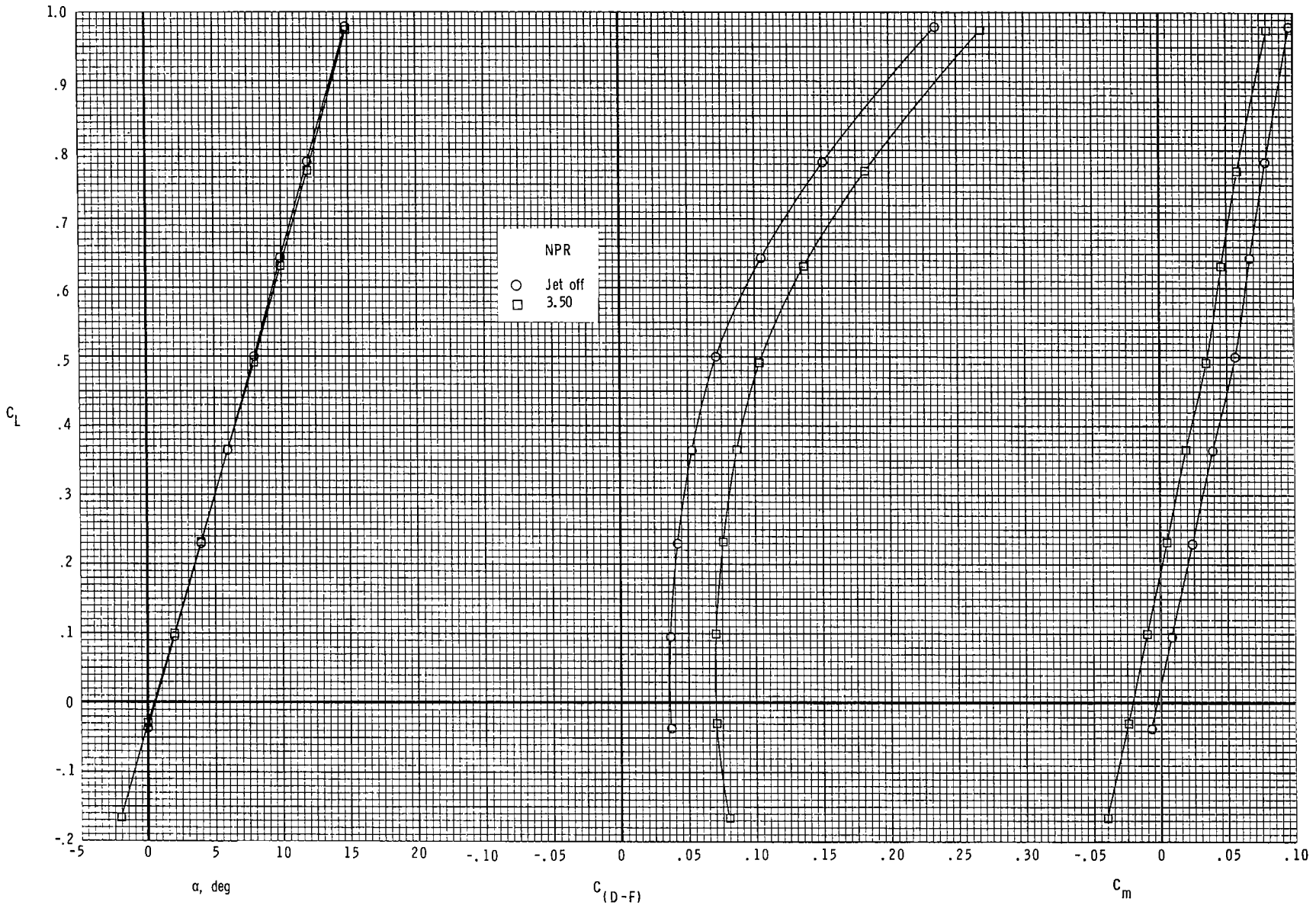

(a) M = 0.60.

Figure 28.- Effect of partially deployed reversers (δ_{REV} = 90°) on drag-minus-thrust performance of configuration with dry-power 2-D C-D SSW nozzles.

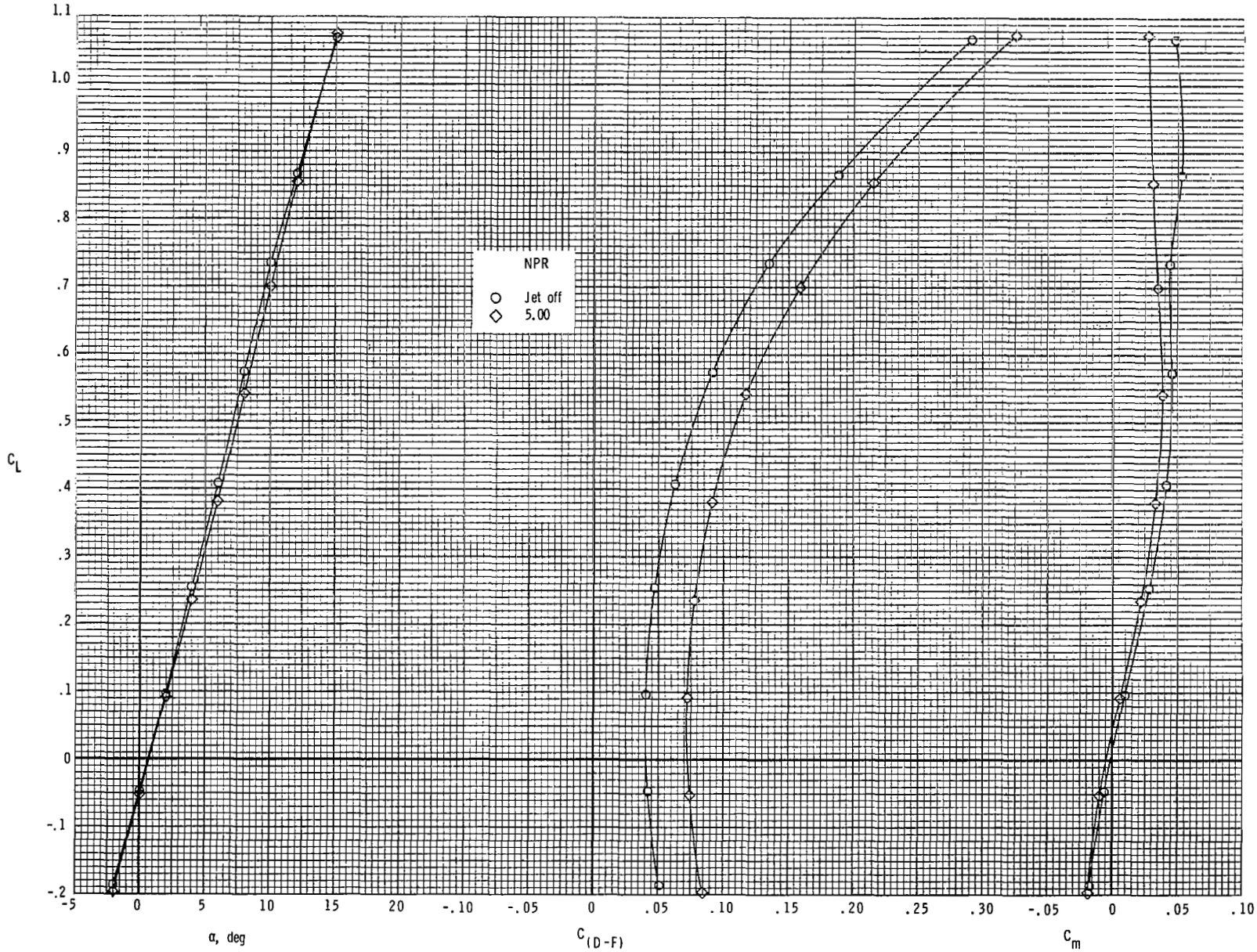

(b) M = 0.90.

Figure 28.- Continued.

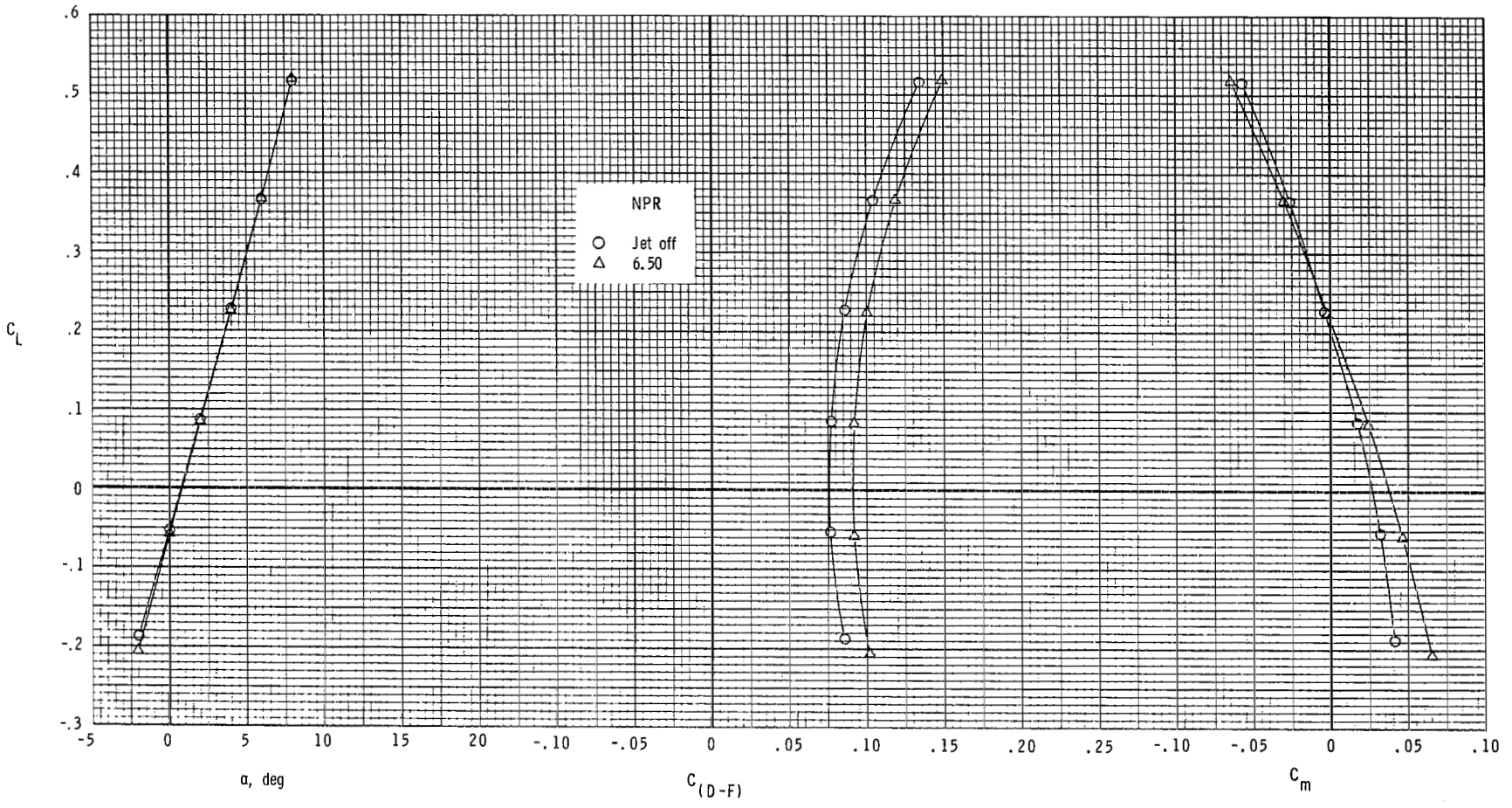

(c) M = 1.20.

Figure 28.- Concluded.

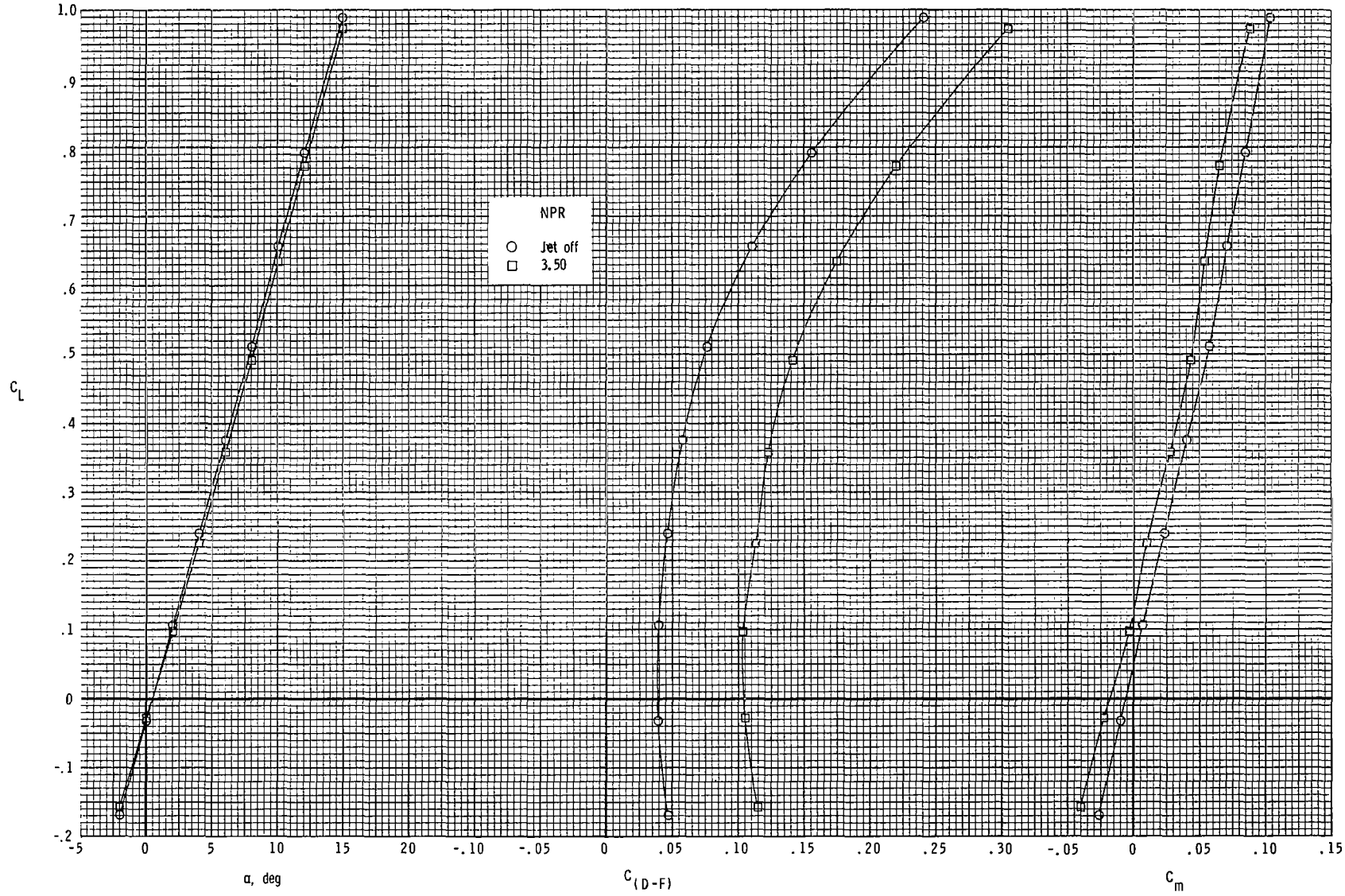

(a) M = 0.60.

Figure 29.- Effect of fully deployed reversers (δ_{REV} = 130°) on drag-minus-thrust performance of configuration with dry-power 2-D C-D SSW nozzles.

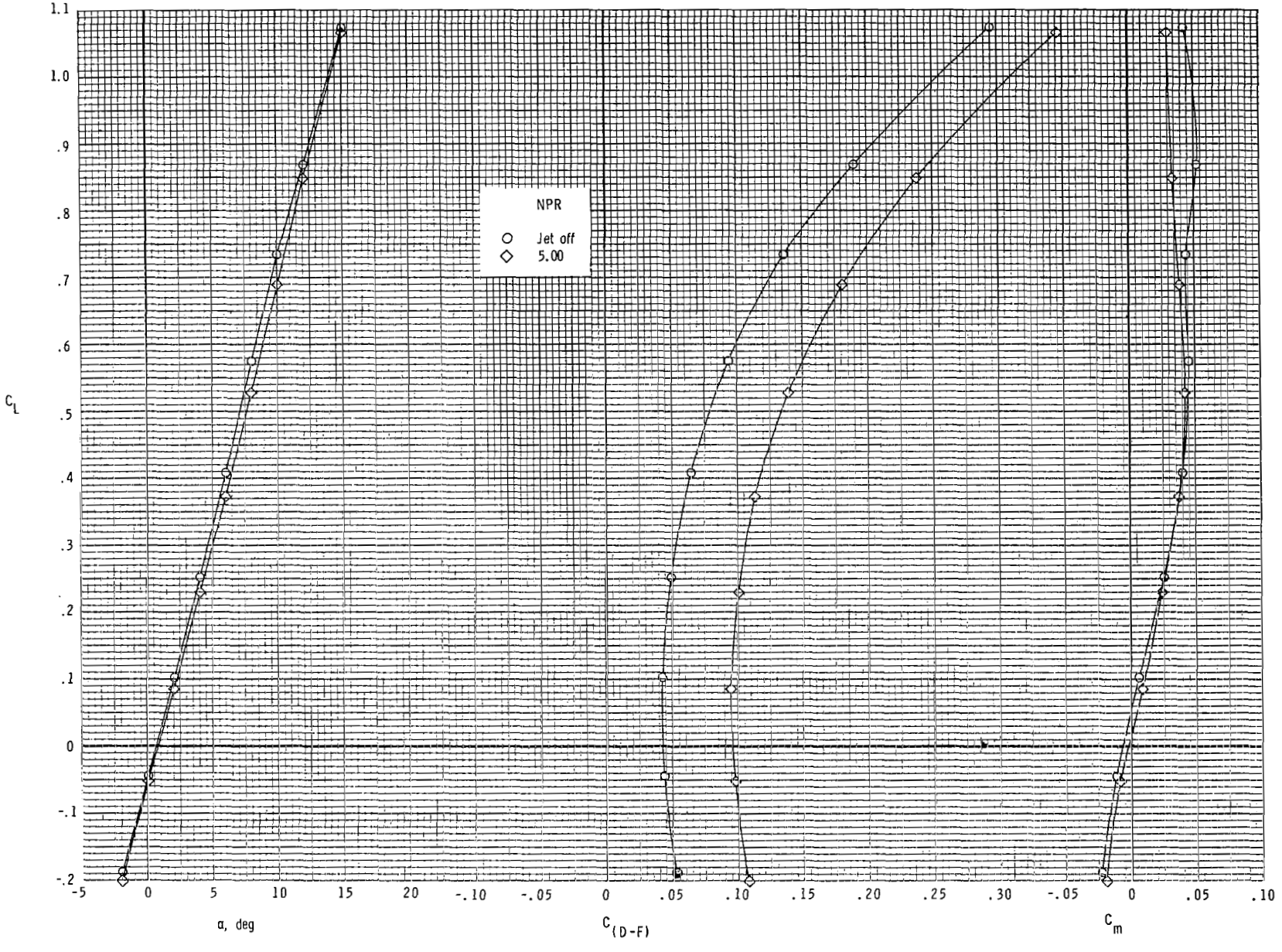

(b) M = 0.90.

Figure 29.- Continued.

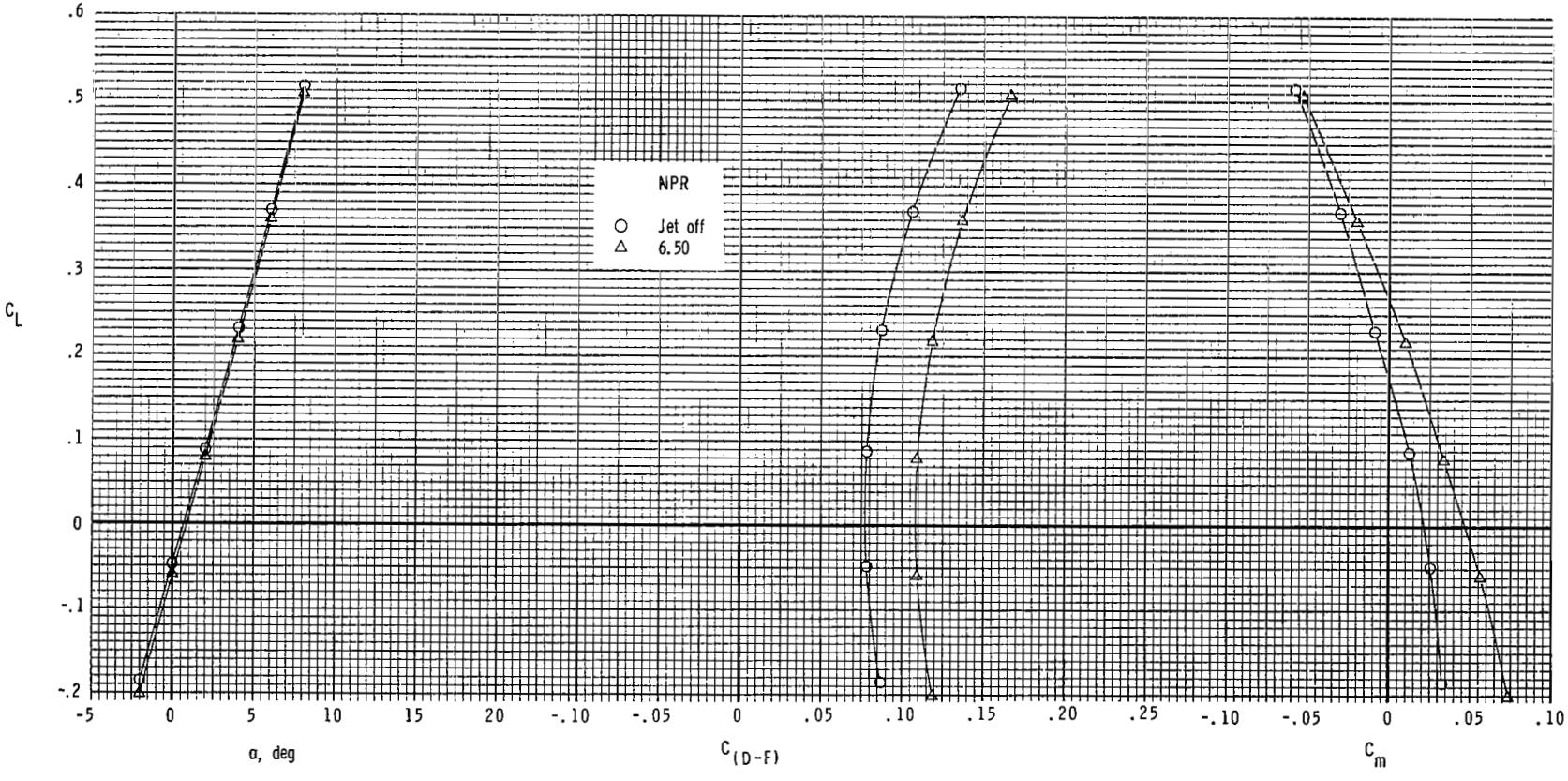

(c) M = 1.20.

Figure 29.- Concluded.

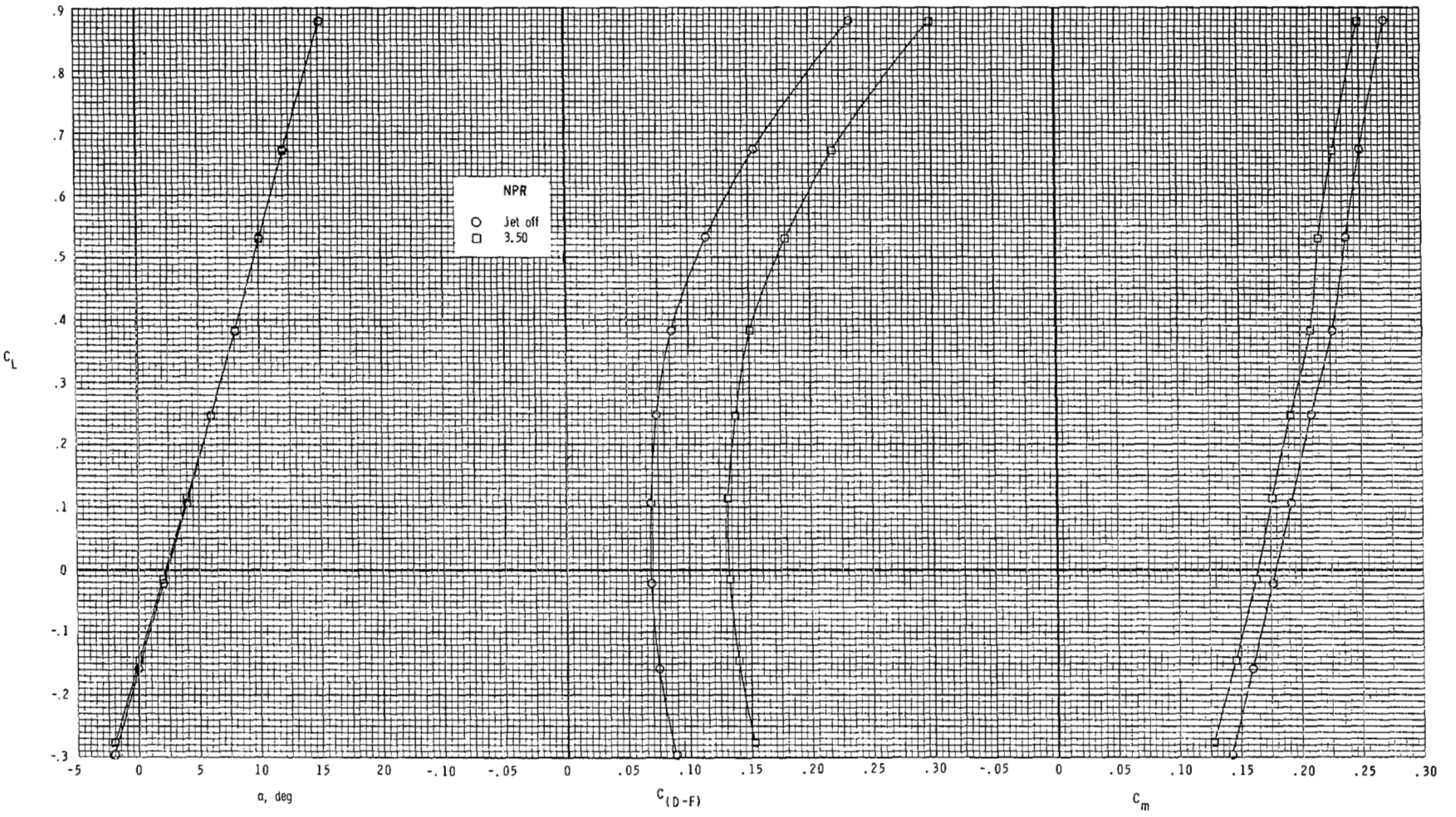

(a) M = 0.60.

Figure 30.- Effect of fully deployed reversers (δ_{REV} = 130°) on drag-minus-thrust performance of configuration with dry-power 2-D C-D SSW nozzles and horizontal-tail deflection of -15° (L.E. down).

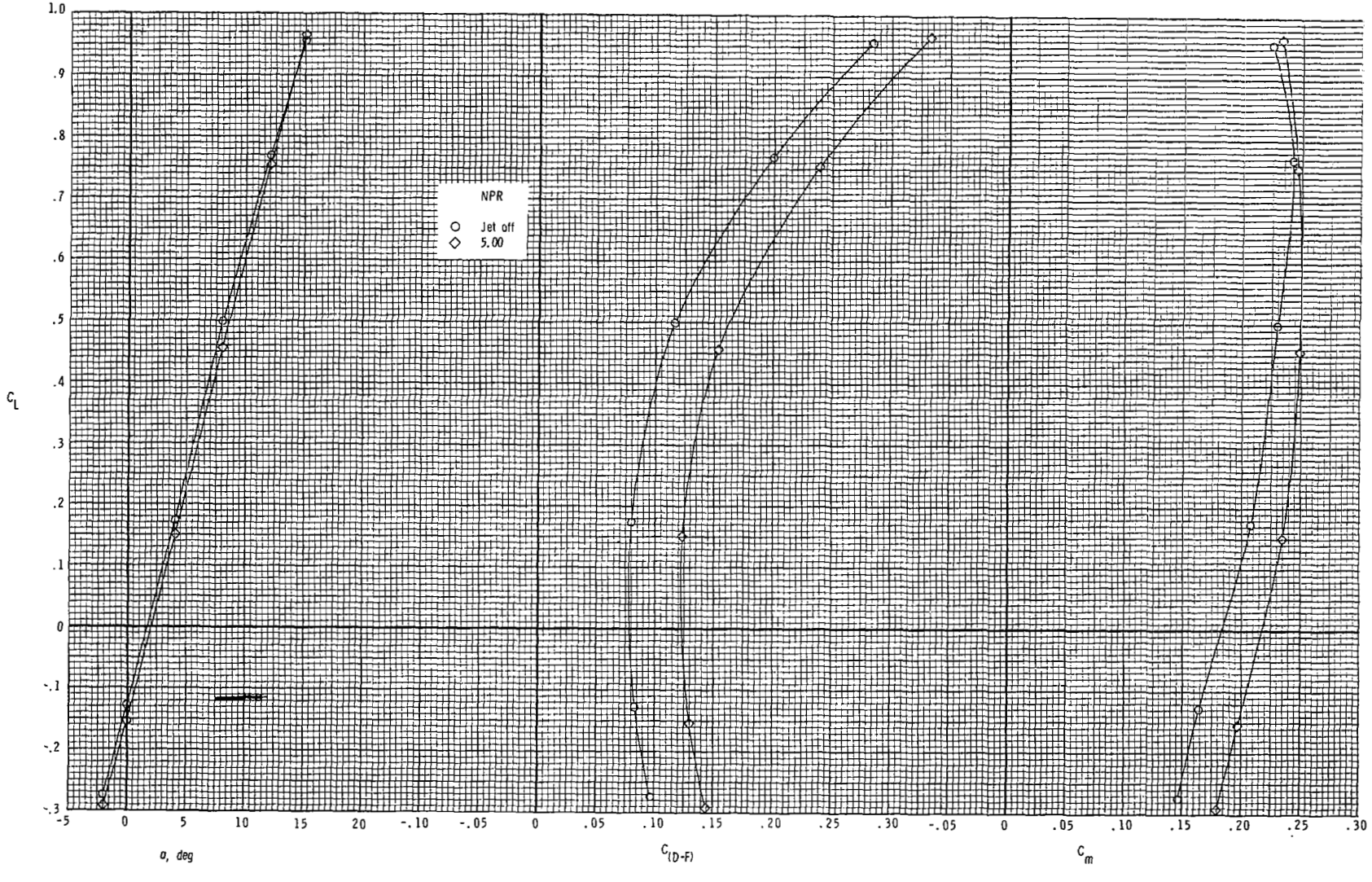

(b) M = 0.90.

Figure 30.- Concluded.

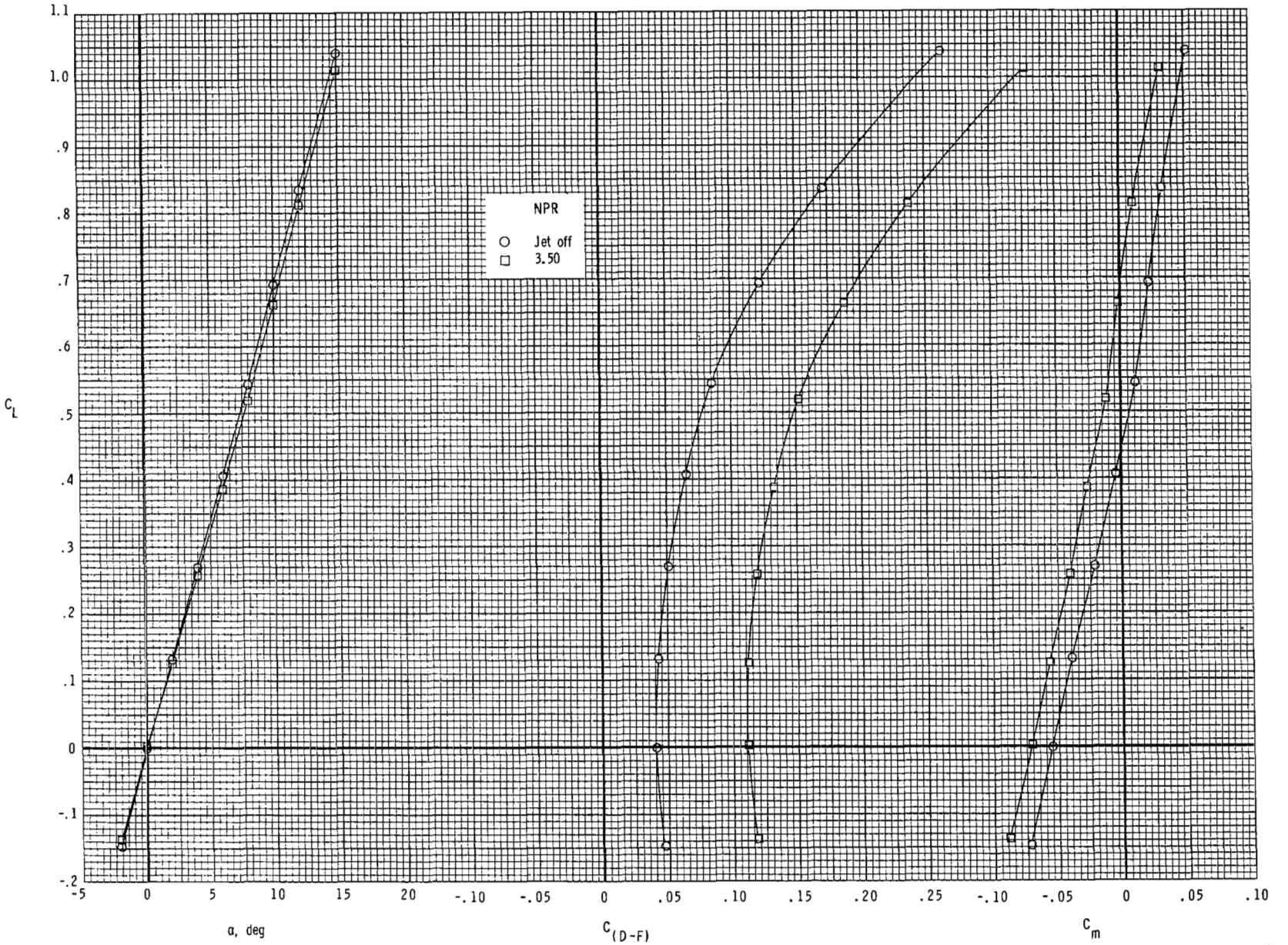

(a) M = 0.60.

Figure 31.- Effect of fully deployed reversers (δ_{REV} = 130°) on drag-minus-thrust performance of configuration with dry-power 2-D C-D SSW nozzles and horizontal-tail deflection of 5° (L.E. up).

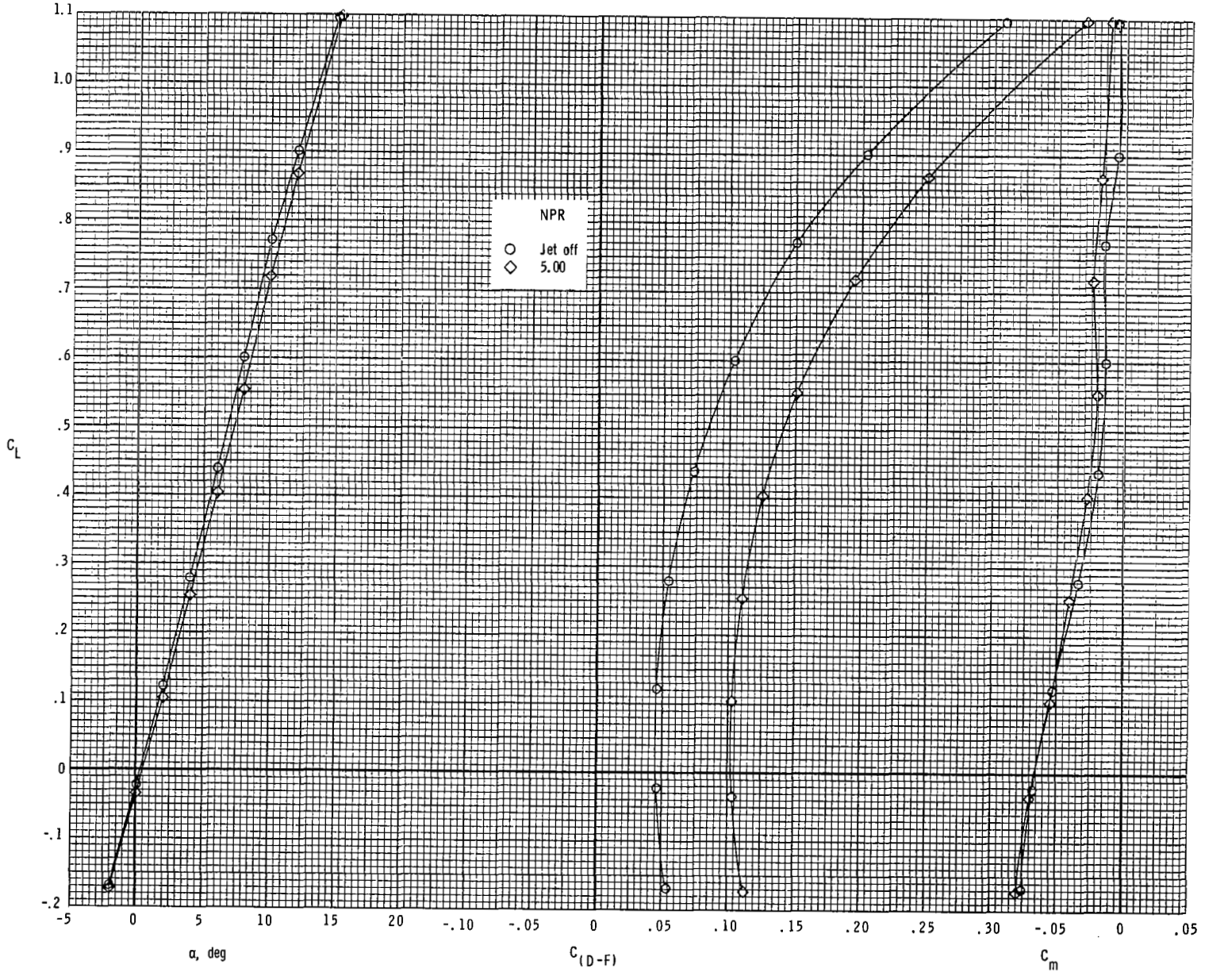

(b) M = 0.90.

Figure 31.- Concluded.

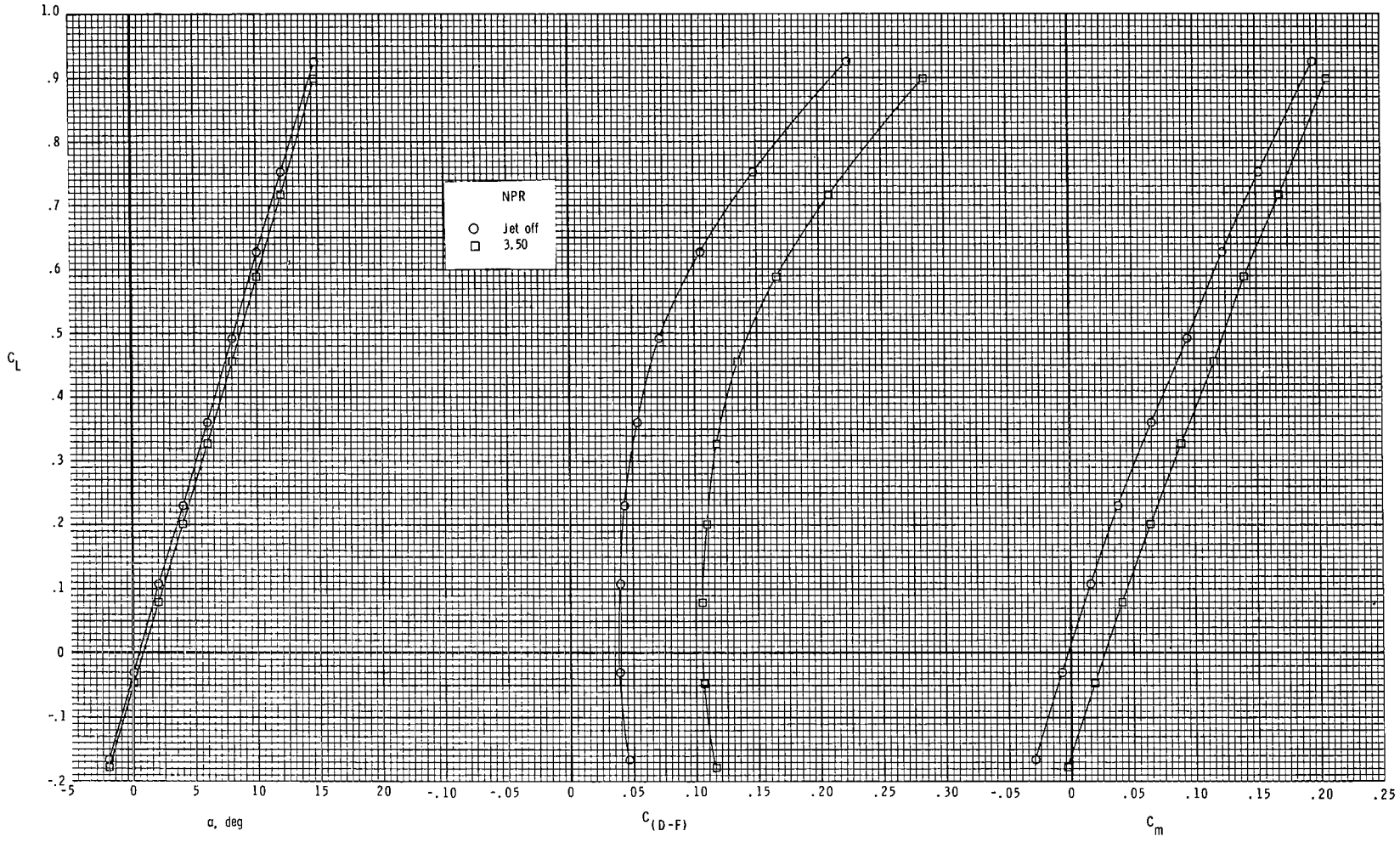

(a) M = 0.60.

Figure 32.- Effect of fully deployed reversers (δ_{REV} = 130°) on drag-minus-thrust performance of configuration with dry-power 2-D C-D SSW nozzles and horizontal tails off.

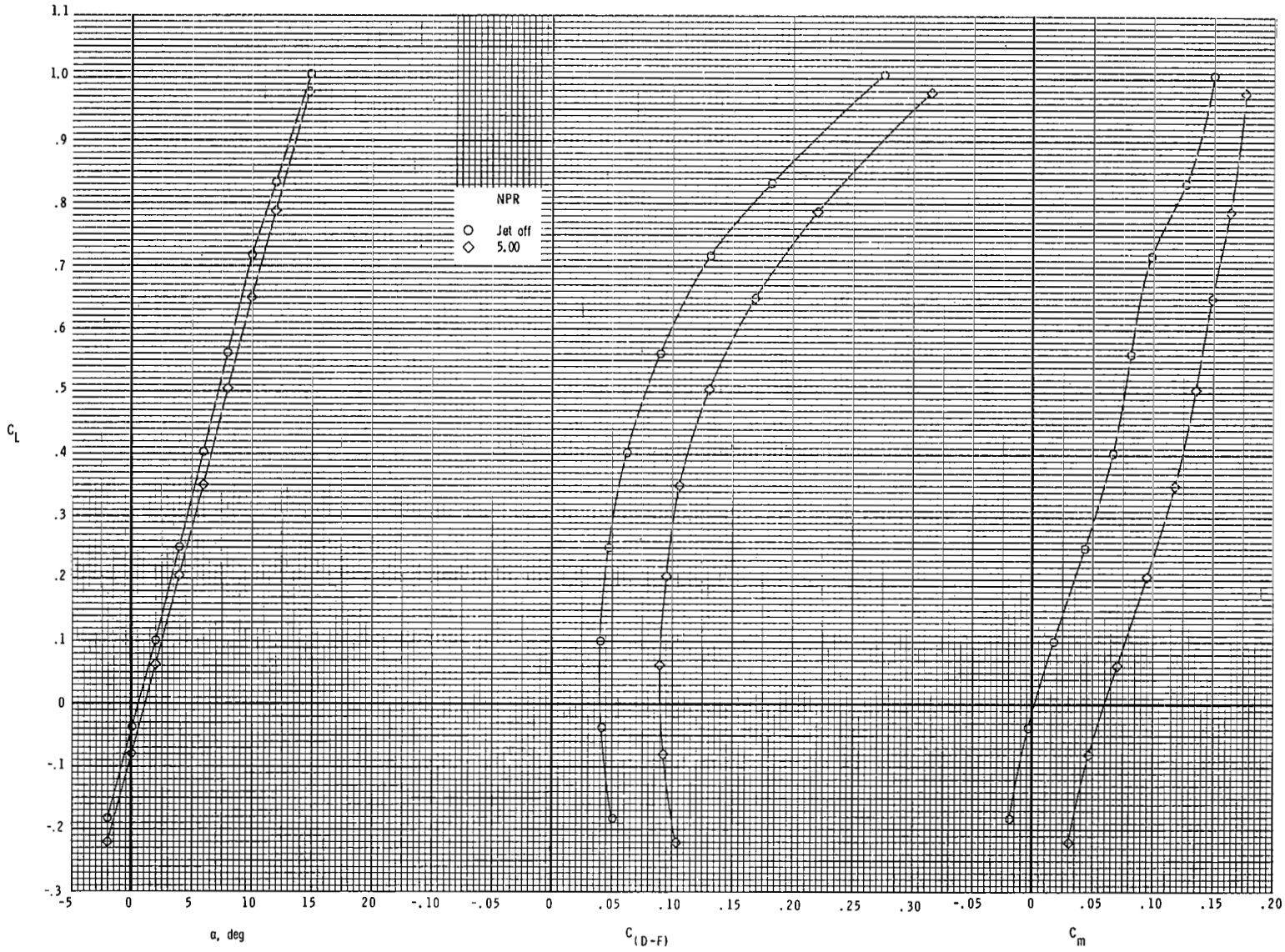

(b) M = 0.90.

Figure 32.- Continued.

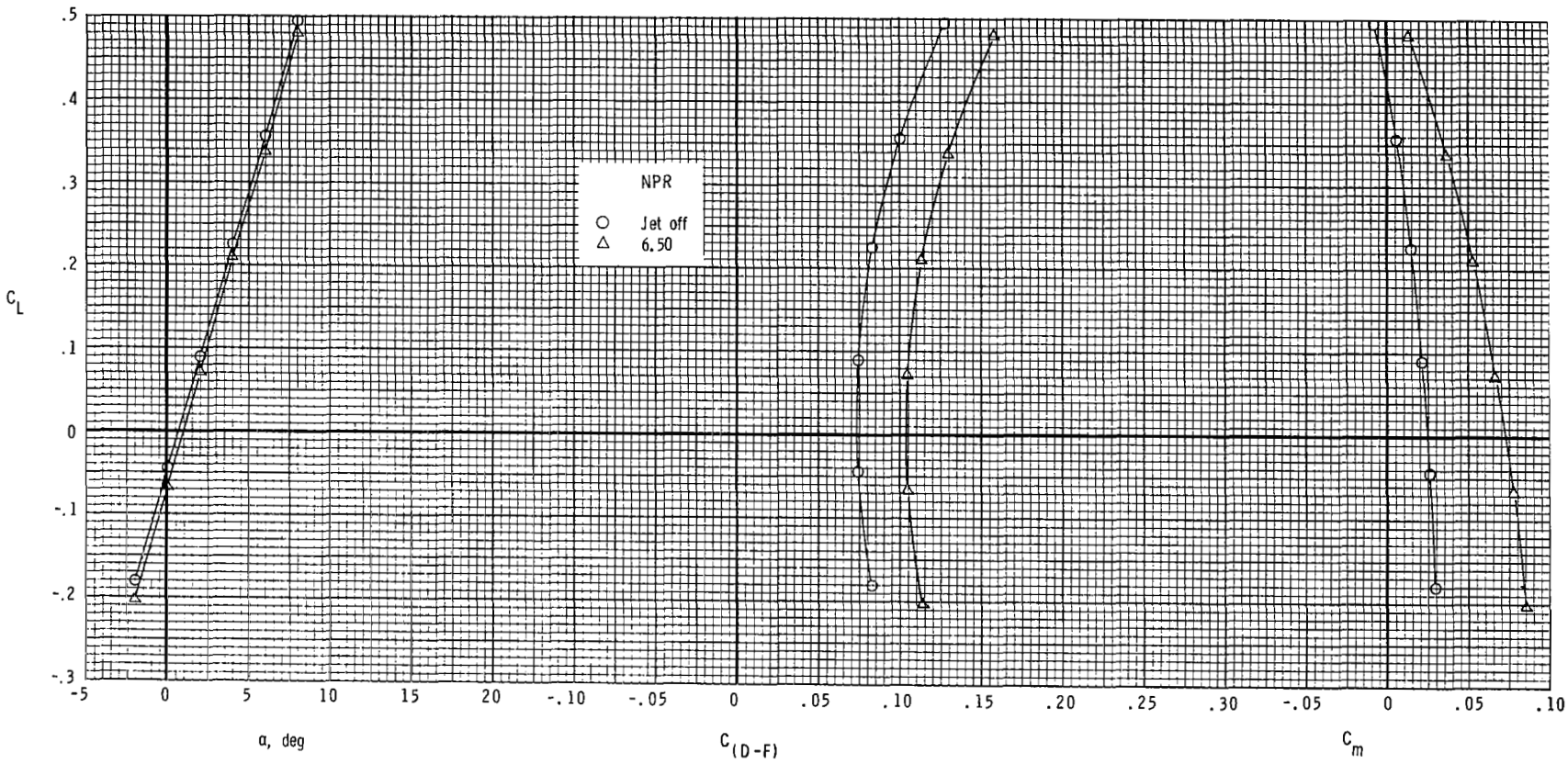

(c) M = 1.20.

Figure 32.- Concluded.

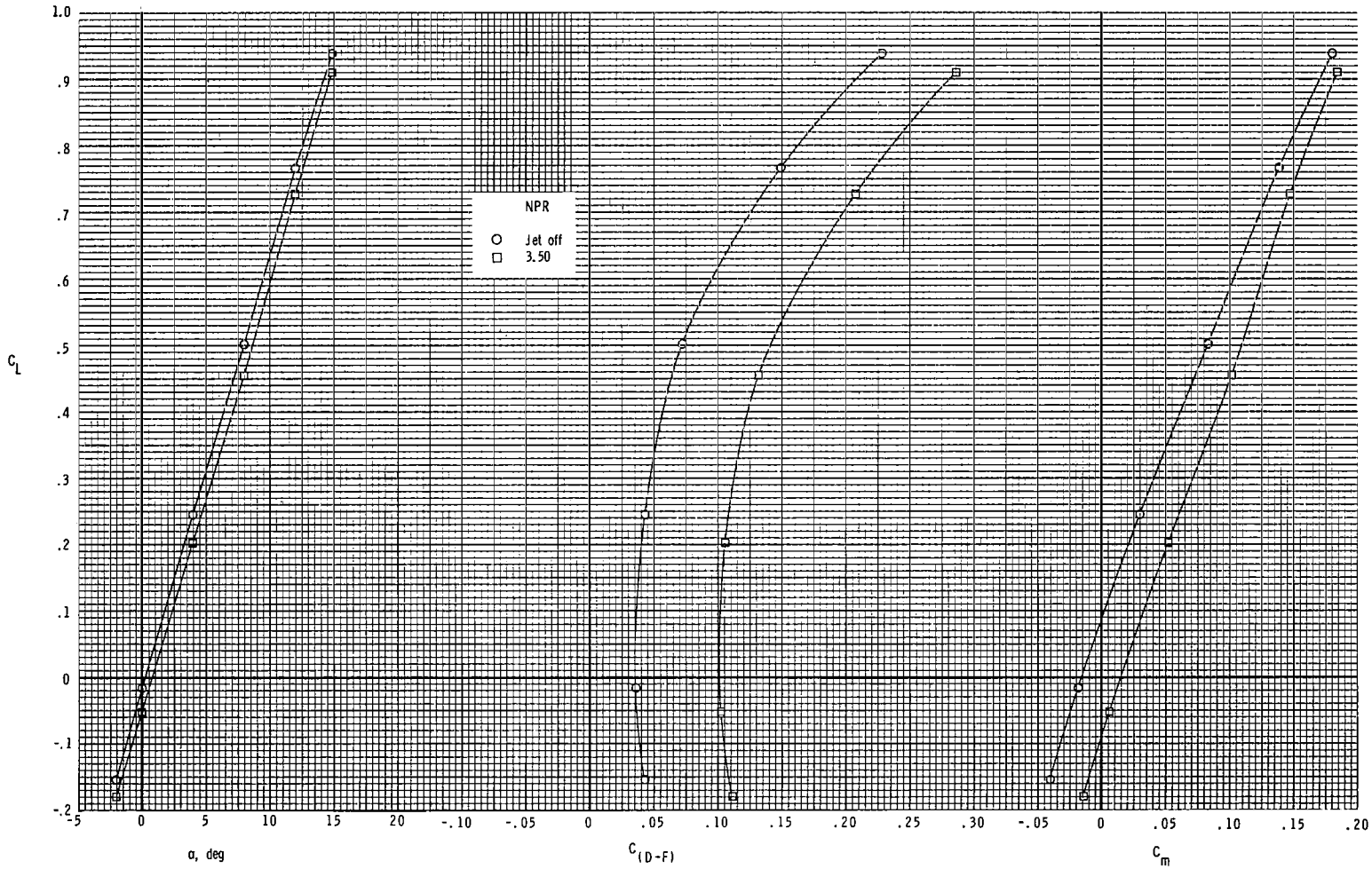

(a) M = 0.60.

Figure 33.- Effect of fully deployed reversers (δ_{REV} = 130°) on drag-minus-thrust performance of configuration with dry-power 2-D C-D SSW nozzles and vertical and horizontal tails off.

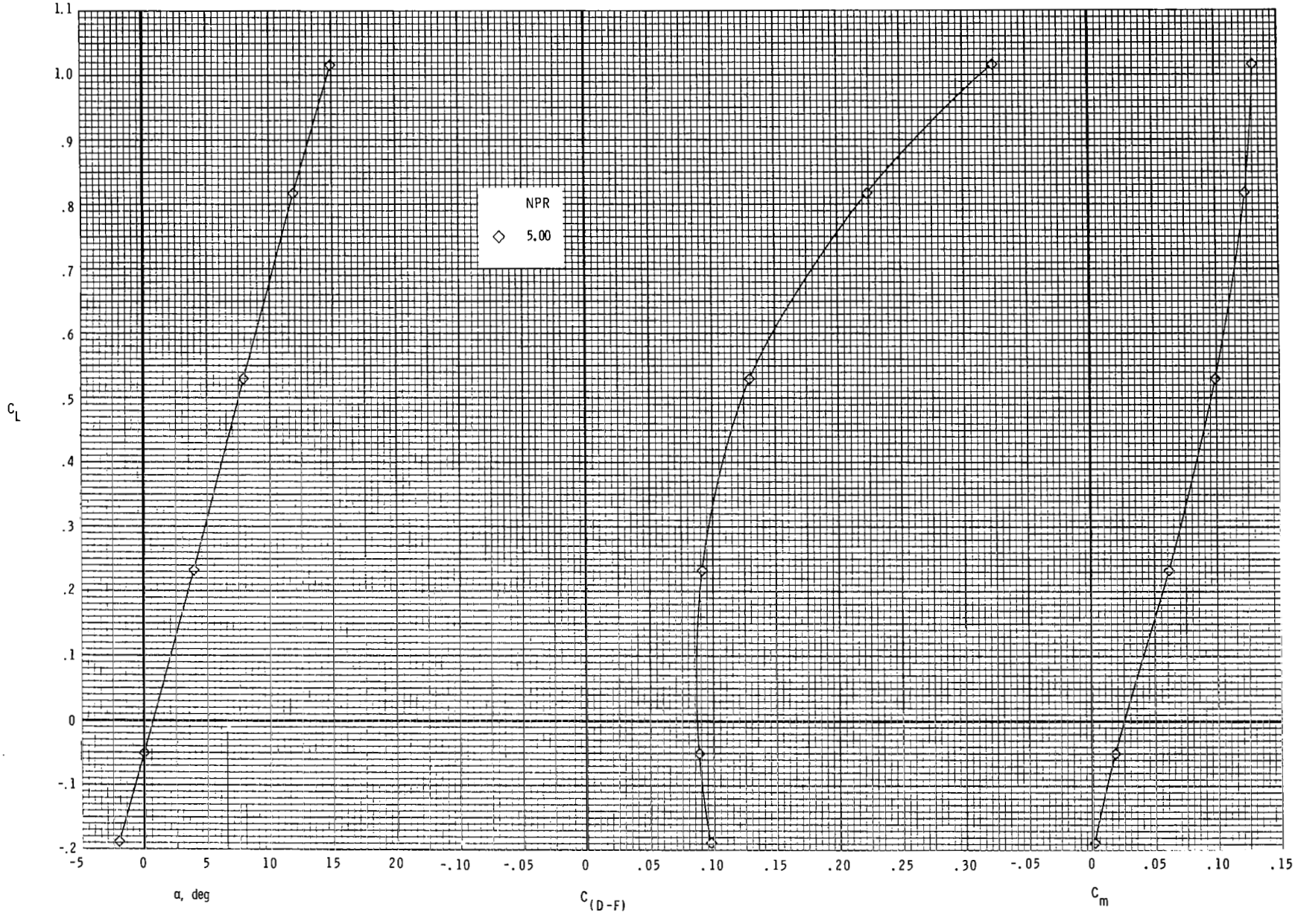

(b) M = 0.90.

Figure 33.- Concluded.

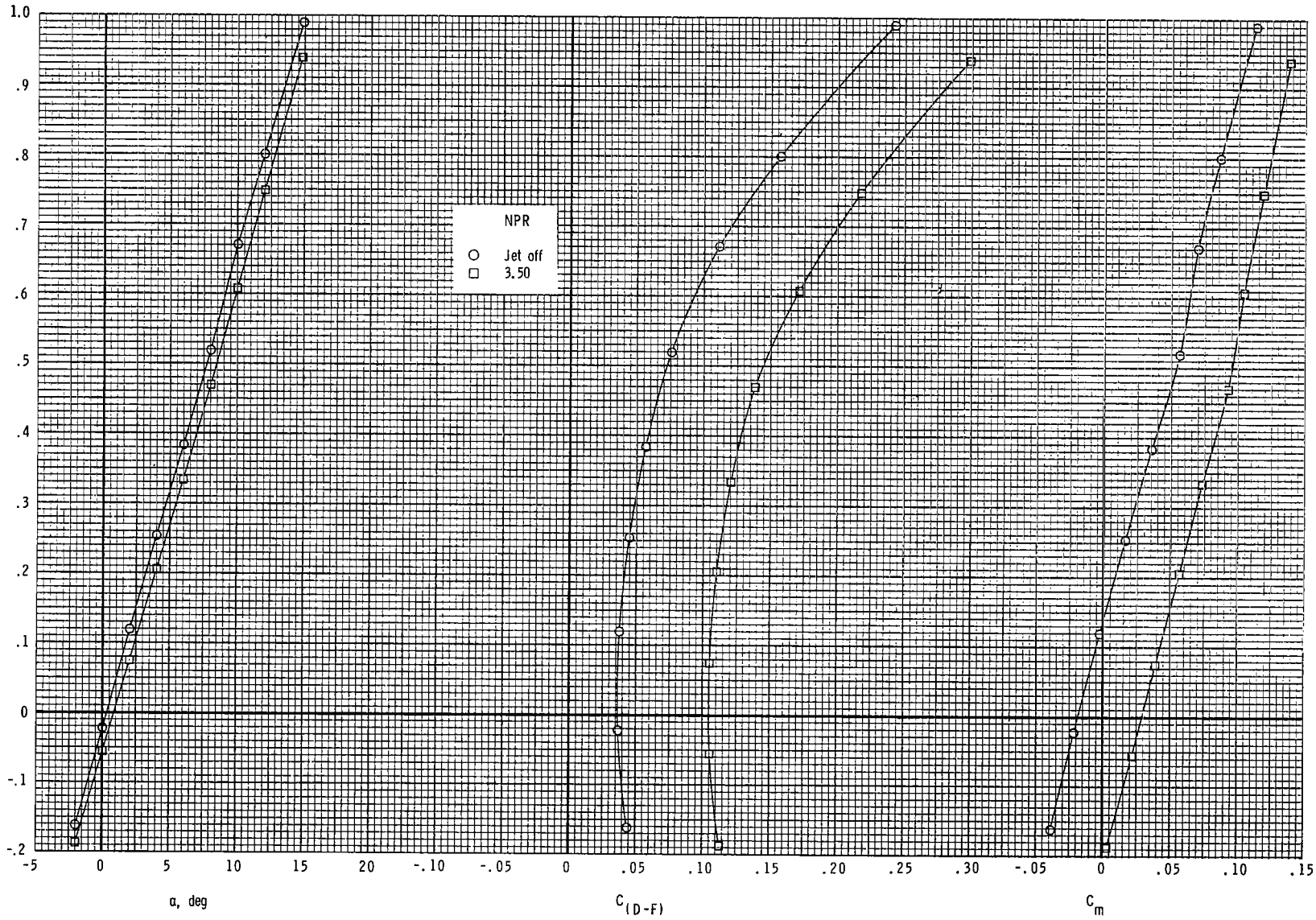

(a) M = 0.60.

Figure 34.- Effect of fully deployed reversers (δ_{REV} = 130°) on drag-minus-thrust performance of configuration with dry-power 2-D C-D SSW nozzles and vertical tails off.

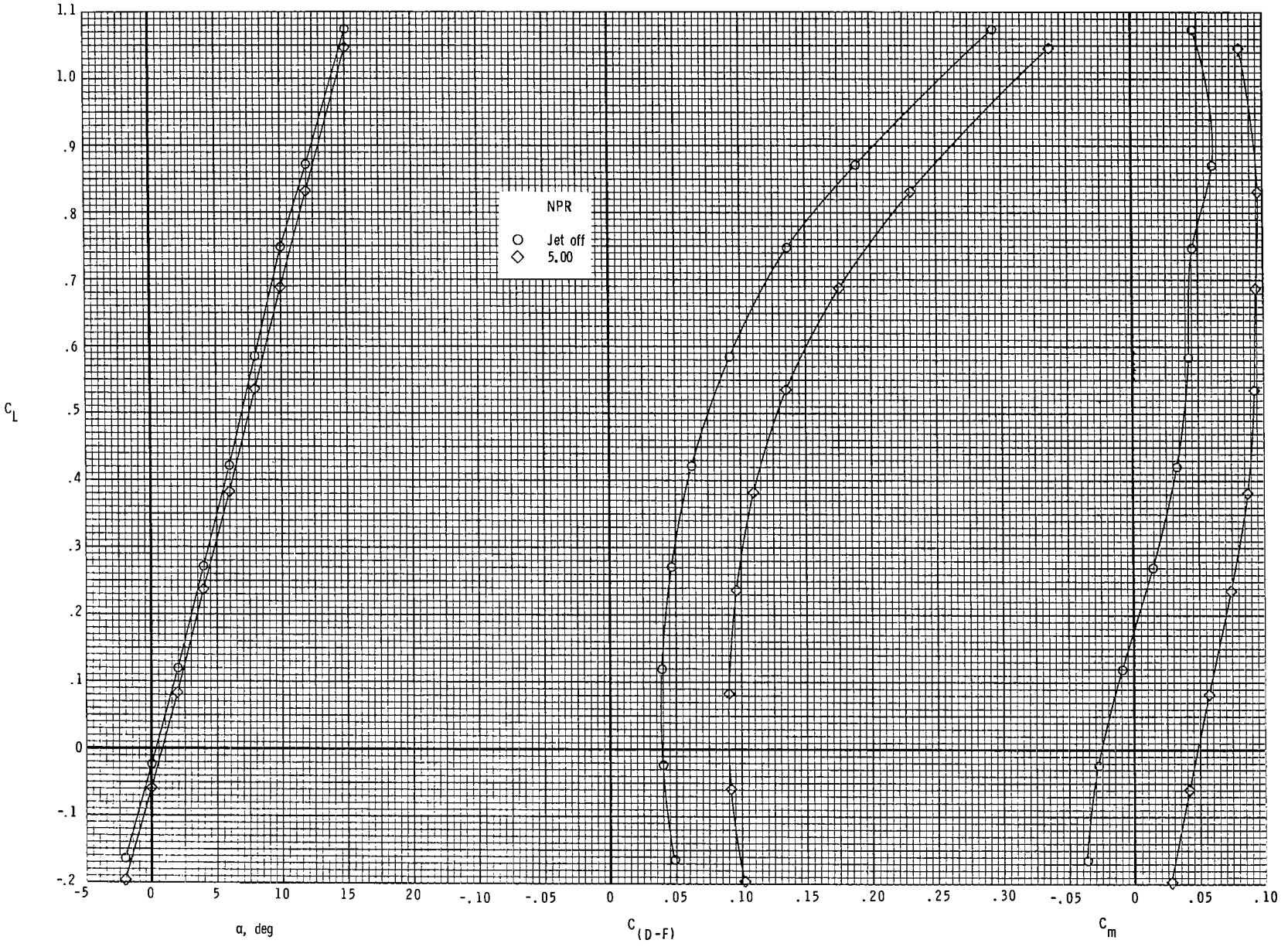

(b) M = 0.90.

Figure 34.- Concluded.

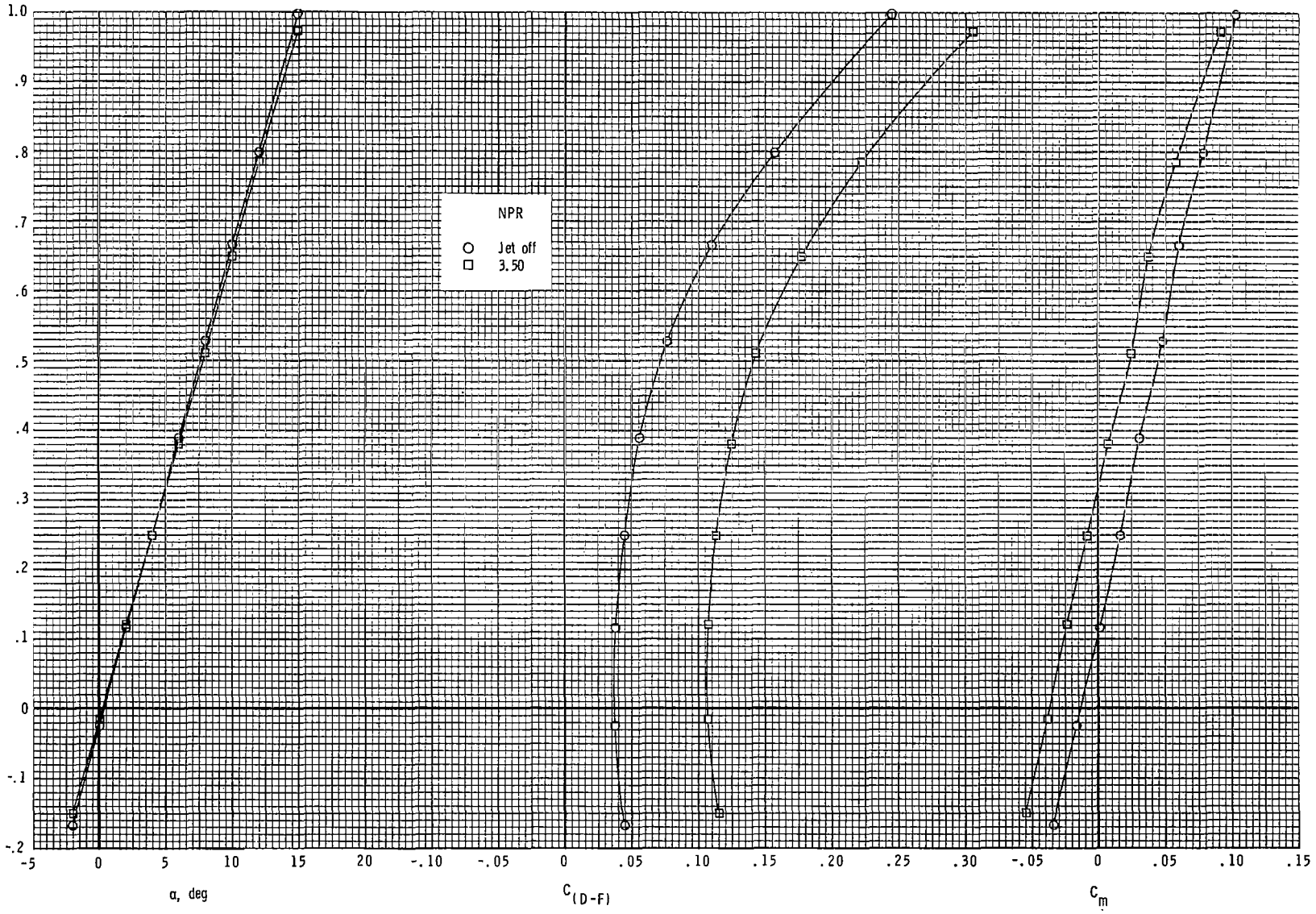

(a) M = 0.60.

Figure 35.- Effect of fully deployed reversers (δ_{REV} = 130°) on drag-minus-thrust performance of configuration with nacelle-mounted twin vertical tails, toe angle (L.E. out) of 2°, modified tail booms, and dry-power 2-D C-D SSW nozzles.

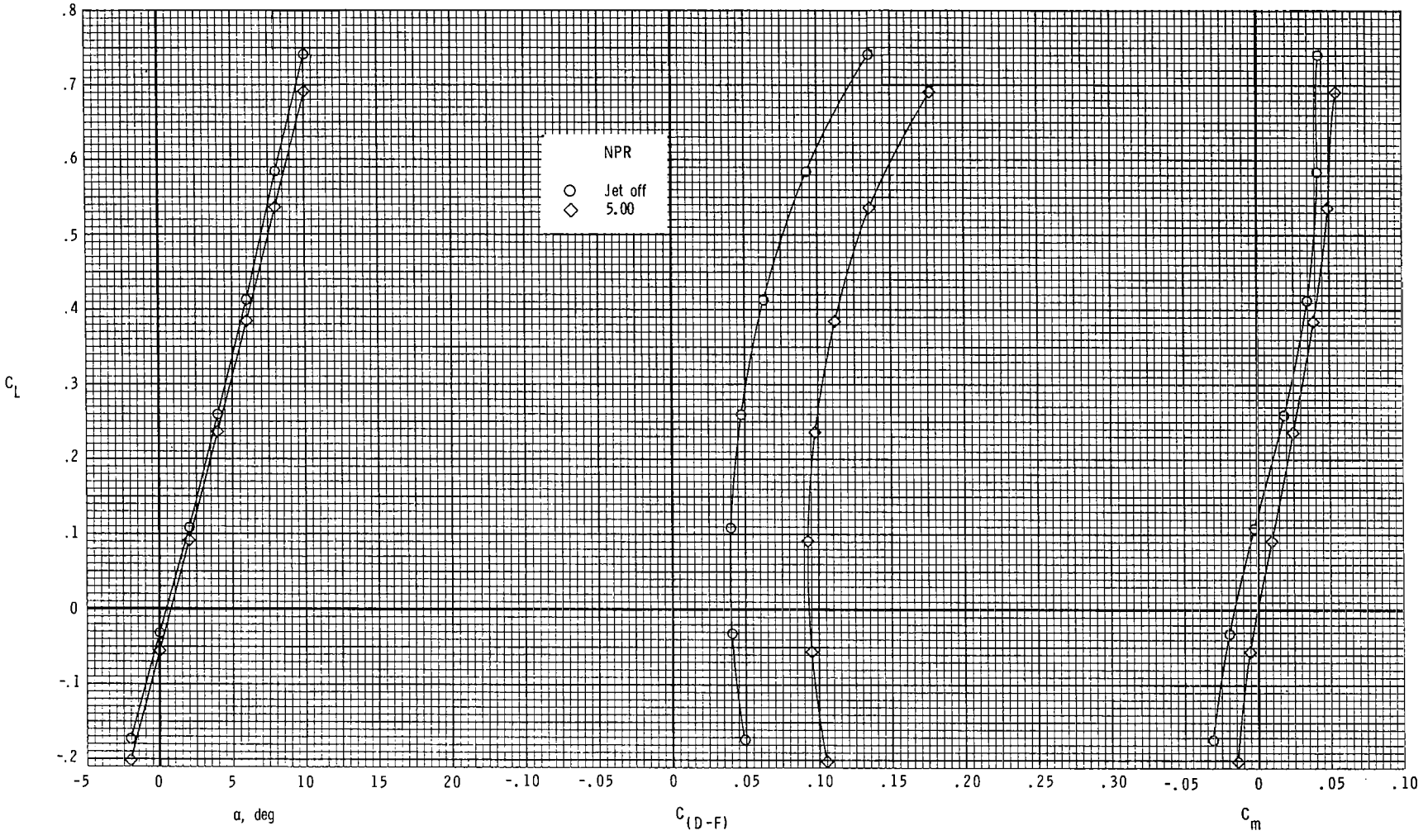

(b) M = 0.90.

Figure 35.- Concluded.

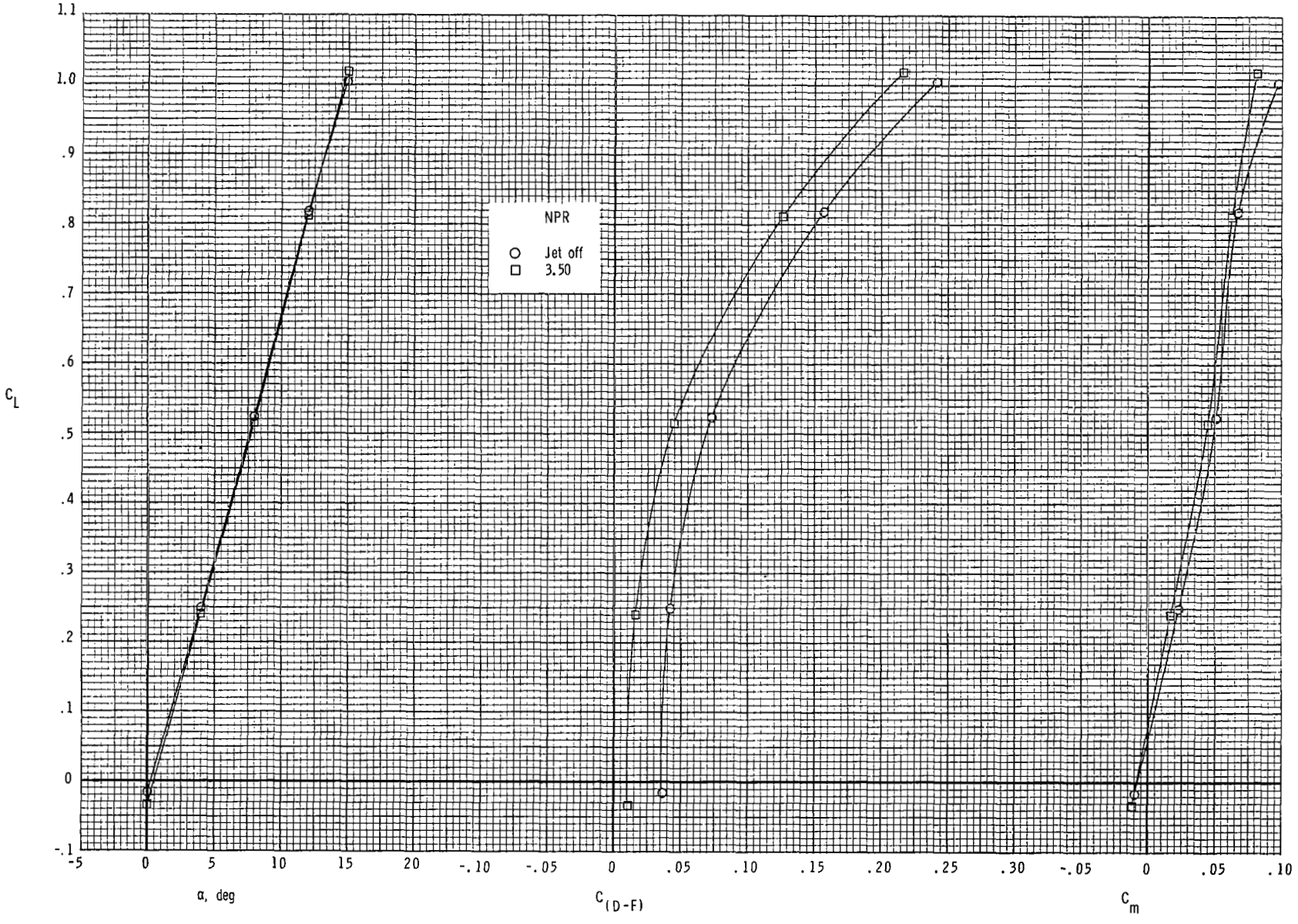

(a) M = 0.60.

Figure 36.- Effect of differential reversing (δ_{REV} = 0° for L.H. and δ_{REV} = 130° for R.H. nozzles) on drag-minus-thrust performance of configuration with dry-power 2-D C-D SSW nozzles.

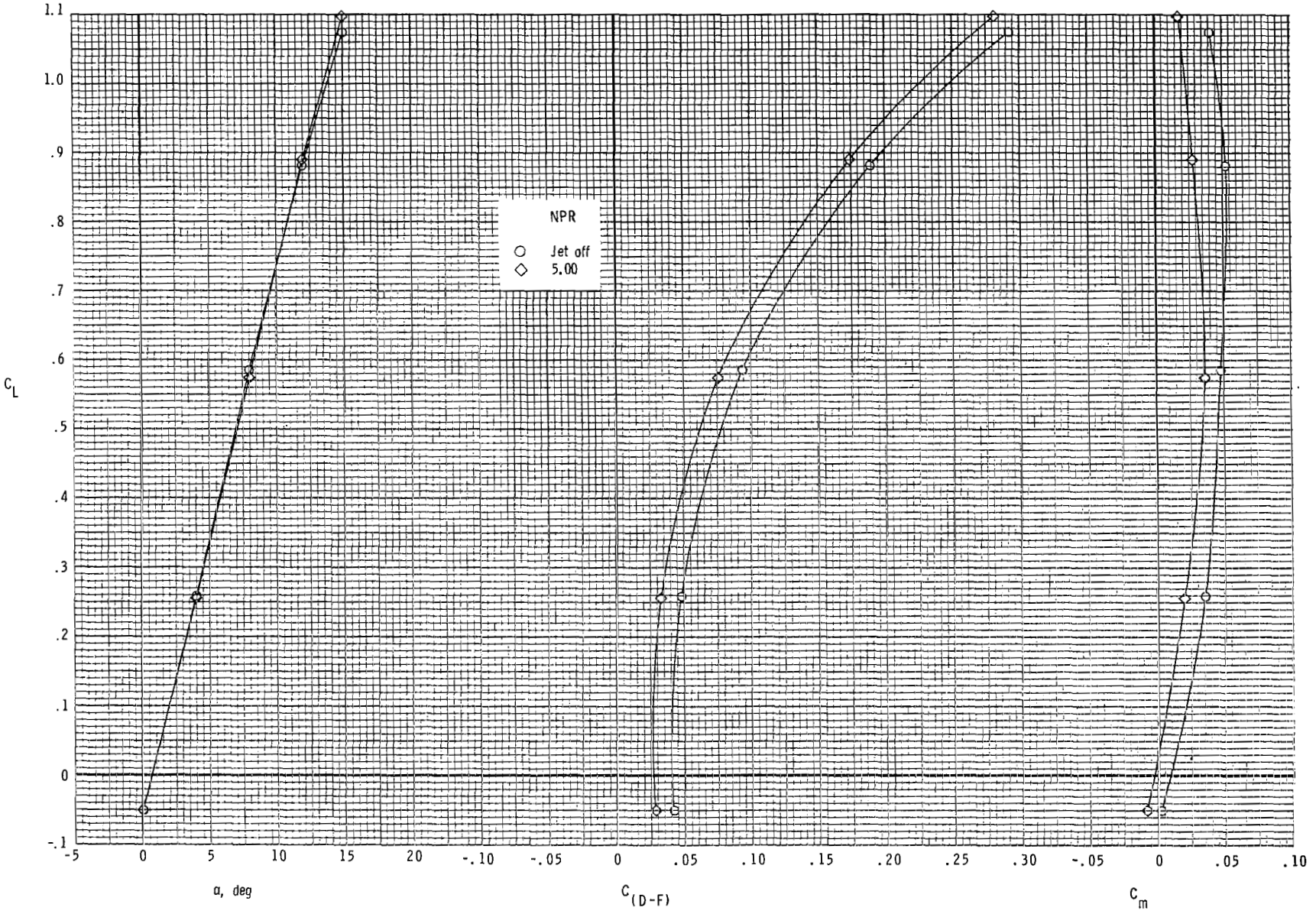

(b) M = 0.90.

Figure 36.- Concluded.

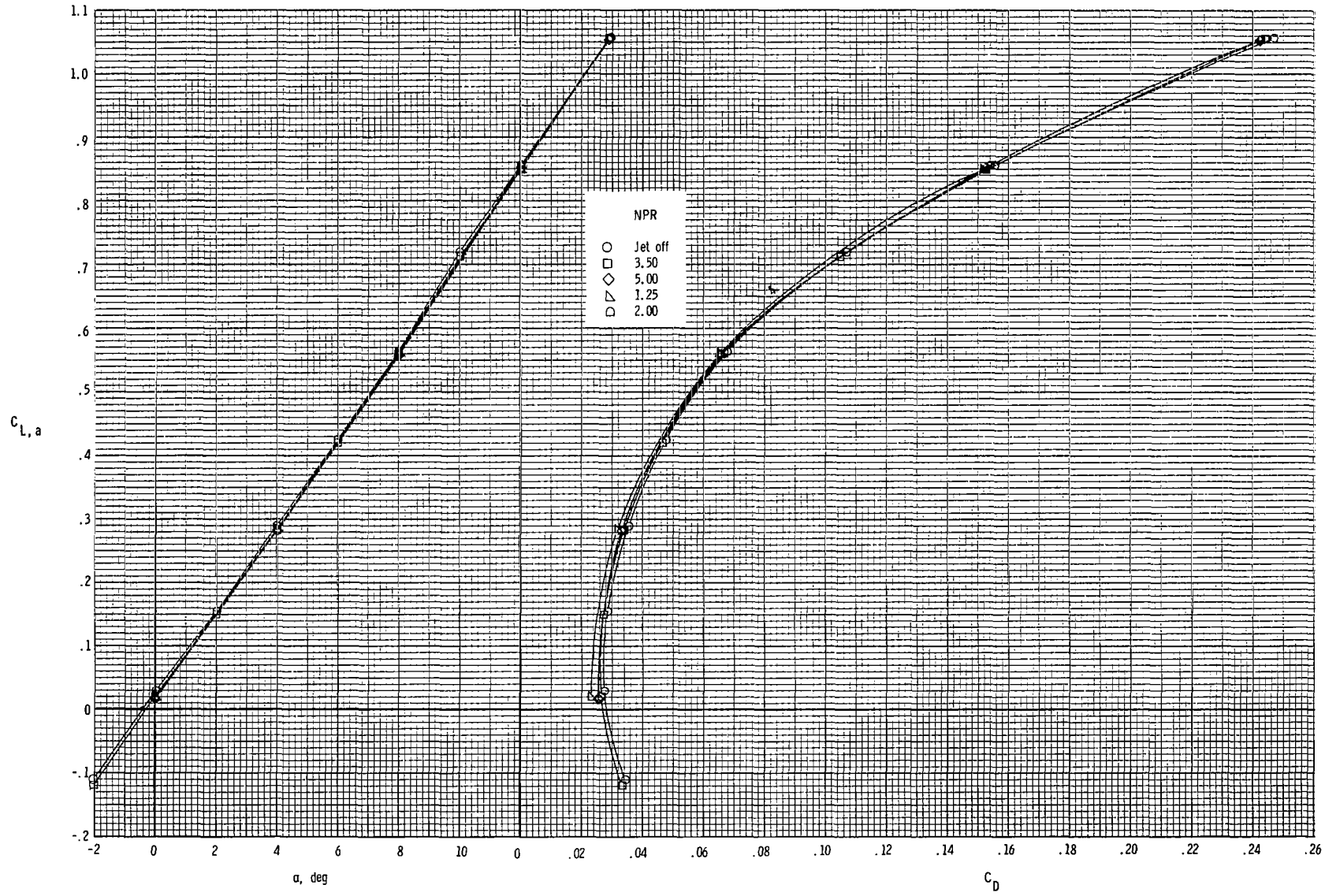

(a) M = 0.60.

Figure 37.- Thrust-removed longitudinal aerodynamic characteristics of baseline 0.047-scale three-surface F-15 configuration with dry-power axisymmetric nozzles.

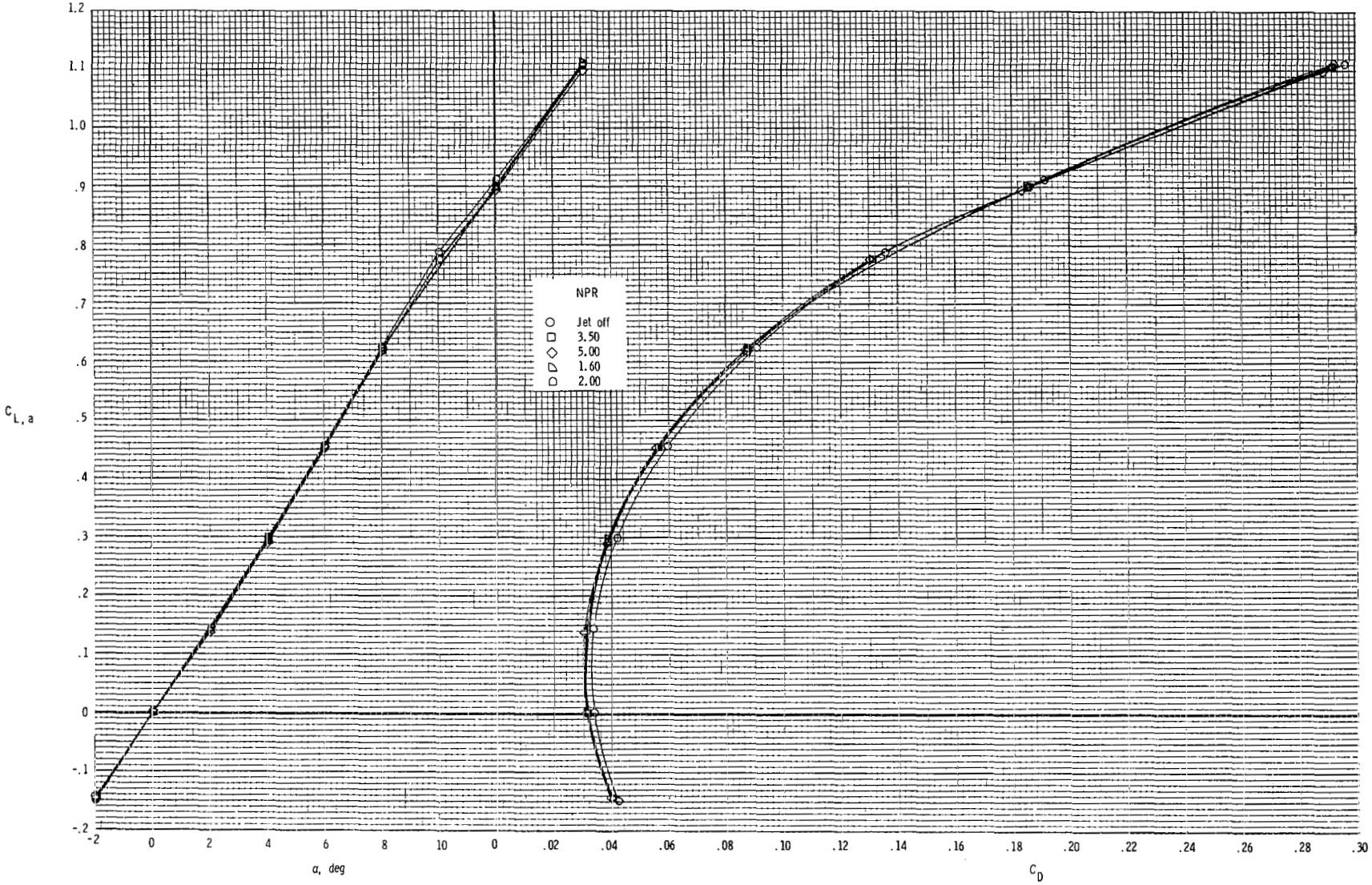

(b) M = 0.90.

Figure 37.- Continued.

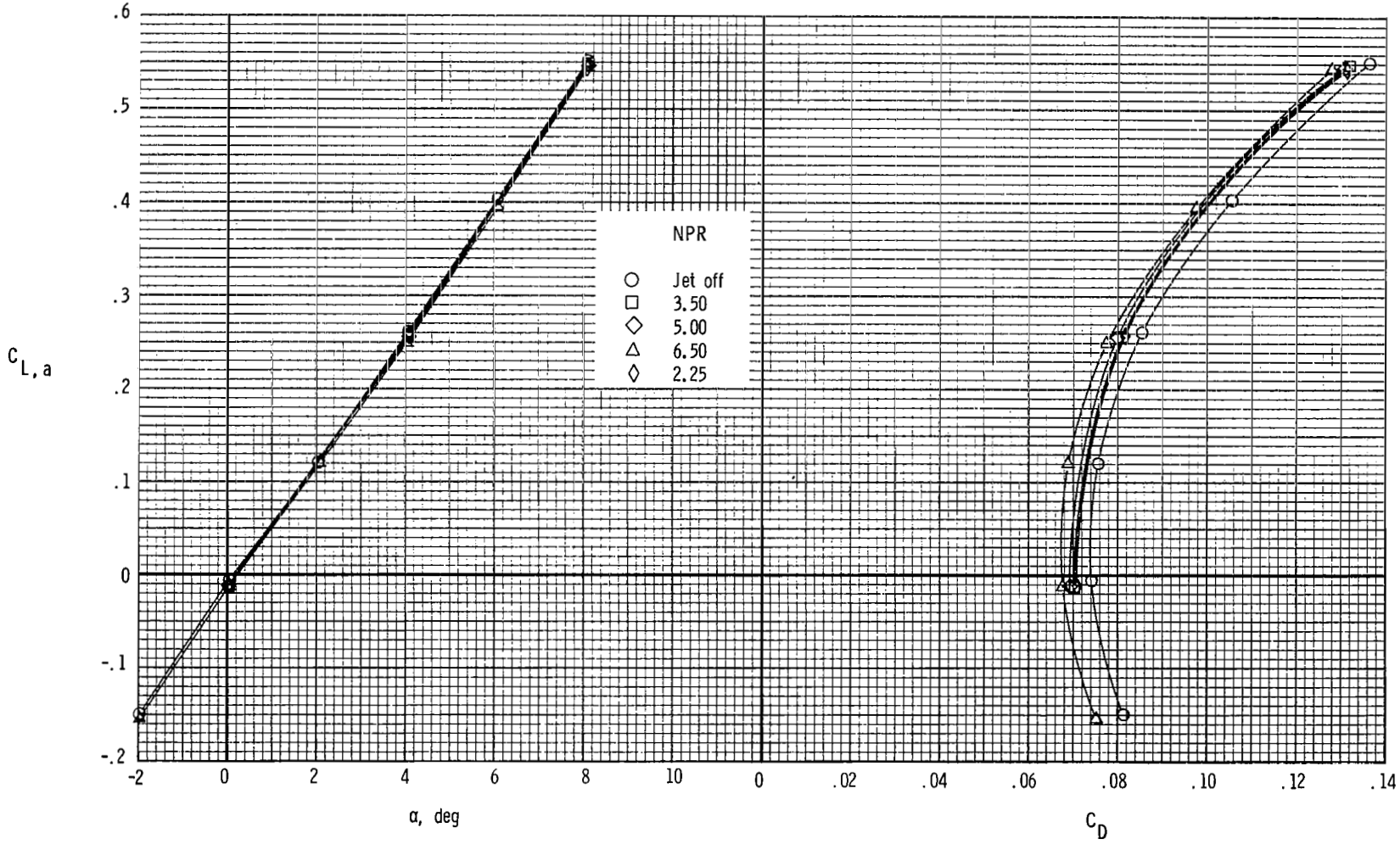

(c) M = 1.20.

Figure 37.- Concluded.

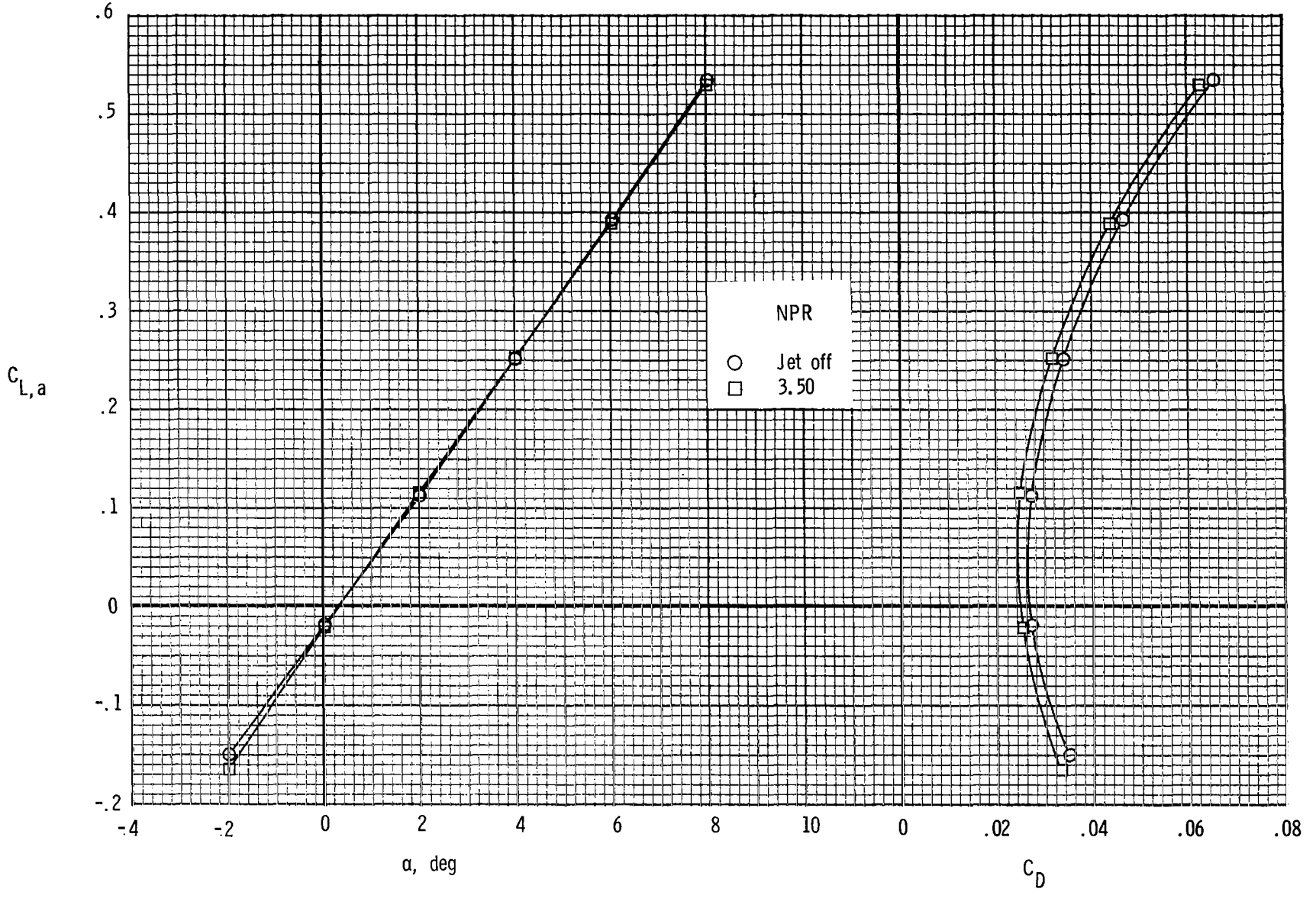

(a) M = 0.60.

Figure 38.- Thrust-removed longitudinal aerodynamic characteristics of baseline configuration with maximum-afterburning-power nozzles.

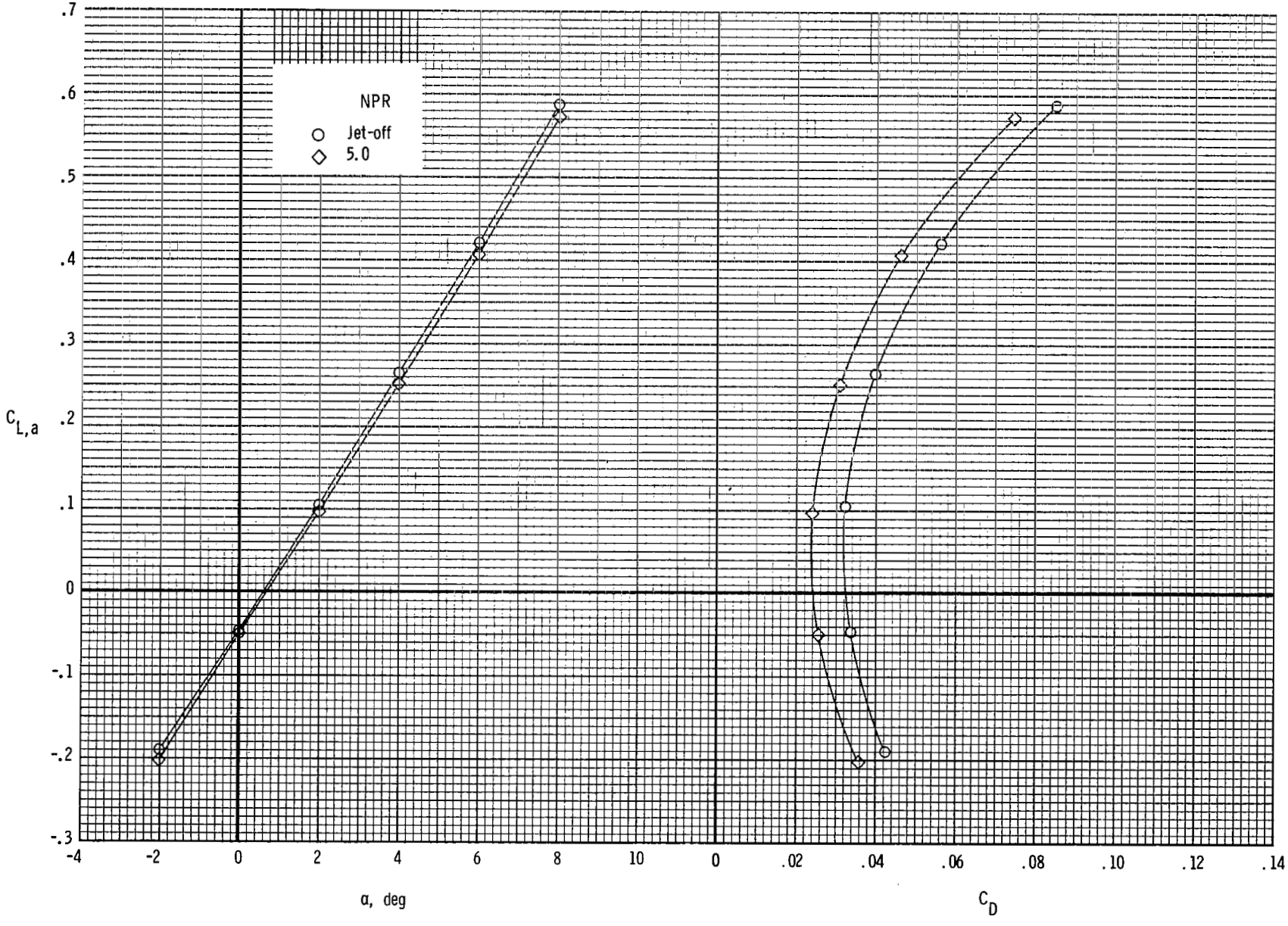

(b) M = 0.90.

Figure 38.- Concluded.

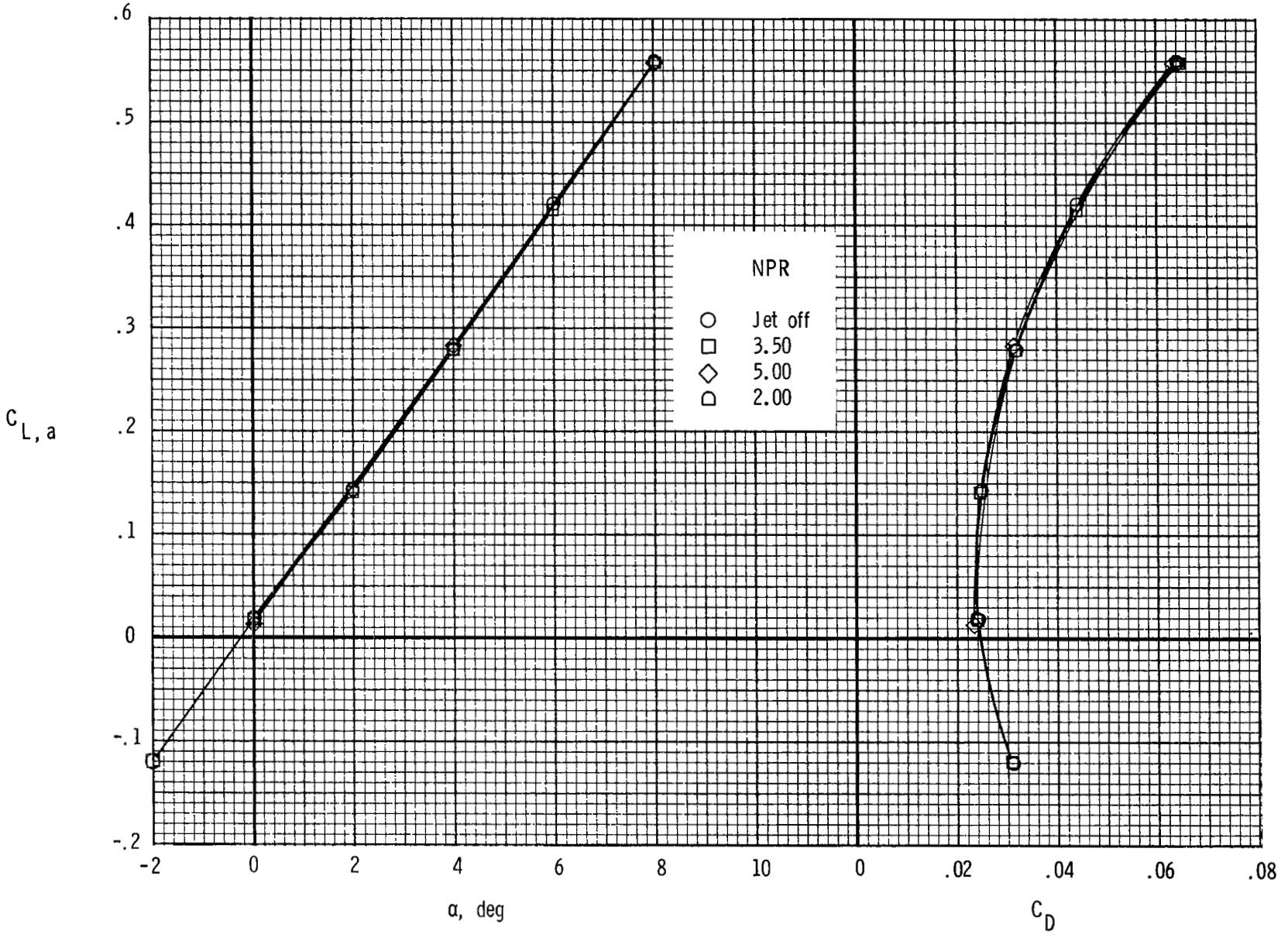

(a) M = 0.60.

Figure 39.- Thrust-removed longitudinal aerodynamic characteristics of configuration with nacelle-mounted twin vertical tails, toe angle (L.E. out) of 2°, modified tail booms, and dry-power axisymmetric nozzles.

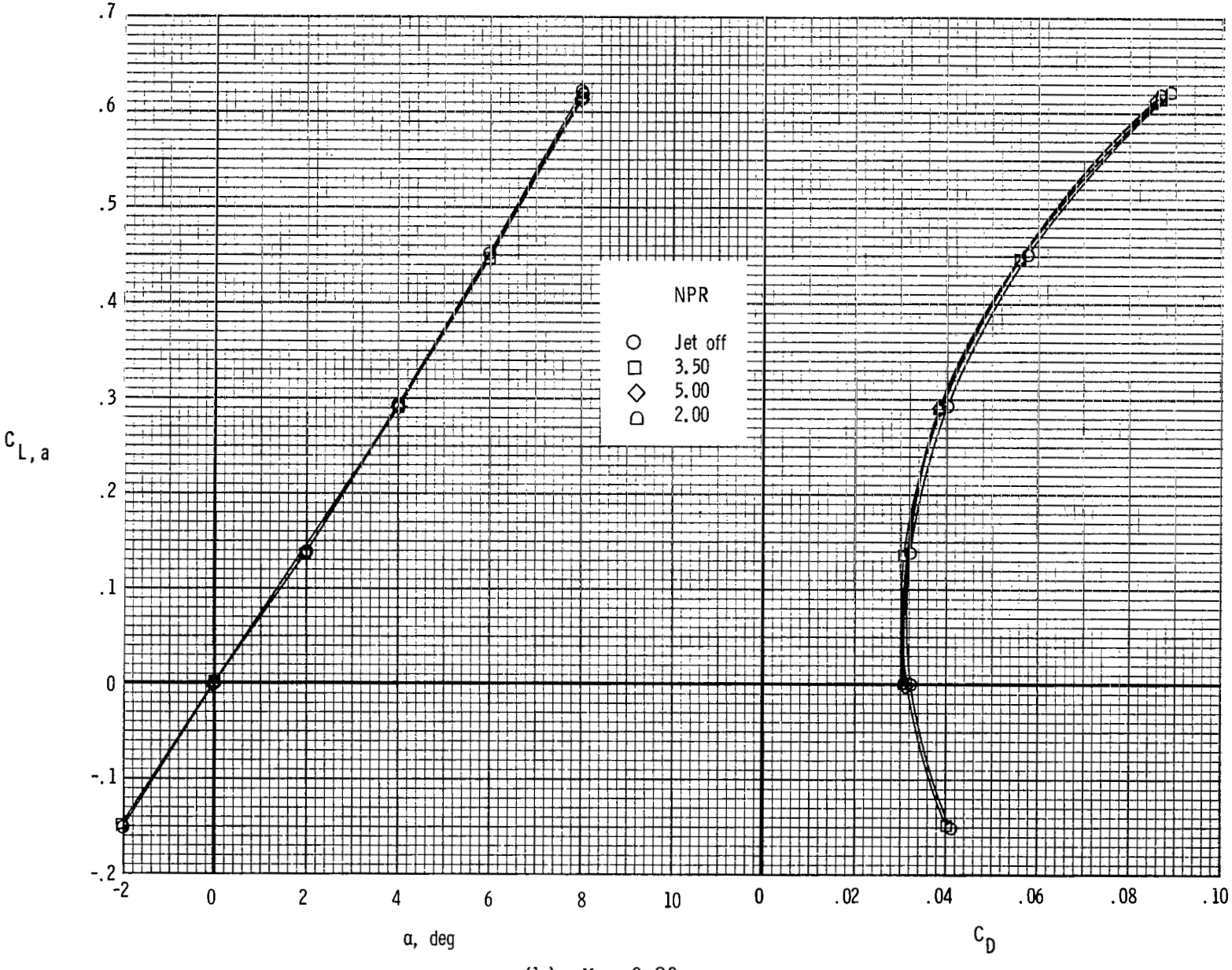

(b) M = 0.90.

Figure 39.- Concluded.

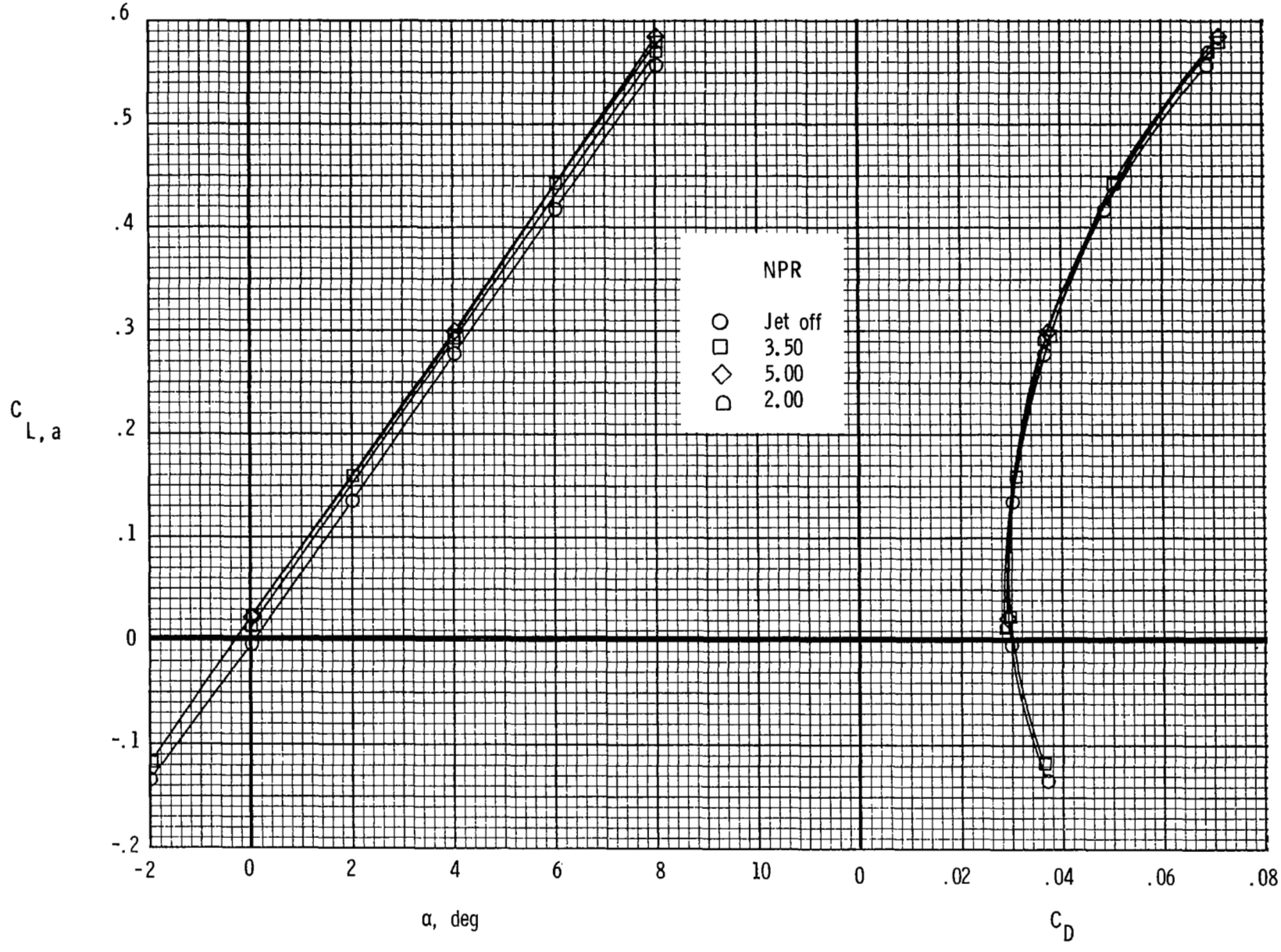

(a) M = 0.60.

Figure 40.- Thrust-removed longitudinal aerodynamic characteristics of configuration with 2-D C-D dry-power nozzles and divergent sidewalls (DSW).

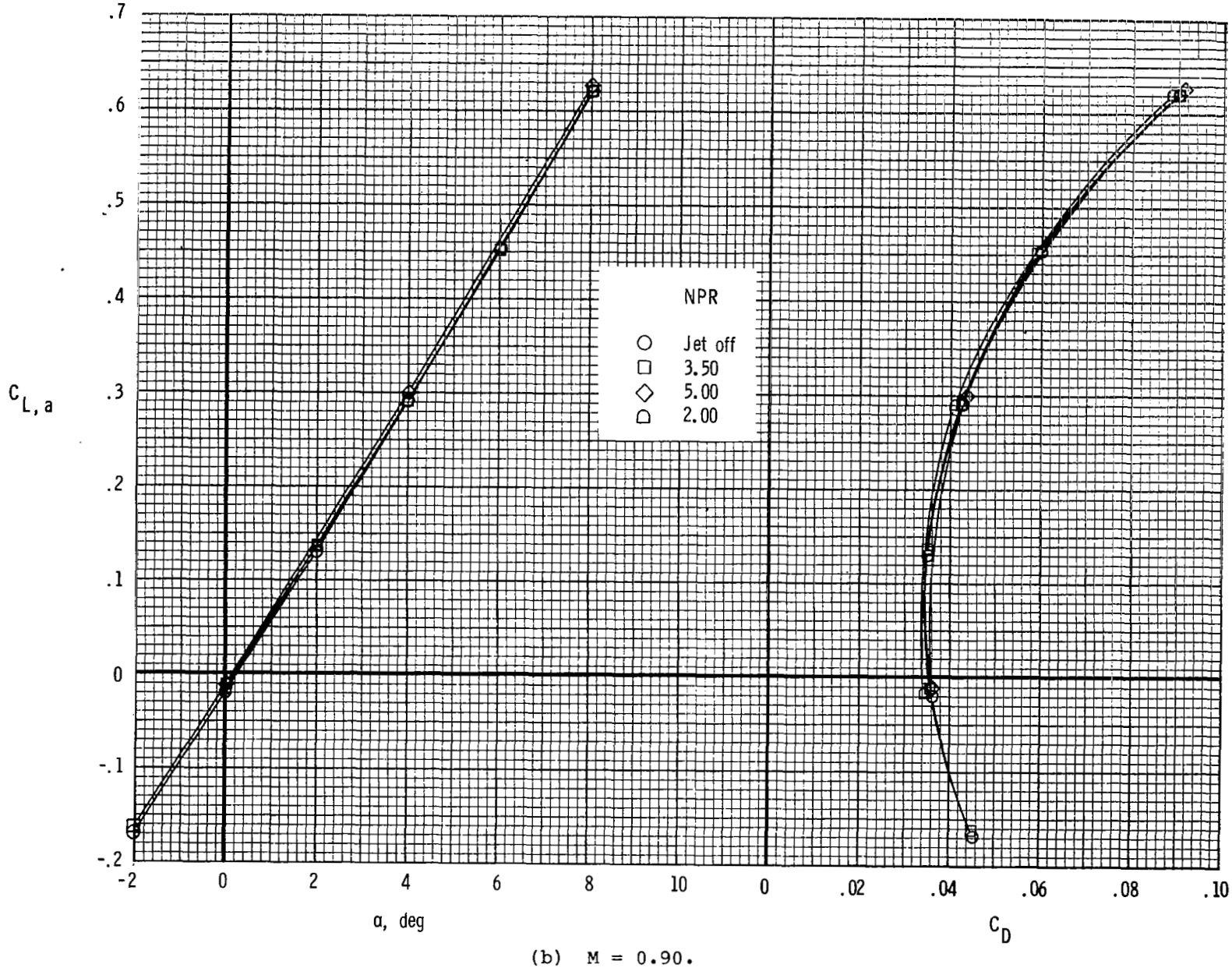

(b) M = 0.90.

Figure 40.- Concluded.

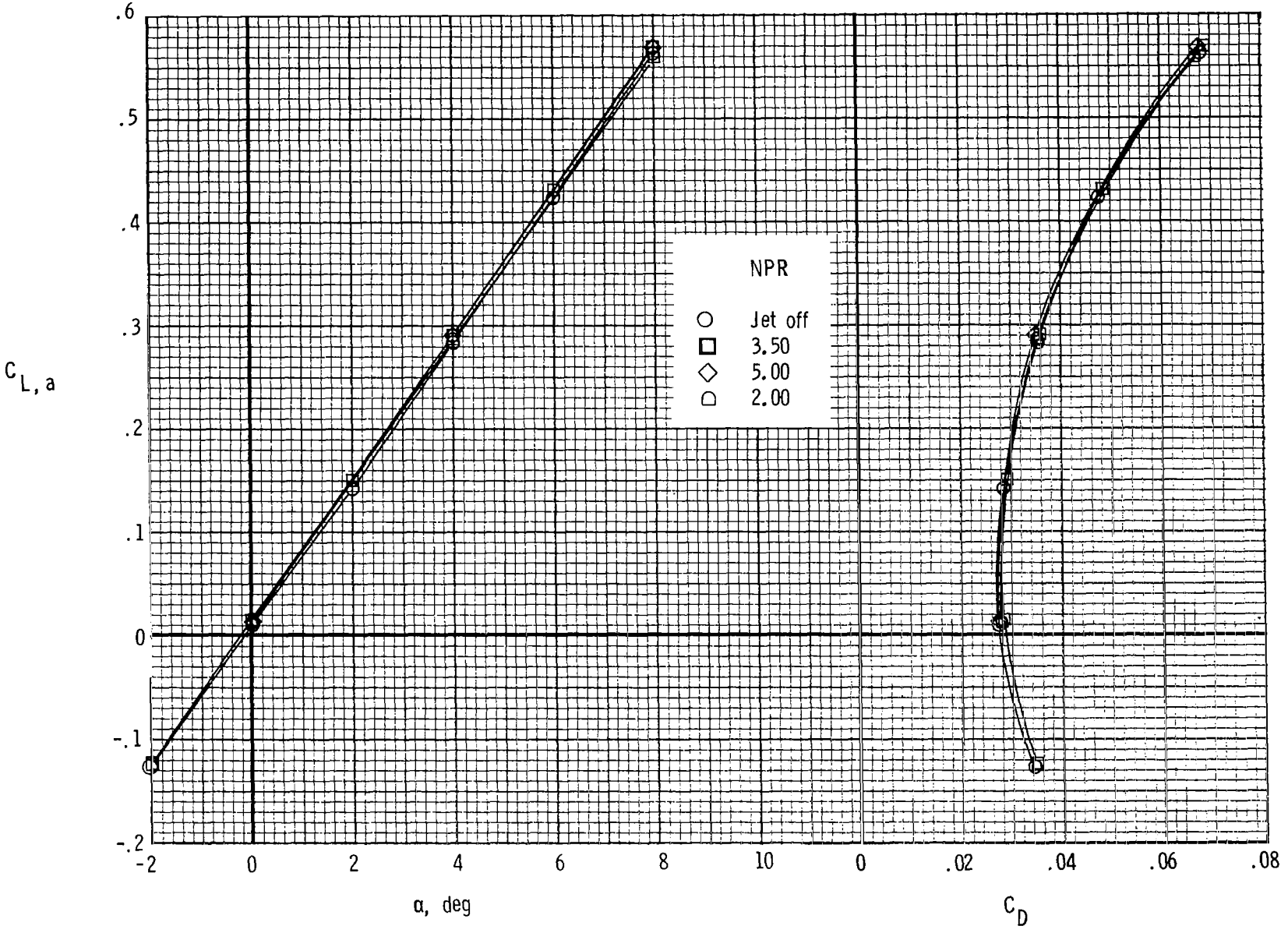

(a) M = 0.60.

Figure 41.- Thrust-removed longitudinal aerodynamic characteristics of configuration with 2-D C-D dry-power nozzles and variable sidewalls (VSW).

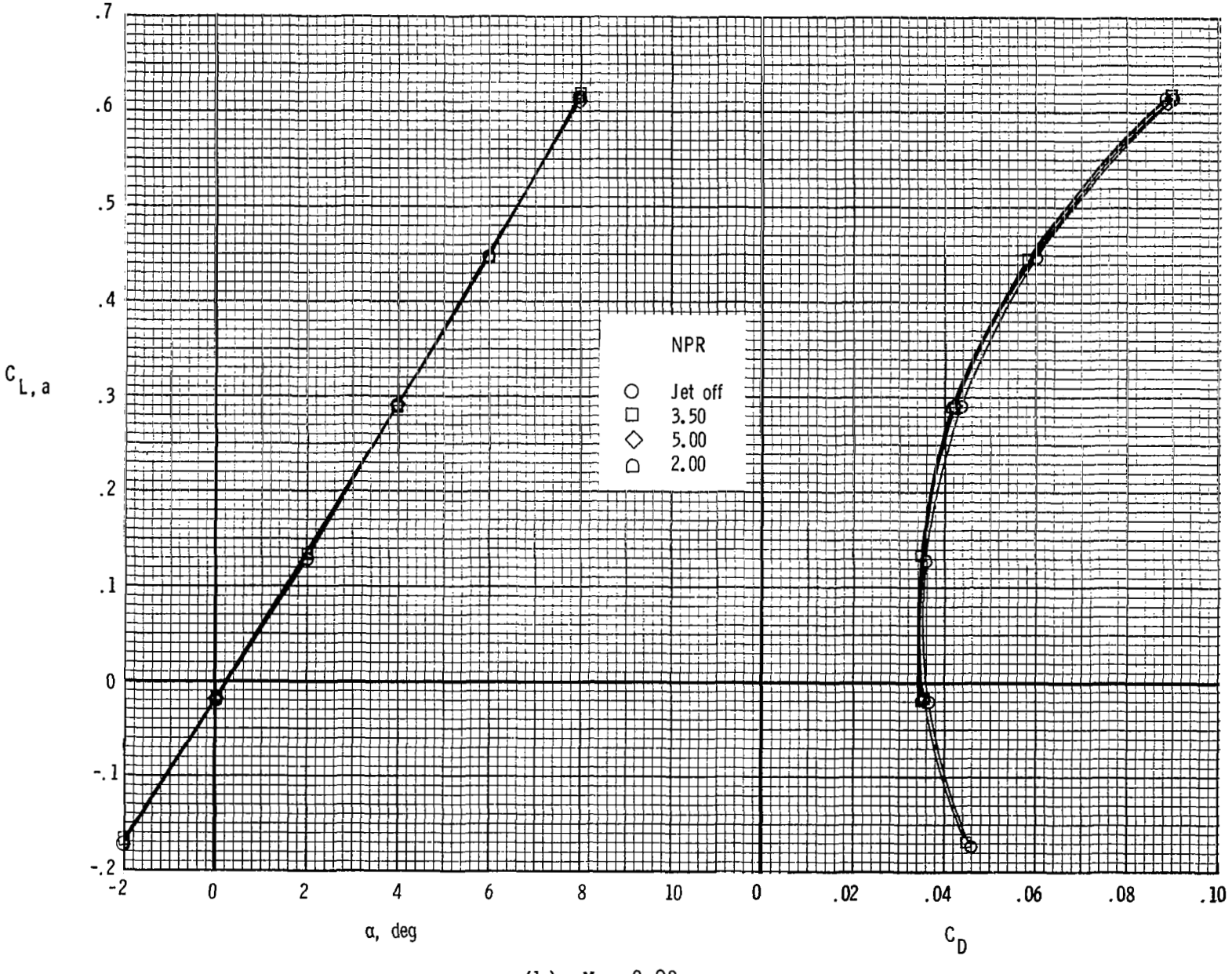

(b) M = 0.90.

Figure 41.- Concluded.

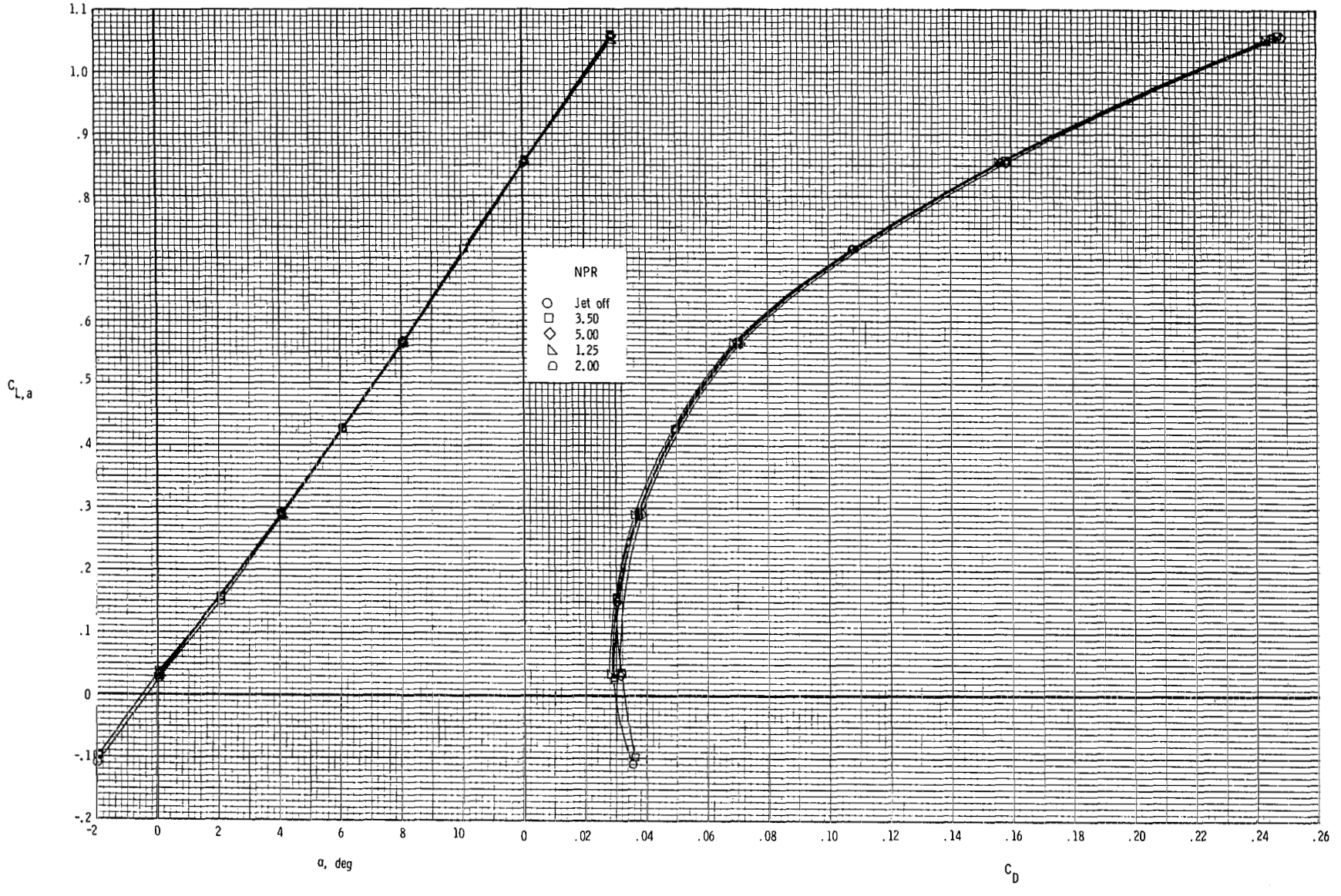

(a) M = 0.60.

Figure 42.- Thrust-removed longitudinal aerodynamic characteristics of configuration with 2-D C-D dry-power nozzles and fixed, straight sidewalls (SSW).

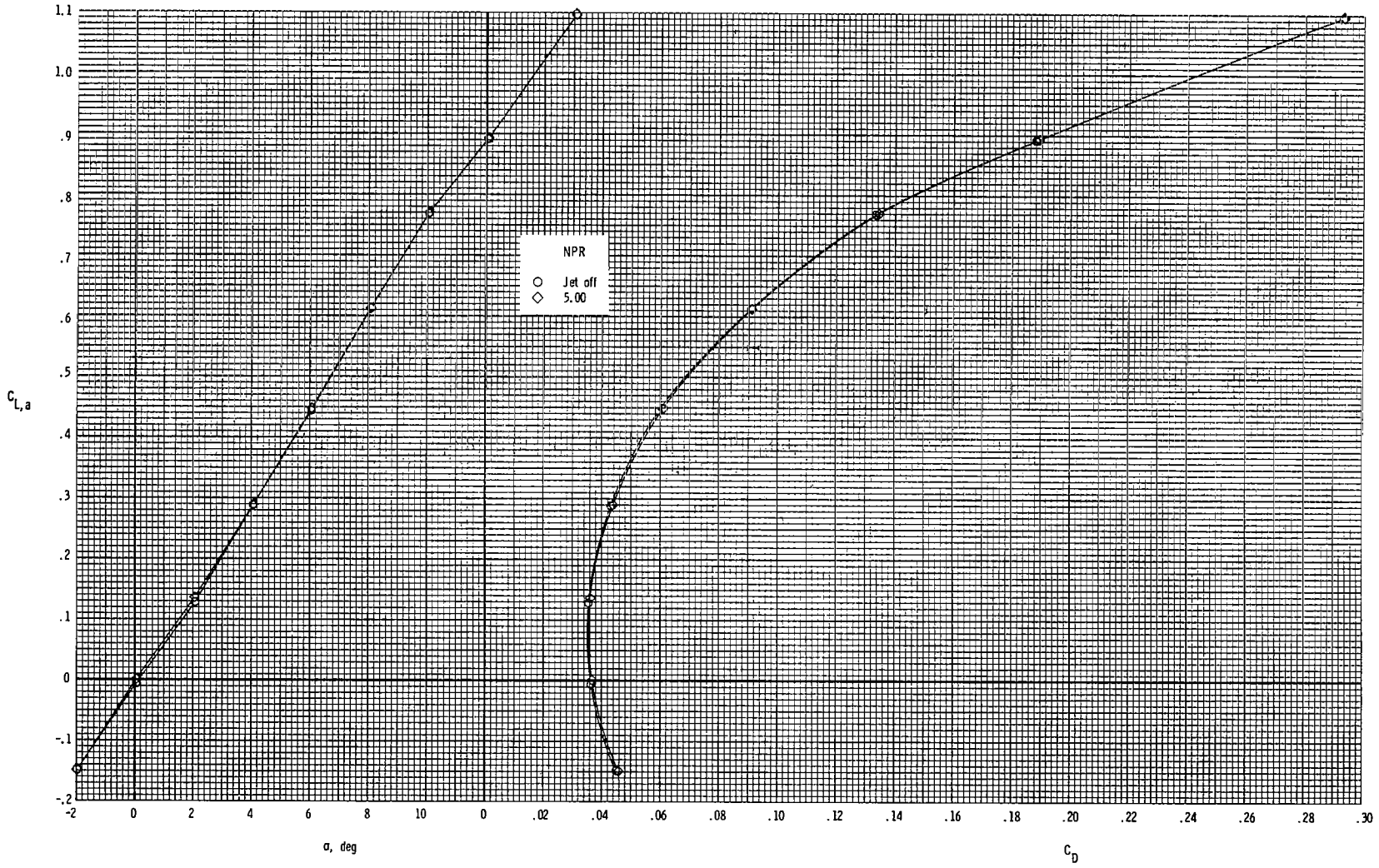

(b) M = 0.90.

Figure 42.- Continued.

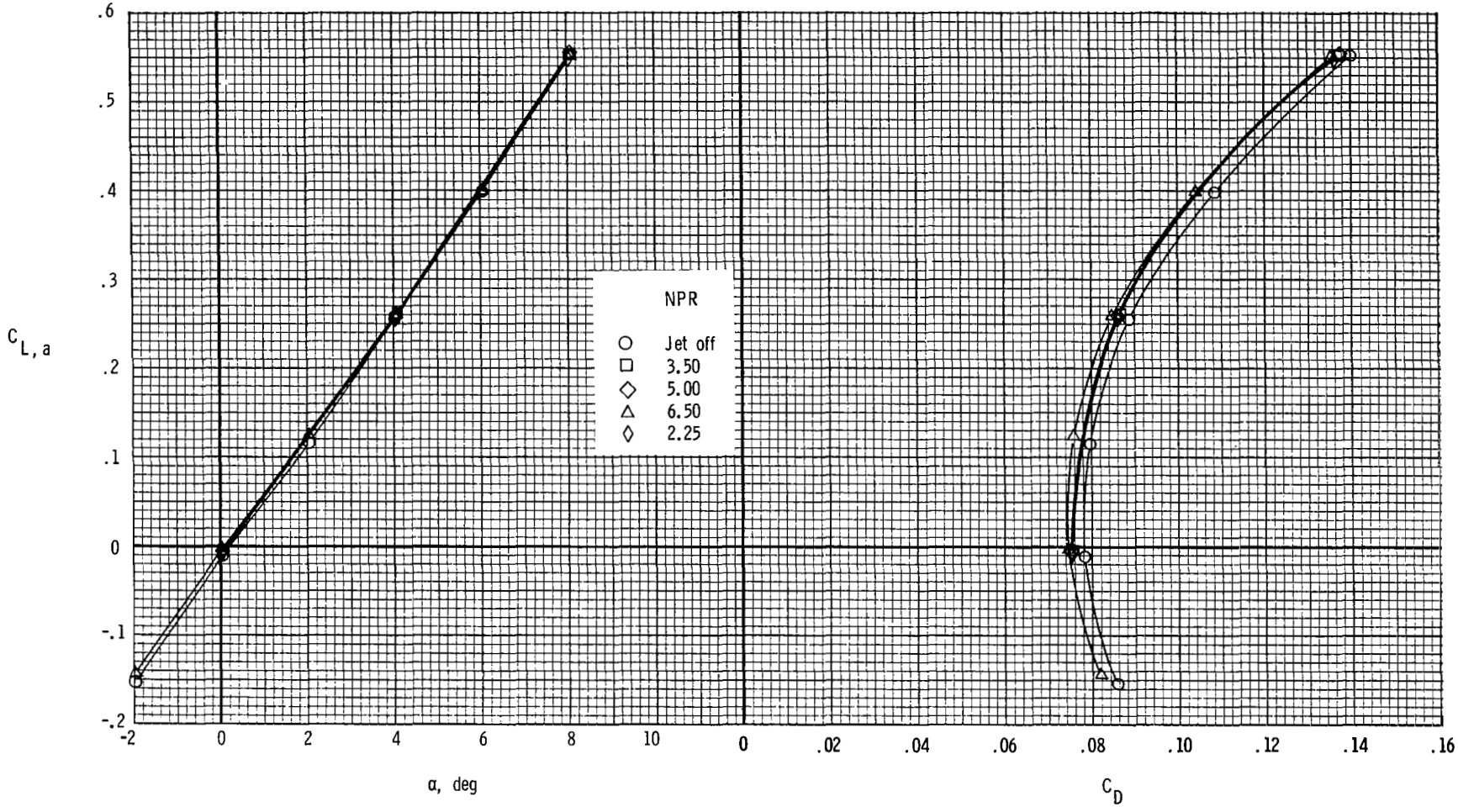

(c) M = 1.20.

Figure 42.- Concluded.

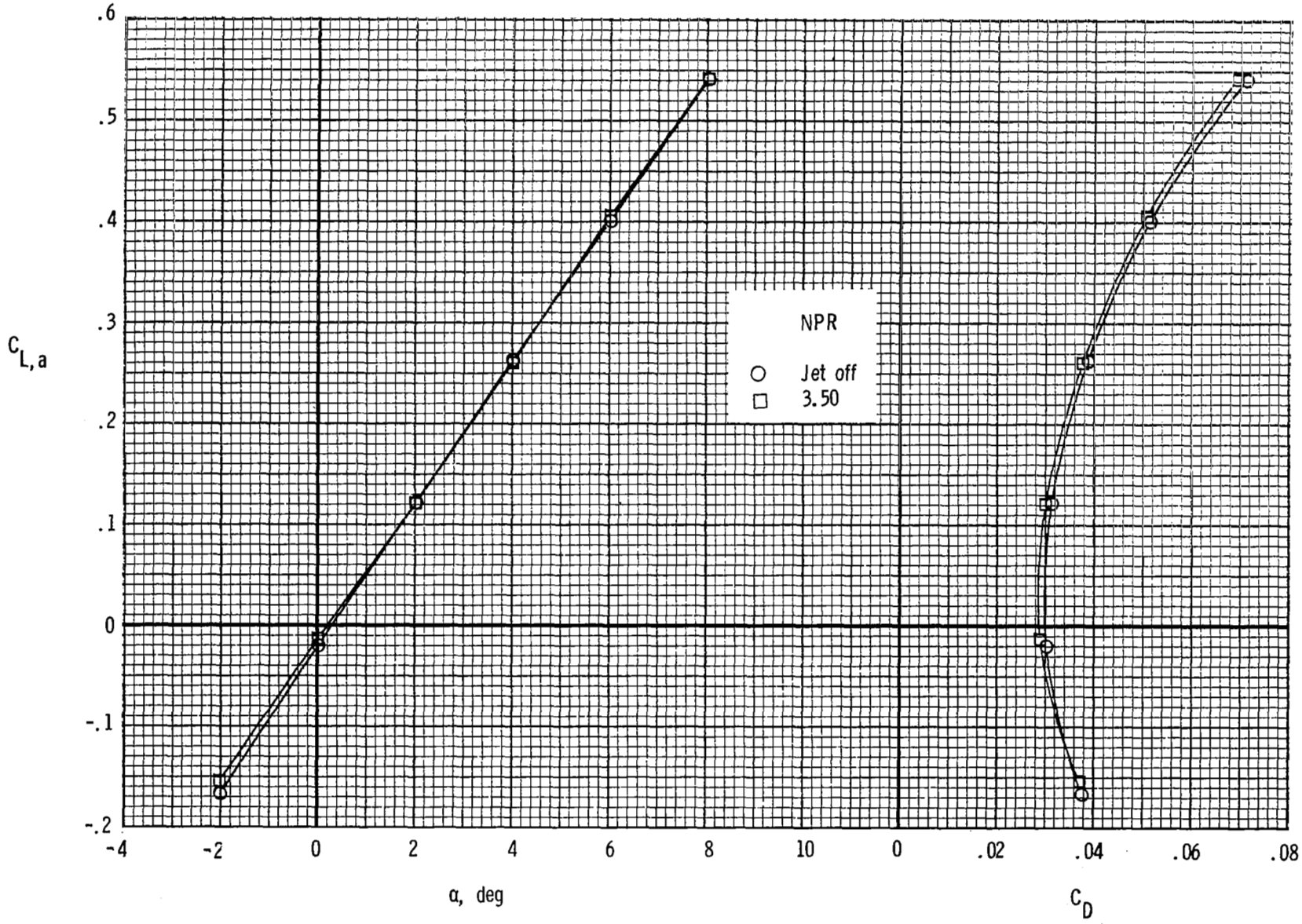

(a) M = 0.60.

Figure 43.- Thrust-removed longitudinal aerodynamic characteristics of configuration with maximum-afterburning-power 2-D C-D SSW nozzles.

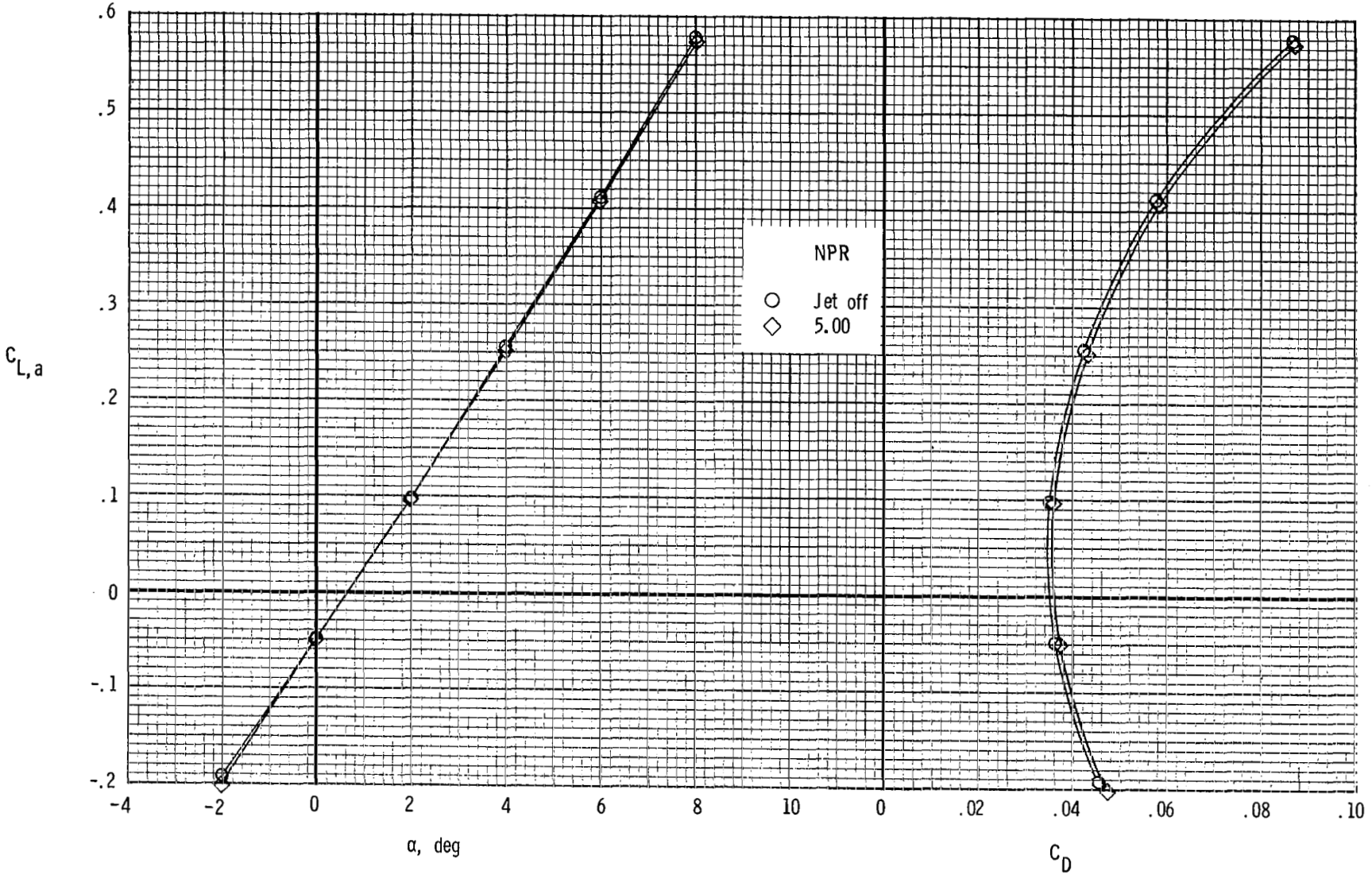

(b) M = 0.90.

Figure 43.- Concluded.

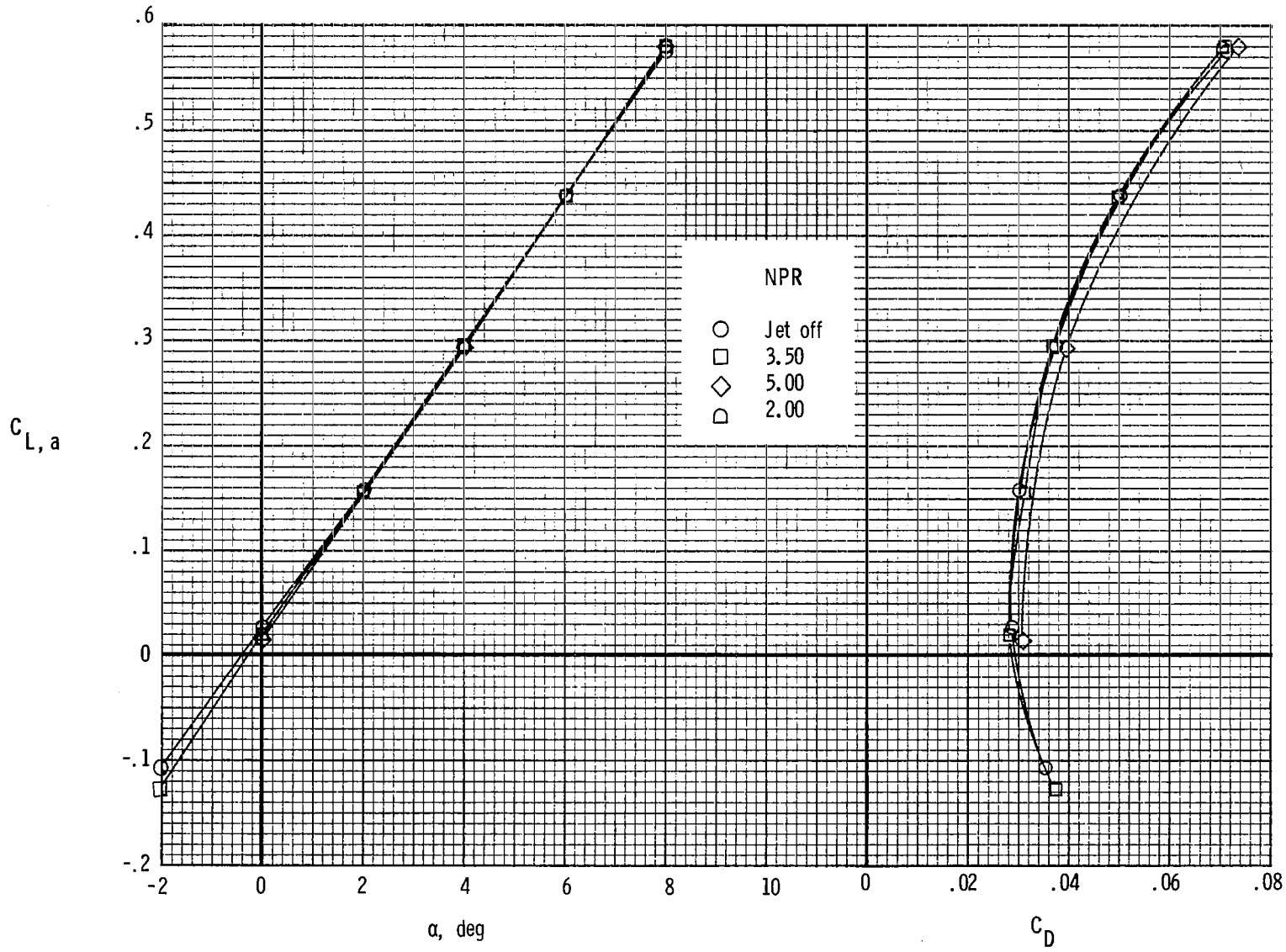

(a) M = 0.60.

Figure 44.- Thrust-removed longitudinal aerodynamic characteristics of configuration with nacelle-mounted twin vertical tails, toe angle (L.E. out) of 2°, modified tail booms, and dry-power 2-D C-D SSW nozzles.

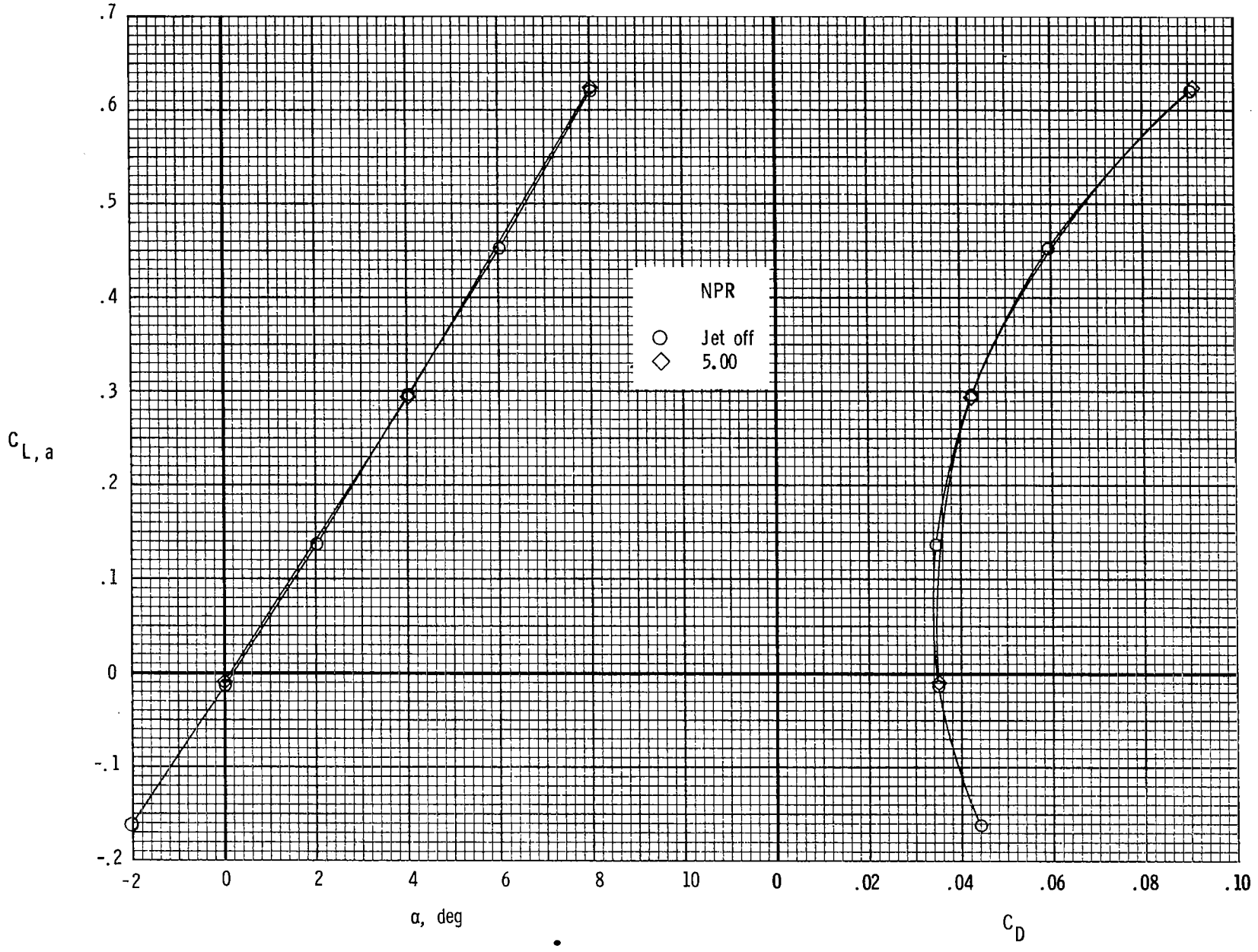

(b) M = 0.90.

Figure 44.- Concluded.

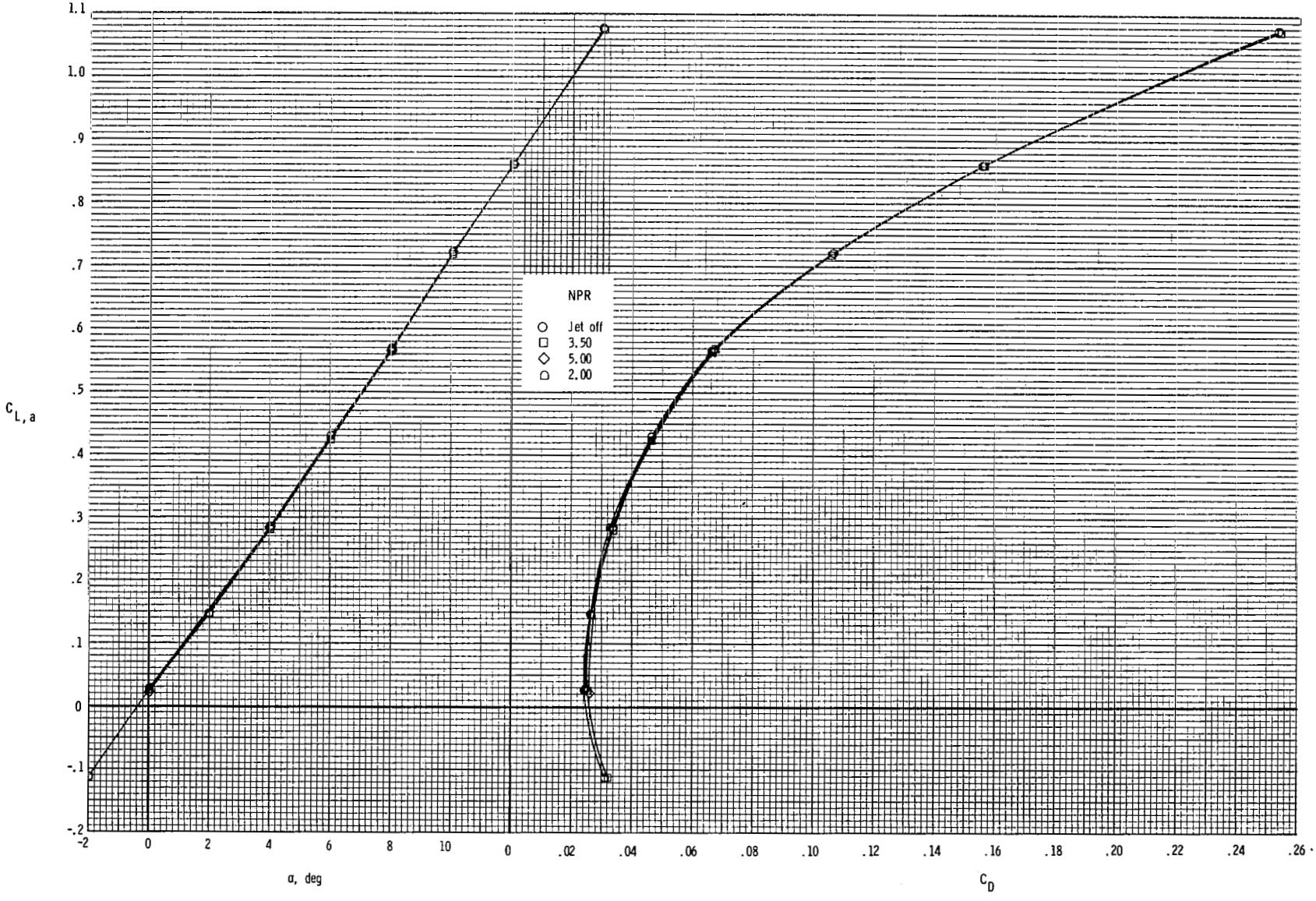

(a) M = 0.60.

Figure 45.- Thrust-removed longitudinal aerodynamic characteristics of configuration with dry-power 2-D C-D SSW nozzles and twin vertical tails off.

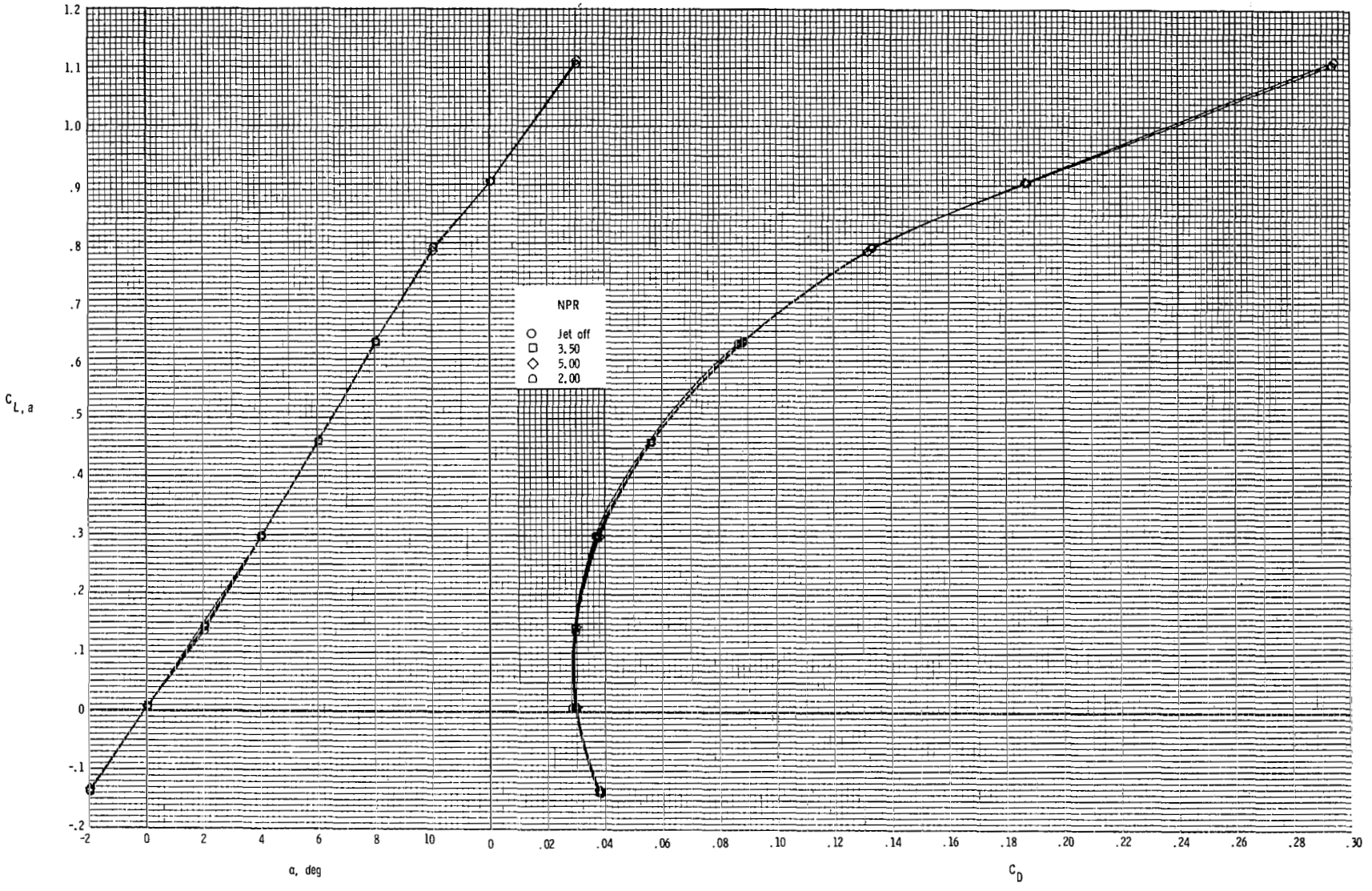

(b) M = 0.90.

Figure 45.- Continued.

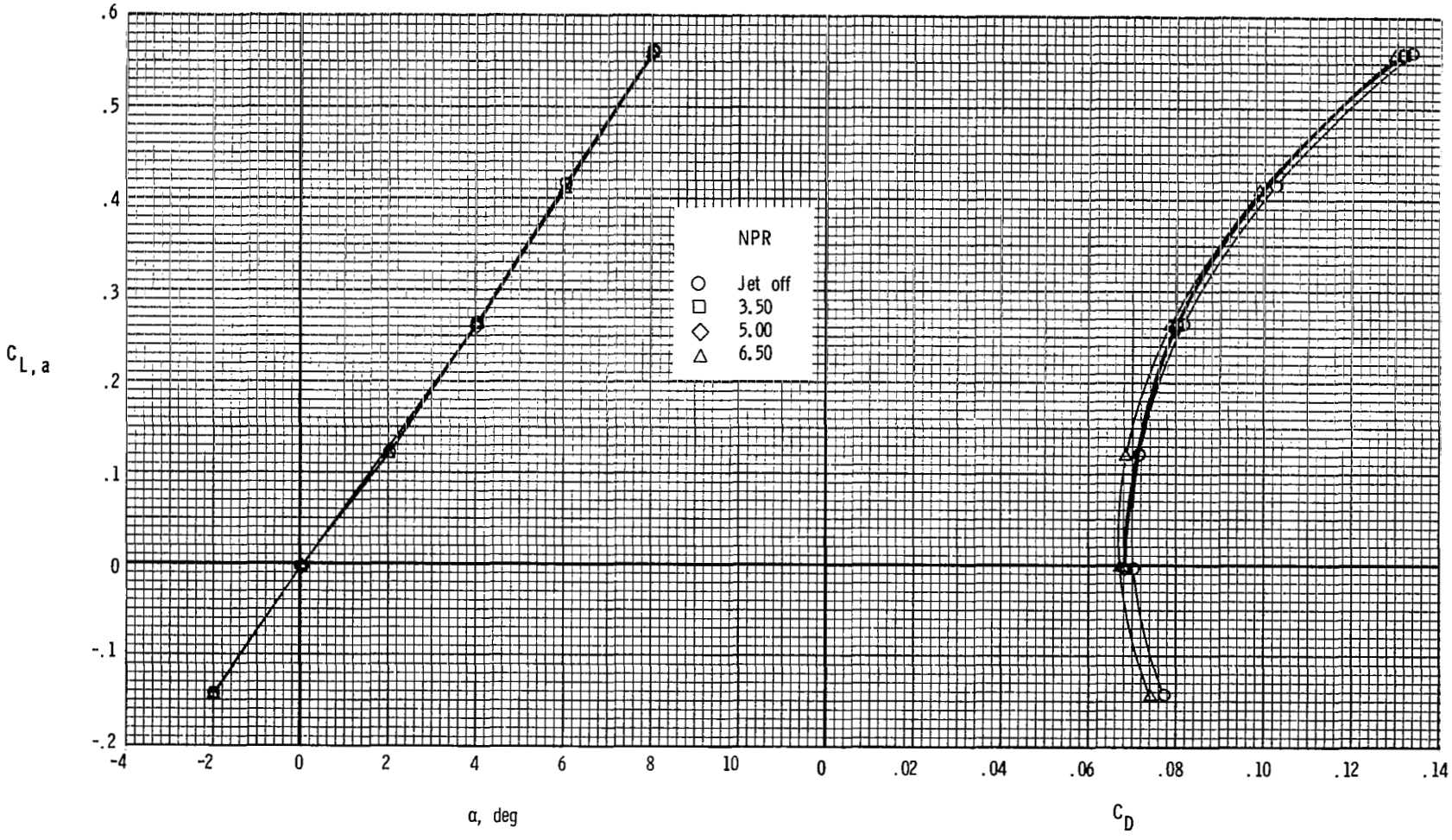

(c) M = 1.20.

Figure 45.- Concluded.

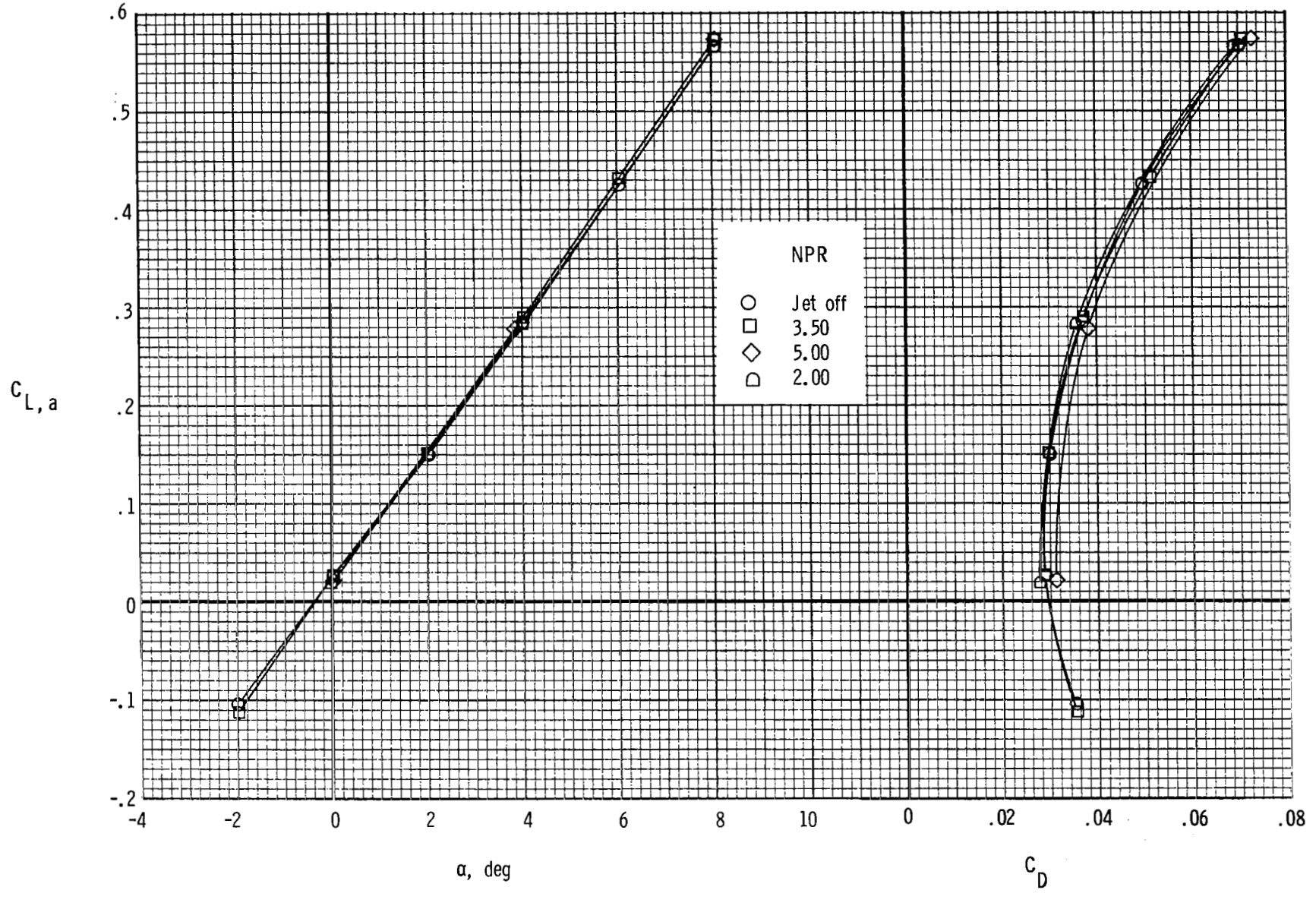

(a) M = 0.60.

Figure 46.- Thrust-removed longitudinal aerodynamic characteristics of configuration with dry-power 2-D C-D SSW nozzles, boom-mounted twin vertical tails, and toe angle of 0°.

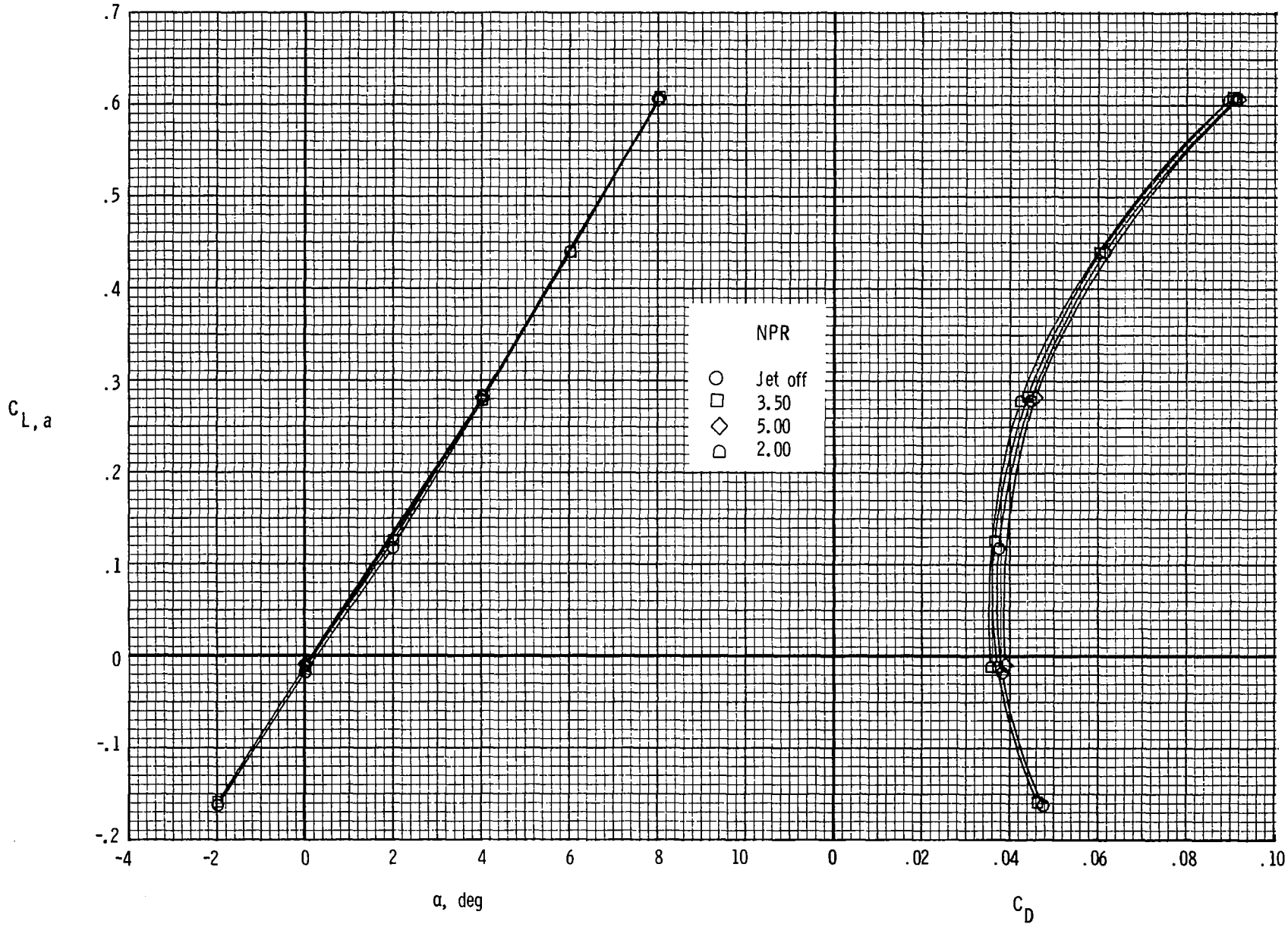

(b) M = 0.90.

Figure 46.- Concluded.

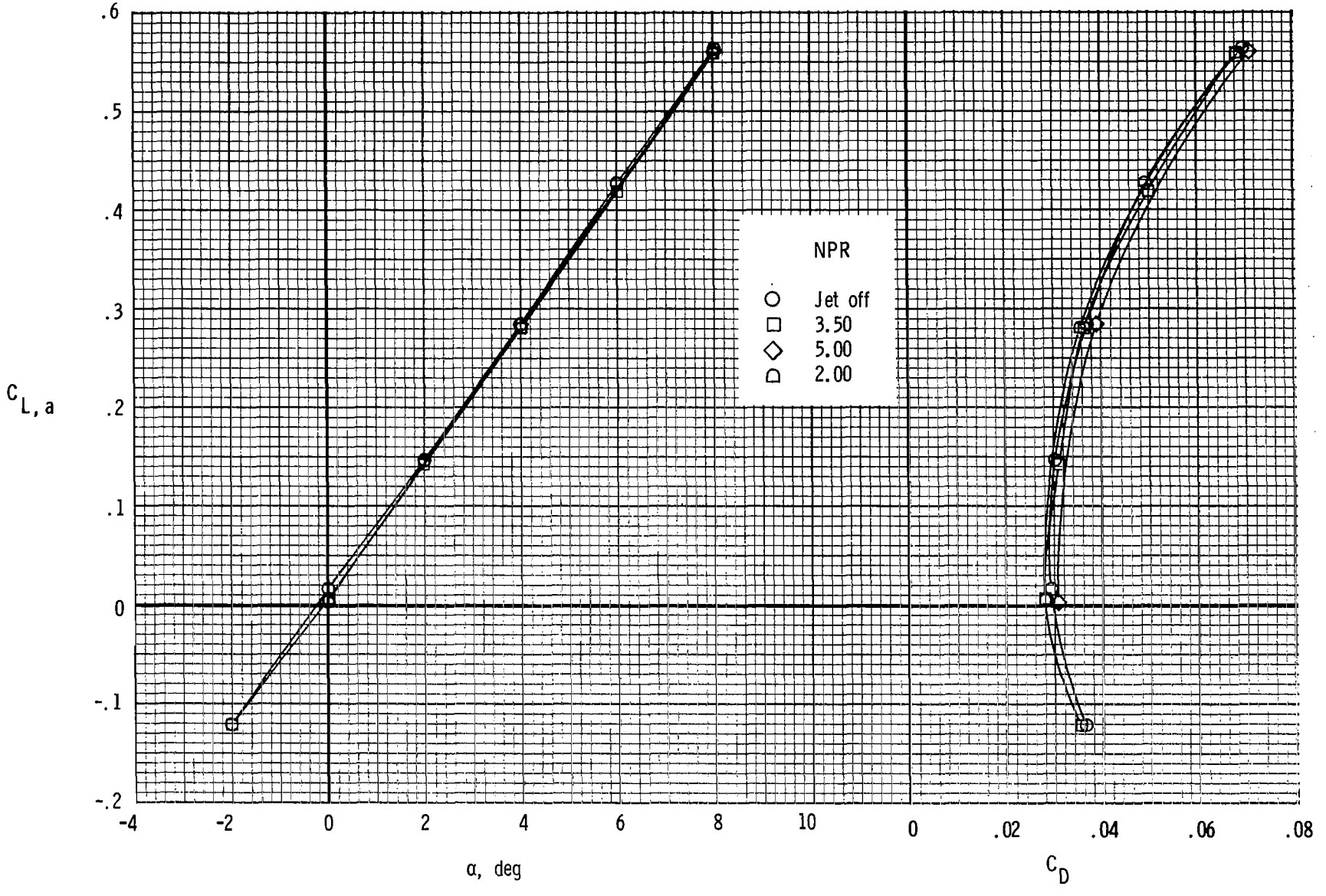

(a) M = 0.60.

Figure 47.- Thrust-removed longitudinal aerodynamic characteristics of configuration with dry-power 2-D C-D SSW nozzles, boom-mounted twin vertical tails, and toe angle (L.E. out) of 4°.

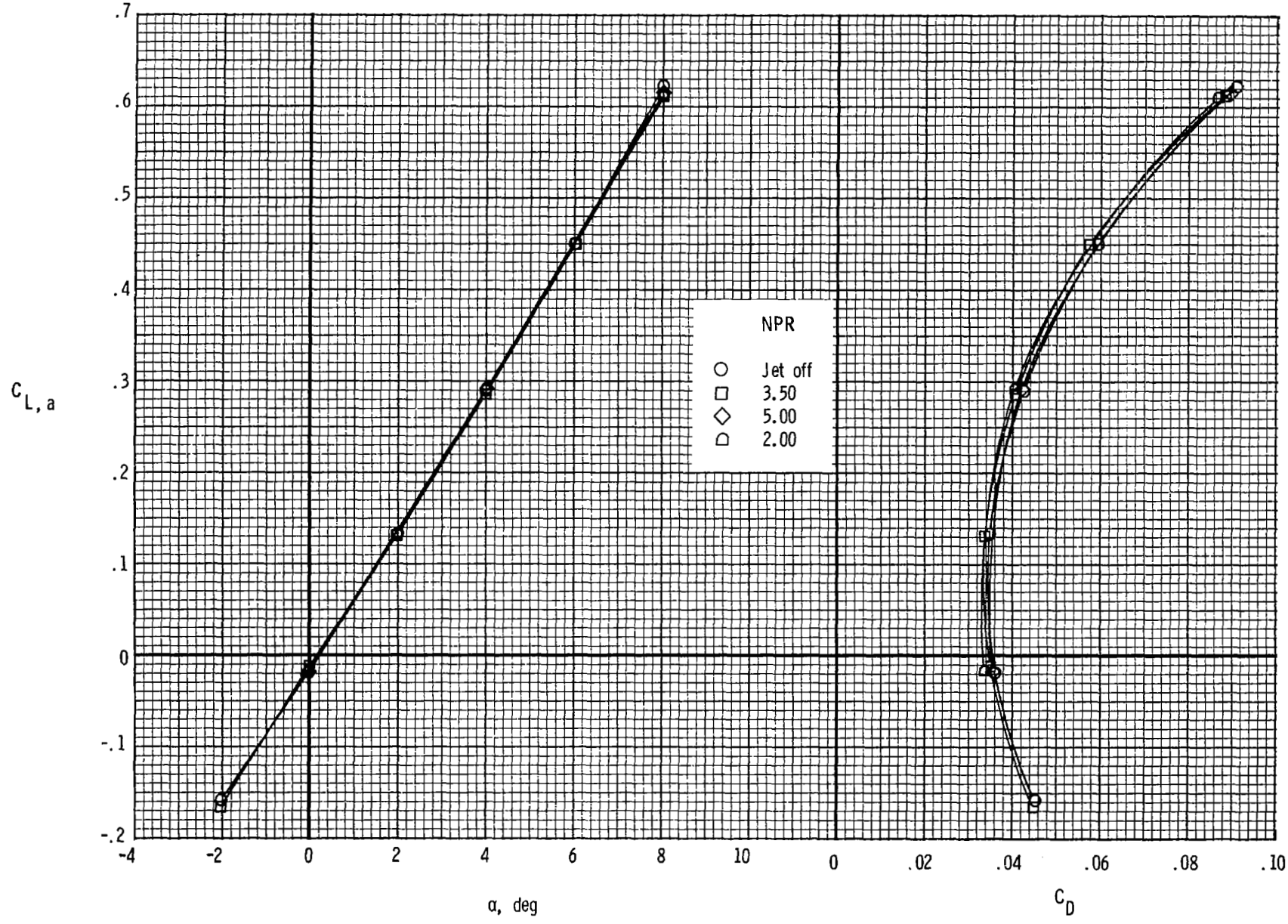

(b) M = 0.90.

Figure 47.- Concluded.

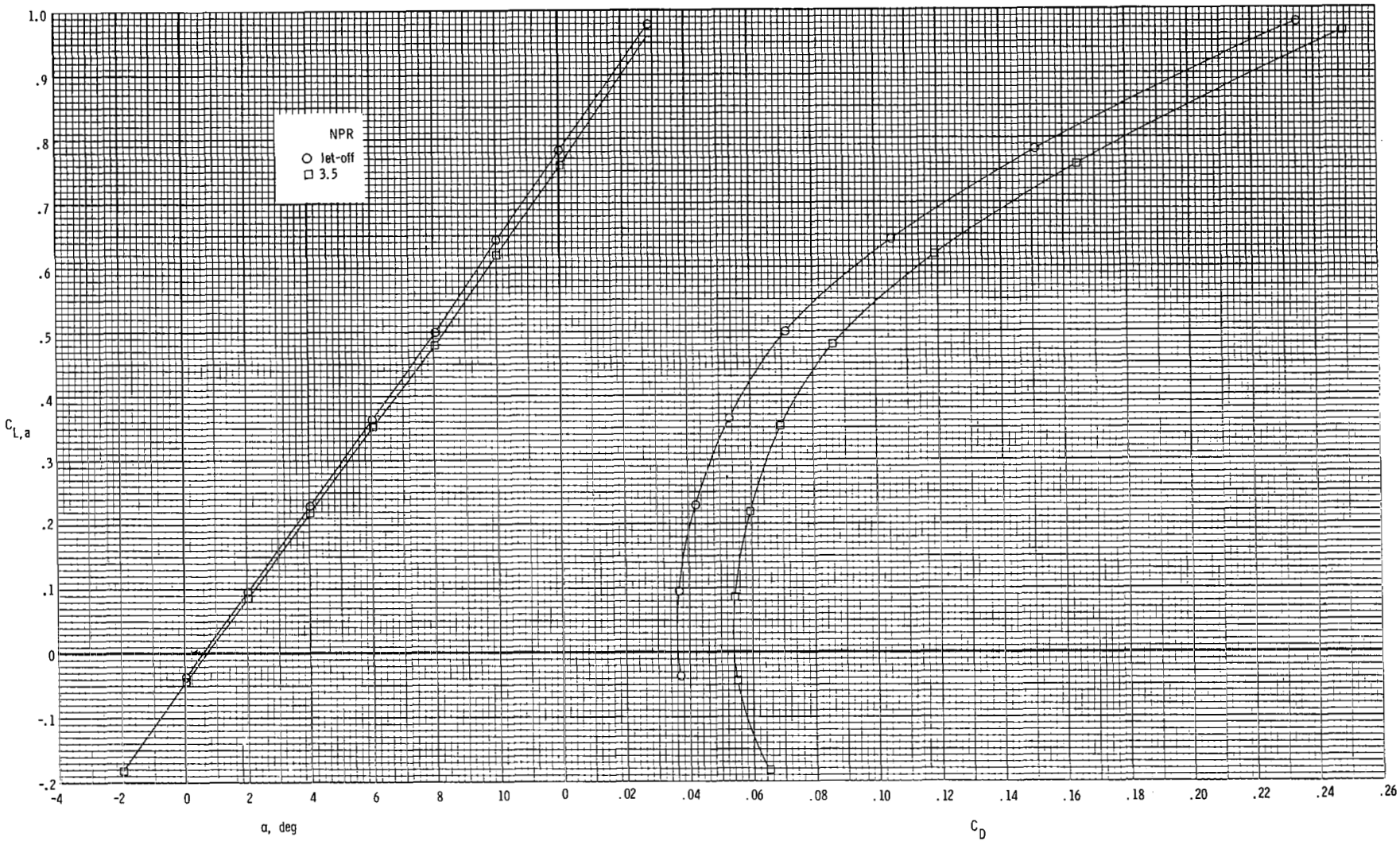

(a) M = 0.60.

Figure 48.- Effect of partially deployed reversers (δ_{REV} = 90°) on thrust-removed longitudinal aerodynamic characteristics of configuration with dry-power 2-D C-D SSW nozzles.

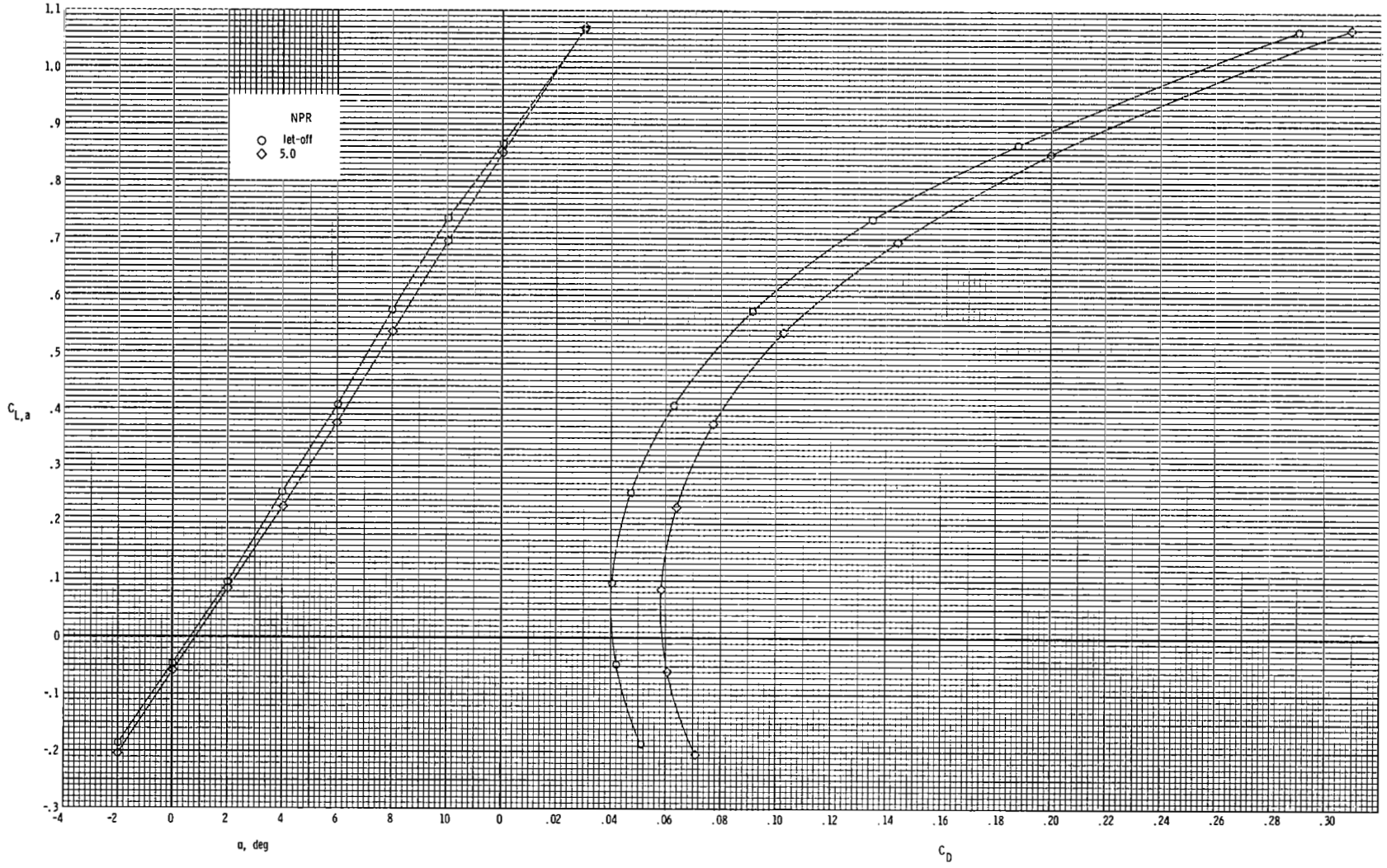

(b) M = 0.90.

Figure 48.- Continued.

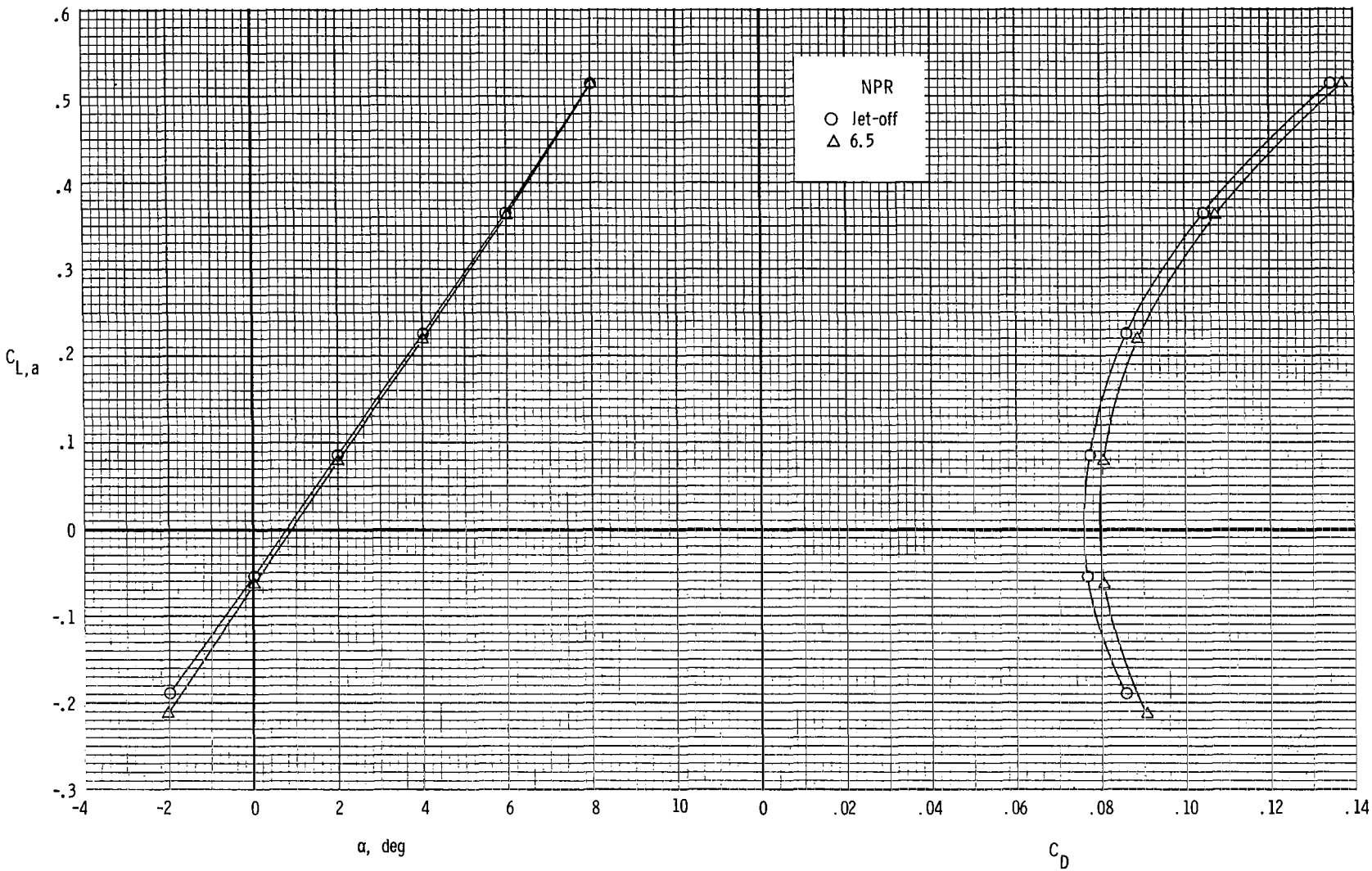

(c) M = 1.20.

Figure 48.- Concluded.

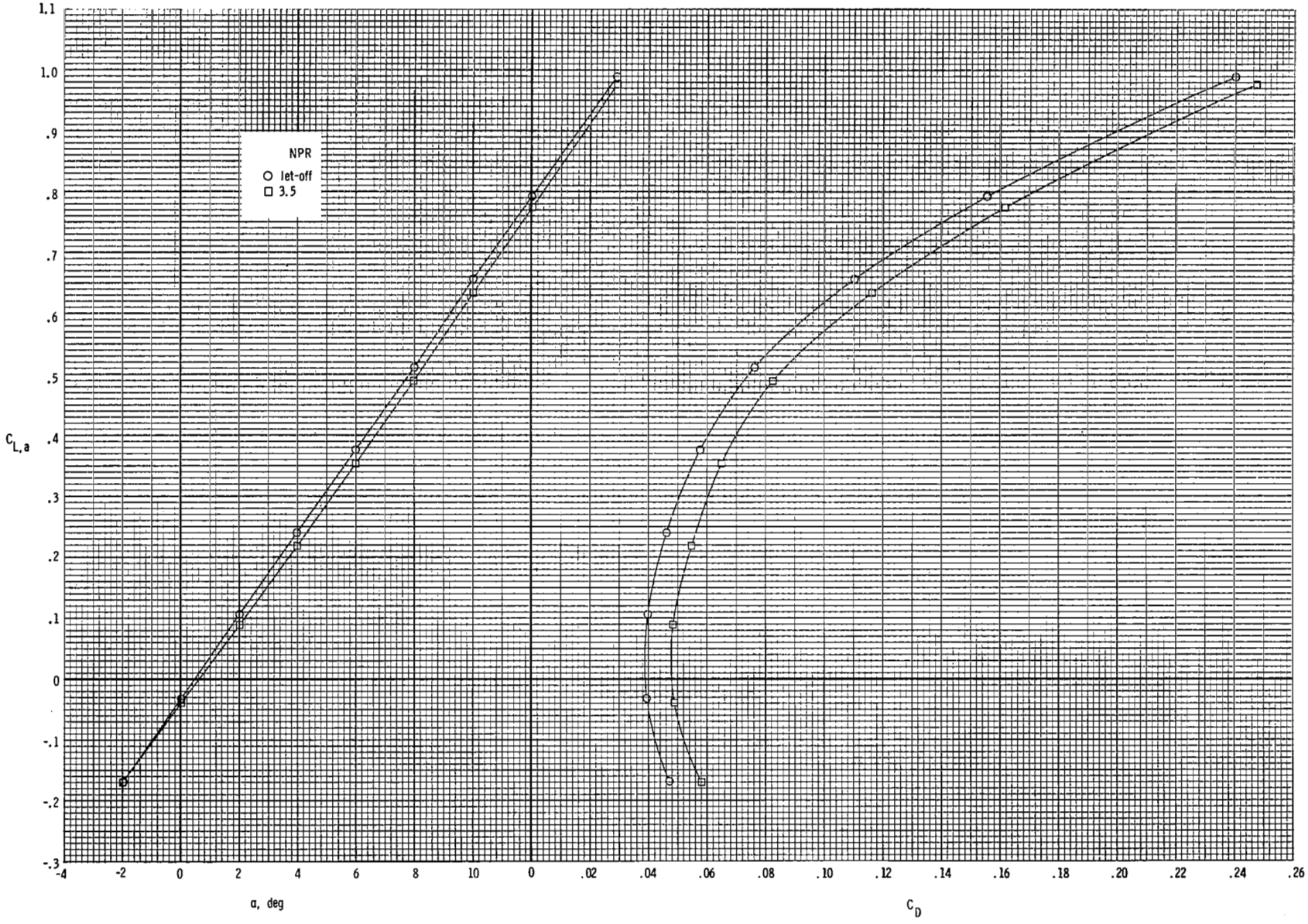

(a) M = 0.60.

Figure 49.- Effect of fully deployed reversers (δ_{REV} = 130°) on thrust-removed longitudinal aerodynamic characteristics of configuration with dry-power 2-D C-D SSW nozzles.

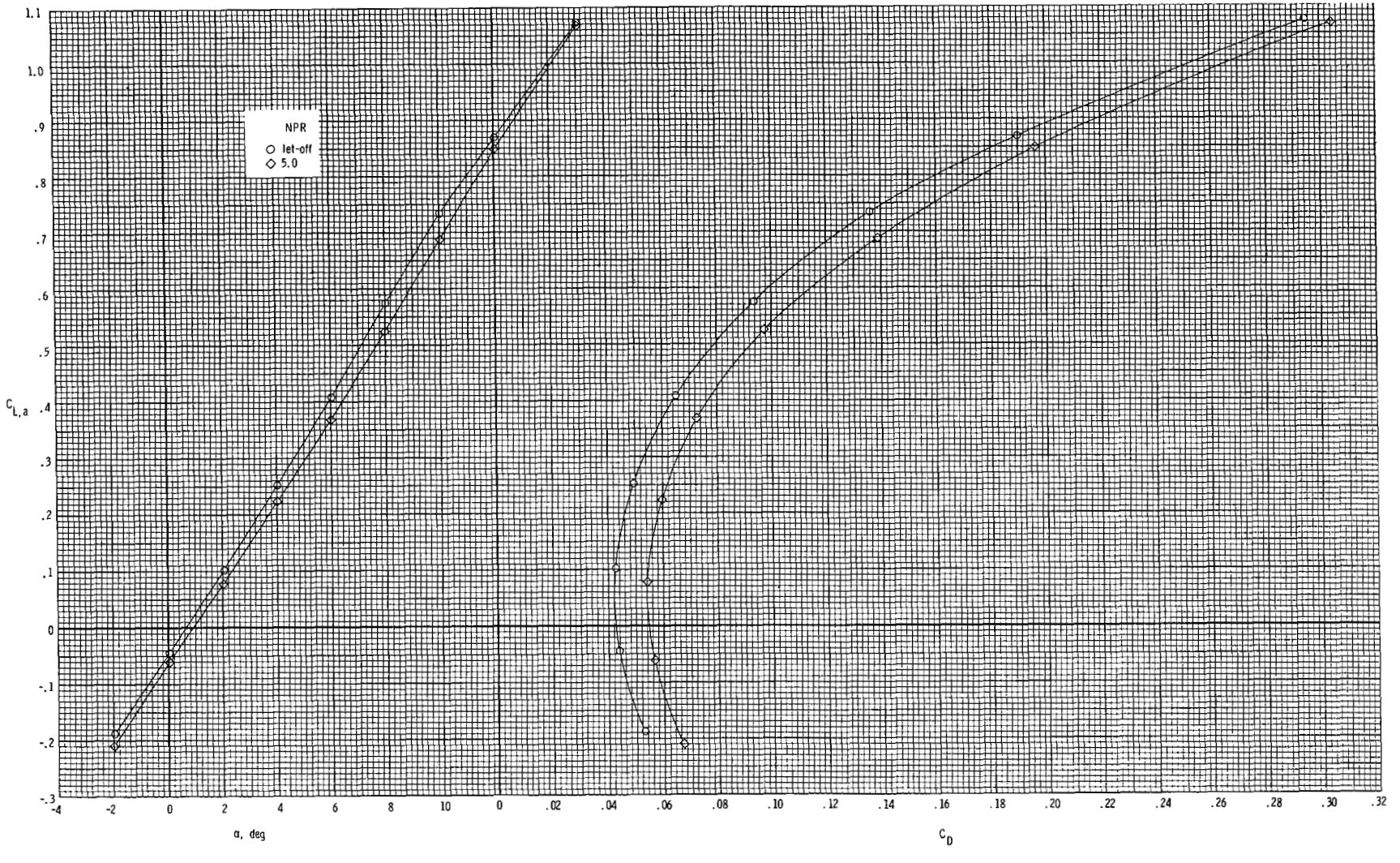

(b) M = 0.90.

Figure 49.- Continued.

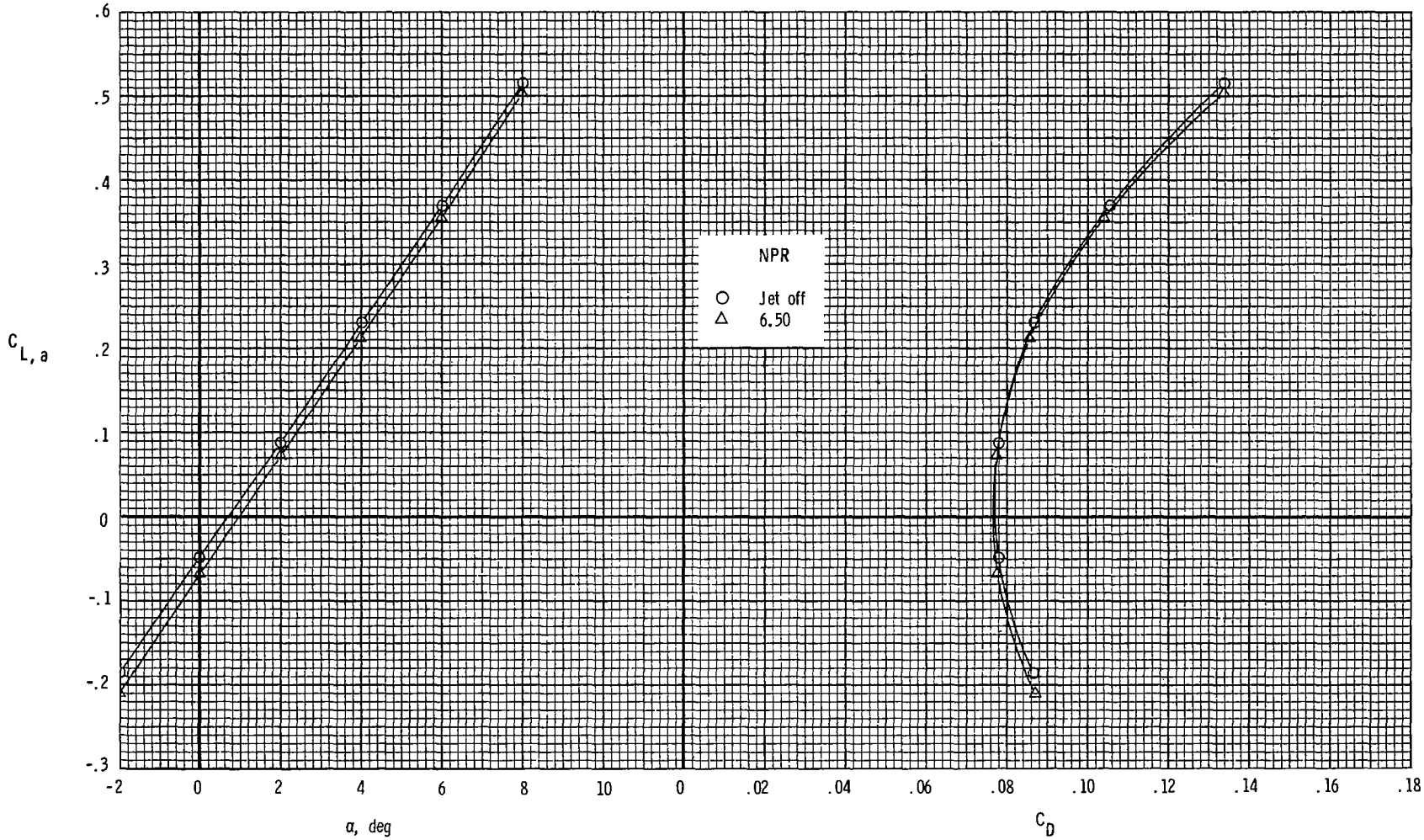

(c) M = 1.20.

Figure 49.- Concluded.

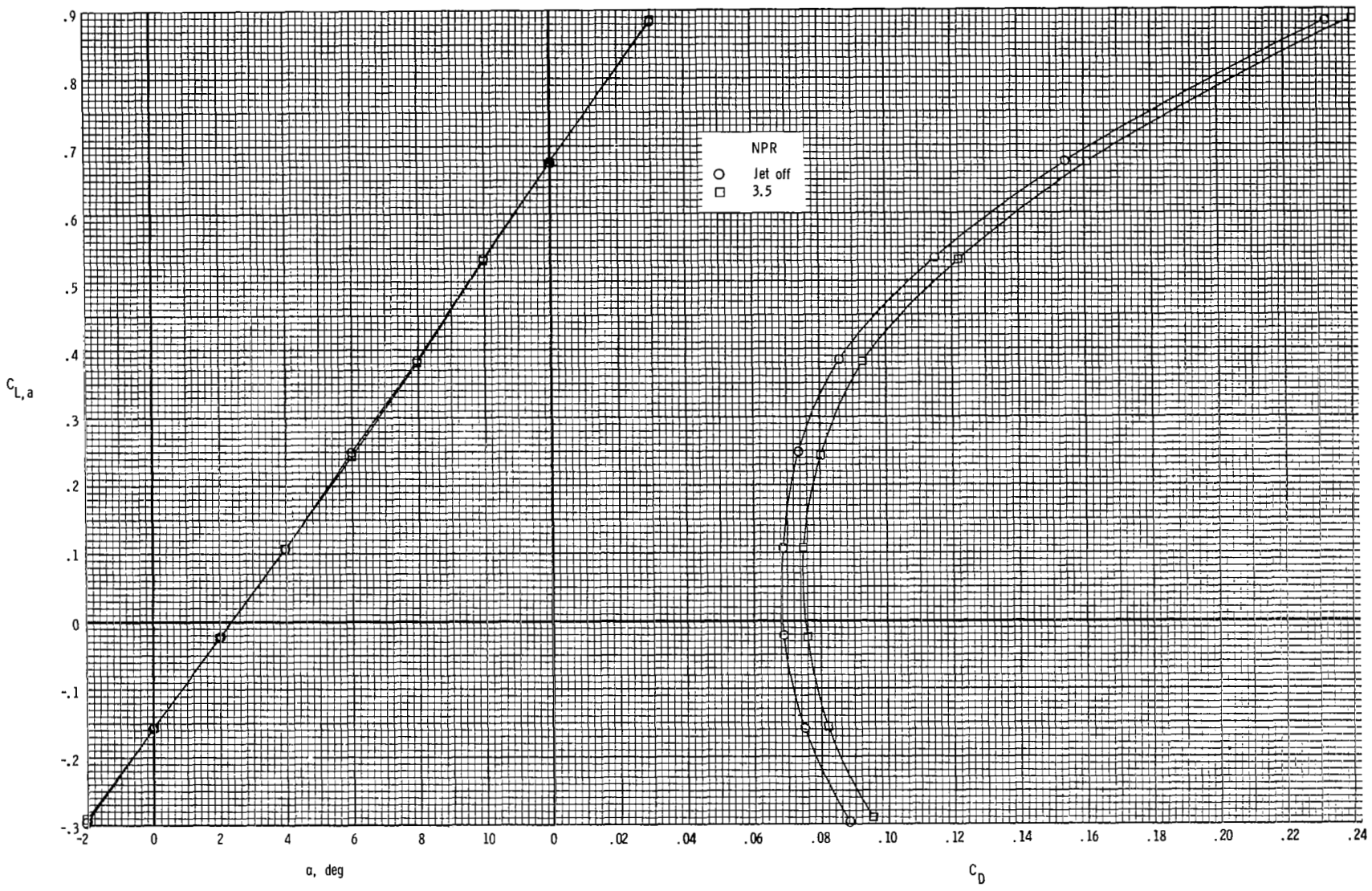

(a) M = 0.60.

Figure 50.- Effect of fully deployed reversers (δ_{REV} = 130°) on thrust-removed longitudinal aerodynamic characteristics of configuration with dry-power 2-D C-D SSW nozzles, and horizontal-tail deflection of -15° (L.E. down).

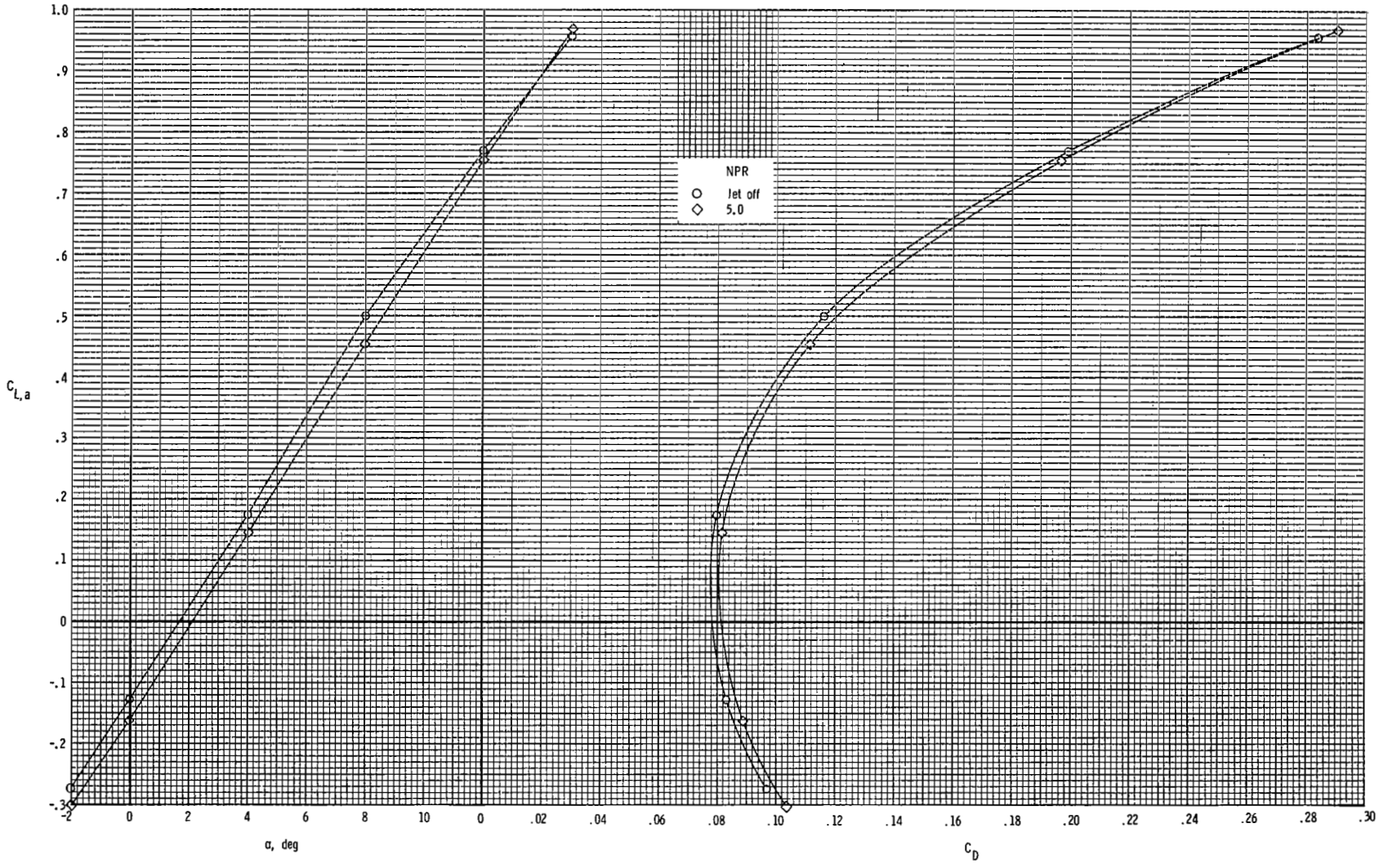

(b) M = 0.90.

Figure 50.- Concluded.

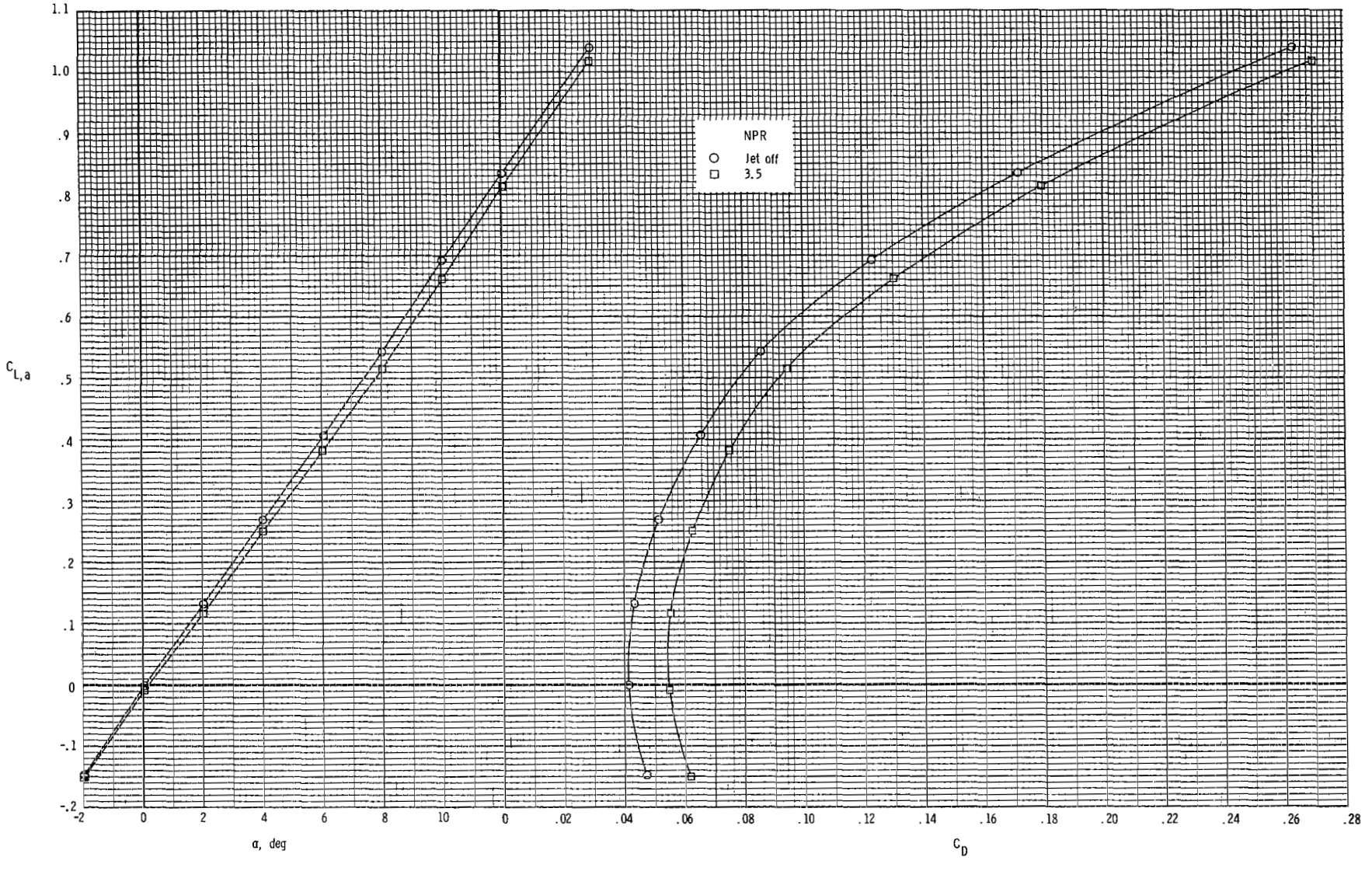

(a) M = 0.60.

Figure 51.- Effect of fully deployed reversers (δ_{REV} = 130°) on thrust-removed longitudinal aerodynamic characteristics of configuration with dry-power 2-D C-D SSW nozzles and horizontal-tail deflection of 5° (L.E. up).

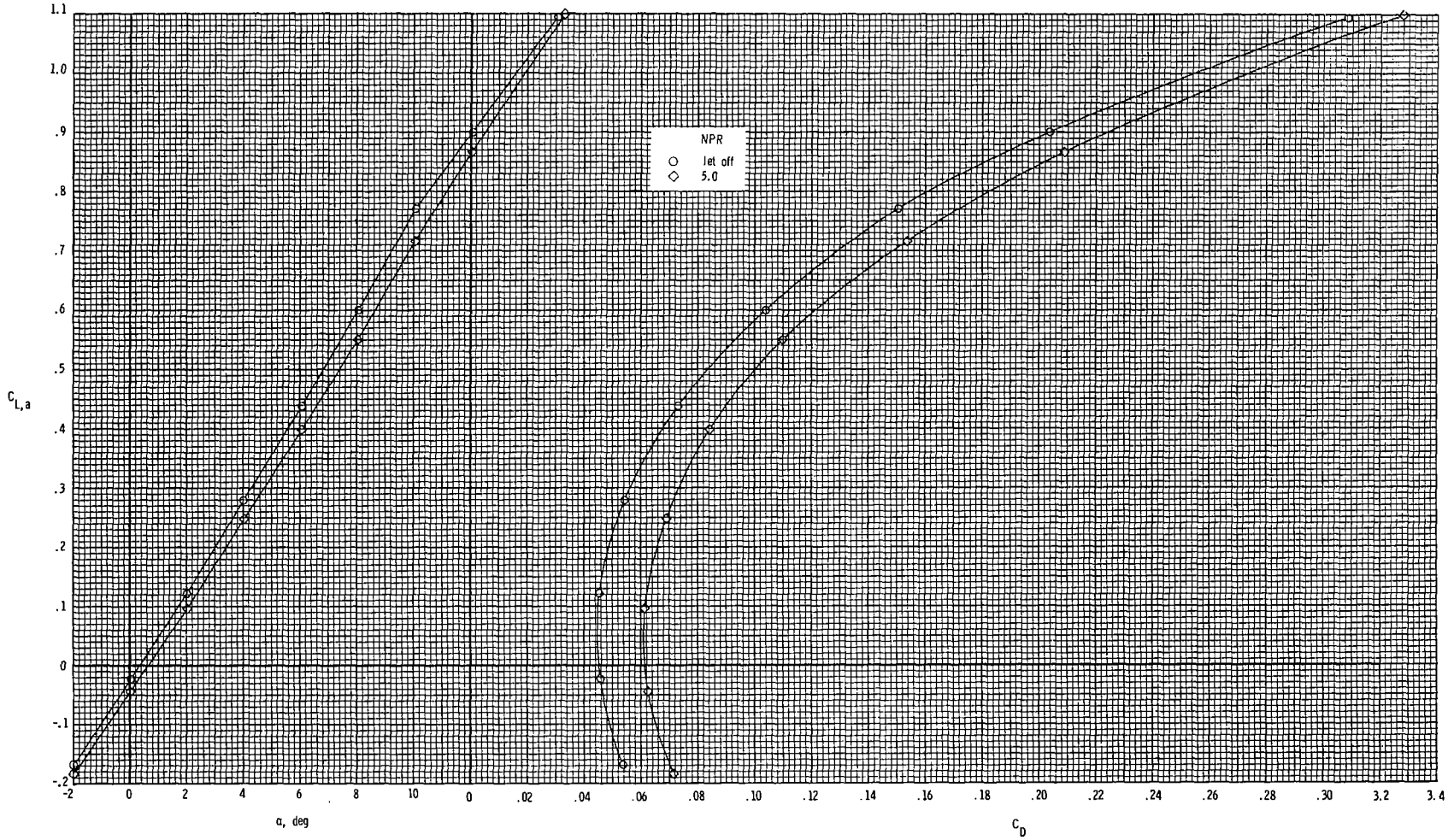

(b) M = 0.90.

Figure 51.- Concluded.

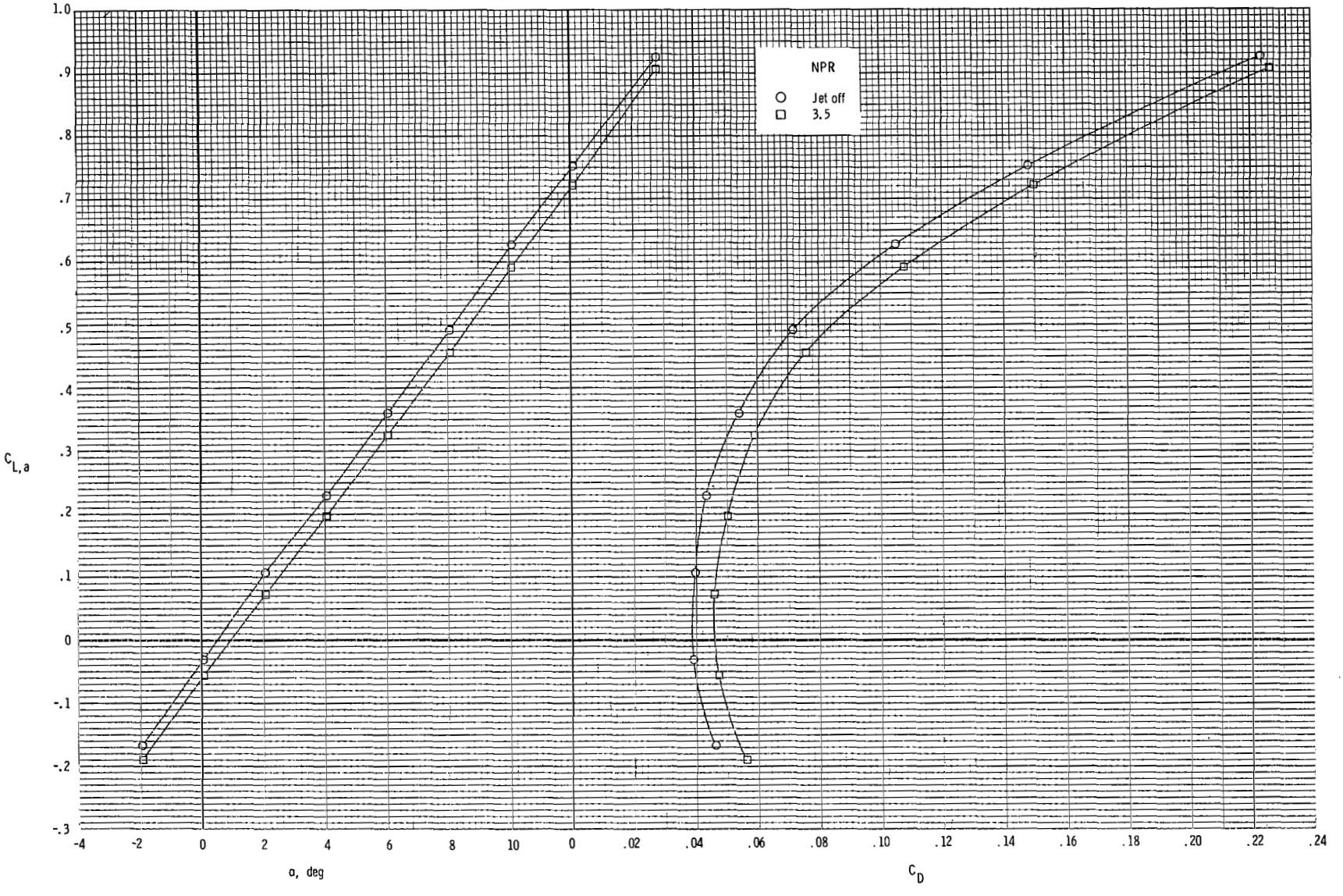

(a) M = 0.60.

Figure 52.- Effect of fully deployed reversers (δ_{REV} = 130°) on thrust-removed longitudinal aerodynamic characteristics of configuration with dry-power 2-D C-D SSW nozzles and horizontal tails off.

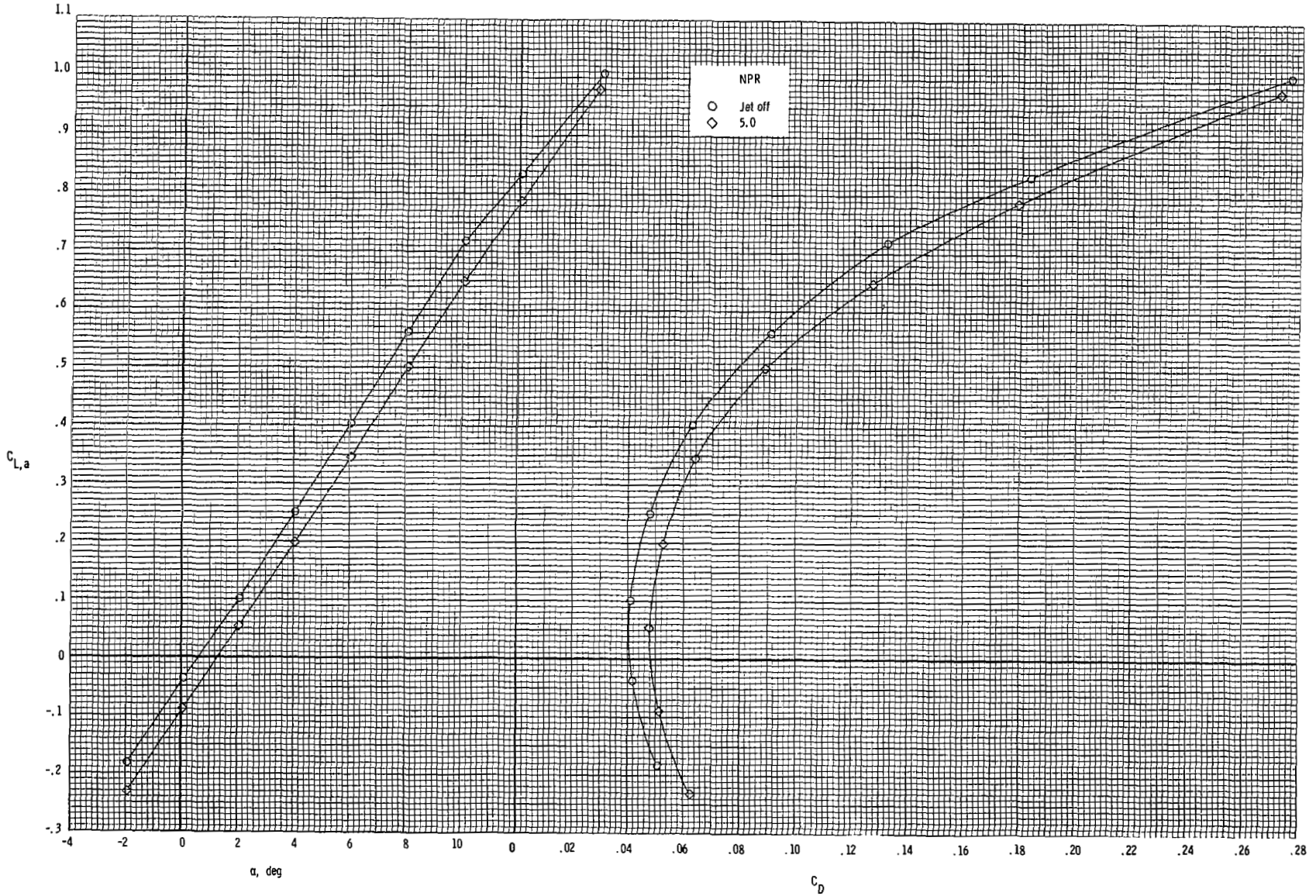

(b) M = 0.90.

Figure 52.- Continued.

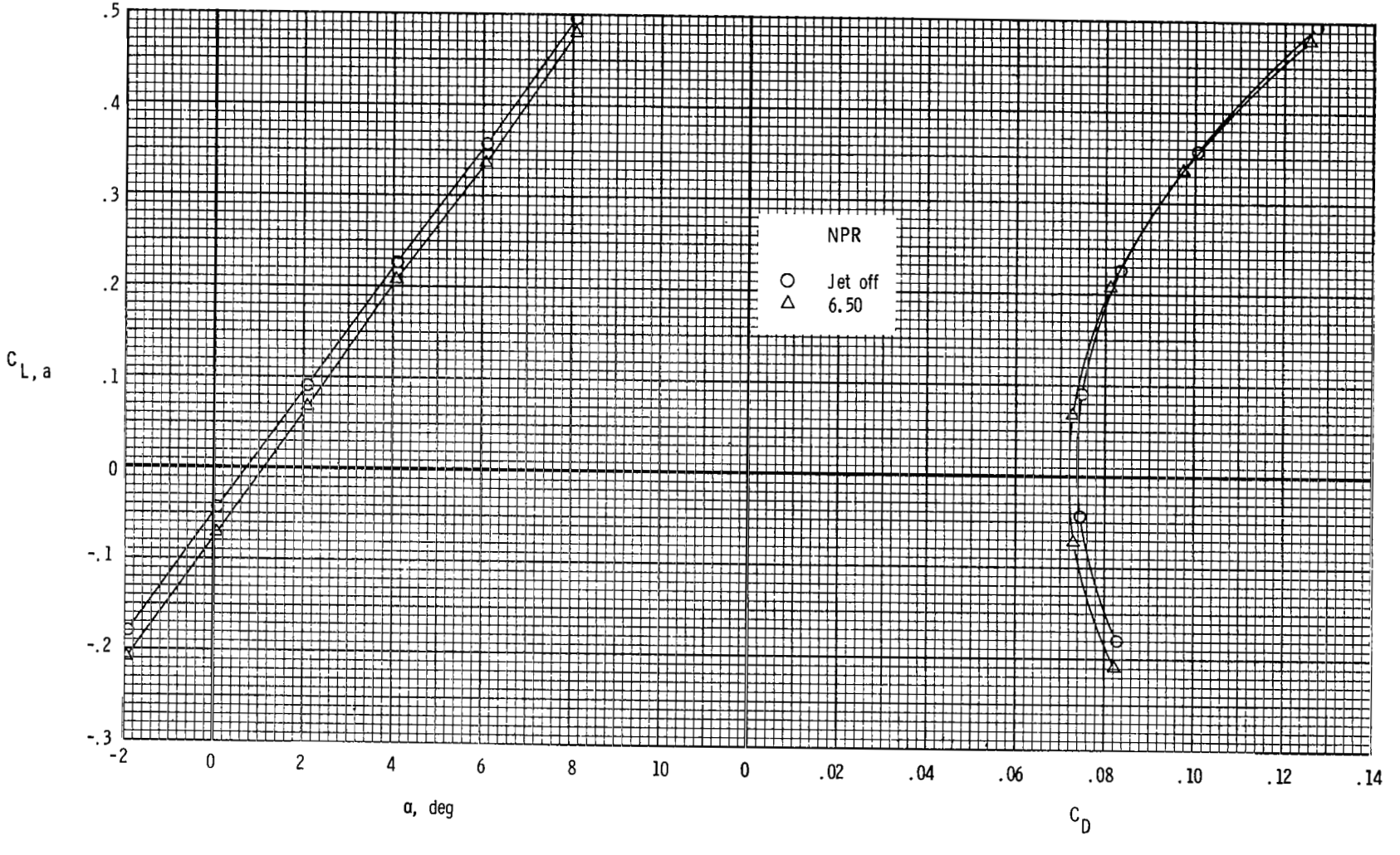

(c) M = 1.20.

Figure 52.- Concluded.

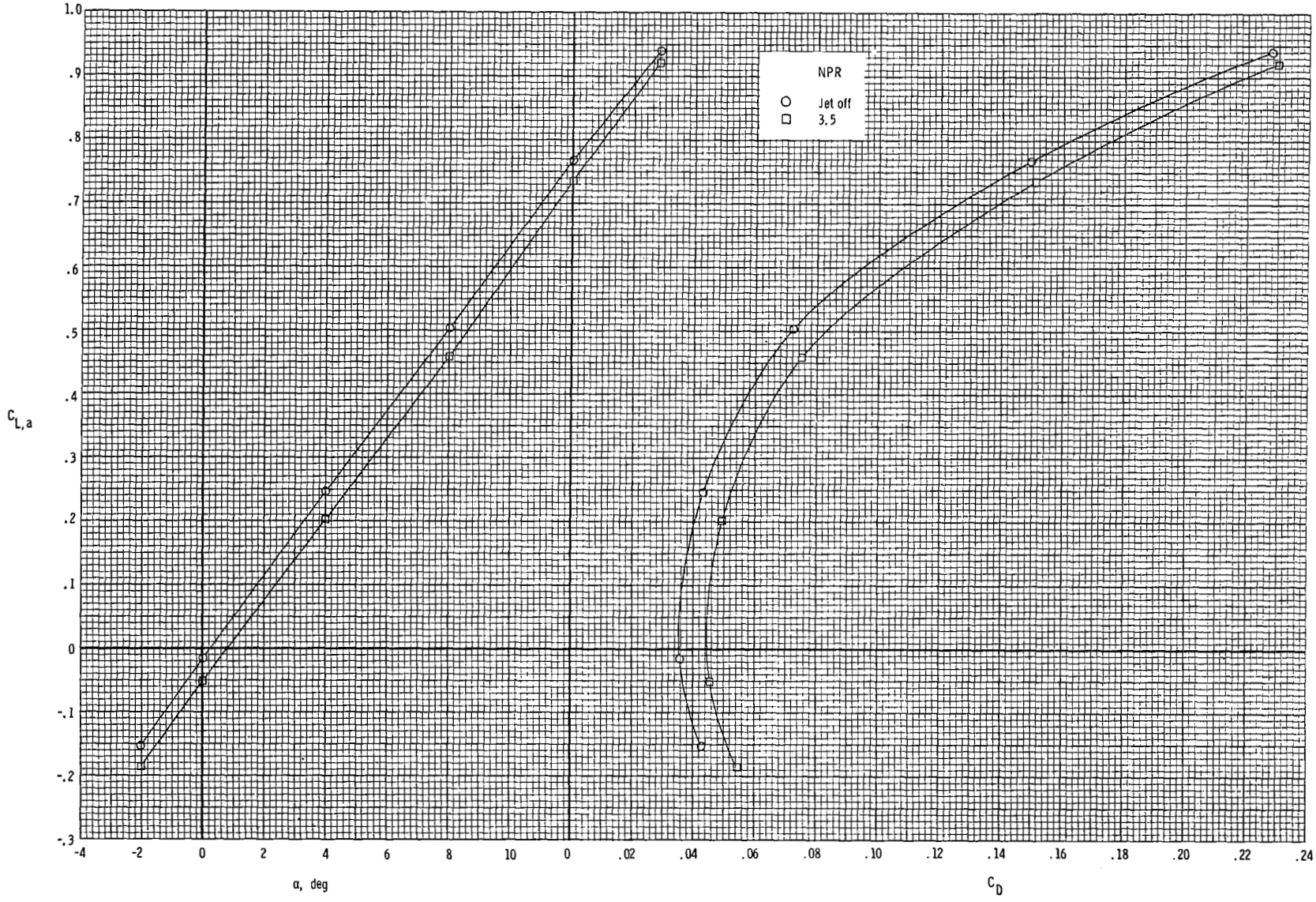

(a) M = 0.60.

Figure 53.- Effect of fully deployed reversers (δ_{REV} = 130°) on thrust-removed longitudinal aerodynamic characteristics of configuration with dry-power 2-D C-D SSW nozzles and vertical and horizontal tails off.

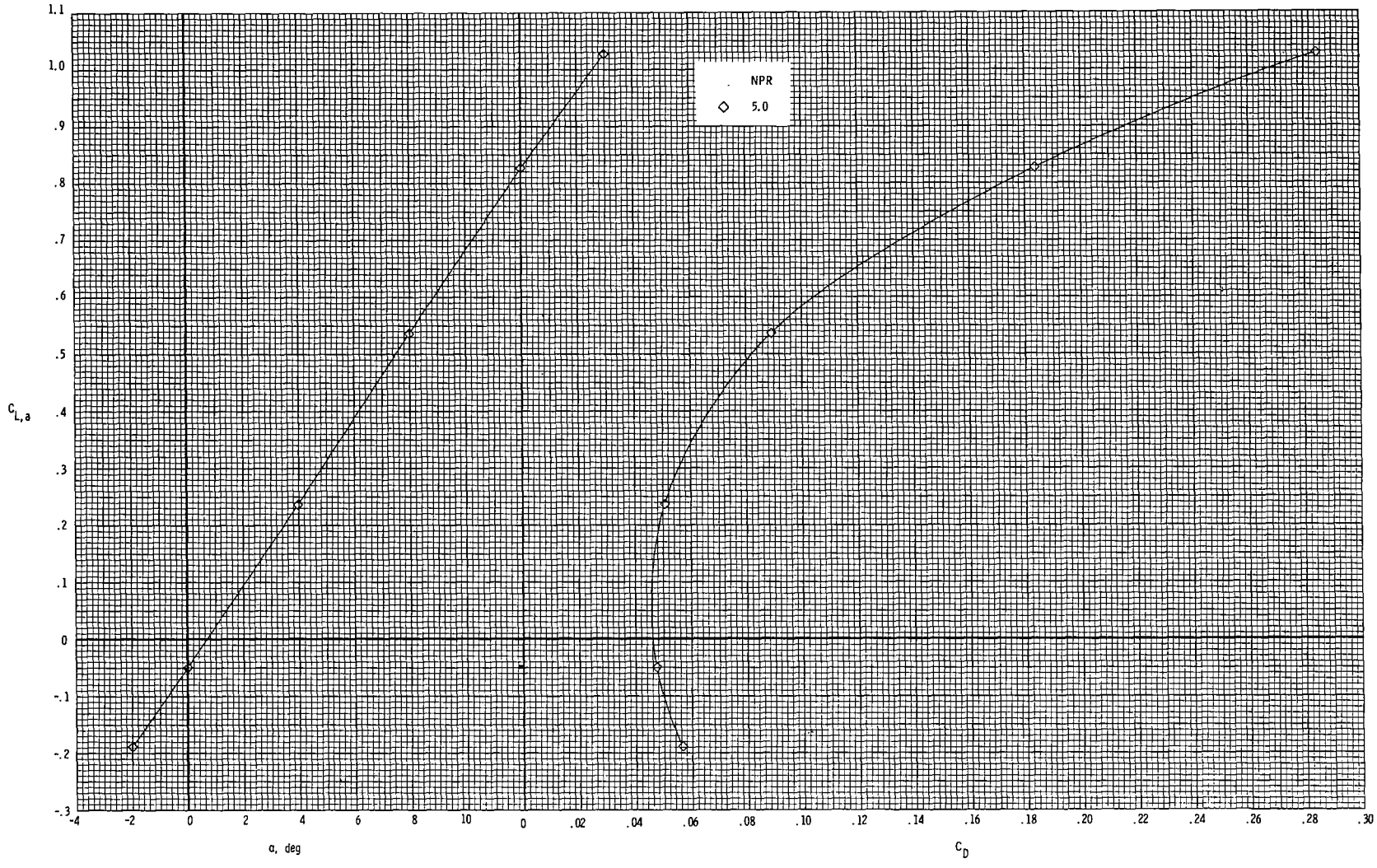

(b) M = 0.90.

Figure 53.- Concluded.

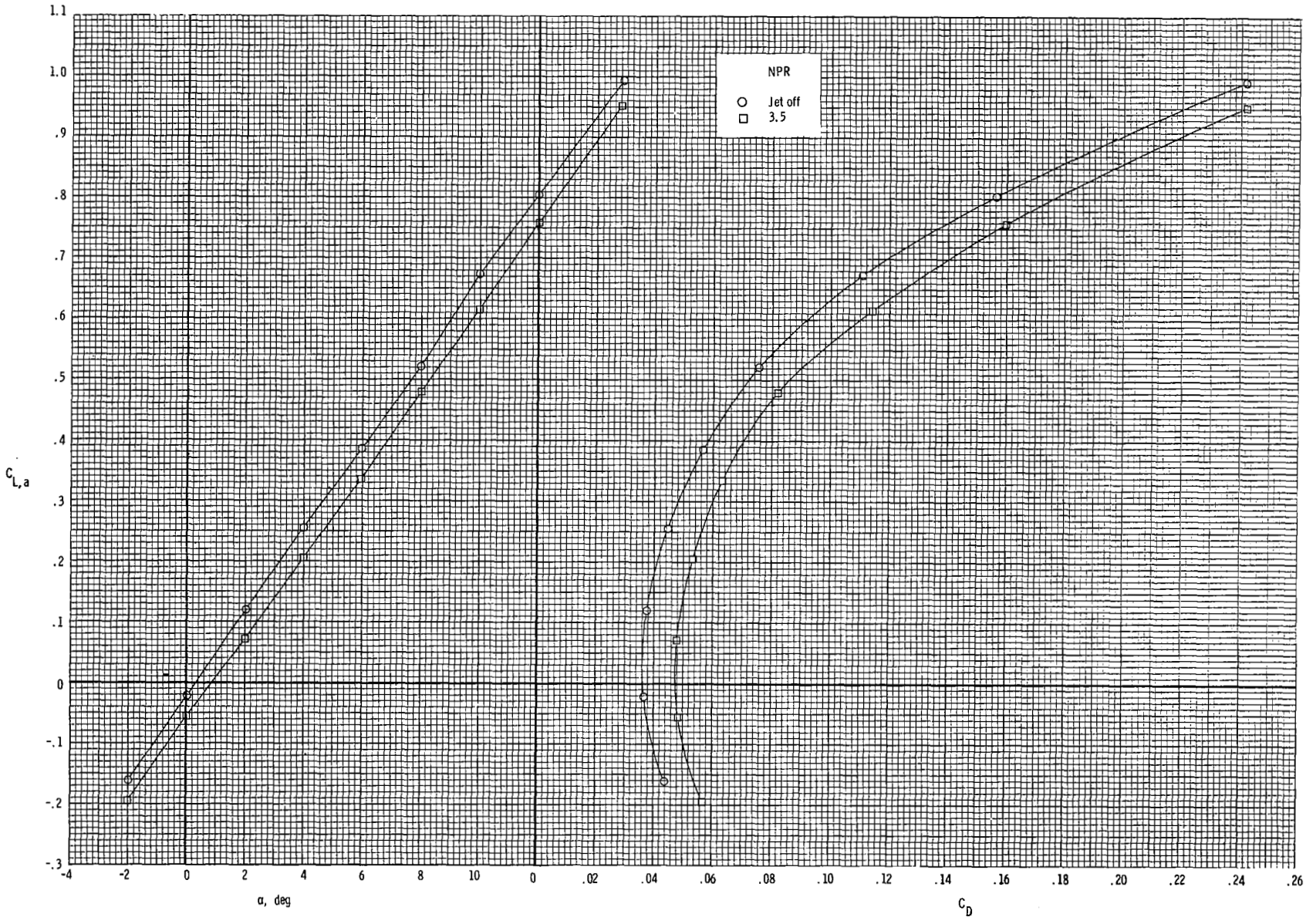

(a) M = 0.60.

Figure 54.- Effect of fully deployed reversers (δ_{REV} = 130°) on thrust-removed longitudinal aerodynamic characteristics of configuration with dry-power 2-D C-D SSW nozzles and vertical tails off.

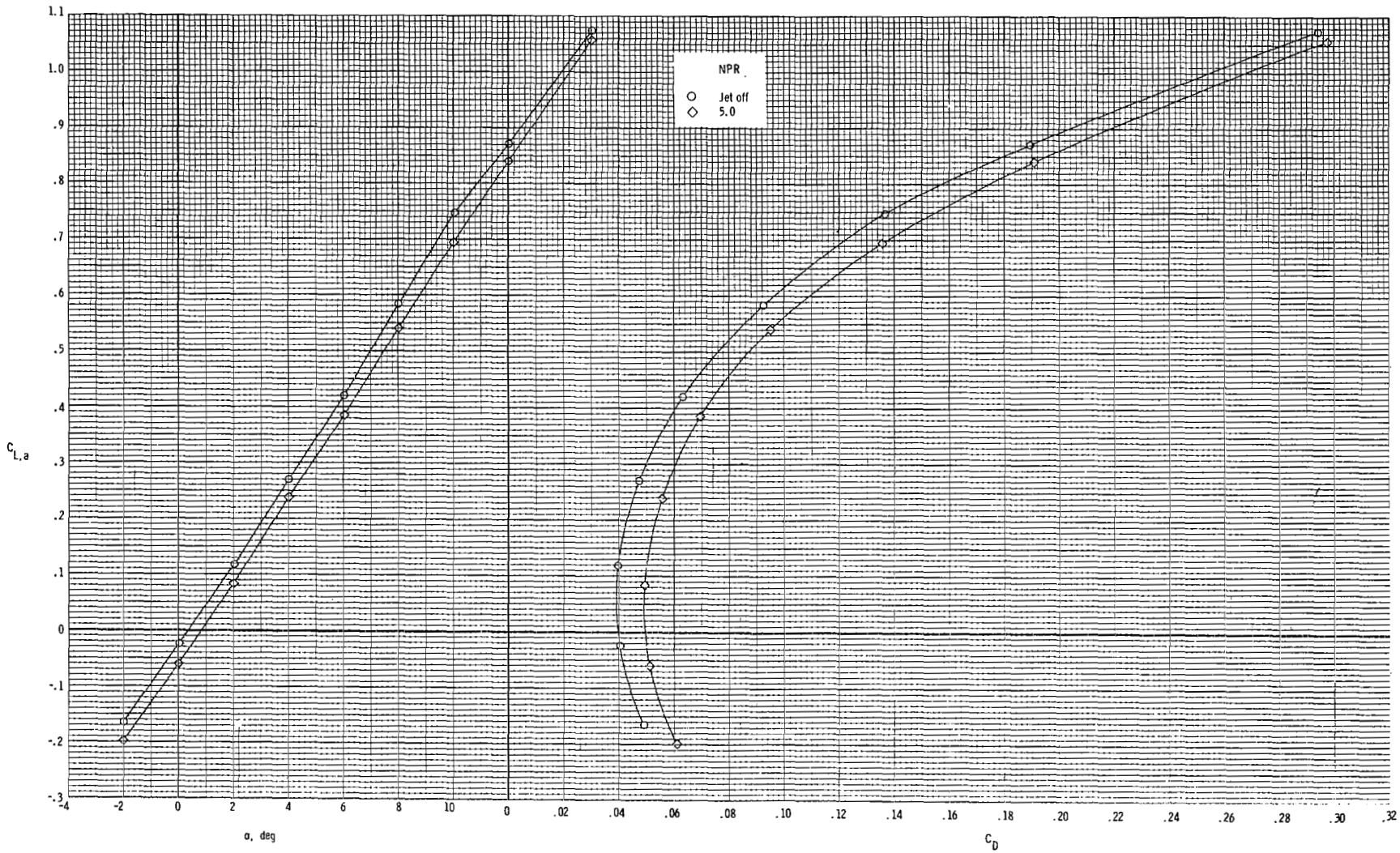

(b) M = 0.90.

Figure 54.- Concluded.

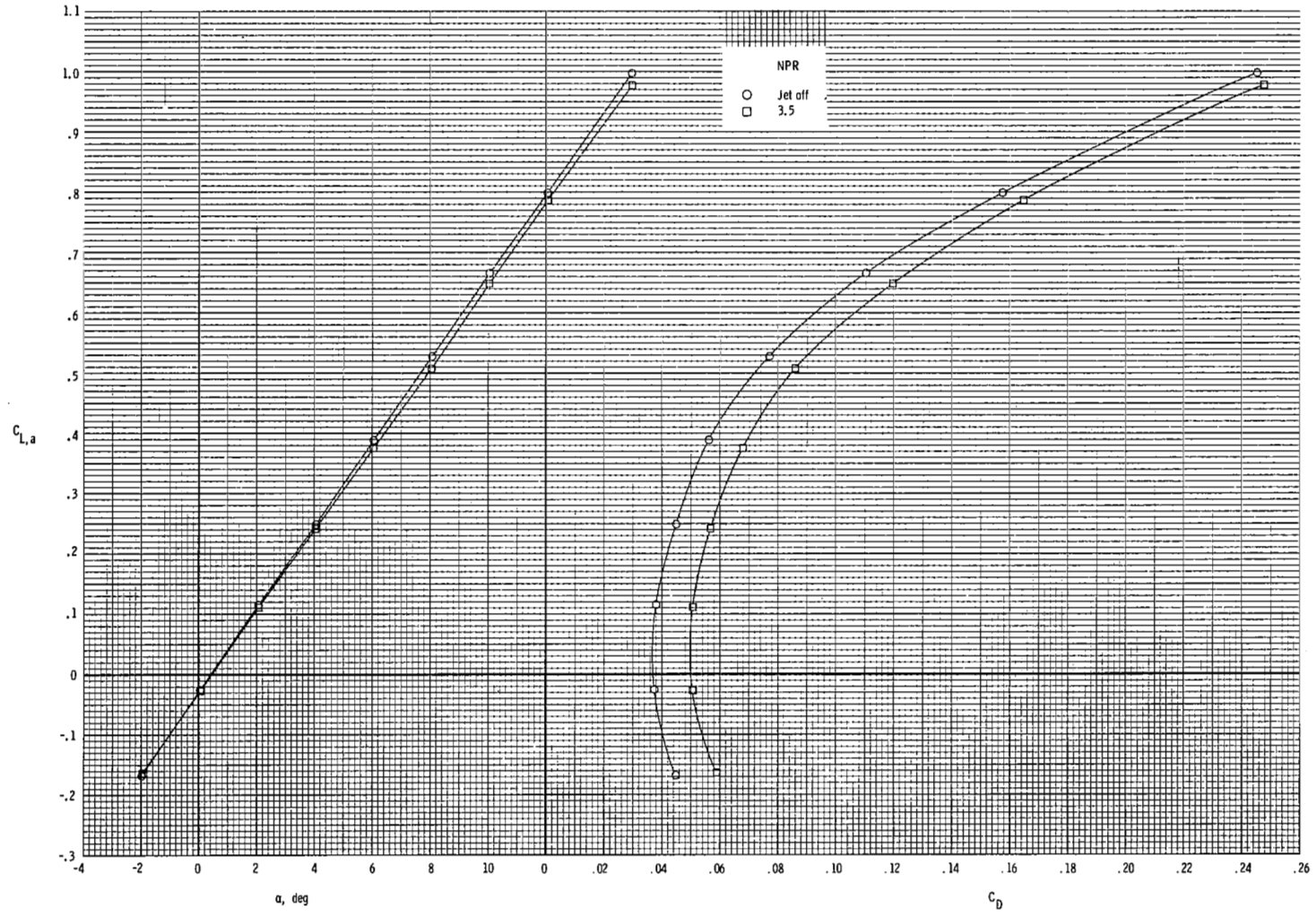

(a) M = 0.60.

Figure 55.- Effect of fully deployed reversers (δ_{REV} = 130°) on thrust-removed longitudinal aerodynamic characteristics of configuration with dry-power 2-D C-D SSW nozzles, nacelle-mounted twin vertical tails, toe angle (L.E. out) of 2°, and modified tail booms.

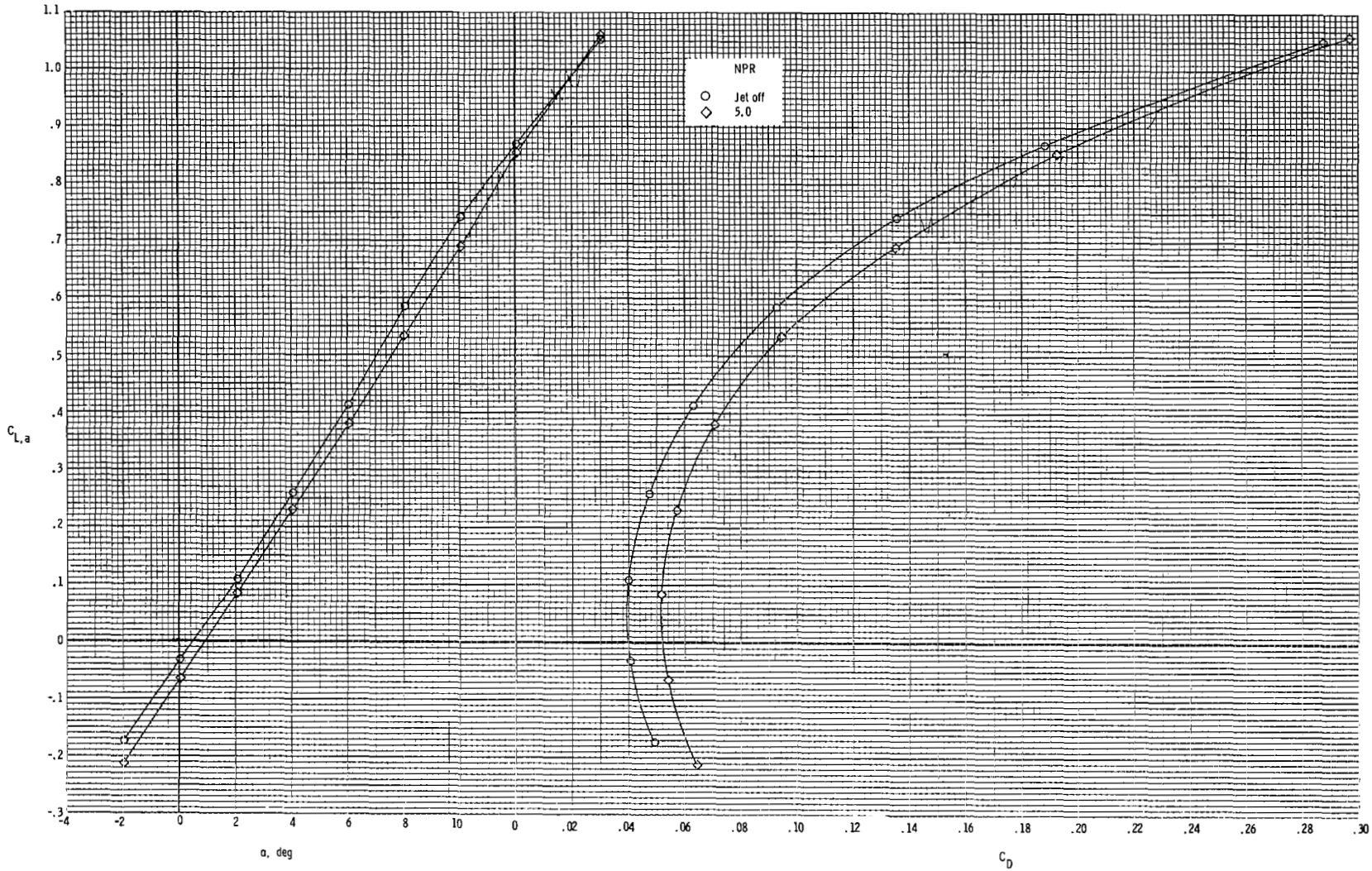

(b) M = 0.90.

Figure 55.- Concluded.

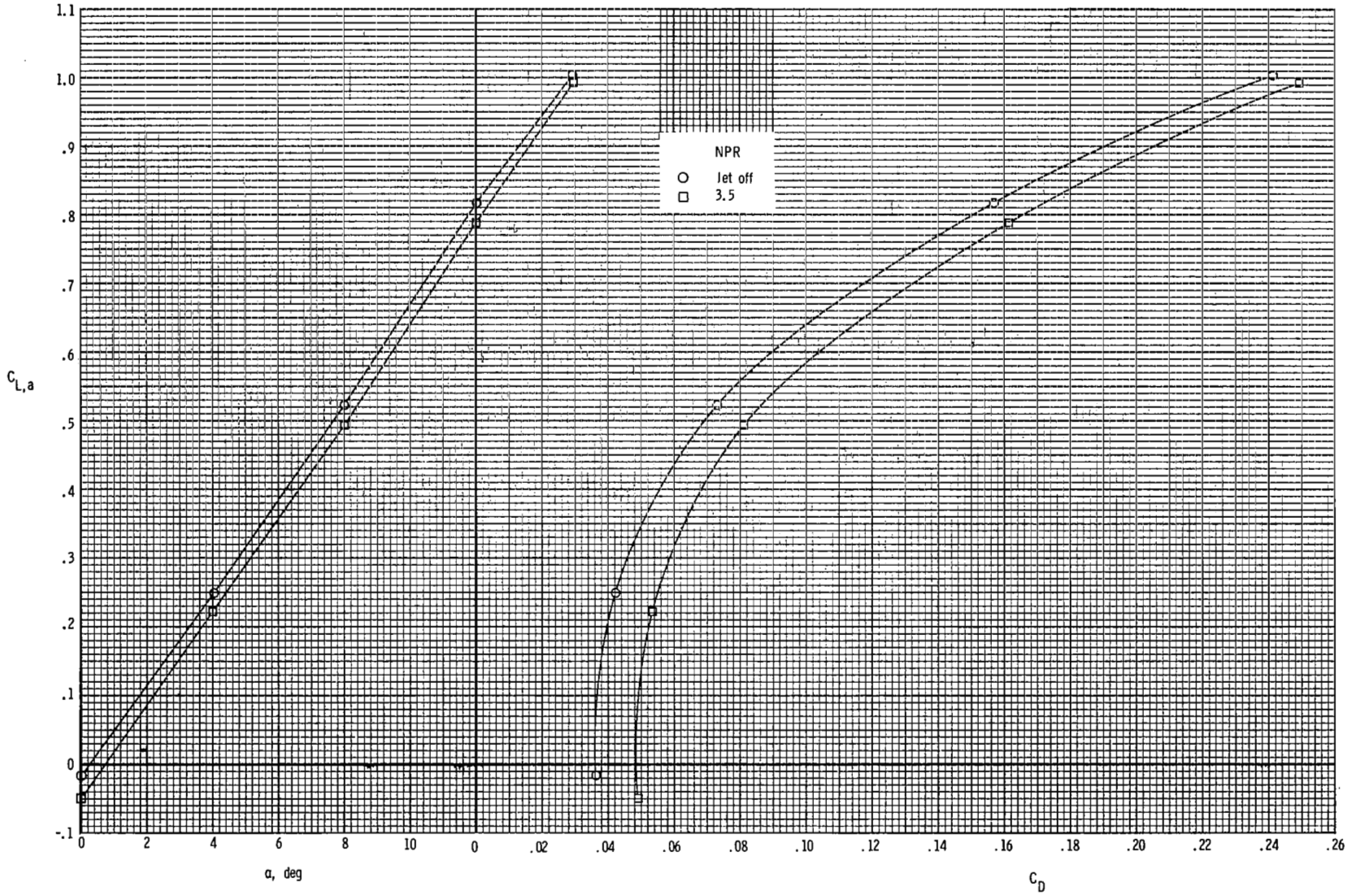

(a) M = 0.60.

Figure 56.- Effect of differential reversing (δ_{REV} = 0° for L.H. and δ_{REV} = 130° for R.H. nozzles) on thrust-removed longitudinal aerodynamic characteristics of configuration with dry-power 2-D C-D SSW nozzles.

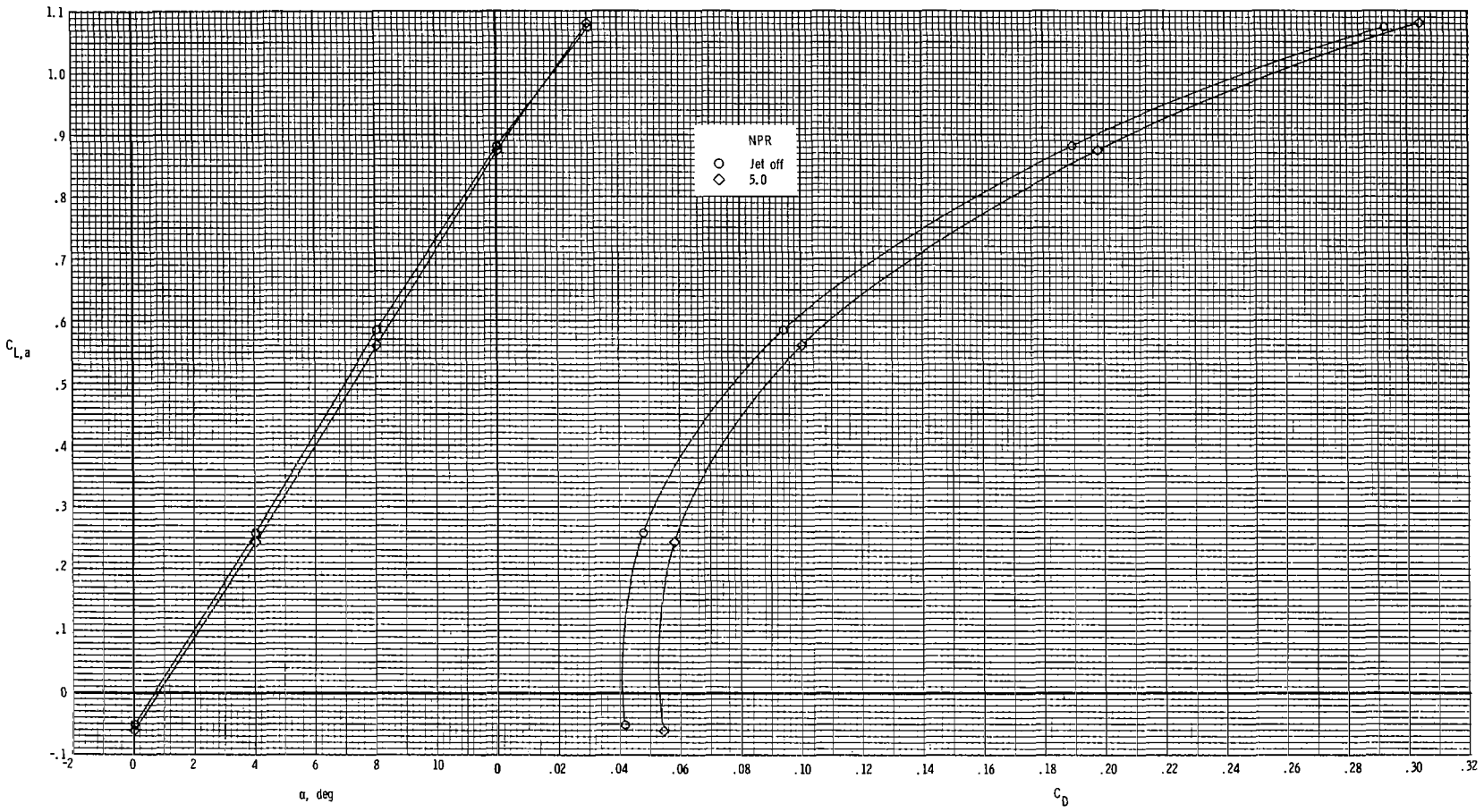

(b) M = 0.90.

Figure 56.- Concluded.

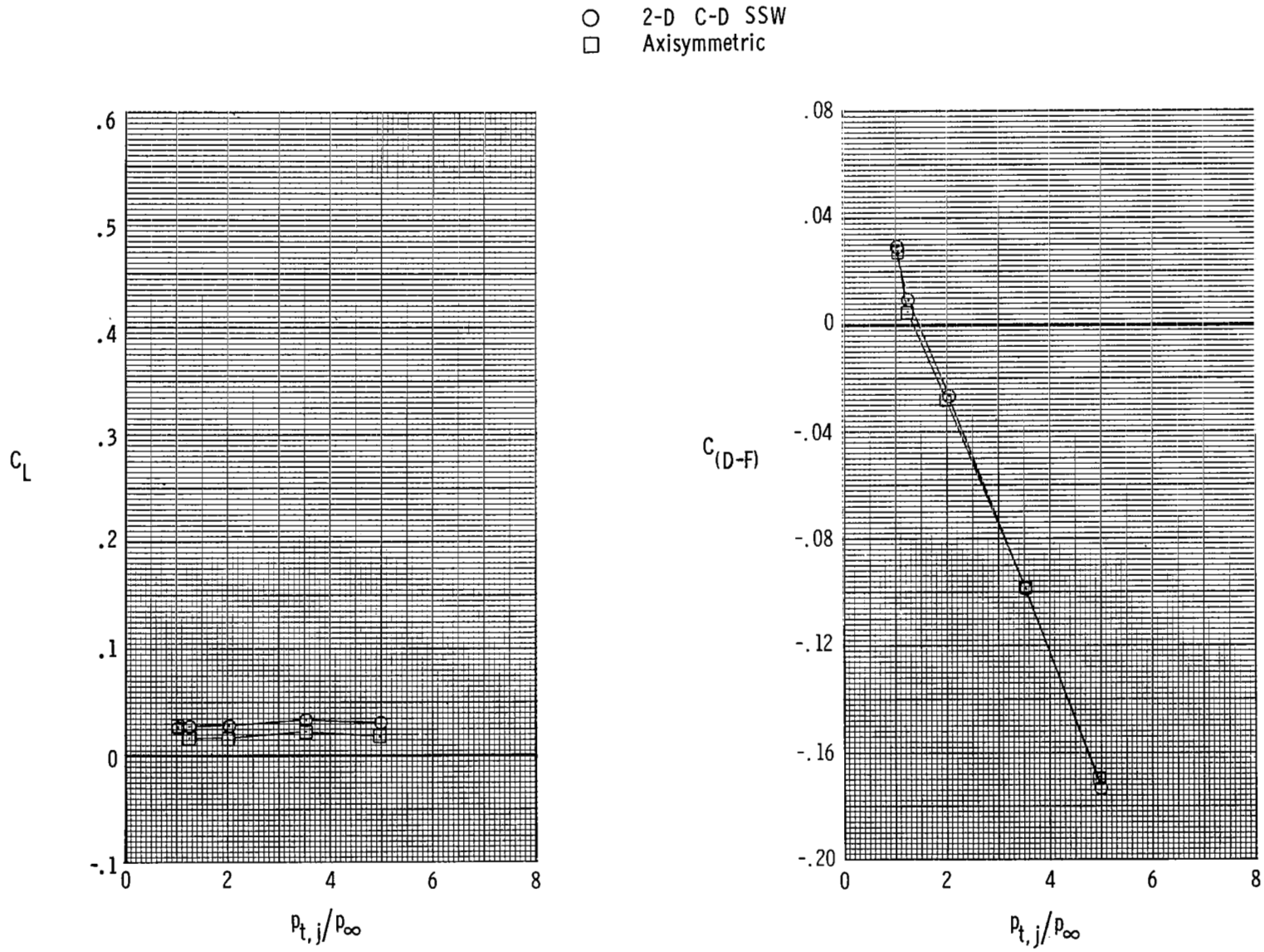

(a) $\alpha = 0°$.

Figure 57.- Effect of axisymmetric and 2-D C-D afterbody/nozzle shapes on drag-minus-thrust performance of configuration with dry-power nozzles at M = 0.60.

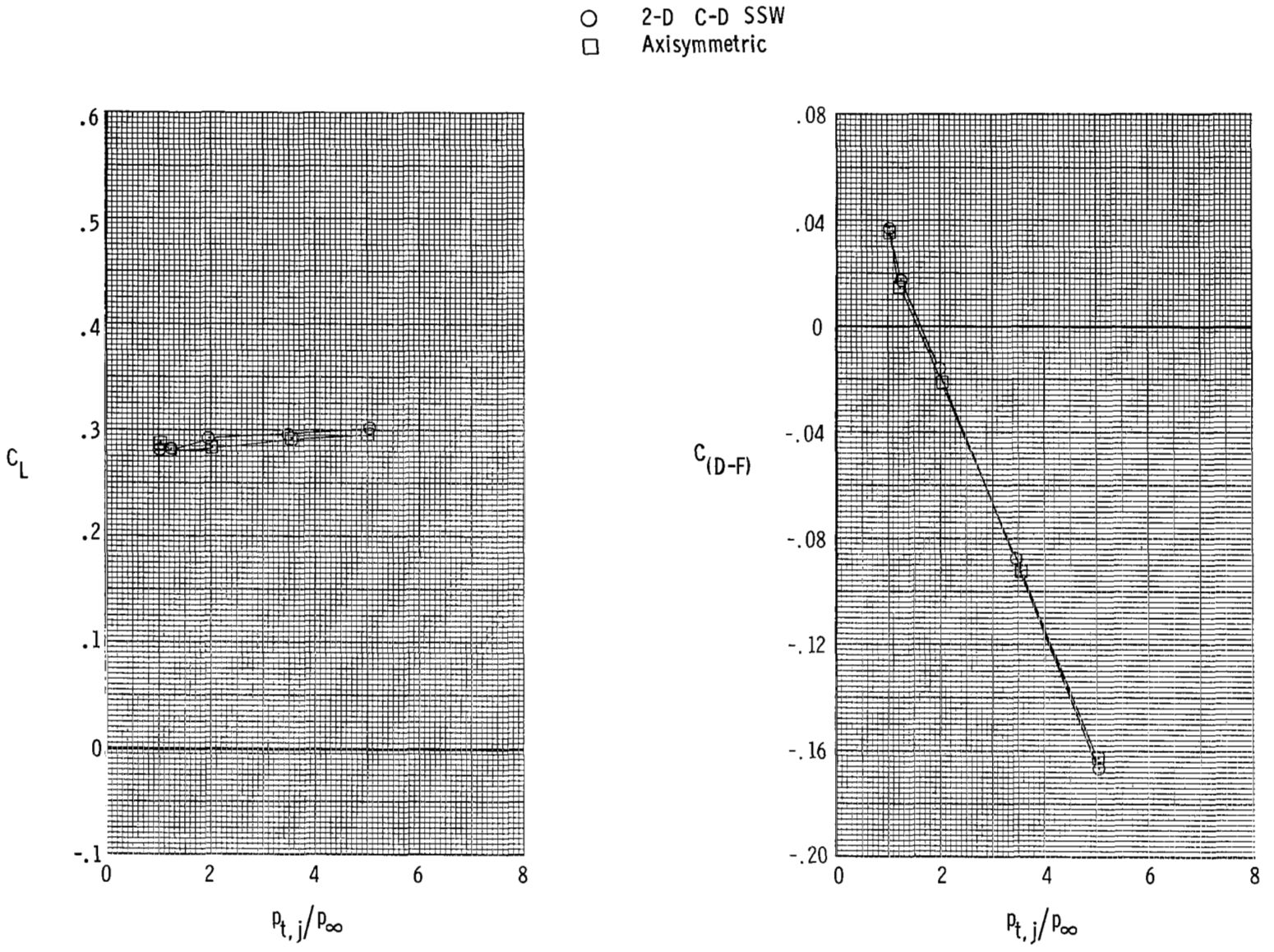

(b) $\alpha = 4°$.

Figure 57.- Continued.

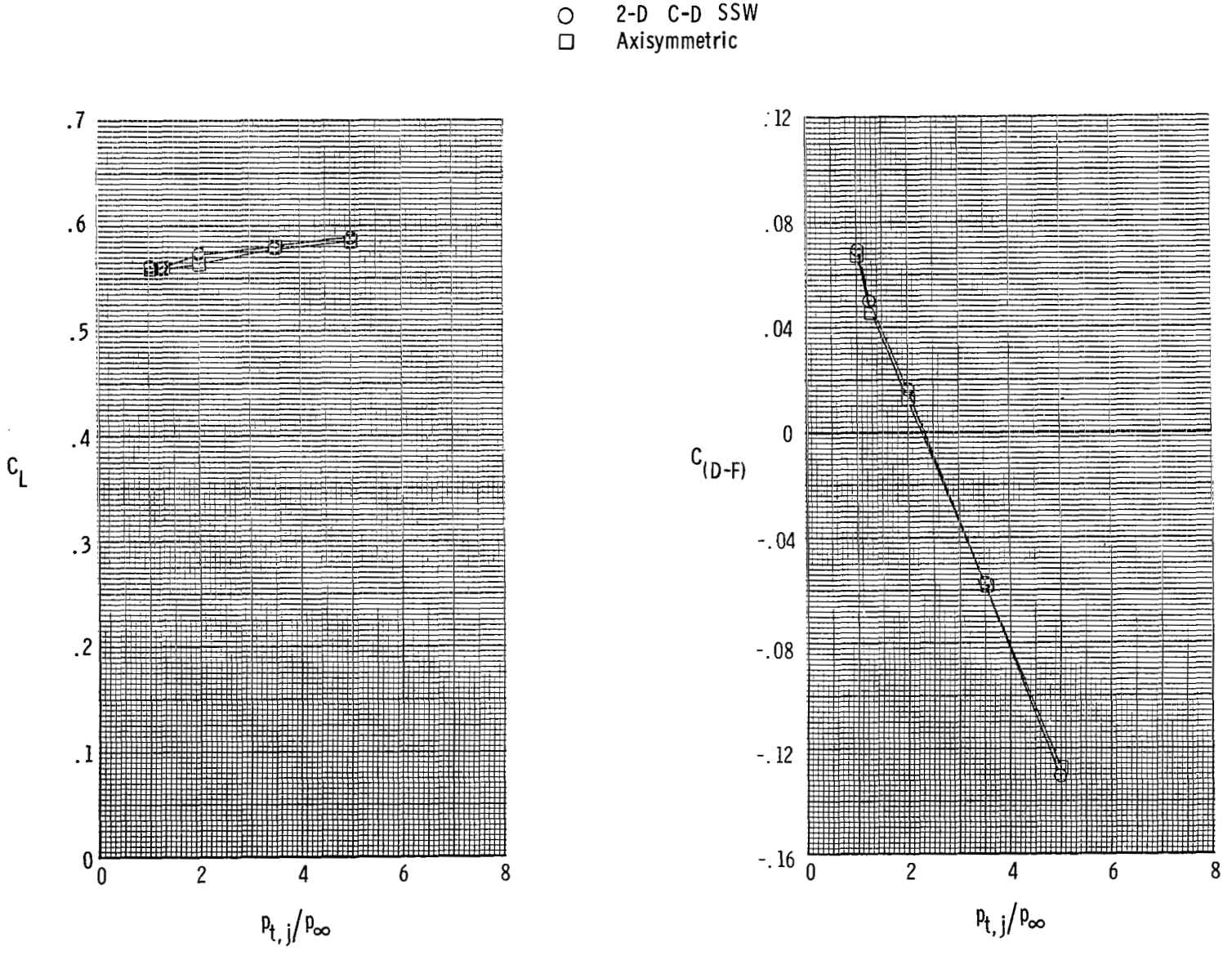

(c) $\alpha = 8°$.

Figure 57.- Continued.

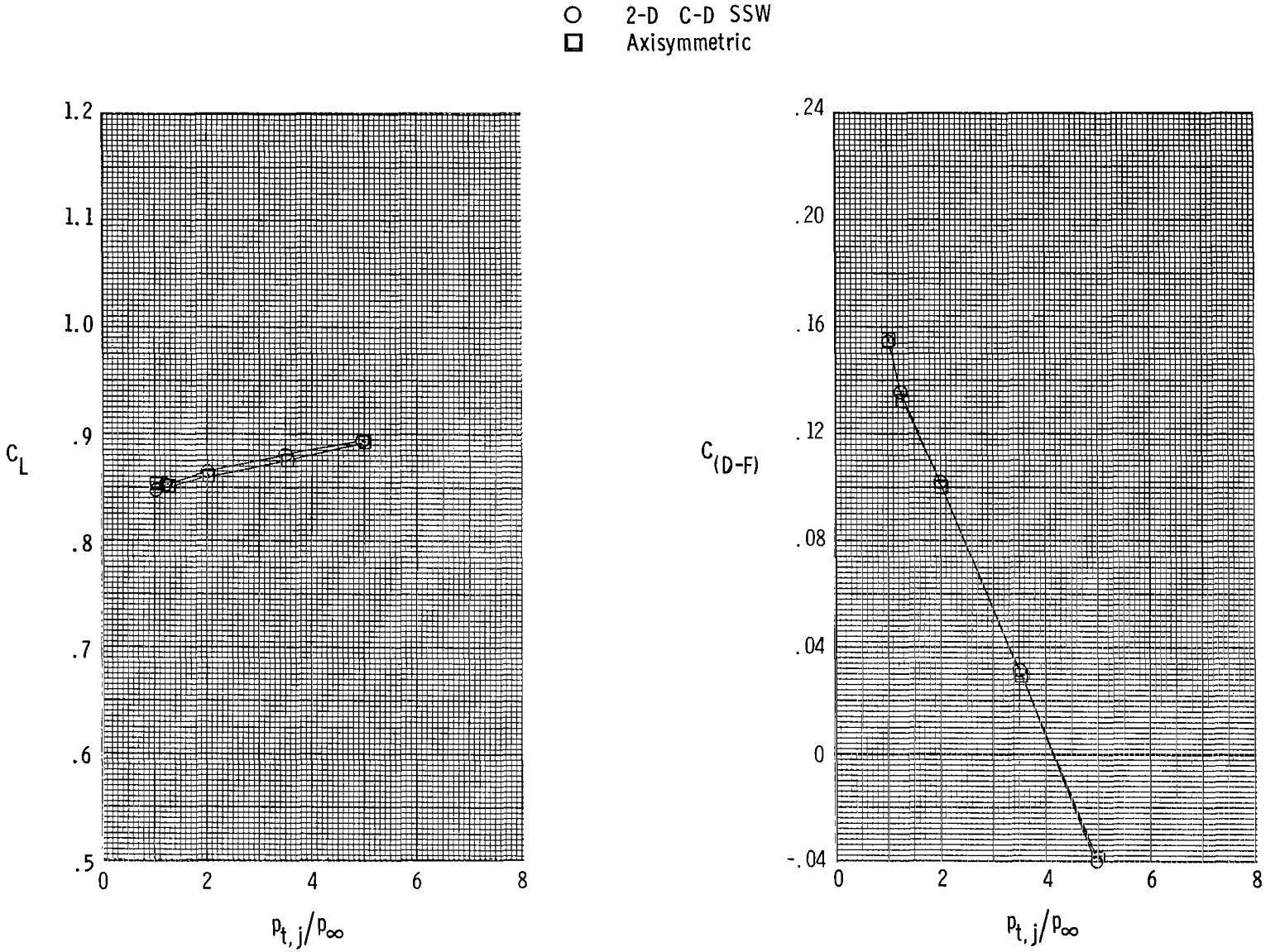

(d) $\alpha = 12°$.

Figure 57.- Continued.

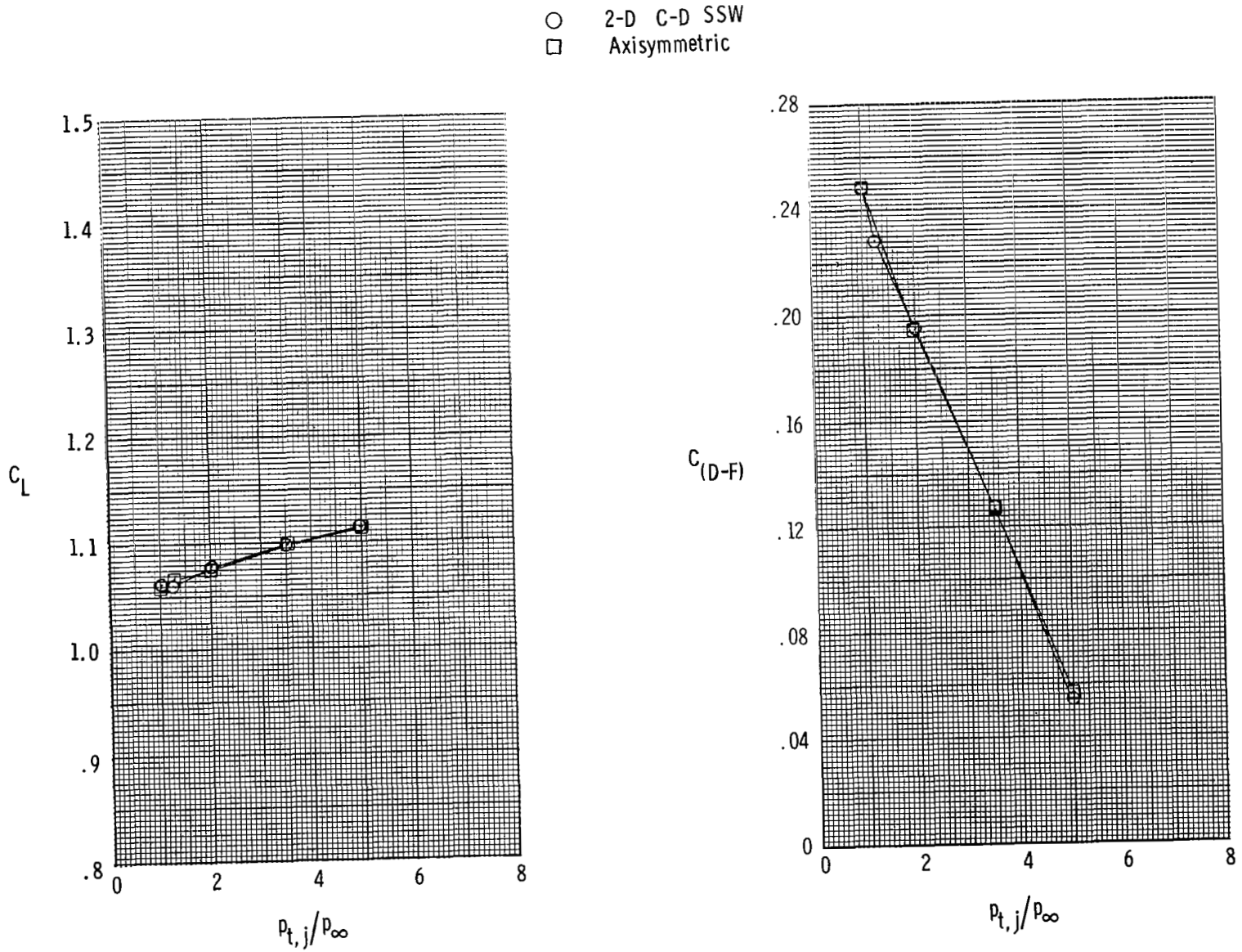

(e) $\alpha = 15°$.

Figure 57.- Concluded.

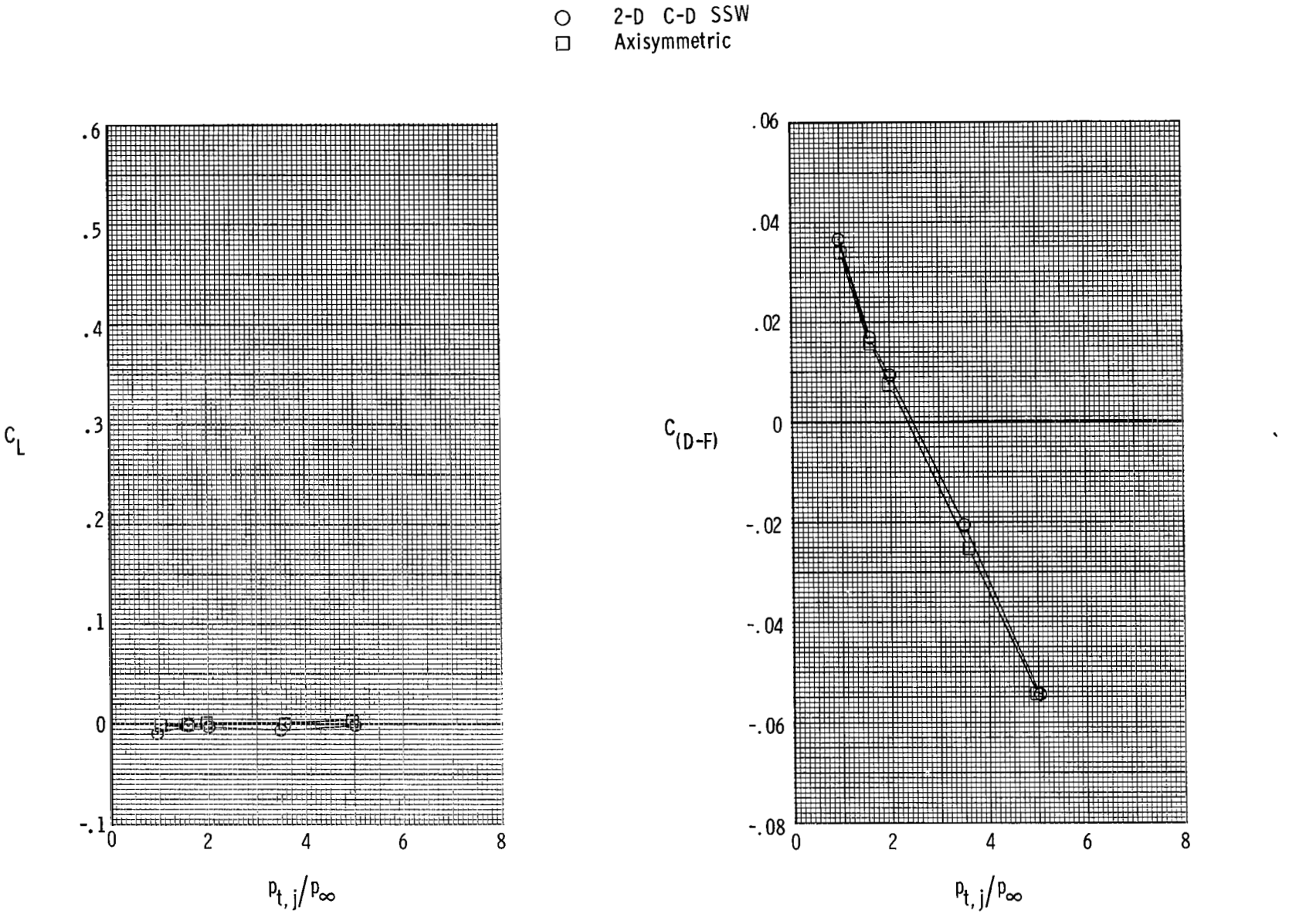

(a) $\alpha = 0°$.

Figure 58.- Effect of axisymmetric and 2-D C-D afterbody/nozzle shapes on drag-minus-thrust performance of configuration with dry-power nozzles at M = 0.90.

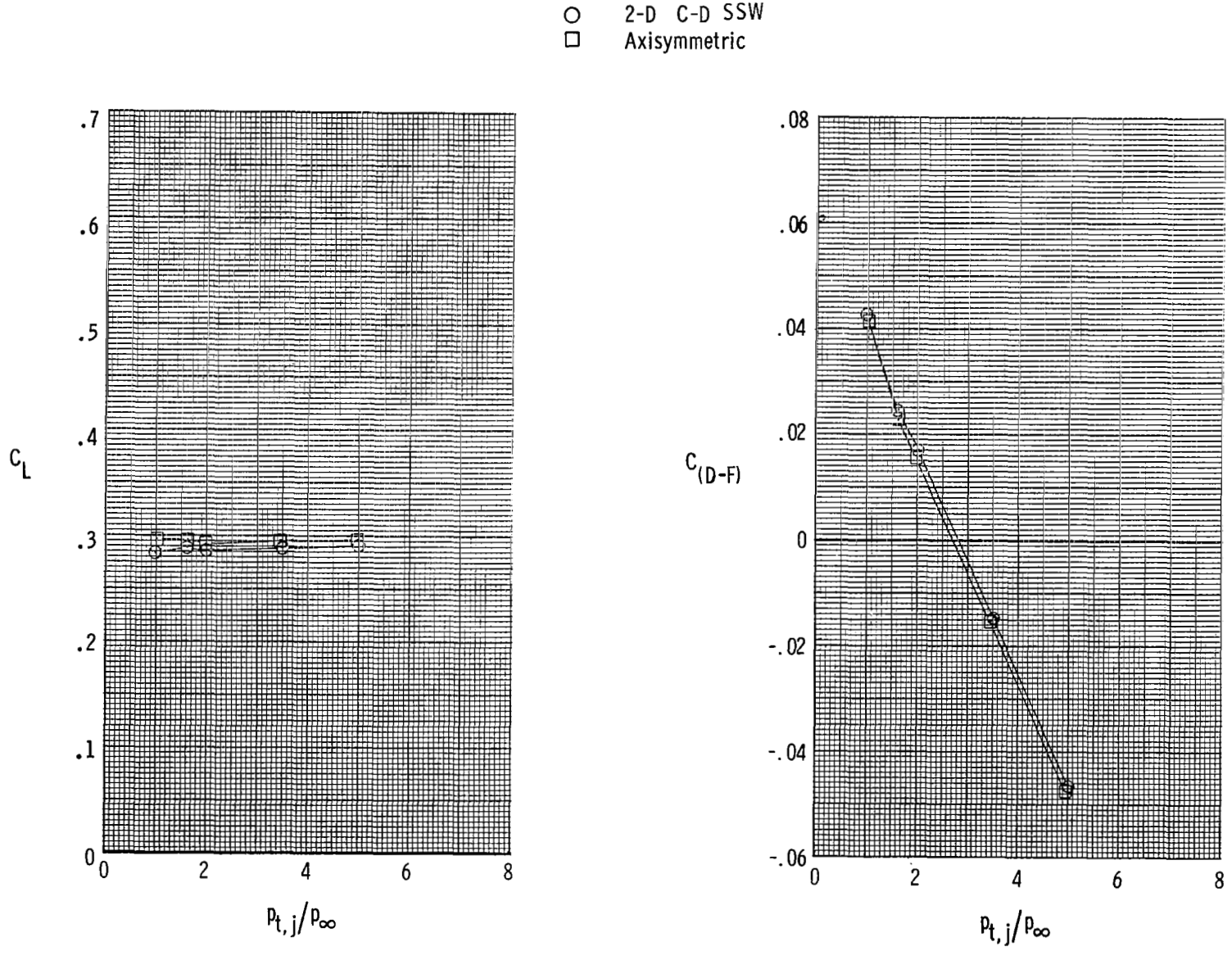

(b) $\alpha = 4°$.

Figure 58.- Continued.

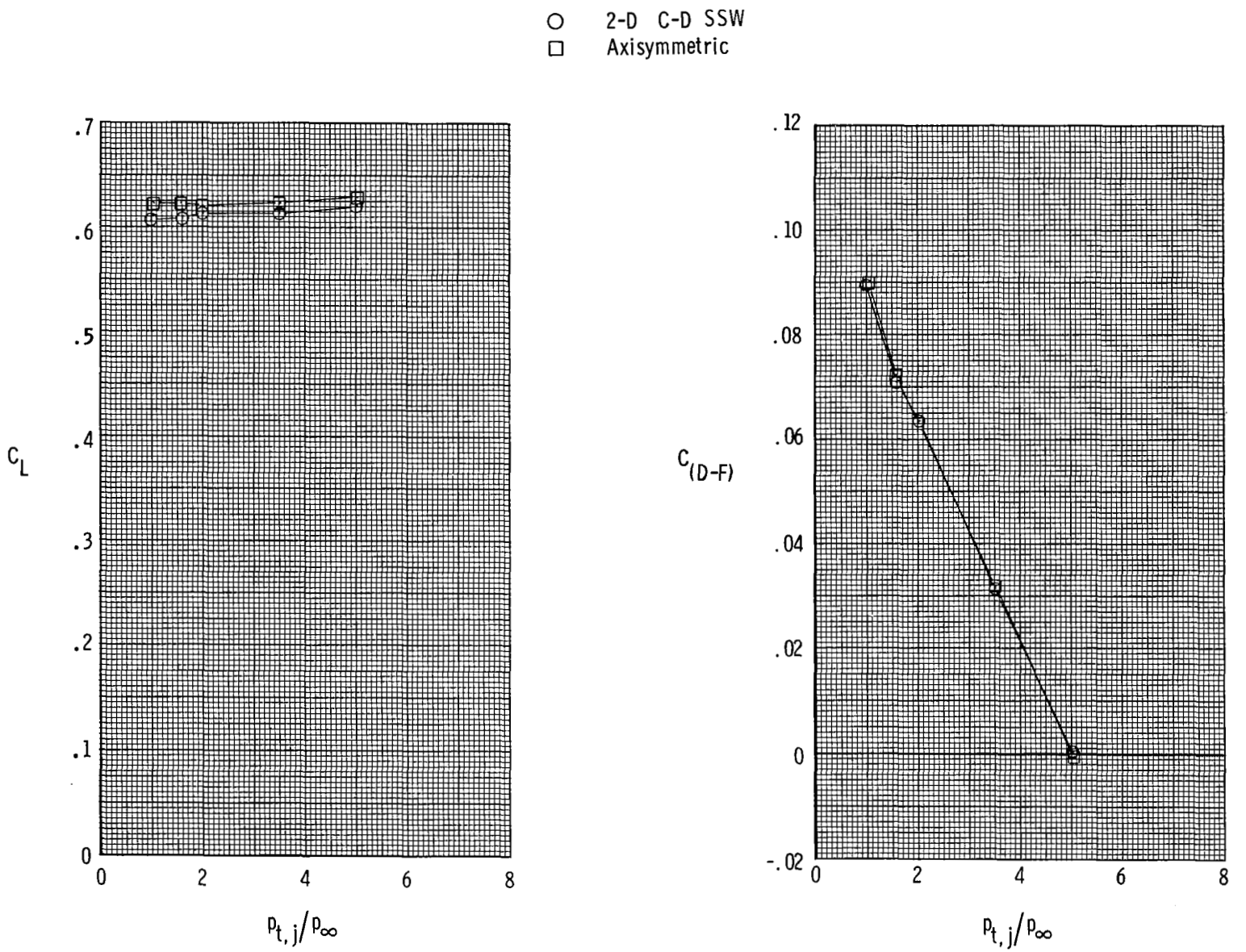

(c) $\alpha = 8°$.

Figure 58.- Continued.

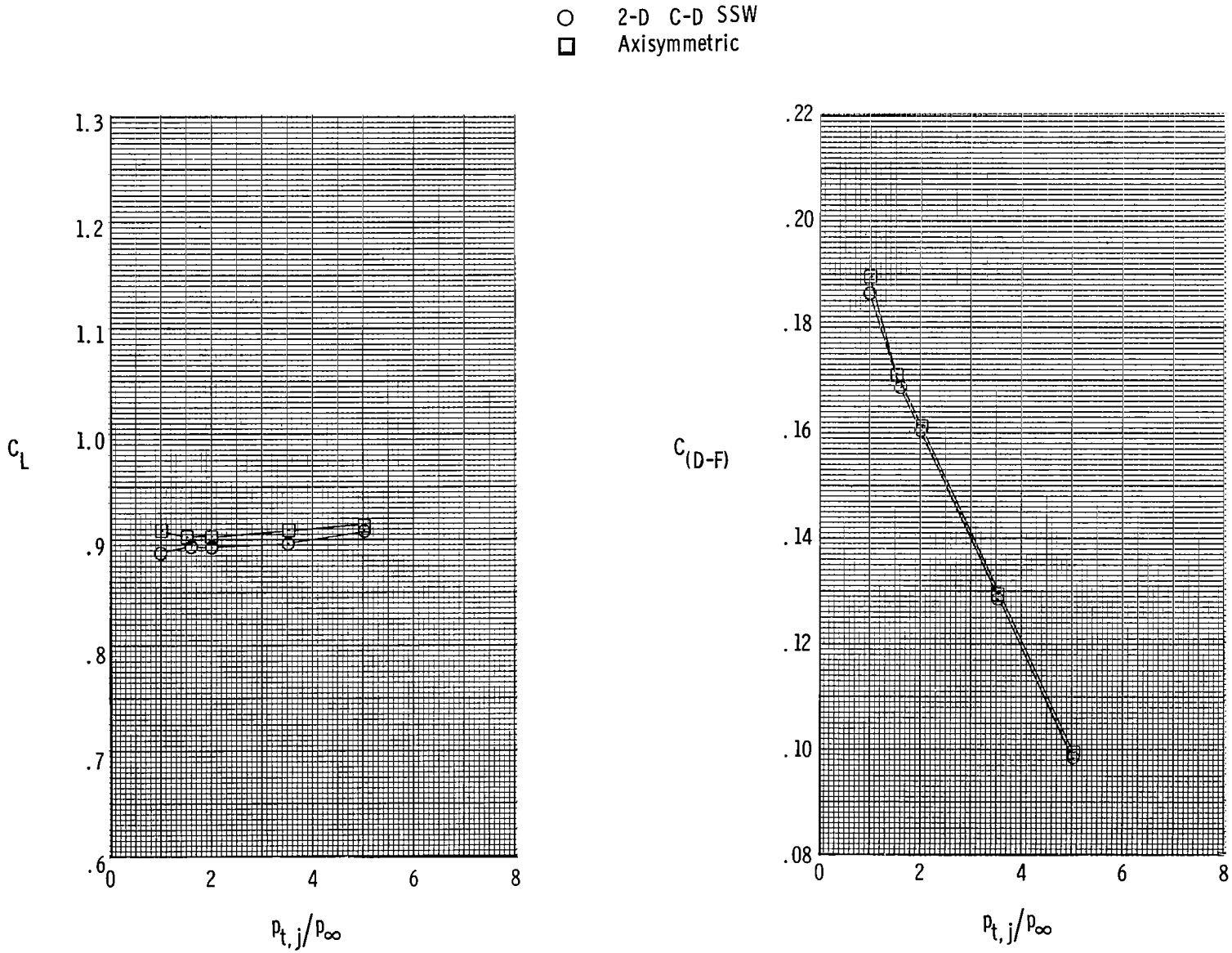

(d) $\alpha = 12°$.

Figure 58.- Continued.

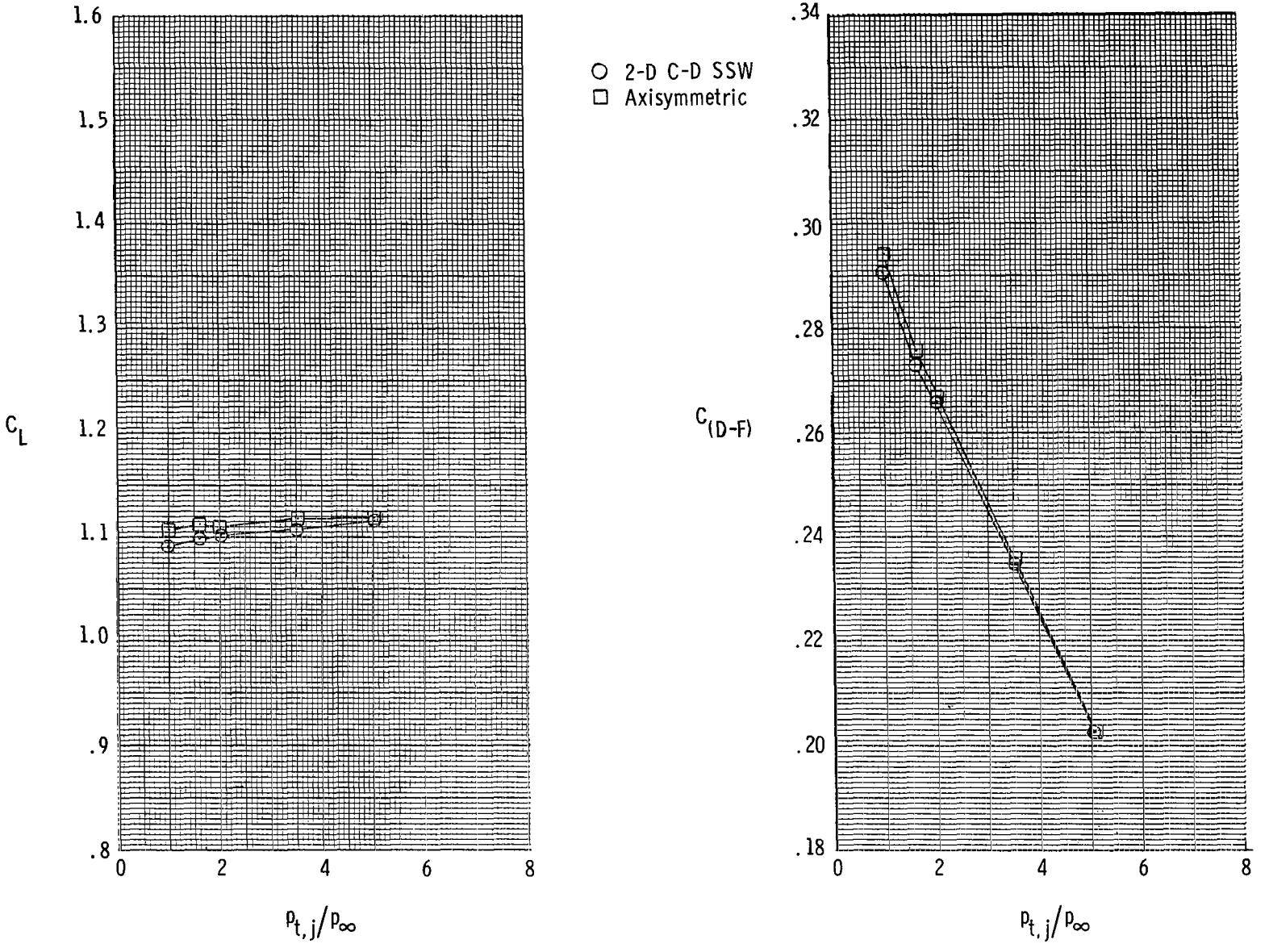

(e) $\alpha = 15°$.

Figure 58.- Concluded.

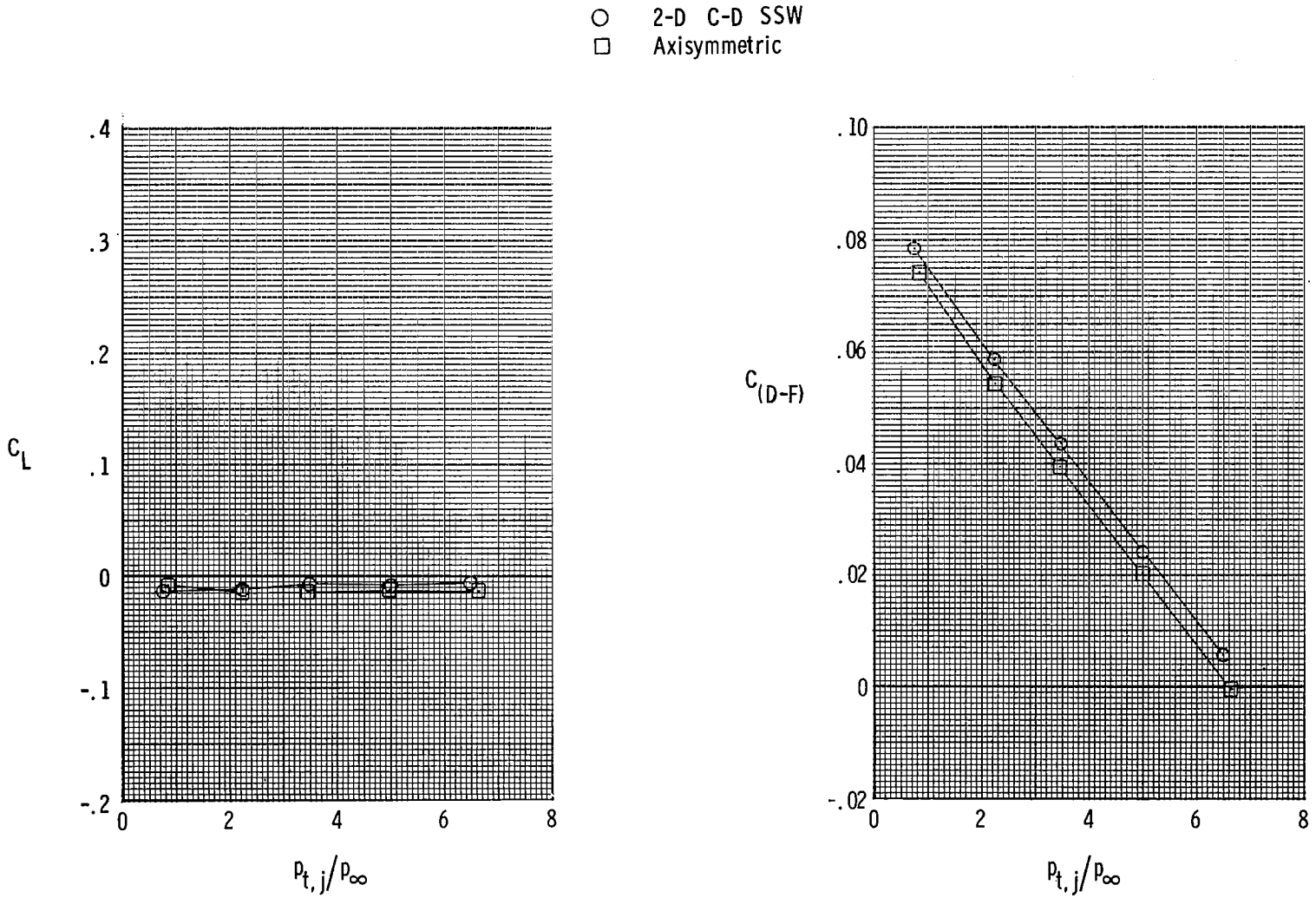

(a) $\alpha = 0°$.

Figure 59.- Effect of axisymmetric and 2-D C-D afterbody/nozzle shapes on drag-minus-thrust performance of configuration with dry-power nozzles at M = 1.20.

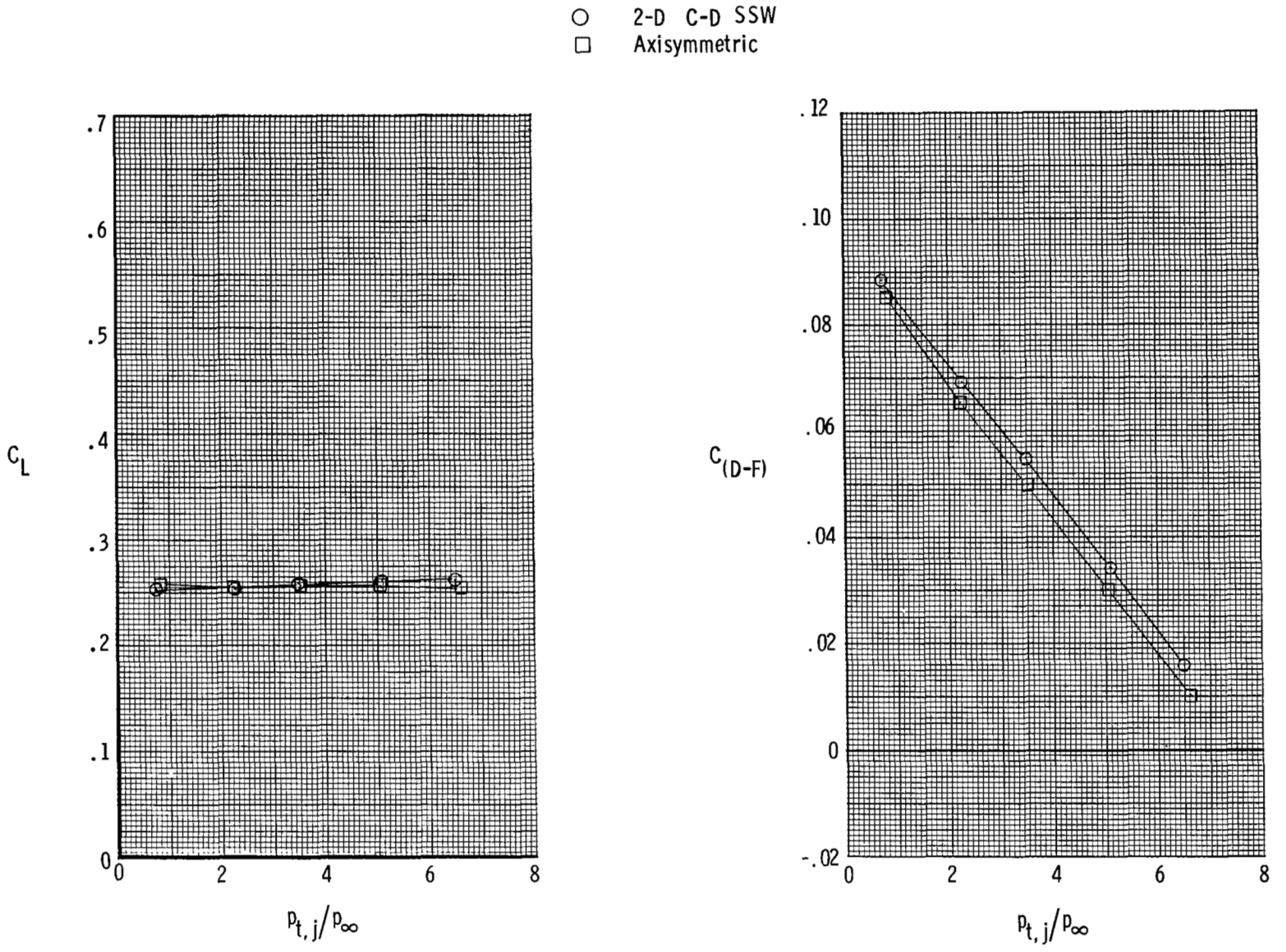

(b) $\alpha = 4°$.

Figure 59.- Continued.

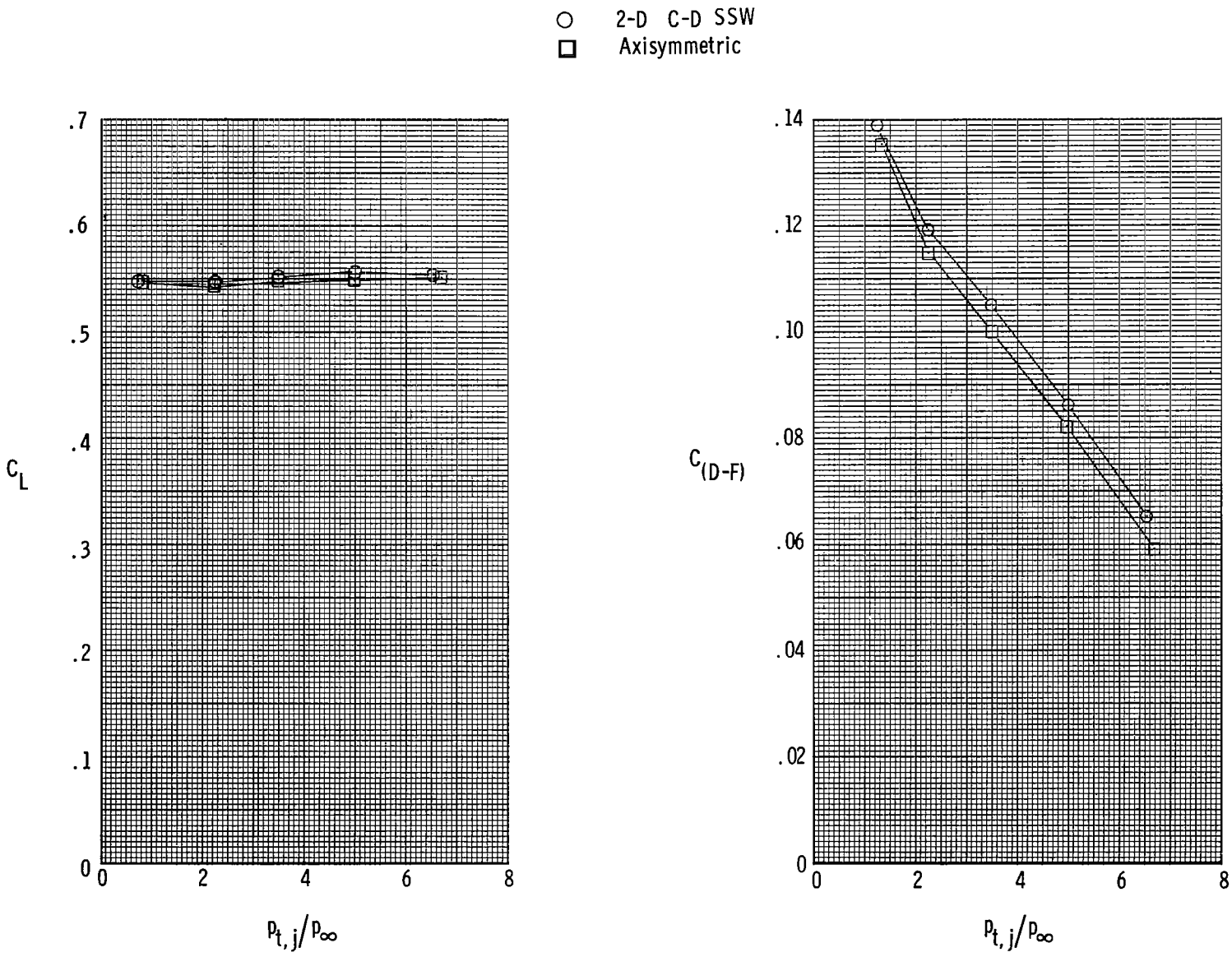

(c) $\alpha = 8°$.

Figure 59.- Concluded.

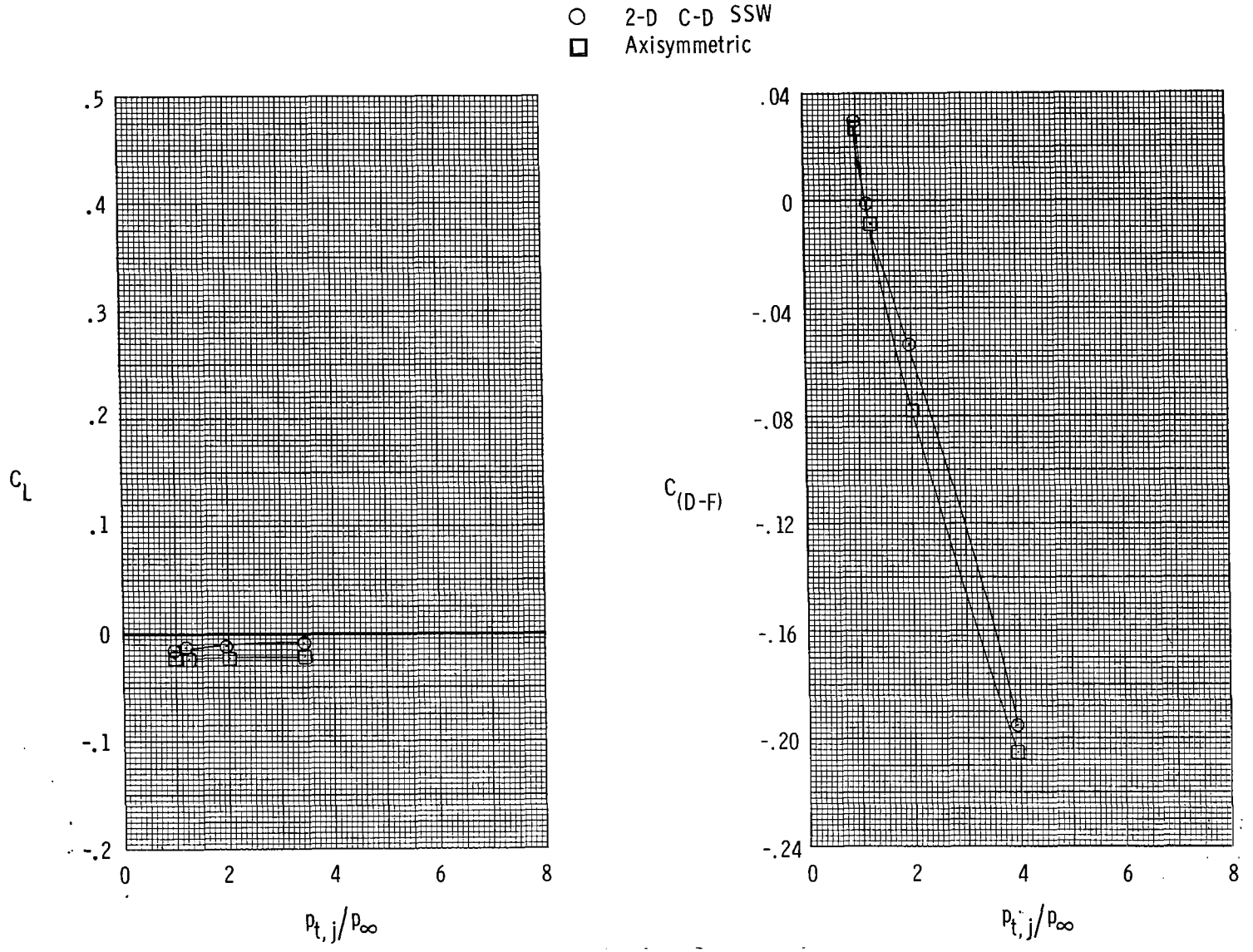

(a) M = 0.60.

Figure 60.- Effect of axisymmetric and 2-D C-D afterbody/nozzle shapes on drag-minus-thrust performance of configuration with maximum-afterburning-power nozzles at $\alpha = 0°$.

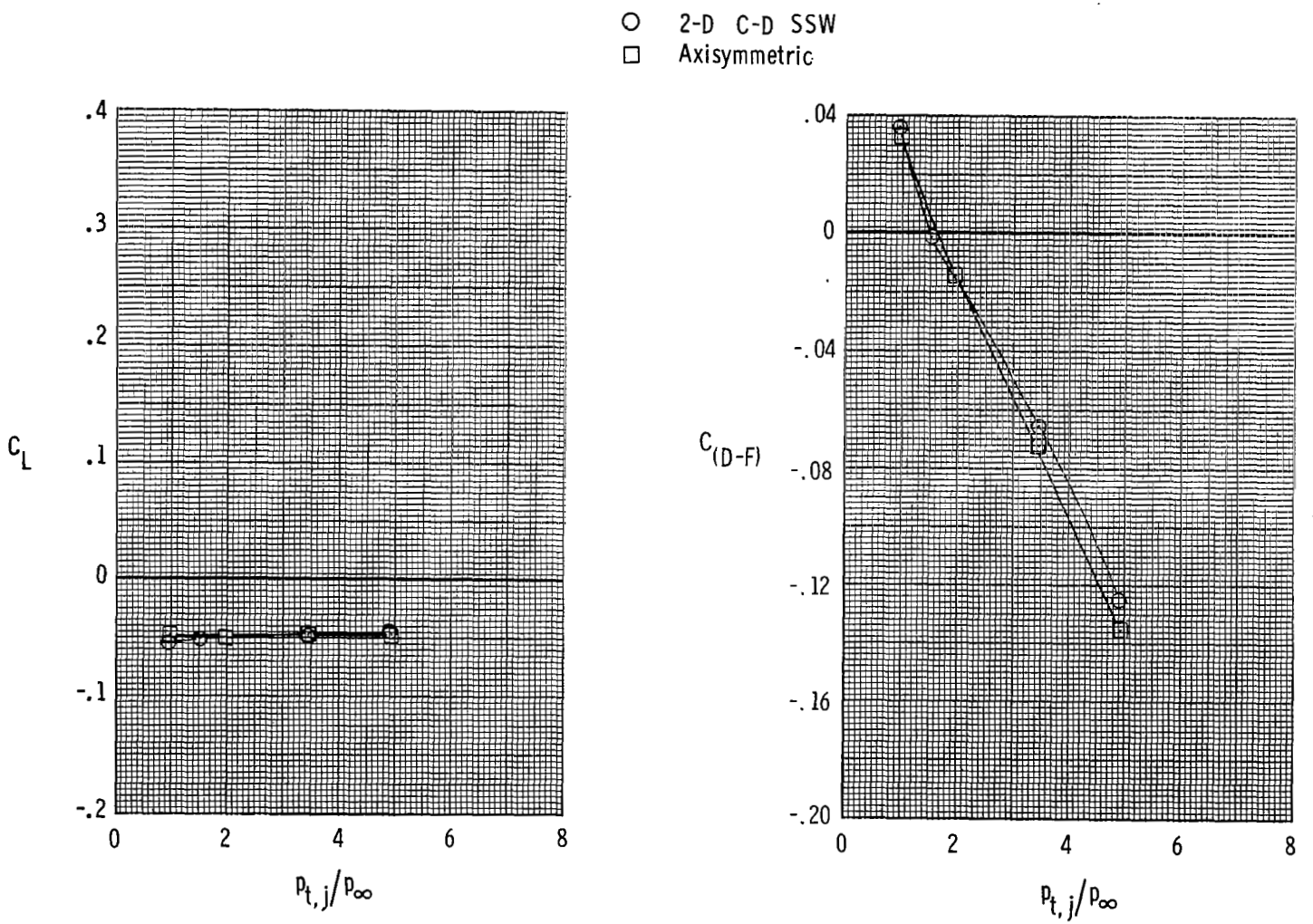

(b) M = 0.90.

Figure 60.- Concluded.

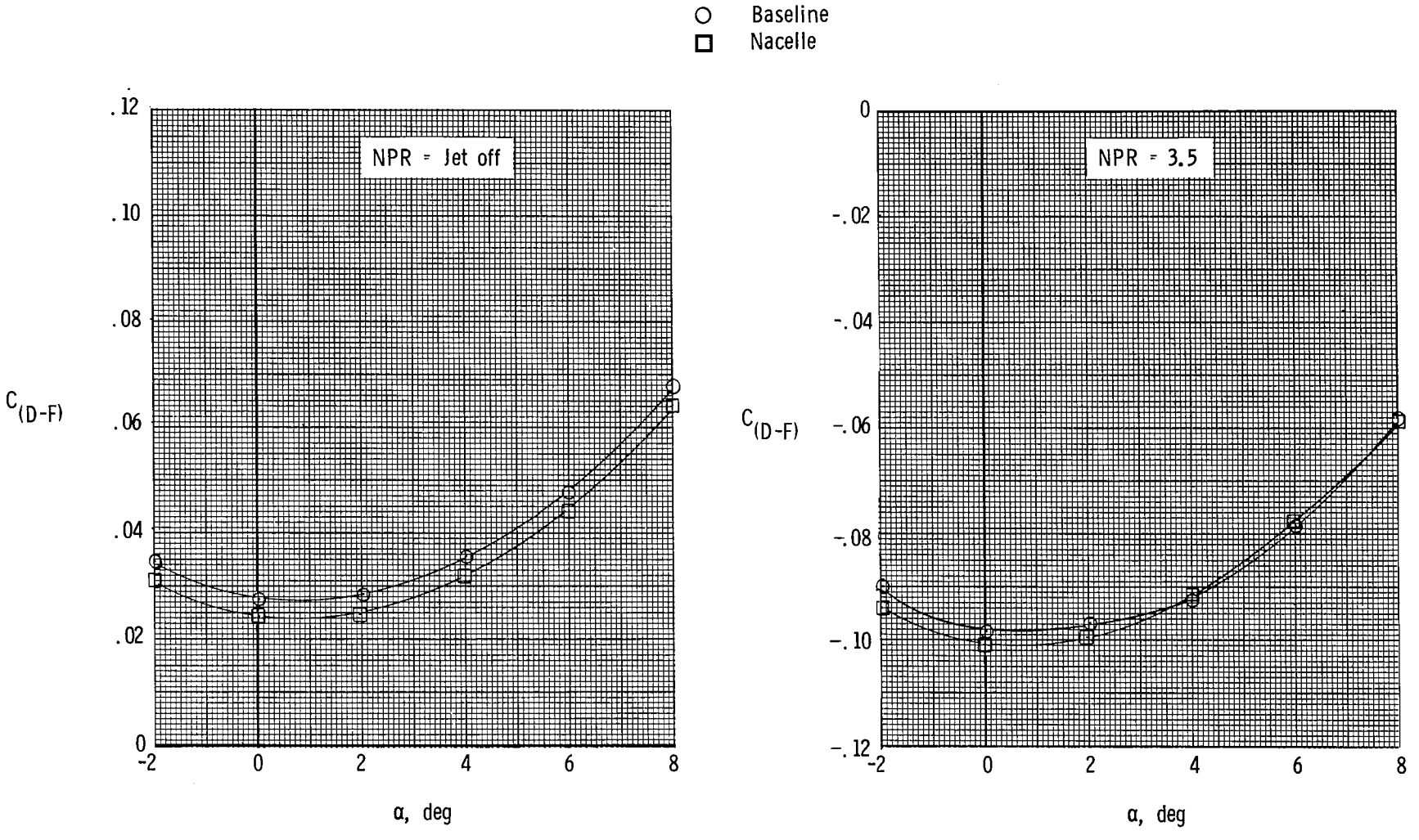

(a) M = 0.60.

Figure 61.- Effect of twin-vertical-tail location on drag-minus-thrust performance of configuration with axisymmetric dry-power nozzles and twin-vertical-tail toe angle (L.E. out) of 2°.

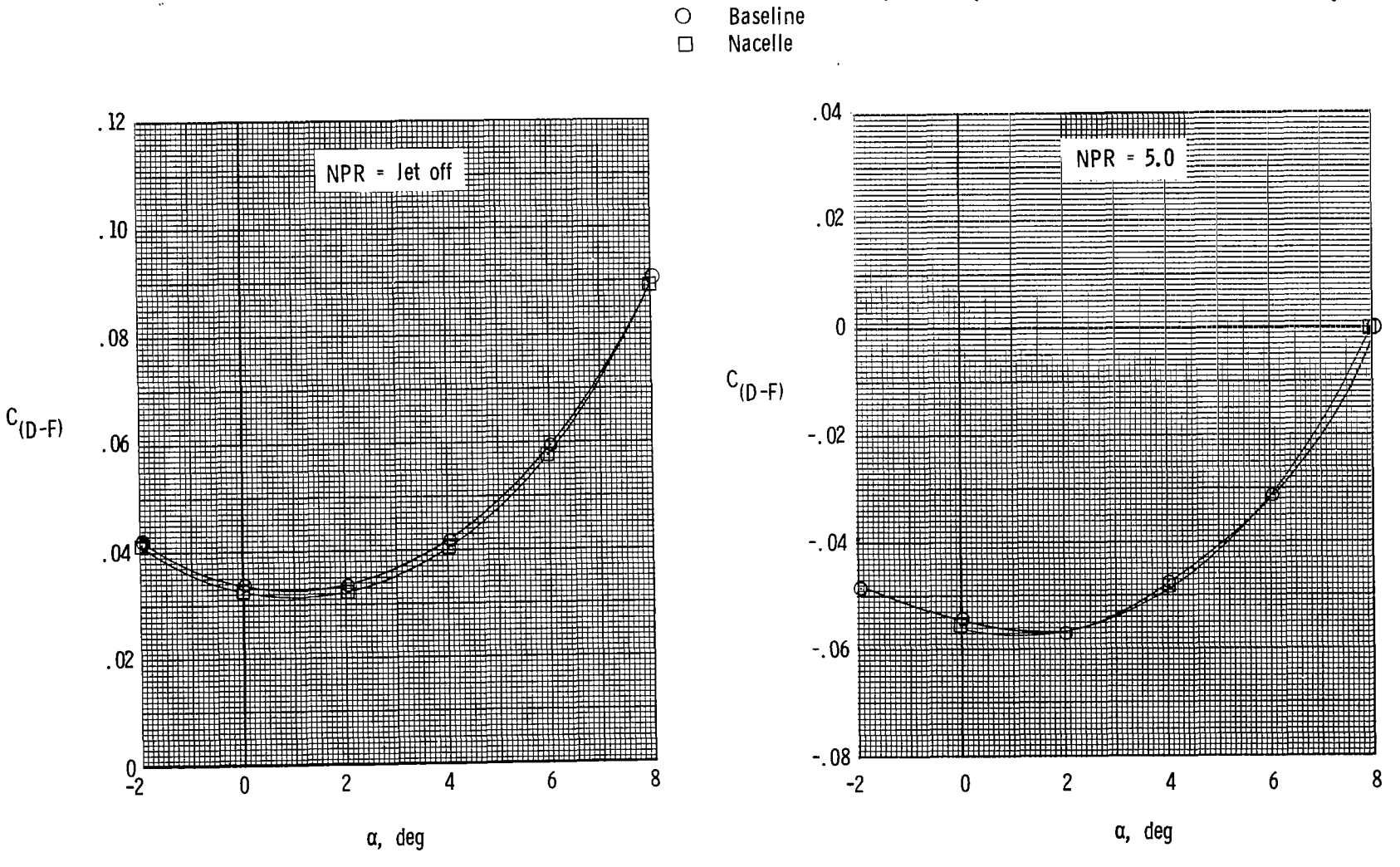

(b) M = 0.90.

Figure 61.- Concluded.

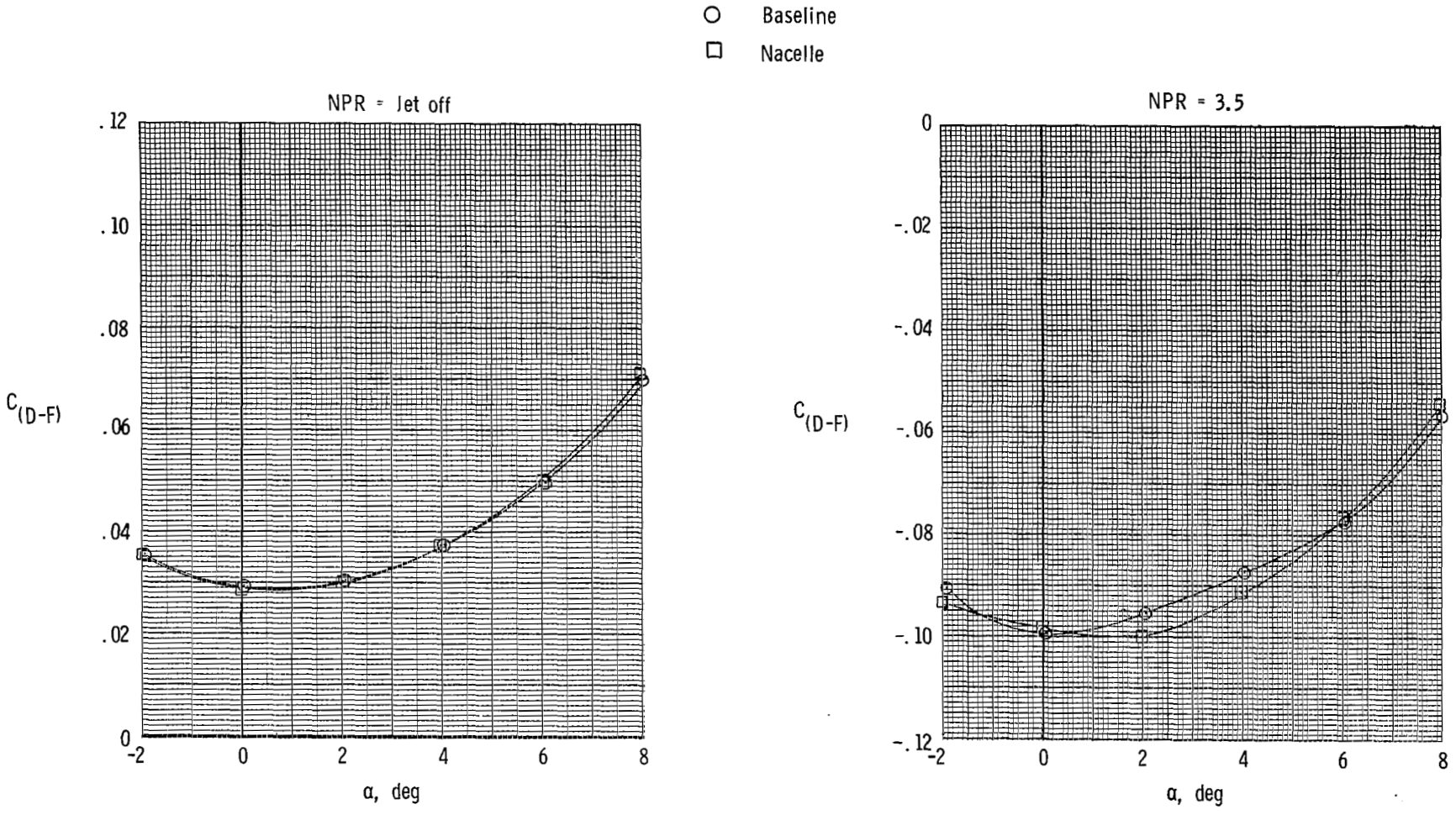

(a) M = 0.60.

Figure 62.- Effect of twin-vertical-tail location on drag-minus-thrust performance of configuration with 2-D C-D SSW dry-power nozzles and twin-vertical-tail toe angle (L.E. out) of 2°.

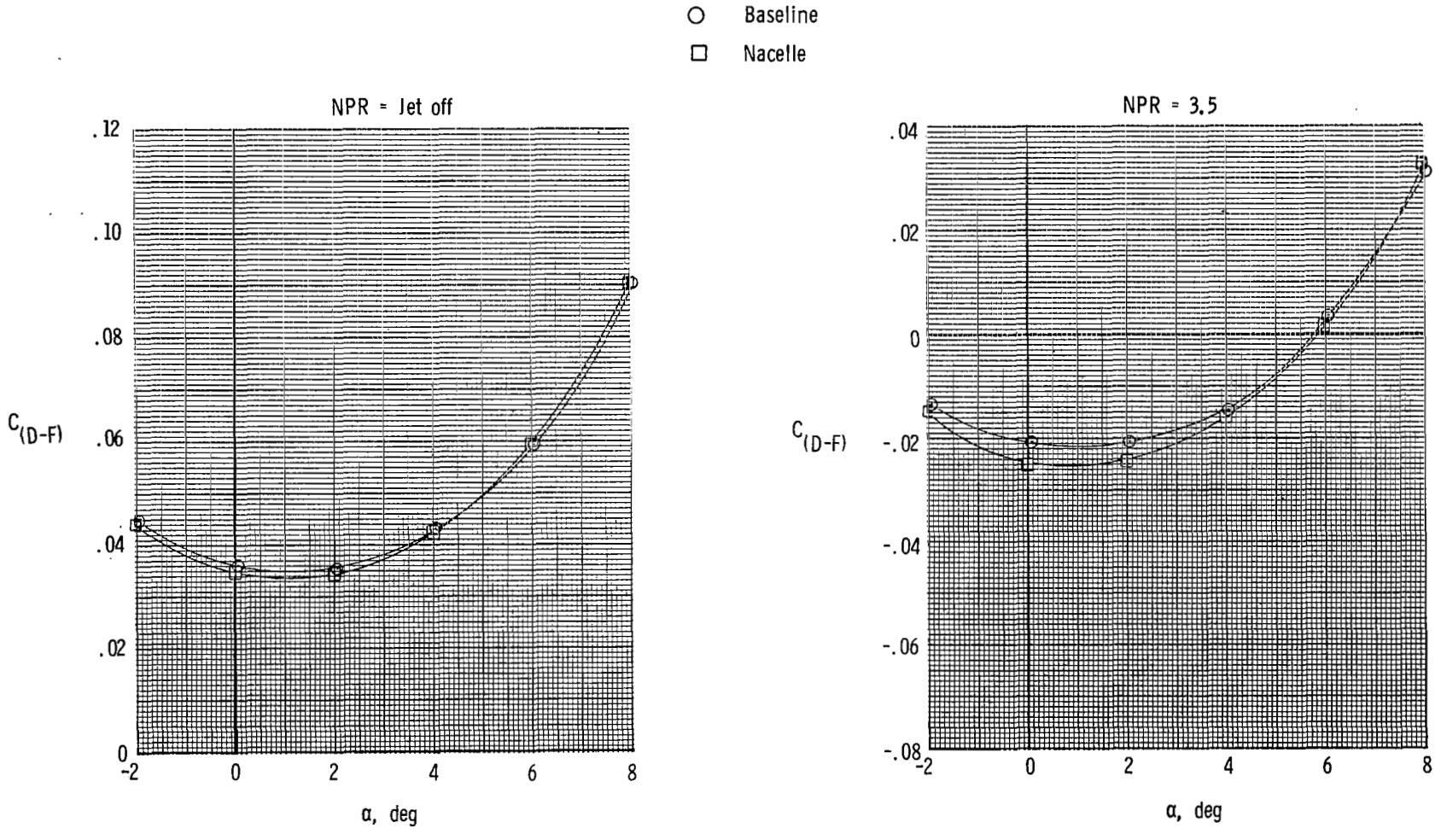

(b) M = 0.90.

Figure 62.- Concluded.

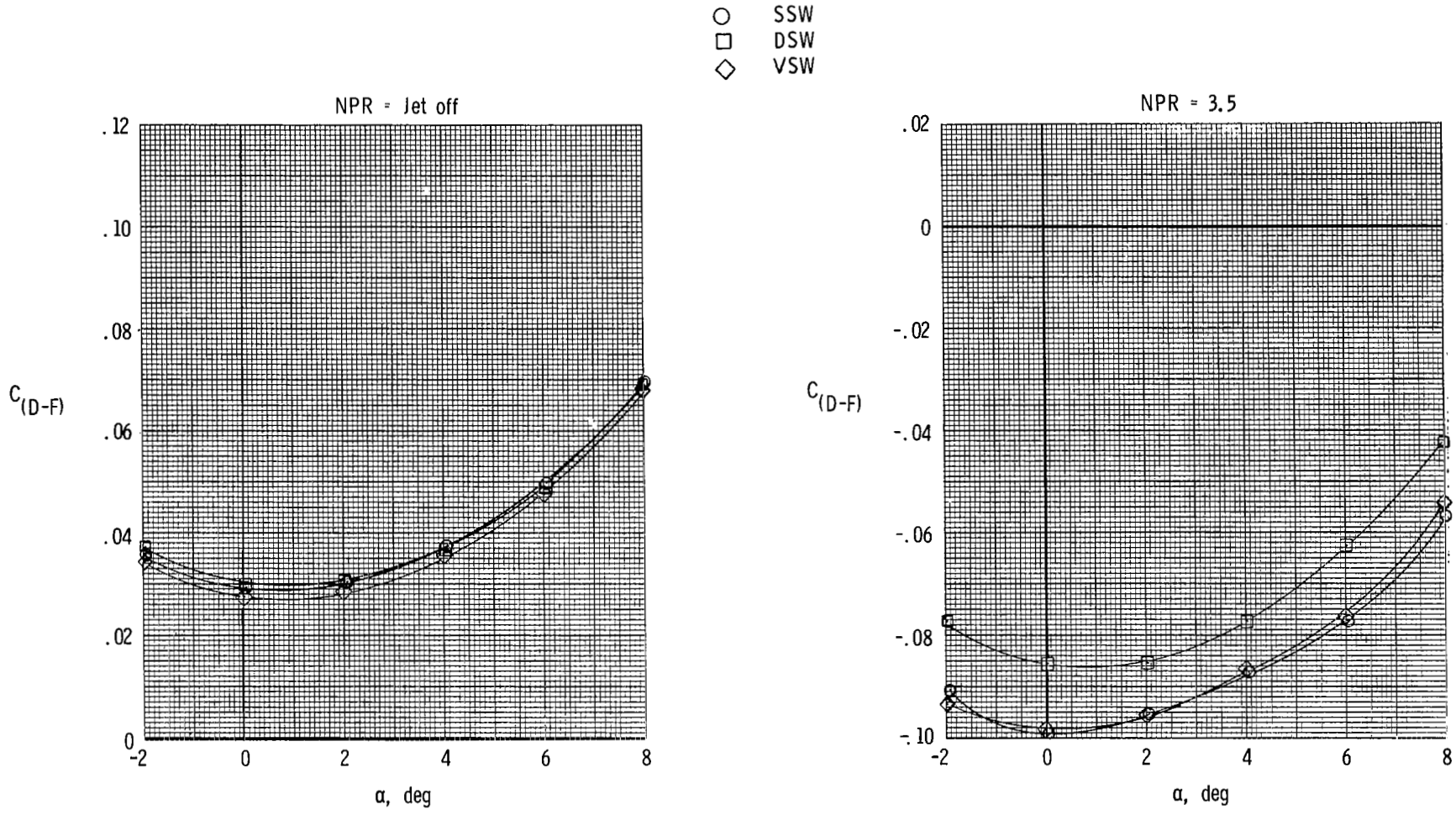

(a) M = 0.60.

Figure 63.- Effect of different nozzle sidewalls on drag-minus-thrust performance of configuration with 2-D C-D dry-power nozzles.

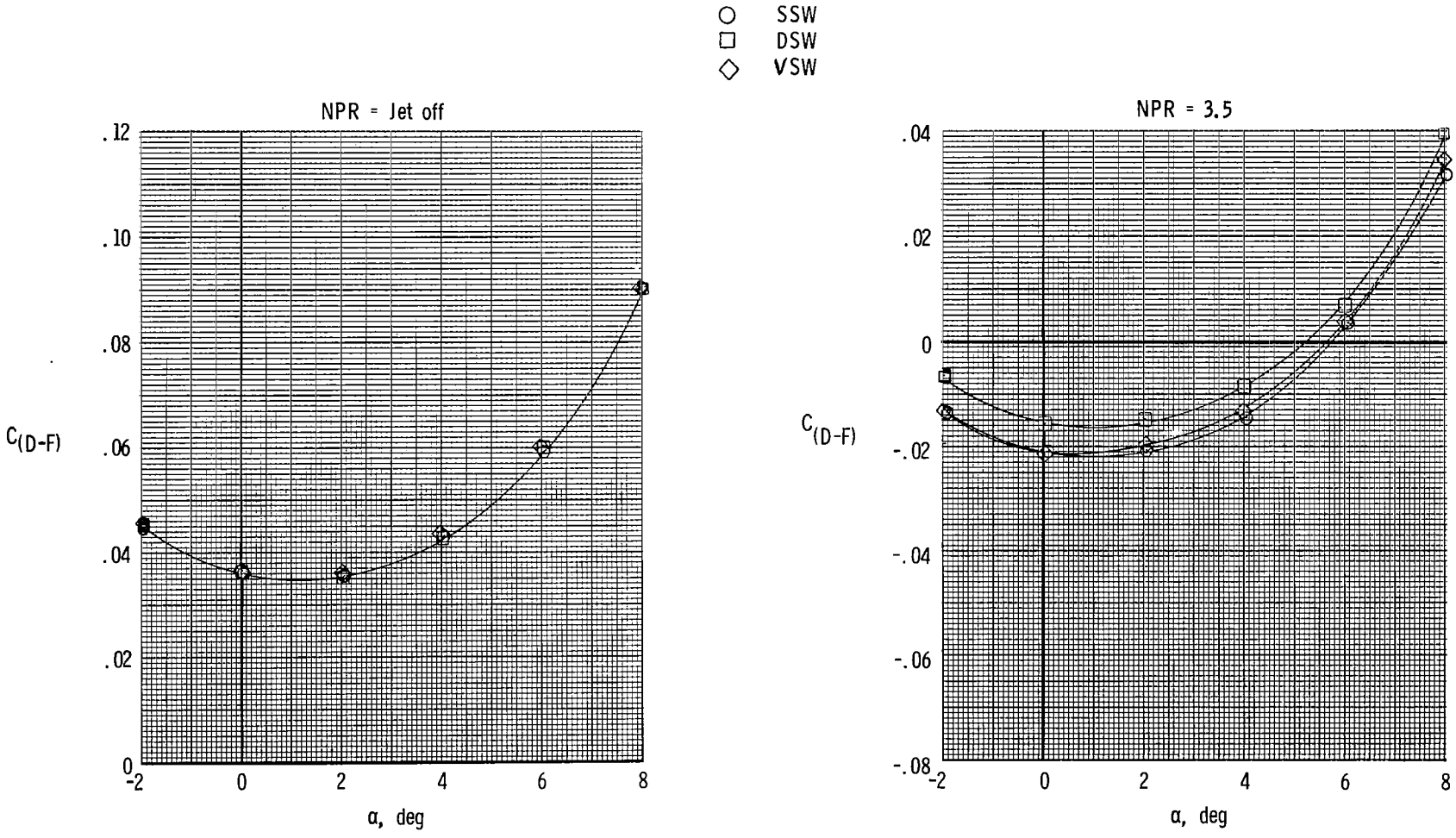

(b) M = 0.90.

Figure 63.- Concluded.

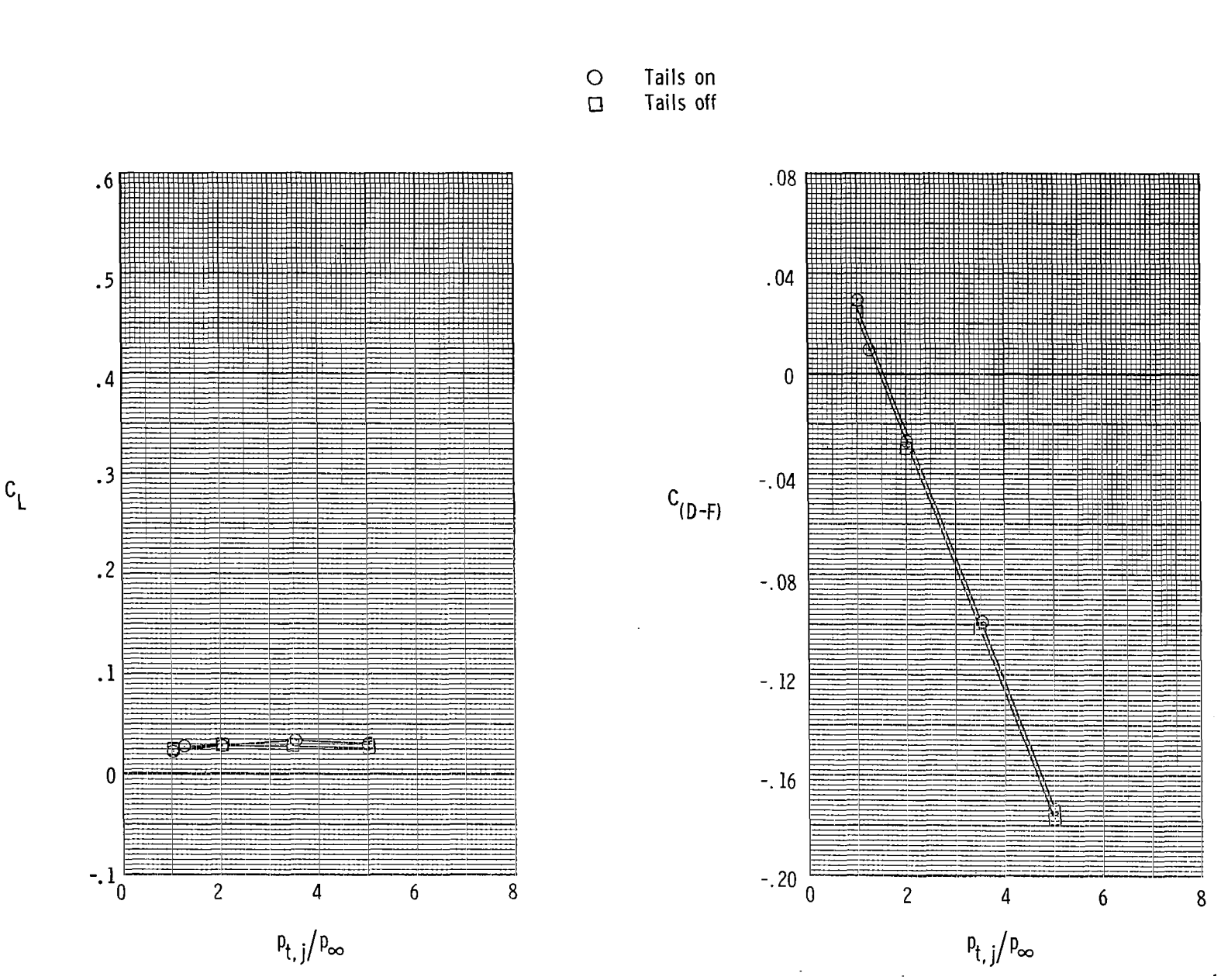

(a) $\alpha = 0°$.

Figure 64.- Effect of vertical tails on drag-minus-thrust performance of configuration with 2-D C-D SSW dry-power nozzles at M = 0.60.

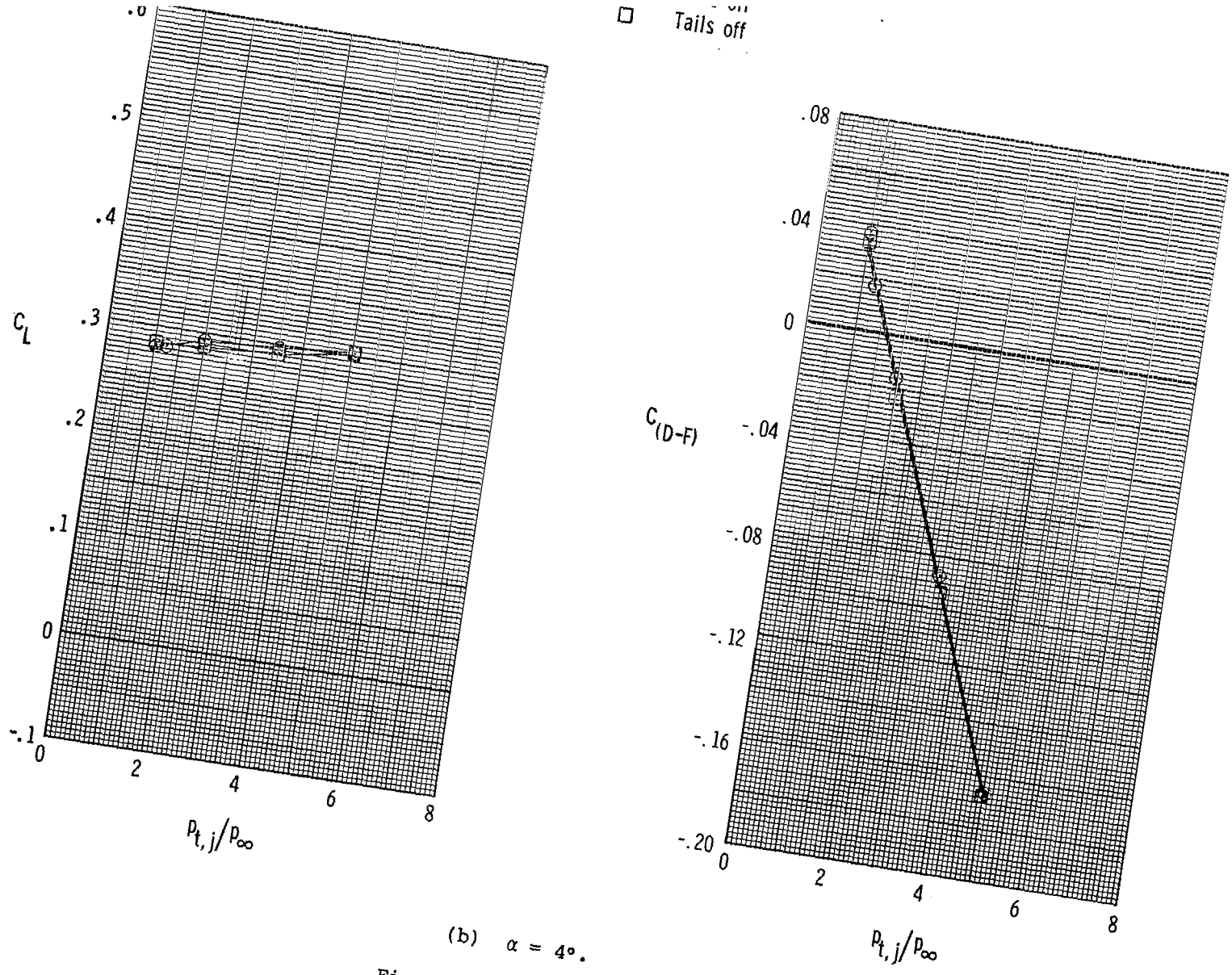

(b) $\alpha = 4°$.

Figure 64.- Continued.

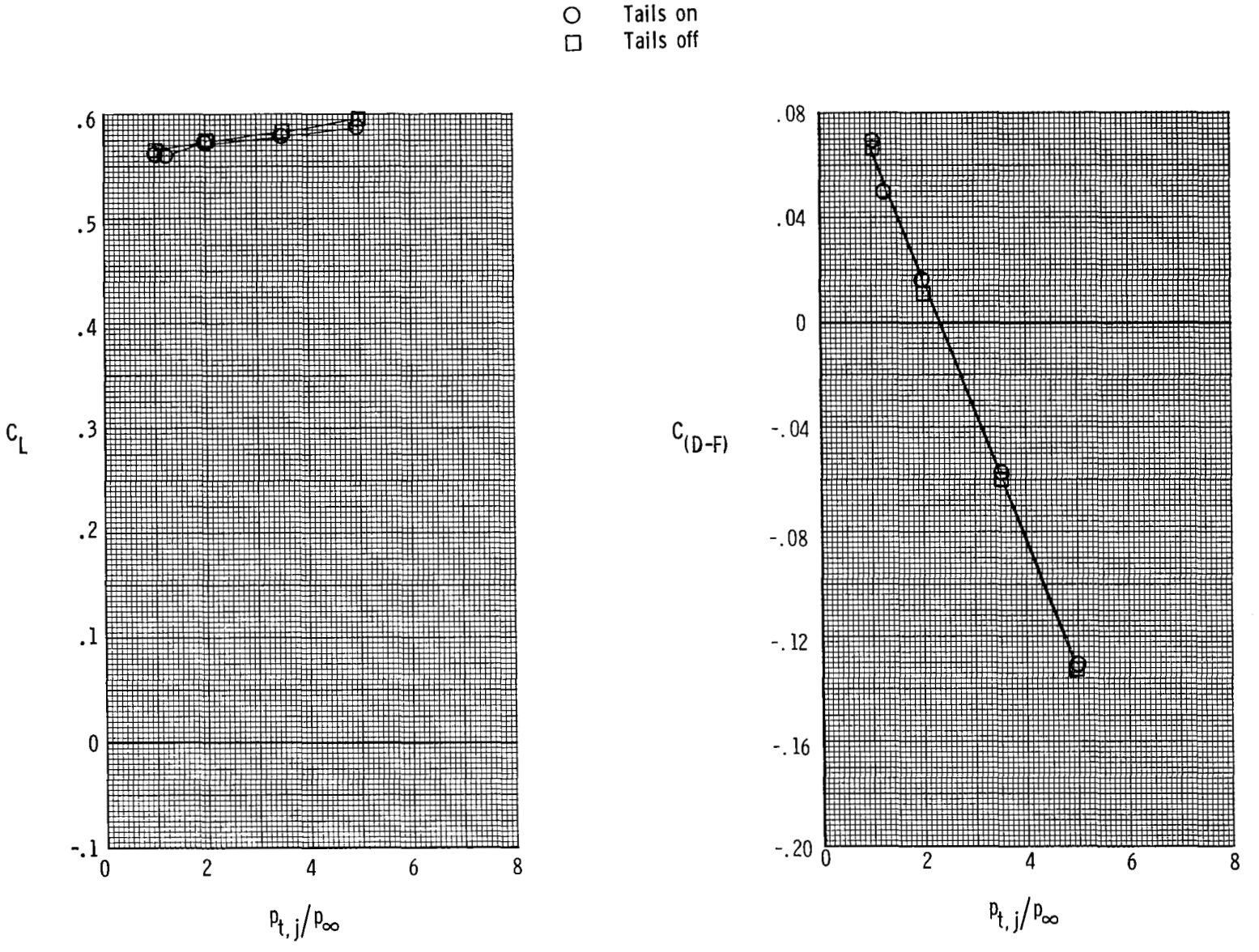

(c) $\alpha = 8°$.

Figure 64.- Concluded.

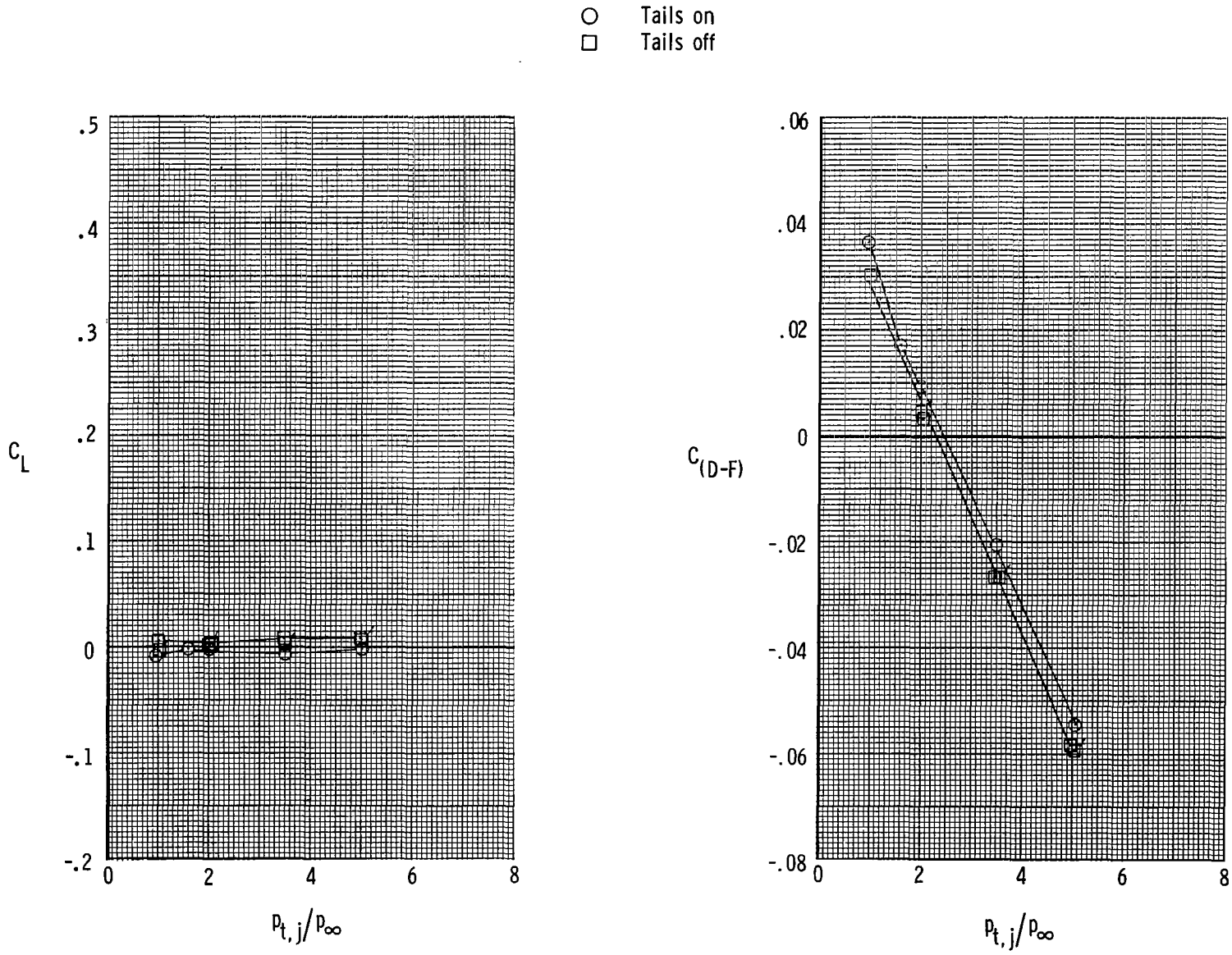

(a) $\alpha = 0°$.

Figure 65.- Effect of vertical tails on drag-minus-thrust performance of configuration with 2-D C-D SSW dry-power nozzles at M = 0.90. (Flagged symbols are repeat points.)

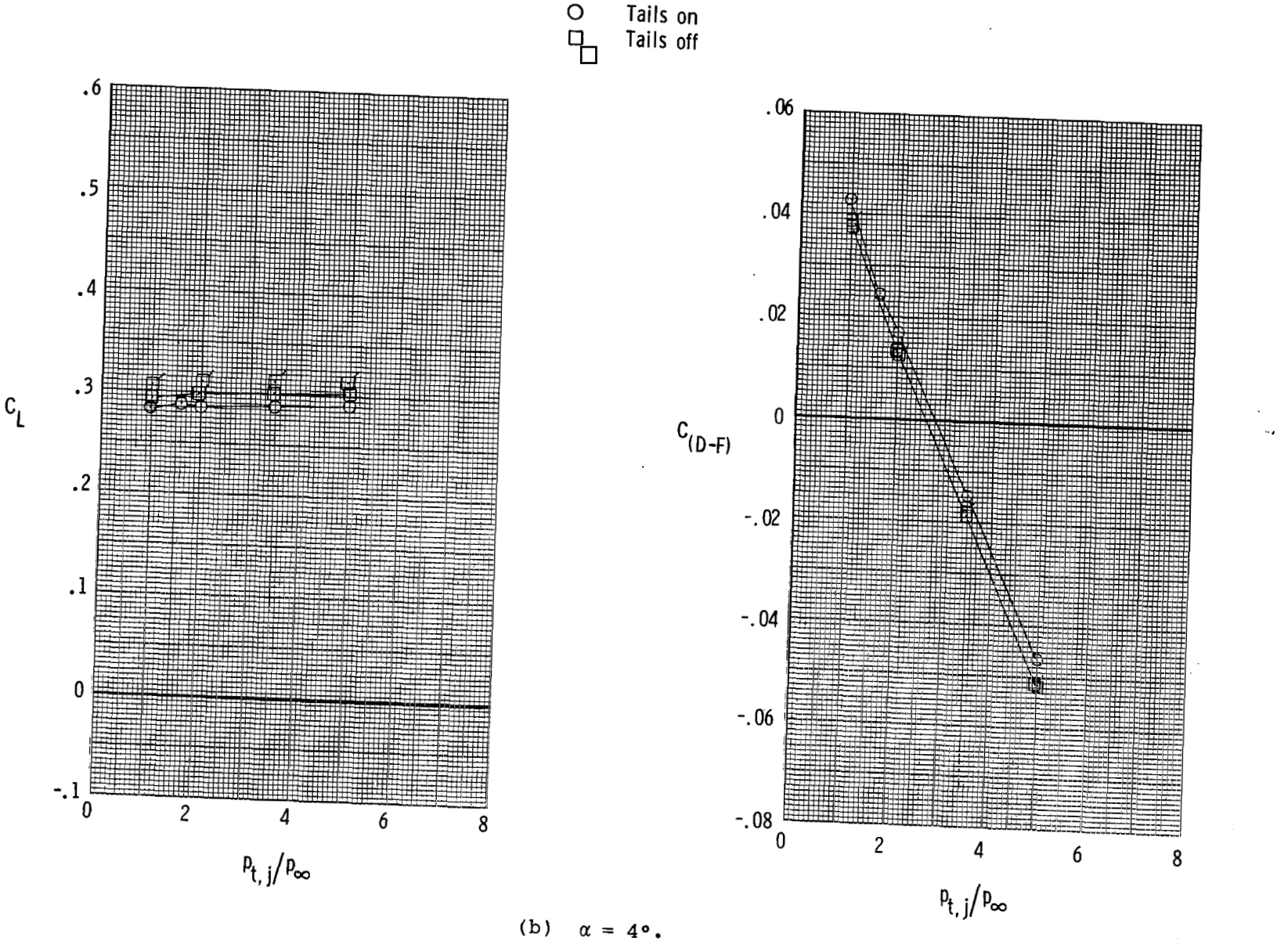

(b) $\alpha = 4°$.

Figure 65.- Continued.

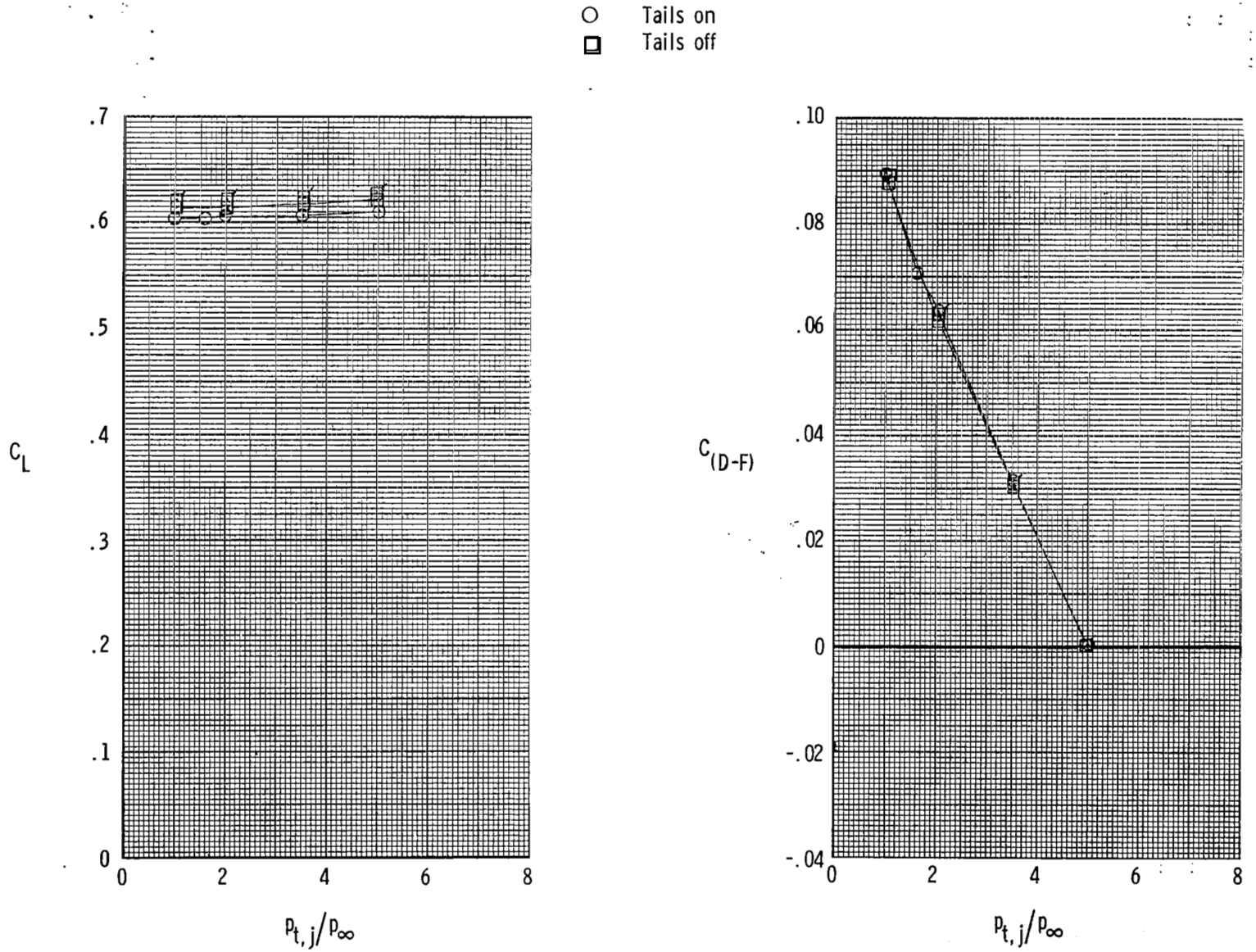

(c) $\alpha = 8°$.

Figure 65.- Concluded.

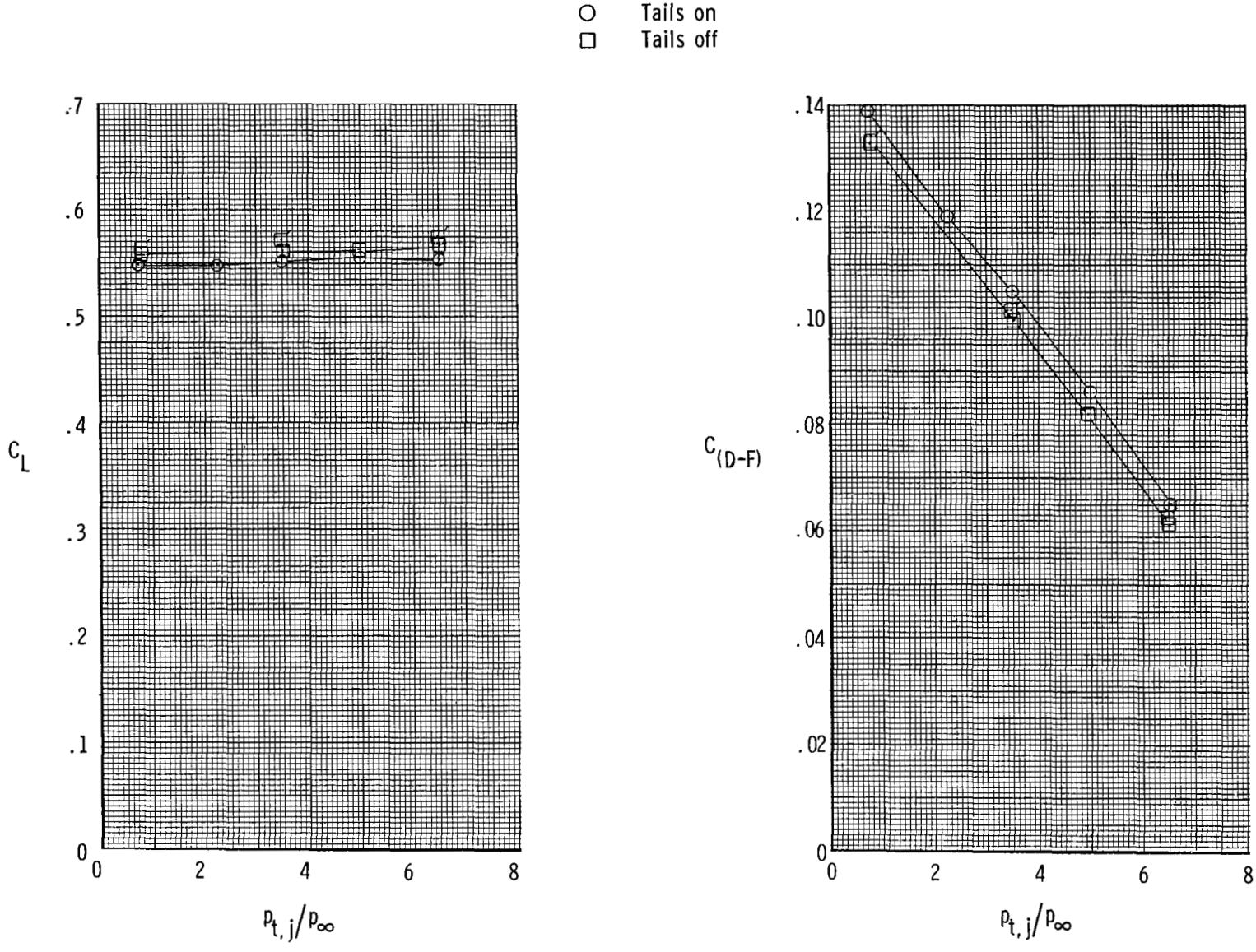

(c) $\alpha = 8°$.

Figure 66.- Concluded.

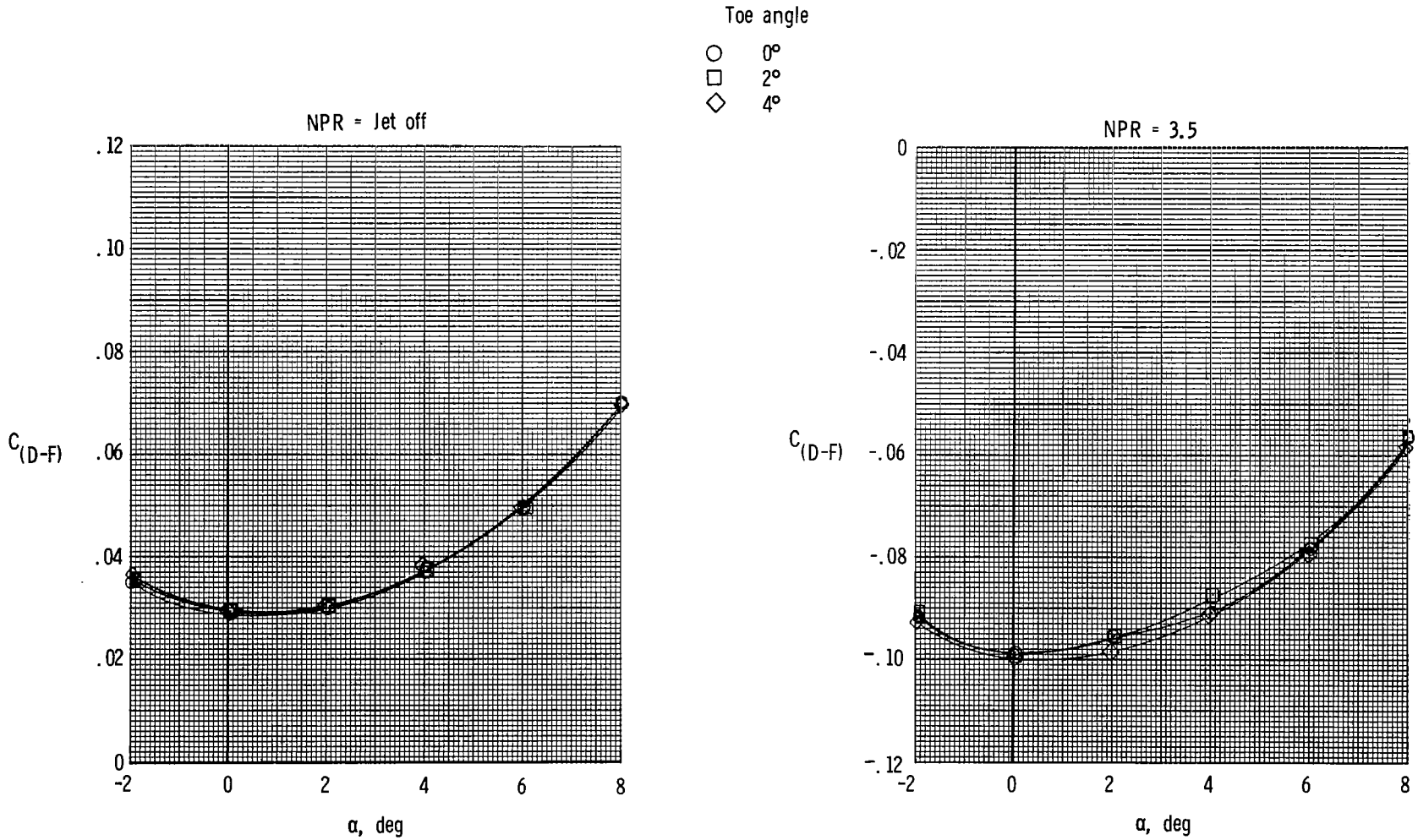

(a) M = 0.60.

Figure 67.- Effect of twin-vertical-tail toe angle (L.E. out) on drag-minus-thrust performance of configuration with 2-D C-D SSW dry-power nozzles.

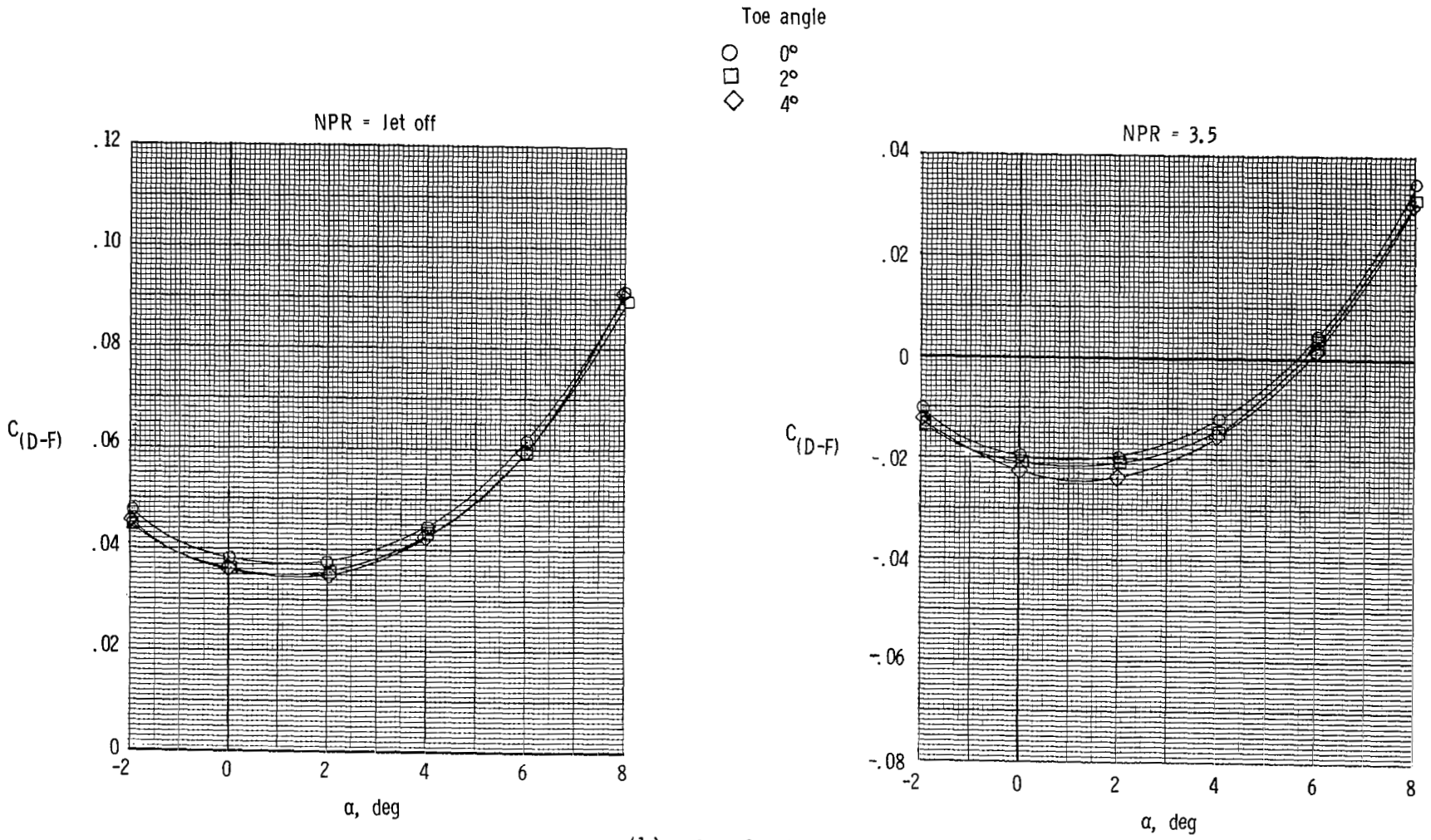

(b) M = 0.90.

Figure 67.- Concluded.

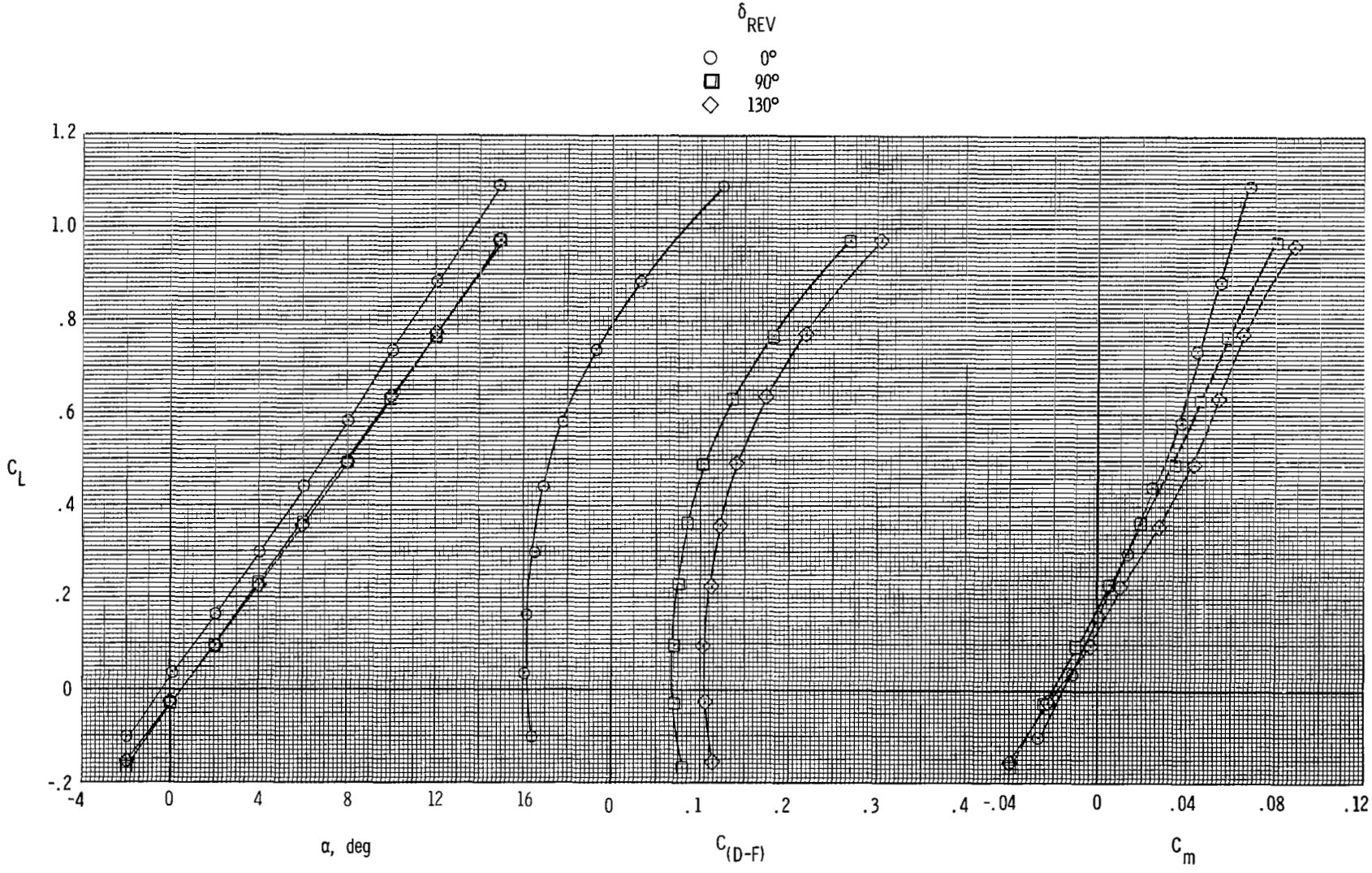

(a) M = 0.60; NPR = 3.5.

Figure 68.- Effect of thrust reversers on drag-minus-thrust performance of configuration with 2-D C-D SSW dry-power nozzles.

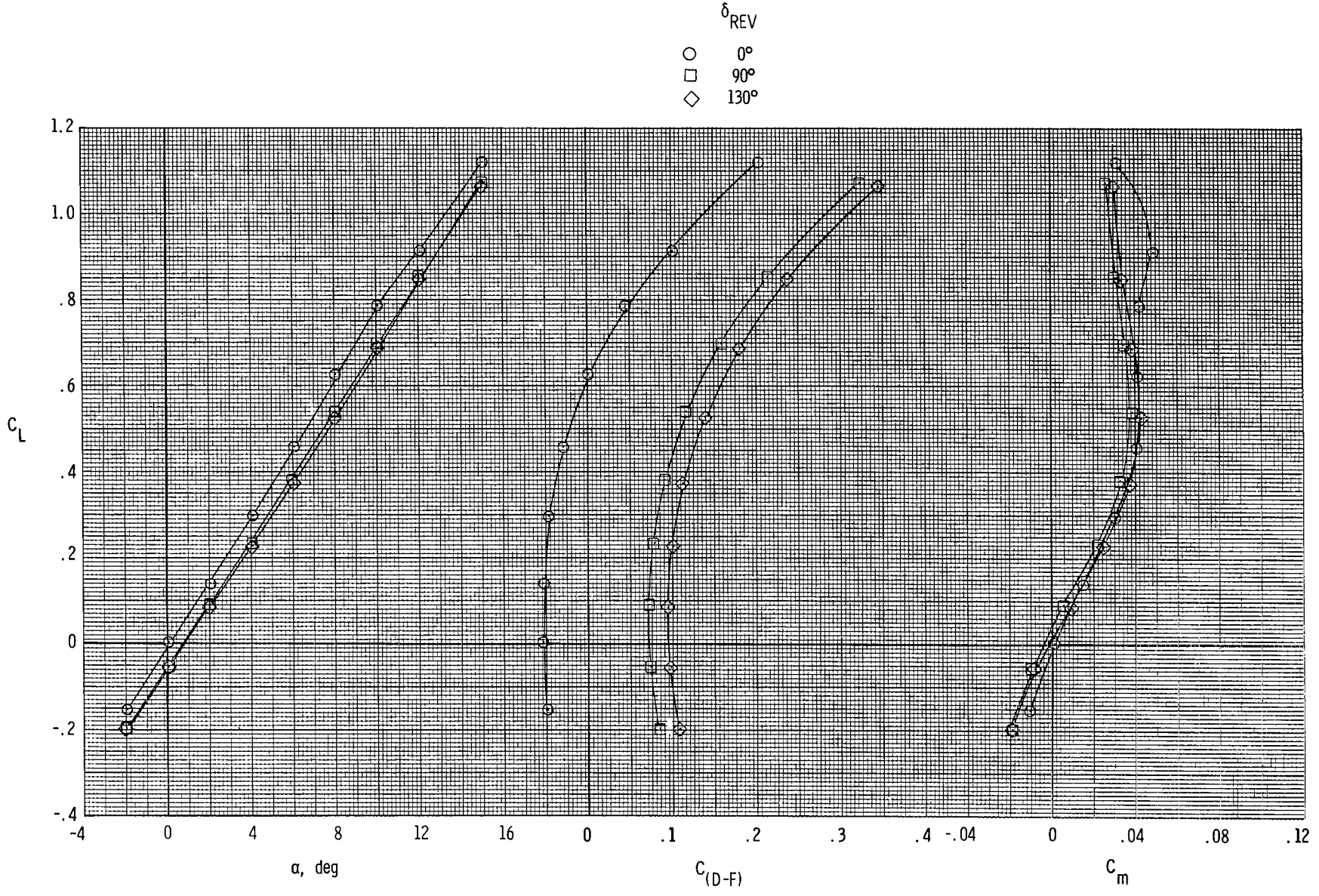

(b) M = 0.90; NPR = 5.0.

Figure 68.- Continued.

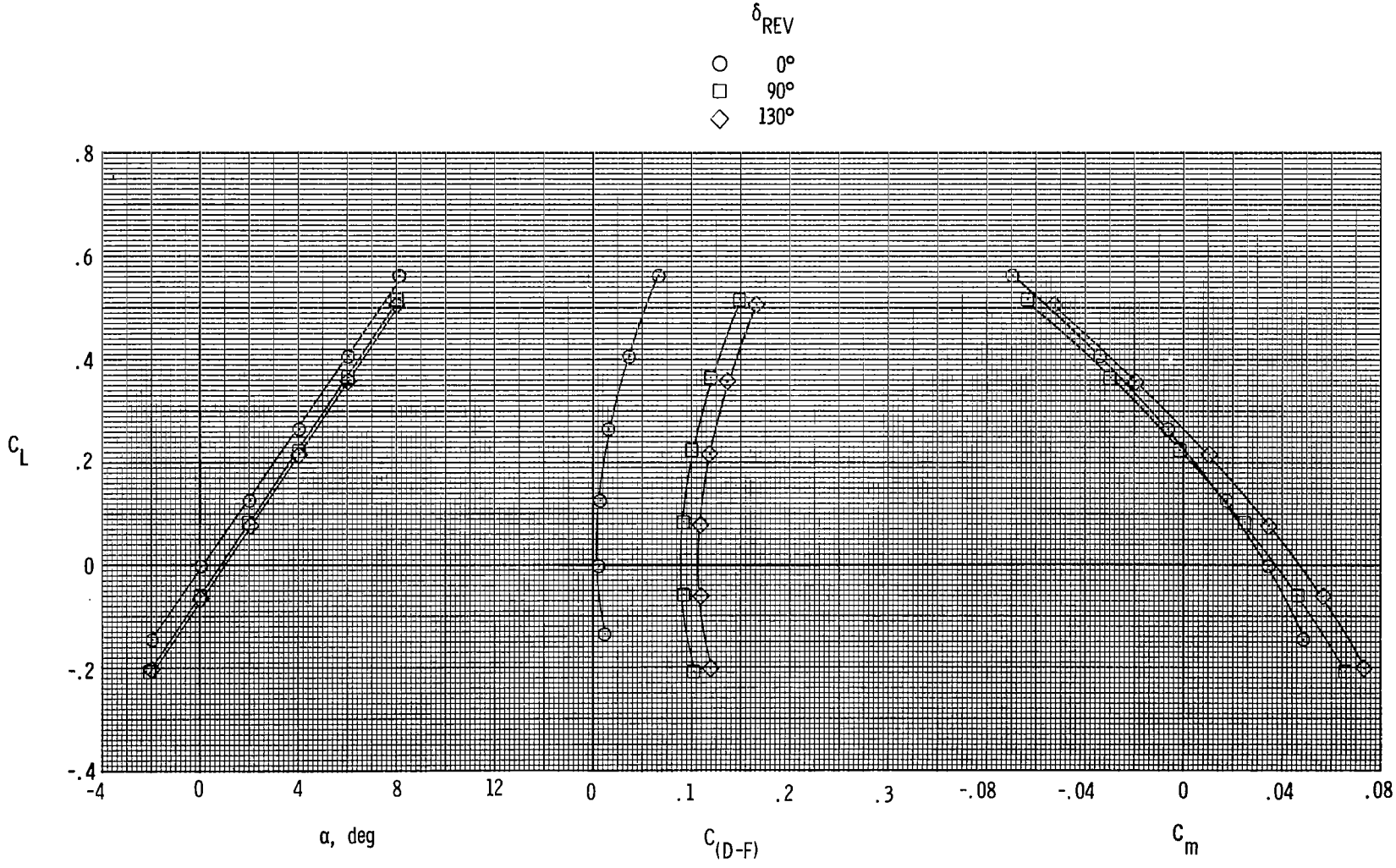

(c) M = 1.20; NPR = 6.5.

Figure 68.- Concluded.

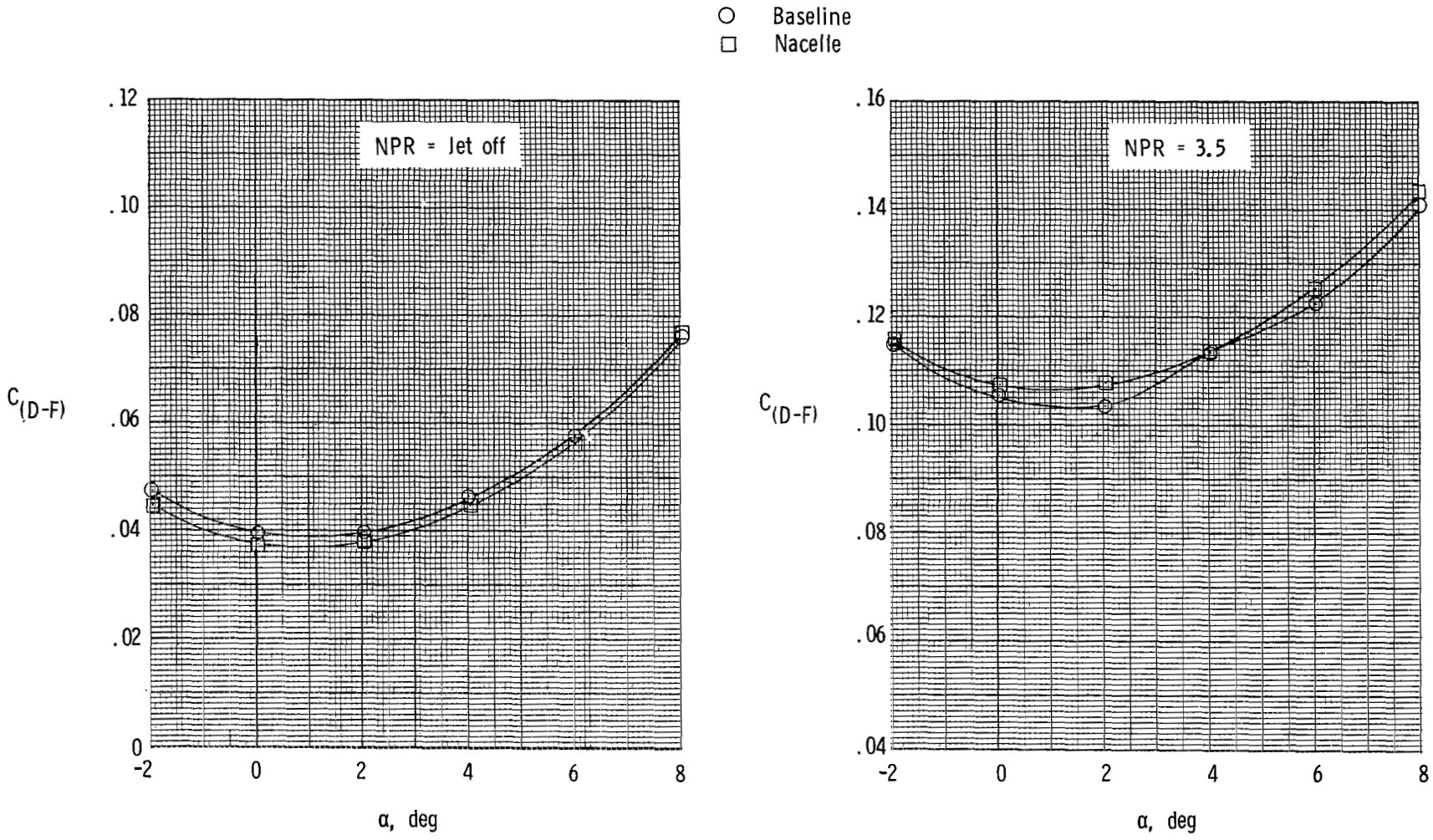

(a) M = 0.60.

Figure 69.- Effect of twin-vertical-tail location on drag-minus-thrust performance of configuration with 2-D C-D SSW dry-power nozzles and δ_{REV} = 130°.

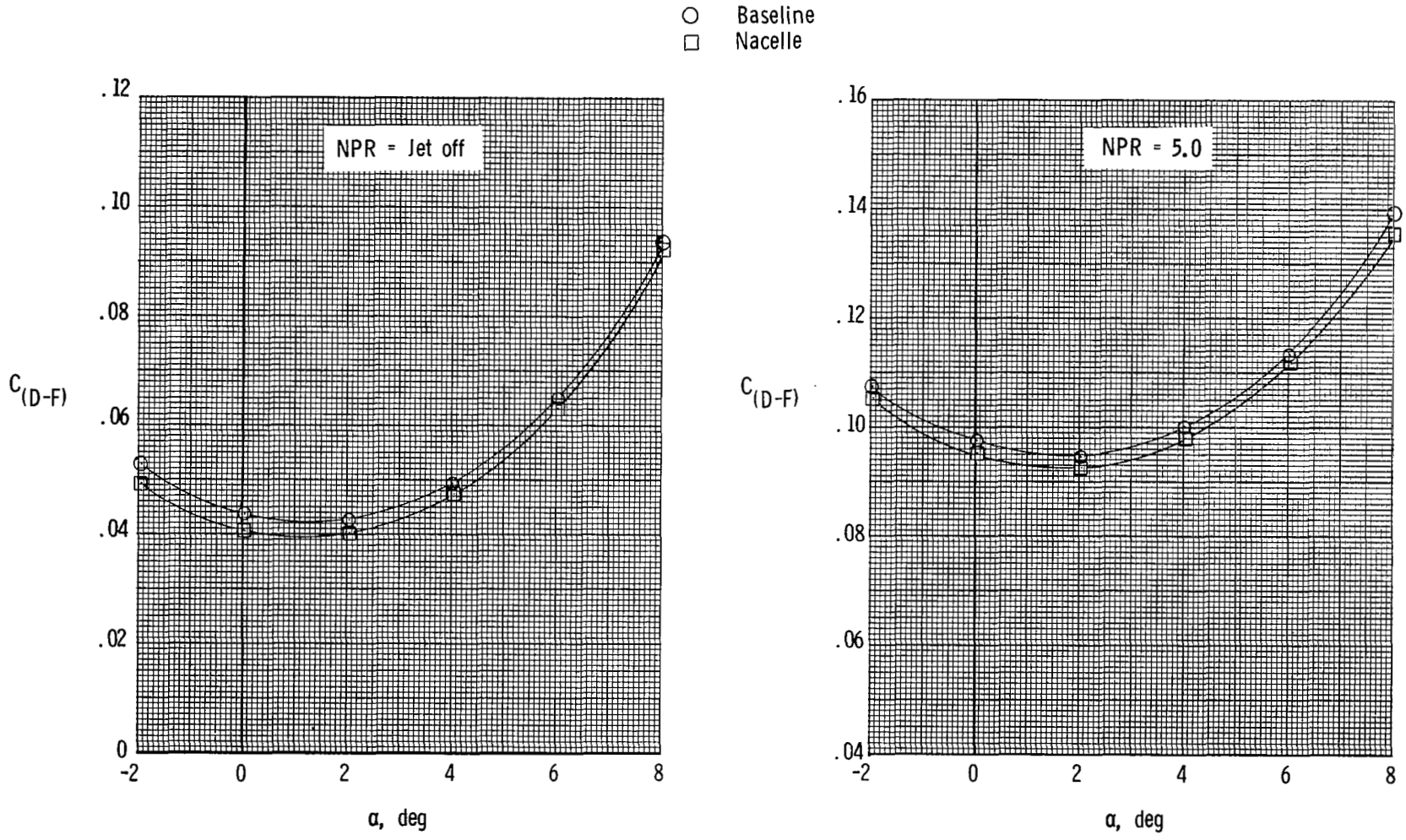

(b) M = 0.90.

Figure 69.- Concluded.

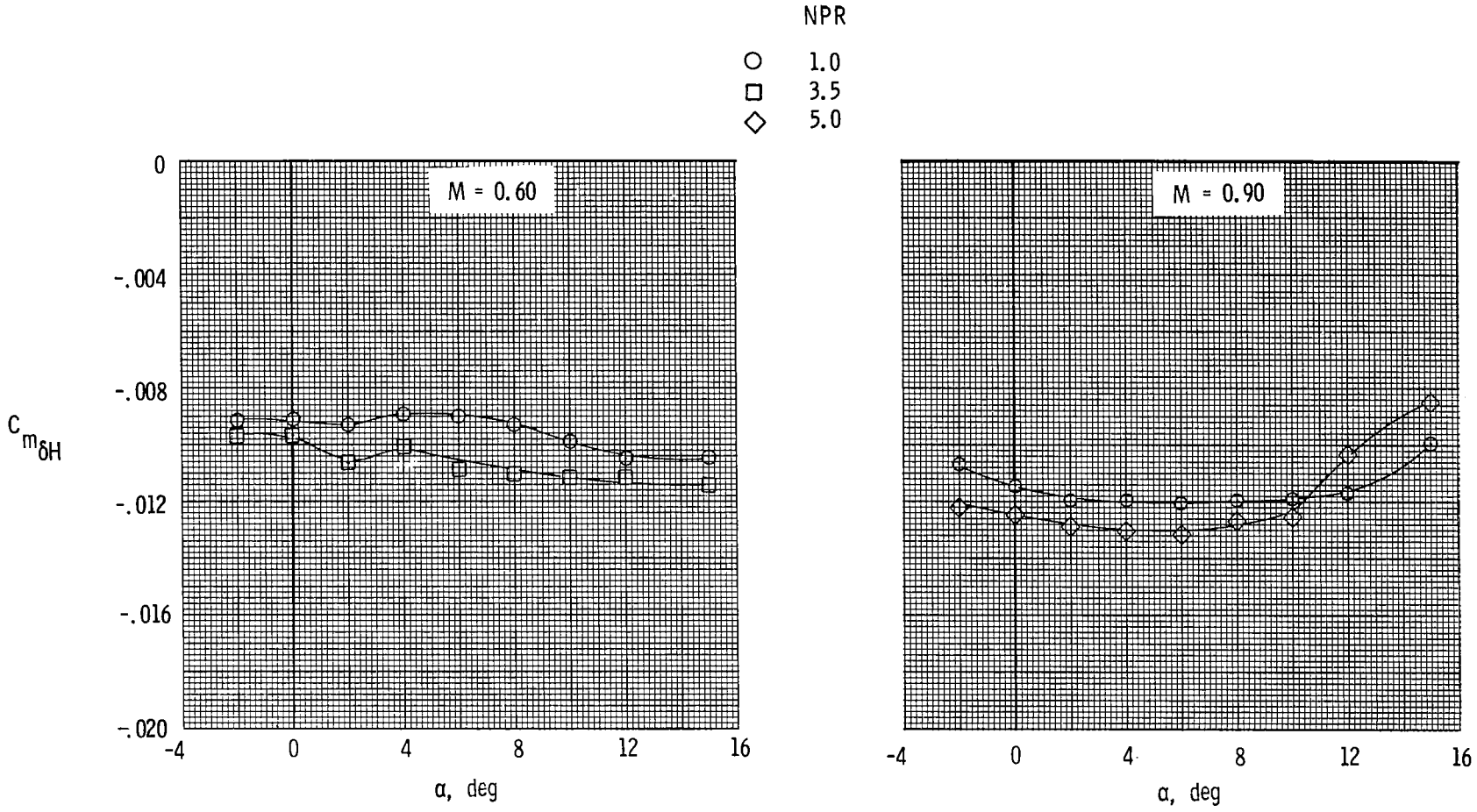

Figure 70.- Horizontal-tail pitch-control effectiveness for configuration with 2-D C-D SSW dry-power nozzles and $\delta_{REV} = 130°$.

1. Report No.	2. Government Accession No.	3. Recipient's Catalog No.
NASA TP-2043		

4. Title and Subtitle	5. Report Date
EFFECT OF NOZZLE AND VERTICAL-TAIL VARIABLES ON THE PERFORMANCE OF A THREE-SURFACE F-15 MODEL AT TRANSONIC MACH NUMBERS	August 1982
	6. Performing Organization Code 505-43-23-01
7. Author(s) Odis C. Pendergraft, Jr., and E. Ann Bare	8. Performing Organization Report No. L-15304
	10. Work Unit No.
9. Performing Organization Name and Address NASA Langley Research Center Hampton, VA 23665	11. Contract or Grant No.
	13. Type of Report and Period Covered Technical Paper
12. Sponsoring Agency Name and Address National Aeronautics and Space Administration Washington, DC 20546	14. Sponsoring Agency Code

15. Supplementary Notes

16. Abstract

An investigation was conducted in the Langley 16-Foot Transonic Tunnel to determine the longitudinal aerodynamic characteristics of twin two-dimensional (2-D) nozzles and twin baseline axisymmetric nozzles installed on a fully metric 0.047-scale model of the F-15 three-surface configuration (canards, wing, horizontal tails). The effects on performance of 2-D nozzle in-flight thrust reversing, locations and orientation of the vertical tails, and deflections of the horizontal tails were also determined. Test data were obtained at static conditions and at Mach numbers from 0.60 to 1.20 over an angle of attack range from -2° to 15°. Nozzle pressure ratio was varied from jet off to about 6.5.

17. Key Words (Suggested by Author(s))

Nozzle performance
Twin vertical tails
Two-dimensional nozzles
Thrust reversers
Propulsion effects
Horizontal-tail effectiveness

18. Distribution Statement

Unclassified - Unlimited

Subject Category 02

19. Security Classif. (of this report)	20. Security Classif. (of this page)	21. No. of Pages	22. Price
Unclassified	Unclassified	169	A08

For sale by the National Technical Information Service, Springfield, Virginia 22161

NASA-Langley, 1982